Effect of Crystallite Size and Water Partial Pressure on the Activity and Selectivity of Low Temperature Iron-based Fischer-Tropsch Catalysts

Virginia Cheang

Submitted to the University of Cape Town
in fulfilment of the requirements
for the degree of
Doctor of Philosophy

November 15, 2009

Acknowledgements

During the course of completing this PhD study, I have come to realize that this was not an individual endeavour. I would like to thank all the people that have helped me in various ways throughout this process. My supervisor, A/Prof. Michael Claeys, whose immense knowledge in the field of Fischer-Tropsch catalysis has been invaluable. He has given up much of his time during the course of this project, and made himself available during my numerous technical glitches in the laboratory, I cannot state how important this was to me. My co-supervisor, Prof. Eric van Steen; whose advice has been priceless.

All the members of the Centre for Catalysis Research at the University of Cape Town, who have all made it a wonderful place to work. Marc Wust, who always had time to help me, no matter how trivial the problem may have seemed to him. The same is true for Elma, Shaun and Rachel and various in-service trainees who worked in the group during the course of my studies. A special thanks also goes to Itai, Cathrin and Pete, who worked on similar projects to mine, they were wonderful in their advice and helping me learn to use different pieces of equipment. Also to Michael, Jako, Jurie and Youqi, whom I often asked for help and always got it. Joe and Peter at the workshop, who helped me with mechanical issues, and Granville with electrical issues as well as Helen and Suzana in the main labs, their advice and help were invaluable. Mohammed at the TEM labs, who spent many hours taking pictures for me.

Thanks to Remy Bucher and the XRD group at ITEMBA Labs in Stellenbosch, who ran XRD patterns for many of my samples. Esna du Plessis and Siyanda Lubhelwana at Sasol, who ran further XRD samples and helped

me with interpretation. Bruce Anderson, Lonzeche Lodya and their team at Sasol who ran Mössbauer experiments for me and taught me the concepts behind it. To Lodya in particular, who gave up his time to help in interpretation. To Sasol, UCT, THRIP and the NRF for the financial support, without which this work would not have been possible.

My friends and family deserve a very special thanks, and are foremost in making this thesis a success. My husband Nick, who has seen the best and worst moments, he has celebrated the triumphs with me and reassured me in the lowest moments. Certainly, he has been the rock I've hung on to throughout this rollercoaster ride. This PhD study would definitely not have been possible without my parents, whose love and support are unparalleled. This thesis is dedicated to my father who passed away in 1999, who is sorely missed.

Synopsis

Fischer-Tropsch synthesis is a reaction between hydrogen and carbon monoxide to produce long-chained hydrocarbons and water. It has been stated that the Fischer-Tropsch synthesis reaction is a surface phenomenon, thus for optimum catalyst performance, maximum metal usage must be achieved. Therefore it is expected that the smaller the crystallite size of the metal, the more active the catalyst will be under test conditions. This work investigates the influence of iron crystallite size and water co-feed on the activity and selectivity of low temperature Fischer-Tropsch synthesis.

In heterogeneous catalysis it is well known that with smaller crystallites, more active surface area is exposed allowing for higher overall activities. However the subject of size sensitivity remains an issue as research has shown that nano-meter sized crystallites below a certain point (ie. 6 nm) can behave differently to larger crystallites in terms of activity and selectivity in Fischer-Tropsch synthesis. It has been suggested that this behaviour may be due to the effect of crystallite size on iron phase changes such as oxidation by product water during the Fischer-Tropsch (FT) reaction. Alternatively, effects of structure sensitivity may play a role.

This work can essentially be divided into 3 sections; firstly, the preparation and characterisation of a model alumina supported iron catalyst with iron crystallites in the nano-meter range between 2 and 16 nm. Secondly, Fischer-Tropsch testing in a fixed bed reactor of model catalyst systems, testing the effect of differing crystallite size on the activity and selectivity of Fischer-Tropsch synthesis, followed by the characterisation of spent catalyst samples. Finally, Fischer-Tropsch testing of model catalyst systems under different conditions of water addition simulating conditions under high syn-

thesis gas conversion, again followed by the characterisation of spent samples.

The first major objective of this work was the preparation of a model catalyst sample, where a narrow size distribution was required as well as a good distribution of the metal crystallites onto the support material. A narrow size distribution was successfully achieved through the utilisation of the reverse micelle technique. Size control can be achieved through variation of the water to surfactant ratio, with a high ratio leading to larger crystallites being formed. An even distribution of metal crystallites onto the support material was harder to achieve. Four different support addition methods were tested as well as different support materials, drying conditions and calcination conditions. It was shown that the support addition method previously used by Mabaso (2005) was the one that achieved the best dispersion. Furthermore, the variation of support, drying and calcination conditions can have a large impact on the final catalyst with different supports and conditions leading to increased clustering and sintering. Alumina was found to be the best support material and a threshold temperature of 300 °C existed for calcination past which severe sintering took place. Model catalysts were successfully prepared with a narrow size distribution and a good dispersion of metal crystallites onto the support material. Six catalyst samples were prepared with crystallite sizes ranging between 2 and 16 nm with a metal loading of 13 wt%.

Examination of the synthesis gas conversion showed that the specific Fischer-Tropsch rate shows a decrease with decreasing crystallite size. This change in rate has been theorized to be due to either the thermodynamically simpler oxidation of smaller crystallites or the lack of ensembles of atoms required for Fischer-Tropsch synthesis on smaller crystallites. Through the characterisation of spent samples, it has been shown that the 'Ensemble Effects' theory to be the more likely one as bulk oxidation was not observed.

In terms of product formation, smaller crystallites showed a higher inclination for the production of methane. This is further support for the 'Ensemble effects' theory, as this result leads to the conclusion that less chain growth sites and more methanation sites may be available on smaller crystallites leading to an increased methane selectivity on small crystallites.

Other product selectivities such as olefin and oxygenate formation did not follow the trend of hydrogen richer products obtained on smaller crystallites, instead it was the catalyst samples in the middle metal crystallite size range that showed increased propensity toward secondary reactions. This was believed to be due to either an extension of the 'Ensemble Effects' theory or the electronic effects between readsorbing olefins and the metal surface.

A conversion level of below 10% was chosen for this work in order to fully and directly compare the activity and selectivity results of the various catalyst samples. However this condition means that the effect of higher conversion levels are not shown. In order to overcome this problem the water partial pressure was increased, where a higher water partial pressure simulates the conditions of higher conversion via addition of water. The 'basecase' water partial pressure was set at 0 bar, while water addition conditions had water partial pressures of 3 and 6 bar.

In terms of specific Fischer-Tropsch rate it was shown that the addition of water leads to deactivation of the catalyst irrespective of crystallite size. This deactivation has been theorized by previous work to be either due to oxidation or sintering. Again characterisation results, including an *in-situ* method, show that oxidation is not the likely cause of the deactivation, instead the clustering and agglomeration of metal crystallites show that sintering is the more likely candidate.

Product formation results show that the addition of water leads to a decrease in methane selectivity and an increase in olefin production. It is theorized that these selectivity results are caused by water inhibiting desorption and readsorption mechanisms leading to increased chain growth and decreased secondary reactions respectively.

Contents

Acknowledgements **i**

Synopsis **iii**

Contents **xi**

List of Figures **xxvii**

List of Tables **xxxi**

1 Introduction **1**

2 Literature Review **3**

2.1 Fischer-Tropsch Synthesis 3

2.1.1 Fischer-Tropsch Reaction 4

2.1.2 Fischer-Tropsch Mechanisms 5

2.1.2.1 Alkyl Mechanism 6

2.1.2.2 Alkenyl Mechanism 7

2.1.2.3 Enol Mechanism 9

2.1.2.4 CO-Insertion Mechanism 10

2.1.3 Fischer-Tropsch Products 10

2.1.4 Fischer-Tropsch Catalysts 14

2.2 Catalyst Deactivation 15

2.2.1 Poisoning 16

2.2.2 Fouling 18

2.2.3 Thermal Degradation 19

2.2.4 Vapour-Solid and Solid-Solid Reactions 22
2.3 Effect of Water 24
2.4 Conventional Catalyst Preparation Techniques 26
2.4.1 Impregnation 27
2.4.2 Precipitation 29
2.5 Microemulsion Technique 29
2.5.1 Microemulsion Systems 30
2.5.2 Preparation of Nano-particles 31
2.6 Effect of Crystallite Size in Fischer-Tropsch Synthesis 34

3 Scope of Thesis **43**

4 Experimental Methodology **45**
4.1 Catalyst Preparation 45
4.1.1 Synthesis of Supported Model Catalysts 45
4.1.1.1 Variation of Support Addition Method 47
4.1.1.2 Variation of Support Material 51
4.1.1.3 Variation of Solvent 54
4.1.1.4 Variation of Drying Technique 54
4.1.1.5 Variation of Calcination Conditions 54
4.2 Characterisation of Support Material 56
4.3 Characterisation of Supported Model Catalyst 56
4.3.1 Transmission Electron Microscopy (TEM) 56
4.3.2 Atomic Absorption Spectroscopy (AAS) 57
4.3.3 Temperature Programmed Reduction (TPR) 57
4.3.4 X-Ray Diffraction (XRD) 58
4.3.5 Mössbauer Spectroscopy (MAS) 59
4.3.6 Magnetic Measurements 60
4.4 Fischer-Tropsch Synthesis Experiments 62
4.4.1 Test Unit Set-up 62
4.4.2 Reactor Set-up 62
4.4.3 Experimental Procedure 65
4.4.3.1 Base Case Runs 65

4.4.3.2 Runs with Water Co-feeding 66
4.4.4 Offline Sampling Technique 67
4.5 Fischer-Tropsch Synthesis Experiments in Set-up for Magnetic *in-situ* Characterisation 68
4.5.1 Test Unit Set-up 68
4.5.2 Reactor Set-up 70
4.5.3 Experimental Procedure 72
4.5.4 Magnetic Sampling Procedure 74
4.6 Product Analysis 75
4.6.1 Analysis of Permanent Gases 75
4.6.2 Analysis of Organic Products 76
4.6.3 Data Work-up 77

5 Model Catalyst Synthesis Results 83
5.1 Method Variation 83
5.2 Support Variation 85
5.3 Solvent Variation 89
5.4 Variation of Drying and Calcination Conditions 92
5.5 Summary of Model Catalyst Synthesis Results 97

6 Results of Characterisation of Model Catalysts 101
6.1 TEM Analysis 102
6.2 XRD Analysis 107
6.3 TPR Analysis 108
6.4 AAS Analysis 111
6.5 Summary of Characterisation Results for Supported Crystallites 112

7 Fischer-Tropsch Testing 115
7.1 Dependence on Crystallite Size 115
7.1.1 Fischer-Tropsch Activity and Characterisation of Spent Catalysts 115
7.1.1.1 Characterisation of Spent Catalysts 121
7.1.2 Product Formation 124
7.1.2.1 Carbon Dioxide Formation 125

7.1.2.2 Methane Formation and Chain Growth Probability . . . 126
7.1.2.3 Olefin Formation . . . 132
7.1.2.4 Oxygenate Formation . . . 140
7.1.2.5 Branched Product Formation . . . 142
7.1.3 Summary and Discussion of Results for Fischer-Tropsch Dependency on Crystallite Size . . . 144
7.2 Dependence on Water Partial Pressure . . . 146
7.2.1 Fischer-Tropsch Activity and Characterisation of Spent Catalysts . . . 148
7.2.1.1 Characterisation of Spent Catalysts - Water Series . . . 152
7.2.2 Product Formation . . . 163
7.2.2.1 Carbon Dioxide Formation . . . 163
7.2.2.2 Methane Formation and Chain Growth Probability . . . 169
7.2.2.3 Olefin Formation . . . 172
7.2.2.4 Oxygenate Formation . . . 181
7.2.3 Summary of Results for Fischer-Tropsch Dependence on Water Partial Pressure . . . 181
7.3 Magnetic in-situ Characterisation of Catalysts . . . 184
7.3.1 Phase Changes in FT Synthesis as followed by an $in-situ$ Magnetometer . . . 186
7.3.2 Crystallite Size changes in FT Synthesis as followed by an $in-situ$ Magnetometer . . . 192

8 Conclusions **199**

9 Recommendations and Future Work **203**

A List of Chemicals **217**

B Data Work-up : Anderson-Schulz-Flory Distributions **219**

C Fischer-Tropsch Testing **223**

D Dependence on Water Partial Pressure **239**

E Calculation of Surface Area **251**

List of Figures

2.1 Reaction pathway for alkyl mechanism in Fischer-Tropsch synthesis (Adapted from Claeys and van Steen (2004)) 7

2.2 Reaction pathway for alkenyl mechanism in Fischer-Tropsch synthesis (Adapted from Claeys and van Steen (2004)) 8

2.3 Reaction pathway for enol mechanism in Fischer-Tropsch synthesis (Adapted from Claeys and van Steen (2004)) 9

2.4 Reaction pathway for CO insertion mechanism in Fischer-Tropsch synthesis (Adapted from Claeys and van Steen (2004)) 11

2.5 Fischer-Tropsch stepwise growth process - a series of chain growth and product desorption. 13

2.6 Selective (*top*) and non-selective (*bottom*) poisoning in heterogeneous catalysis. 17

2.7 Schematic of the various stages in the formation and growth of particles from a monomer dispersion (Moulijn et al. (2001)) 21

2.8 Change in composition of an iron catalyst in high temperature Fischer-Tropsch synthesis (Dry (1981)) 23

2.9 Schematic of microemulsion system 31

2.10 Ternary phase diagram for a surfactant-oil-water system (Mabaso (2005)) 32

2.11 Preparation of nano-crystallites using two reverse-micelle solutions; one containing the metal precursor in the aqueous phase and another with the precipitating agent. 34

2.12 Preparation of nano-crystallites using a single reverse-micelle solution, with the precipitating agent added to the solution directly. 35

2.13 Effect of cobalt crystallite size on the turn-over frequency of Fischer-Tropsch synthesis (Bezemer et al. (2006)). 36

2.14 Effect of iron crystallite size on the turn-over frequency of Fischer-Tropsch synthesis (Mabaso (2005)). 36

2.15 Effect of cobalt crystallite size on the methane selectivity and C_8 olefin to paraffin ratio of Fischer-Tropsch synthesis (Bezemer et al. (2006)). 37

2.16 Effect of iron crystallite size on the methane selectivity and C_8 olefin to paraffin ratio of Fischer-Tropsch synthesis (Mabaso (2005)). 38

2.17 "The Ensemble Effect" explaining structure sensitivity in Fischer-Tropsch synthesis (Niemantsverdriet et al. (1980)). 40

2.18 "The Oxidation Theory" stability region of spherical β-Co(fcc) and CoO crystallites in H_2O/H_2 atmosphere at 493K as a function of the cobalt crystallite size (van Steen et al. (2005)). . . 41

4.1 Water(W) - Berol 050(S) - n-hexane(O) ternary diagram, showing the stability region and the composition of the reverse micelle system from which the microemulsion solutions were formed (Determined by Mabaso (2005)). Sample codes: a:'2 nm', b:'3 nm', c:'7 nm', d:'9 nm', e:'14 nm' and f:'16 nm' . . . 48

4.2 Schematic of preparation method 1, single reverse micelle solution used, no precipitation step, addition of support material directly into the reverse micelle solution 50

4.3 Schematic of preparation method 2, precipitation using two reverse micelle solutions. Support addition after precipitate formation as used by Mabaso (2005) 51

4.4 Schematic of preparation method 3, preparation of unsupported metal crystallites via precipitation of two reverse micelle solutions, followed by re-dispersion of metal crystallites and support addition in a new solvent 52
4.5 Schematic of preparation method 4, preparation of unsupported metal crystallites via precipitation of two reverse micelle solutions, followed by re-dispersion of metal crystallites and support addition in a new solvent 53
4.6 Schematic set-up of experimental test unit for Fischer-Tropsch synthesis 63
4.7 Schematic set-up of fixed-bed U-tube reactor used for Fischer-Tropsch synthesis 64
4.8 Schematic of offline amouple sampling set-up 68
4.9 Schematic set-up of experimental test unit for magnetic *in-situ* characterisation during Fischer-Tropsch synthesis 69
4.10 (A): Drawing of fixed bed reactor set-up for *in-situ* characterisation of magnetic properties. (B) Top view of magnetic reactor set up. (C): Side view of magnetic reactor set up, showing position of infrared heaters. 71

5.1 XRD patterns of iron crystallites on alumina (a) Method 1 - Hematite, (b) Method 2 - Hematite, (c) Method 3 - Maghemite and (d) Method 4 - Hematite 85
5.2 TEM images showing the effect of method of support addition on iron crystallite dispersion on alumina (a) Method 1, (b) Method 2, (c) Method 3 and (d) Method 4. Where the red circles indicate clustering of iron crystallites and blue circles indicate individual crystallites well dispersed onto the support material 86
5.3 TPR profile for a Method 3 loading of iron crystallites on alumina with n-hexane as the solvent 87
5.4 Zeta potential of different support materials (a) Silica, (b) Silica modified with alumina and (c) Alumina 88

5.5 XRD patterns of iron crystallites on alumina using Method 4: (a) Alumina - Hematite, (b) Silica modified with alumina - Hematite/Maghemite and (c) Silica - Maghemite 89
5.6 TEM images showing the effect of solvent on dispersion of iron crystallites on alumina (a) Alumina, (b) Silica modified with alumina and (c) Silica 90
5.7 XRD patterns of iron crystallites on alumina using Method 4: (a) Ethanol - Hematite, (b) Water - Hematite and (c) n-Hexane - Hematite 92
5.8 TEM images showing the effect of solvent on iron crystallite dispersion on alumina: (a) Ethanol, (b) Water and (c) n-Hexane 93
5.9 TEM images showing the effect of different drying conditions on the metal crystallite size and dispersion on support: (a) '3 nm' catalyst dried in a rotary drier, (b) '3 nm' catalyst dried in oven for 3 hours at 120 °C 95
5.10 TEM images showing the effect of different calcination conditions on the metal crystallite size and dispersion on support: (a) '2 nm' catalyst calcined for 1hr at 350 °C, (b) '2 nm' catalyst calcined for 16 hours at 350 °C and (c) '2 nm' catalyst calcined for 16 hours at 300 °C 96

6.1 TEM images of catalyst samples with the smallest metal crystallites of '2 nm' and '3 nm': *(left)*: Calcined samples, *(right)*: Reduced samples 103
6.2 TEM images of catalyst samples with medium metal crystallites of '7 nm' and '9 nm': *(left)*: Calcined samples, *(right)*: Reduced samples 104
6.3 TEM images of catalyst samples with the largest metal crystallites of '14 nm' and '16 nm': *(left)*: Calcined samples, *(right)*: Reduced samples 105
6.4 Crystallite size distributions of calcined and reduced samples of all six alumina supported tested catalysts as determined by TEM analysis 106

6.5 XRD patterns of a reduced and calcined '9 nm' catalyst and a pure alumina support. Reference patterns for hematite, maghemite, magnetite, and metallic iron are also shown 108

6.6 XRD patterns of calcined iron catalysts on an alumina support. Reference patterns for hematite, maghemite and magnetite are also included. (a) '2 nm' (b) '3 nm' (c) '7 nm' (d) '9 nm' (e) '14 nm' (f) '16 nm' 109

6.7 TPR traces for all six different catalysts, measuring H_2 consumption as a function of temperature 111

7.1 Specific Fischer-Tropsch rate as a function of time for three selected catalysts ('2 nm', '9 nm', '16 nm') at initial (reduced) crystallite size (T = 240 °C, P = 12 bar, $P_{syn-gas}$ = 10 bar, H_2/CO ratio = 2) 118

7.2 Specific Fischer-Tropsch rate and methane selectivity as a function of initial (reduced) crystallite size at steady state for all 6 alumina supported iron model catalysts (T = 240 °C, P = 12 bar, $P_{syn-gas}$ = 10 bar, H_2/CO ratio = 2) 118

7.3 TEM micrographs of reduced *(left)* and spent *(right)* samples of two selected alumina supported model iron catalysts ('3 nm' and '14 nm') 119

7.4 Crystallite size distributions of calcined, reduced and spent samples of all six alumina supported model iron catalysts. . . 120

7.5 Selectivity of carbon dioxide as a function of crystallite size for both initial state (10 - 20 min with reduced crystallite sizes) and steady state (50 - 300 min with spent crystallite sizes) (T = 240 °C, P = 12 bar, $P_{syn-gas}$ = 10 bar, H_2/CO ratio = 2) . 126

7.6 Rate of formation of carbon dioxide normalized to initial metal surface area as a function of time of three selected catalysts ('2 nm', '9 nm', '16 nm') (T = 240 °C, P = 12 bar, $P_{syn-gas}$ = 10 bar, H_2/CO ratio = 2) 127

7.7 Carbon dioxide selectivity as a function of time for three selected catalysts ('2 nm', '9 nm', '16 nm') (T = 240 °C, P = 12 bar, $P_{syn-gas}$ = 10 bar, H_2/CO ratio = 2) 128

7.8 Methane selectivity as a function of crystallite size of all six alumina supported iron model catalysts calculated both during initial state (10 - 20 min with reduced crystallite sizes) and steady state (50 - 300 min with spent crystallite sizes) (T = 240 °C, P = 12 bar, $P_{syn-gas}$ = 10 bar, H_2/CO ratio = 2) . . . 130

7.9 Methane selectivity as a function of time for three selected alumina supported model iron catalysts ('2 nm', '9 nm', '16 nm') (T = 240 °C, P = 12 bar, $P_{syn-gas}$ = 10 bar, H_2/CO ratio = 2) 131

7.10 Chain growth probability as a function of crystallite size of all six alumina supported model iron catalysts during both initial state (10 - 20 min with reduced crystallite sizes) and steady state (50 - 300 min with spent crystallite sizes) (T = 240 °C, P = 12 bar, $P_{syn-gas}$ = 10 bar, H_2/CO ratio = 2) 132

7.11 Mole fraction of olefins in the corresponding carbon fraction of linear hydrocarbons as a function of carbon number at steady state (50 - 300 min) of three selected alumina supported model iron catalysts ('2 nm', '9 nm', '16 nm') (T = 240 °C, P = 12 bar, $P_{syn-gas}$ = 10 bar, H_2/CO ratio = 2) 135

7.12 Mole fraction of olefins in the C_5 fraction of linear hydrocarbons as a function of crystallite size at both initial (10 - 20 min reduced crystallite sizes) and steady state (50 - 300 min spent crystallite sizes) (T = 240 °C, P = 12 bar, $P_{syn-gas}$ = 10 bar, H_2/CO ratio = 2) 136

7.13 Molar olefin content of the C_2 fraction as a function of time of 3 selected alumina supported model iron catalysts ('2 nm', '9 nm', '16 nm') (T = 240 °C, P = 12 bar, $P_{syn-gas}$ = 10 bar, H_2/CO ratio = 2) 136

7.14 Molar olefin content of the C_3 fraction as a function of time of 3 selected alumina supported model iron catalysts ('2 nm', '9 nm', '16 nm') (T = 240 °C, P = 12 bar, $P_{syn-gas}$ = 10 bar, H_2/CO ratio = 2) 137

7.15 Mole fraction of α-olefins in linear olefins during the steady state (50 - 300 minutes) for 3 selected alumina supported model iron catalysts ('2 nm', '9 nm', '16 nm') (T = 240 °C, P = 12 bar, $P_{syn-gas}$ = 10 bar, H_2/CO ratio = 2) 138

7.16 Mole fraction of α-olefins in linear olefins during the initial state (10 - 20 minutes) as a function of initial crystallite size ((T = 240 °C, P = 12 bar, $P_{syn-gas}$ = 10 bar, H_2/CO ratio = 2) 139

7.17 Mole fraction of alcohols and aldehydes in linear products during steady state (50 - 300 minutes) on 3 selected alumina supported model iron catalysts ('2 nm', '9 nm', '16 nm') (T = 240 °C, P = 12 bar, $P_{syn-gas}$ = 10 bar, H_2/CO ratio = 2) . . . 141

7.18 Molar ratio of iso(branched) to n(straight) compounds in the C_5 hydrocarbon fraction as a function of crystallite size during both initial state (10 - 20 minutes with reduced crystallite sizes) and steady state (50 - 300 minutes with spent crystallite sizes) on alumina supported model iron catalysts (T = 240 °C, P = 12 bar, $P_{syn-gas}$ = 10 bar, H_2/CO ratio = 2) 143

7.19 Simplified schematic showing the effect of crystallite size on ensembles of atoms available for Fischer-Tropsch synthesis. . . 147

7.20 Difference between the HOMO energy level of the olefin and the Fermi-level of the metal as a function of the crystallite size (From van Steen (2008)). 148

7.21 Specific Fischer-Tropsch reaction rate as a function of time at initial (reduced) crystallite size for three selected catalysts ('2 nm', '9 nm', '16 nm') (T = 240 °C, P = 15 bar, $P_{syn-gas}$ = 10 bar, P_{water} = 3 bar, H_2/CO ratio = 2) 150

7.22 Specific Fischer-Tropsch reaction rate as a function of time at initial (reduced) crystallite size for three selected catalysts ('2 nm', '9 nm', '16 nm') (T = 240 °C, P = 18 bar, $P_{syn-gas}$ = 10 bar, P_{water} = 6 bar, H_2/CO ratio = 2) 151

7.23 Specific Fischer-Tropsch reaction rate as a function of initial crystallite size (T = 240 °C, P = 15 bar, $P_{syn-gas}$ = 10 bar, P_{water} = 3 bar, H_2/CO ratio = 2) 152

7.24 Crystallite size distributions of spent samples all six alumina supported model iron catalysts at conditions of no water addition, 3 bar water addition and 6 bar water addition 155

7.25 TEM micrographs of reduced and spent (no water, 3 bar water and 6 bar water addition) samples of the '14 nm' catalyst . . . 156

7.26 Comparison of XRD pattern of '2 nm catalyst at three different water partial pressure conditions (no water *(bottom)*, 3 bar water *(middle)* and 6 bar water *(top)*)(T = 240 °C, $P_{syn-gas}$ = 10 bar, H_2/CO ratio = 2) 158

7.27 Comparison of XRD patterns of '9 nm' catalyst at three different water partial pressure conditions (no water *(bottom)*, 3 bar water *(middle)* and 6 bar water *(top)*) (T = 240 °C, $P_{syn-gas}$ = 10 bar, H_2/CO ratio = 2) 159

7.28 Comparison of XRD patterns of '16 nm' catalyst at three different water partial pressure conditions (no water *(bottom)*, 3 bar water *(middle)* and 6 bar water *(top)*),(T = 240 °C, $P_{syn-gas}$ = 10 bar, H_2/CO ratio = 2) 159

7.29 Comparison of Mössbauer spectra of '2 nm' catalyst at three different water partial pressure conditions (no water *(top)*, 3 bar water *(middle)* and 6 bar water *(bottom)*) (T = 240 °C, $P_{syn-gas}$ = 10 bar, H_2/CO ratio = 2) 160

7.30 Comparison of Mössbauer spectra of '9 nm' catalyst at three different water partial pressure conditions (no water *(top)*, 3 bar water *(middle)* and 6 bar water *(bottom)*) (T = 240 °C, $P_{syn-gas}$ = 10 bar, H_2/CO ratio = 2) 165

7.31 Comparison of Mössbauer spectra of '16 nm' catalyst at three different water partial pressure conditions (no water *(top)*, 3 bar water *(middle)* and 6 bar water *(bottom)*) (T = 240 °C, $P_{syn-gas}$ = 10 bar, H_2/CO ratio = 2) 167

7.32 Specific Fischer Tropsch reaction rate as a function of initial crystallite size of all six alumina supported model iron catalysts at varying water partial pressures (no water addition, 3 bar water addition, 6 bar water addition) (T = 240 °C, $P_{syn-gas}$ = 10 bar, H_2/CO ratio = 2) 168

7.33 Carbon dioxide selectivity as a function of time of three selected catalysts ('2 nm', '9 nm', '16 nm') (T = 240 °C, P = 15 bar, $P_{syn-gas}$ = 10 bar, P_{water} = 3 bar, H_2/CO ratio = 2) . . . 169

7.34 Carbon dioxide selectivity as a function of time of '9 nm' alumina supported model iron catalysts at 3 different conditions of water addition (no water addition, 3 bar water addition, 6 bar water addition) (T = 240 °C, $P_{syn-gas}$ = 10 bar, H_2/CO ratio = 2) 170

7.35 Methane selectivity as a function of crystallite size at initial state (10 - 20 min) for all six alumina supported model catalysts at varying water addition conditions (no water addition, 3 bar water addition, 6 bar water addition) (T = 240 °C, $P_{syn-gas}$ = 10 bar, H_2/CO ratio = 2) 172

7.36 Methane selectivity as a function of crystallite size at steady state (50 - 300 min) for all six alumina supported model catalysts at varying water addition conditions (no water addition, 3 bar water addition, 6 bar water addition) (T = 240 °C, $P_{syn-gas}$ = 10 bar, H_2/CO ratio = 2) 173

7.37 Chain growth probability as a function of crystallite size at initial state (10 - 20 min) for all six alumina supported model catalysts at varying water addition conditions (no water addition, 3 bar water addition, 6 bar water addition) (T = 240 °C, $P_{syn-gas}$ = 10 bar, H_2/CO ratio = 2) 174

7.38 Chain growth probability as a function of crystallite size at steady state (50 - 300 min) for all six alumina supported model catalysts at varying water addition conditions (no water addition, 3 bar water addition, 6 bar water addition) (T = 240 °C, $P_{syn-gas}$ = 10 bar, H_2/CO ratio = 2) 175
7.39 Molar olefin content of the C_2 fraction as a function of time of the '2 nm' catalyst at varying water partial pressure conditions (no water addition, 3 bar water addition, 6 bar water addition) (T = 240 °C, $P_{syn-gas}$ = 10 bar, H_2/CO ratio = 2) 176
7.40 Molar olefin content of the C_2 fraction as a function of time of the '9 nm' catalyst at varying water partial pressure conditions (no water addition, 3 bar water addition, 6 bar water addition) (T = 240 °C, $P_{syn-gas}$ = 10 bar, H_2/CO ratio = 2) 177
7.41 Molar olefin content of the C_2 fraction as a function of time of the '16 nm' catalyst at varying water partial pressure conditions (no water addition, 3 bar water addition, 6 bar water addition) (T = 240 °C, $P_{syn-gas}$ = 10 bar, H_2/CO ratio = 2) . 178
7.42 Mole fraction of olefins in the C_5 fraction of linear hydrocarbons as a function of crystallite size during the initial state (10 - 20 minutes at reduced crystallite sizes) at varying water partial pressure conditions (no water addition, 3 bar water addition, 6 bar water addition) (T = 240 °C, $P_{syn-gas}$ = 10 bar, H_2/CO ratio = 2) 179
7.43 Mole fractionof α-olefins in linear olefins as a function of crystallite size during the initial state (10 - 20 minutes at reduced crystallite sizes) at varying water partial pressure conditions (no water addition, 3 bar water addition, 6 bar water addition) (T = 240 °C, $P_{syn-gas}$ = 10 bar, H_2/CO ratio = 2) 180
7.44 Mole fraction of alcohols and aldehydes in linear products as function of carbon number during steady state (50 - 300 minutes) for 3 selected alumina supported model iron catalysts of varying crystallite sizes (T = 240 °C, P = 15 bar, $P_{syn-gas}$ = 10 bar, P_{water} = 3 bar H_2/CO ratio = 2) 182

7.45 Mole fraction of alcohols and aldehydes in linear products as function of crystallite size in the C_5 fraction at initial state (10 - 20 min at reduced crystallite sizes) at varying water addition conditions (no water addition, 3 bar water addition, 6 bar water addition) (T = 240 °C, $P_{syn-gas}$ = 10 bar, H_2/CO ratio = 2) 183

7.46 Simplified schematic for the reactor placement and movement in $in-situ$ magnetometer. Adapted from Claeys (2008a) . . . 186

7.47 Saturation magnetisation as function of time for 3 selected alumina supported iron catalysts ('2 nm', '9 nm', '16 nm') (T = 240 °C, $P_{syn-gas}$ = 10 bar, H_2/CO ratio = 2) 190

7.48 Saturation magnetisation as a function of time for 3 selected alumina supported iron catalysts ('2 nm', '9 nm', '16 nm') (no water *(left)*, 6 bar water *(right)* (T = 240 °C, $P_{syn-gas}$ = 10 bar, H_2/CO ratio = 2) 191

7.49 CO conversion as function of time for 3 selected alumina supported iron catalysts at varying stepwise water addition conditions (T = 240 °C, $P_{syn-gas}$ = 10 bar, H_2/CO ratio = 2) . . 191

7.50 Saturation magnetisation as a function of temperature for '9 nm' alumina supported model iron catalyst at different water addition procedures (stepwise addition of water - starting with no water and 6 bar water addition) (T = 240 °C, $P_{syn-gas}$ = 10 bar, H_2/CO ratio = 2) 192

7.51 Hysteresis measurement for 3 selected alumina supported model iron catalysts prior to reduction conditions 194

7.52 Hysteresis measurement for 3 selected alumina supported model iron catalysts post reduction conditions 195

7.53 Percentage of ferro-magnetic material as function of time for 3 selected alumina supported model iron catalysts with stepwise variation of water partial pressure ('2 nm', '9 nm', '16 nm') (T = 240 °C, $P_{syn-gas}$ = 10 bar, H_2/CO ratio = 2) 196

7.54 Percentage of ferro-magnetic material as function of time for 3 selected alumina supported iron catalysts ('2 nm', '9 nm', '16 nm') (T = 240 °C, $P_{syn-gas}$ = 10 bar, H_2/CO ratio = 2) . 197

B.1 Logarithm of mol-% as a function of carbon number, indicating a typical Anderson-Schulz-Flory distribution associated with Fischer-Tropsch synthesis 220

C.1 Mole fraction of alcohols, aldehydes and total oxygenates in the C_2 fraction during initial state(10 - 20 min) on alumina supported model iron catalysts of differing crystallite sizes (T = 240 °C, P = 12 bar, $P_{syn-gas}$ = 10 bar, H_2/CO ratio = 2) . 226

C.2 Mole fraction of alcohols, aldehydes and total oxygenates in the C_2 fraction during steady state (50 - 300 min) on alumina supported model iron catalysts of differing crystallite sizes (T = 240 °C, P = 12 bar, $P_{syn-gas}$ = 10 bar, H_2/CO ratio = 2) . 227

C.3 Molar ratio of iso(branched) to n(straight) in the C_5 hydrocarbon fraction during both initial state (10 - 20 min at reduced crystallite sizes) and steady state (50 - 300 min at spent crystallite sizes) on alumina supported model iron catalysts (T = 240 °C, P = 12 bar, $P_{syn-gas}$ = 10 bar, H_2/CO ratio = 2) . . . 228

C.4 Olefin to paraffin ratio in the C_2 hydrocarbon fraction during both initial state (10 - 20 min at reduced crystallite sizes) and steady state (50 - 300 min at spent crystallite sizes) on alumina supported model iron catalysts of differing crystallite sizes (T = 240 °C, P = 12 bar, $P_{syn-gas}$ = 10 bar, H_2/CO ratio = 2) . 229

C.5 Olefin to paraffin ratio in the C_3 hydrocarbon fraction during both initial state (10 - 20 min at reduced crystallite sizes) and steady state (50 - 300 min at spent crystallite sizes) on alumina supported model iron catalysts of differing crystallite sizes (T = 240 °C, P = 12 bar, $P_{syn-gas}$ = 10 bar, H_2/CO ratio = 2) . 230

C.6 Molar fraction of α-olefins in olefins during initial state (10 - 20 min at reduced crystallite sizes) and steady state (50 - 300 min at spent crystallite sizes) on alumina supported model iron catalysts of differing crystallite sizes (T = 240 °C, P = 12 bar, $P_{syn-gas}$ = 10 bar, H_2/CO ratio = 2) 231

C.7 Molar ratio of α-olefins in olefins as a function of carbon number during the steady state (50 - 300 min) on alumina supported model iron catalysts of differing crystallite sizes (T = 240 °C, P = 12 bar, $P_{syn-gas}$ = 10 bar, H_2/CO ratio = 2) . . . 232

C.8 Mole fraction of linear olefins in hydrocarbons during the initial state (10 - 20 min) on alumina supported model iron catalysts of differing crystallite sizes (T = 240 °C, P = 12 bar, $P_{syn-gas}$ = 10 bar, H_2/CO ratio = 2) 233

C.9 Mole fraction of linear-olefins in hydrocarbon during the steady state (50 - 300 min) on alumina supported model iron catalysts of differing crystallite sizes (T = 240 °C, P = 12 bar, $P_{syn-gas}$ = 10 bar, H_2/CO ratio = 2) 234

C.10 Mole fraction of alchols and aldehydes in linear products as a function of carbon number during the initial (10 - 20 min) on alumina supported model iron catalysts of differing crystallite sizes (T = 240 °C, P = 12 bar, $P_{syn-gas}$ = 10 bar, H_2/CO ratio = 2) 235

C.11 Mole fraction of alchols and aldehydes in linear products as a function of carbon number during the steady state (50 - 300 min) on alumina supported model iron catalysts of differing crystallite sizes (T = 240 °C, P = 12 bar, $P_{syn-gas}$ = 10 bar, H_2/CO ratio = 2) 236

C.12 Change in the olefin content of the C_2 fraction as a function of time (240 °C and 12 bar). 237

C.13 Change in the olefin content of the C_3 fraction as a function of time (240 °C and 12 bar). 237

C.14 A typical chromatogram obtained from GC-FID analysis of Fischer-Tropsch Synthesis at 240 °C and 12 bar. (Catalyst Sample : '7 nm', no water co-feed, 50 minutes run-time) . . . 238

C.15 A typical chromatogram of the first 10 min obtained from GC-FID analysis of Fischer-Tropsch Synthesis at 240 °C and 12 bar. (Catalyst Sample : '7 nm', no water co-feed, 50 min run-time) 238

D.1 Comparison of XRD patterns of '2 nm' catalyst at three different water partial pressure conditions (no water *(bottom)*, 3 bar water *(middle)* and 6 bar water *(top)*), 240 °C and $P_{syn-gas}$ = 10 bar, H_2/CO ratio = 2 244

D.2 Comparison of XRD patterns of '3 nm' catalyst at three different water partial pressure conditions (no water *(bottom)*, 3 bar water *(middle)* and 6 bar water *(top)*), 240 °C and $P_{syn-gas}$ = 10 bar, H_2/CO ratio = 2 244

D.3 Comparison of XRD patterns of '7 nm' catalyst at three different water partial pressure conditions ((no water *(bottom)*, 3 bar water *(middle)* and 6 bar water *(top)*), 240 °C and $P_{syn-gas}$ = 10 bar, H_2/CO ratio = 2 245

D.4 Comparison of XRD patterns of '9 nm' catalyst at three different water partial pressure conditions (no water *(bottom)*, 3 bar water *(middle)* and 6 bar water *(top)*), 240 °C and $P_{syn-gas}$ = 10 bar, H_2/CO ratio = 2 245

D.5 Comparison of XRD patterns of '14 nm' catalyst at three different water partial pressure conditions (no water *(bottom)*, 3 bar water *(middle)* and 6 bar water *(top)*), 240 °C and $P_{syn-gas}$ = 10 bar, H_2/CO ratio = 2 246

D.6 Comparison of XRD patterns of 16nm catalyst at three different water partial pressure conditions (no water *(bottom)*, 3 bar water *(middle)* and 6 bar water *(top)*), 240 °C and $P_{syn-gas}$ = 10 bar, H_2/CO ratio = 2 246

D.7 Comparison of XRD patterns of all 6 catalyst samples at a condition of no water addition, 240 °C and $P_{syn-gas}$ = 10 bar, H_2/CO ratio = 2 247
D.8 Comparison of XRD patterns of all 6 catalyst samples at a condition of 3 bar water addition, 240 °C and $P_{syn-gas}$ = 10 bar, H_2/CO ratio = 2 247
D.9 Comparison of XRD patterns of all 6 catalyst samples at a condition of 6 bar water addition, 240 °C and $P_{syn-gas}$ = 10 bar, H_2/CO ratio = 2 248
D.10 Change in the olefin content of the C_3 fraction as a function of time of the '2 nm' catalyst at different water partial pressure conditions. $T_{reaction}$ = 240 °C, $P_{syn-gas}$ = 10 bar, H_2/CO ratio = 2). 248
D.11 Change in the olefin content of the C_3 fraction as a function of time of the '9 nm' catalyst at different water partial pressure conditions. $T_{reaction}$ = 240 °C, $P_{syn-gas}$ = 10 bar, H_2/CO ratio = 2). 249
D.12 Change in the olefin content of the C_3 fraction as a function of time of the '9 nm' catalyst at different water partial pressure conditions. $T_{reaction}$ = 240 °C, $P_{syn-gas}$ = 10 bar, H_2/CO ratio = 2). 249

List of Tables

2.1 Effect of reaction conditions on product selectivity in Fischer-Tropsch synthesis (Mabaso (2005)) 13

2.2 Common catalyst poisons classified according to chemical structure (Bartholomew (2001)) 18

2.3 Hüttig, Tamman and melting temperatures of metals and supports used in Fischer-Tropsch synthesis from (Moulijn et al. (2001)) 22

4.1 Sample codes indicating the amounts of Berol 050, n-hexane and aqueous phase used in the microemulsion solutions, and amount of support material used in preparation 47

4.2 Experimental procedures carried out for the investigation of variations in method during the preparation of supported catalysts 55

4.3 Magnetic properties of iron compounds (van de Loosdrecht (1994)) 61

4.4 Conditions for on-line gas chromatographic analysis using Thermal Conductivity Detectors (TCD) 76

4.5 Conditions for off-line gas chromatographic analysis using a Flame Ionization Detector (FID) 78

6.1 Average crystallite sizes (d_{cryst}) and variance (σ) observed by means of TEM analysis for calcined and reduced alumina supported iron catalysts 104

6.2 Calculated average metal crystallite size according to the Scherrer formula with respect to XRD traces 109
6.3 Degree of reduction of alumina supported iron catalysts of differing crystallite sizes calculated from TPR characterisation 110
6.4 Metal loading of calcined alumina supported iron catalysts determined by means of AAS and TPR analysis 112

7.1 Average crystallite sizes and standard deviations (in nm) of calcined, reduced and spent catalyst as determined by means of TEM analysis 119
7.2 Percentage crystallite growth of spent catalysts from reduced catalysts 121
7.3 Average crystallite sizes and standard deviations (in nm) of calcined, reduced and spent (no water addition, 3 bar water addition, 6 bar water addition) catalyst as determined by means of TEM analysis 154
7.4 Percentage crystallite growth of spent catalysts from reduced catalysts upon addition of water 154
7.5 Hyperfine splitting parameters of '2 nm' catalyst series and phase determination by means of both Mössbauer spectroscopy and XRD analysis 161
7.6 Hyperfine splitting parameters of '9 nm' catalyst series and phase determination by means of both Mössbauer spectroscopy and XRD analysis 164
7.7 Hyperfine splitting parameters of '16 nm' catalyst series and phase determination by means of both Mössbauer spectroscopy and XRD analysis 166
7.8 Spent catalyst characterisation by Mössbauer Spectroscopy - Total carbide content with varying water co-feed 166
7.9 Relative magnetisation of iron phases found during Fischer-Tropsch synthesis at $T_{reaction} = 240\,^{\circ}C$ 187

A.1 Chemicals used during model catalyst preparation and testing 218

C.1 Results from Fischer-Tropsch testing in the initial stages of the experiment (10 - 20 min) on alumina supported iron catalysts of differing crystallite sizes ($T_{reaction}$ = 240 °C, $P_{syn-gas}$ = 10 bar, H_2/CO ratio = 2) 224
C.2 Results from Fischer-Tropsch testing in the steady state stages of the experiment (50 - 300 min) on alumina supported iron catalysts of differing crystallite sizes ($T_{reaction}$ = 240 °C, $P_{syn-gas}$ = 10 bar, H_2/CO ratio = 2) 225

D.1 Results from Fischer-Tropsch testing in the initial stages of the experiment (10 - 20 min) on alumina supported iron catalysts of differing crystallite sizes ($T_{reaction}$ = 240 °C, $P_{syn-gas}$ = 10 bar, P_{water} = 3 bar, H_2/CO ratio = 2) 240
D.2 Results from Fischer-Tropsch testing in the steady state stages of the experiment (50 - 300 min) on alumina supported iron catalysts of differing crystallite sizes ($T_{reaction}$ = 240 °C, $P_{syn-gas}$ = 10 bar, P_{water} = 3 bar, H_2/CO ratio = 2) 241
D.3 Results from Fischer-Tropsch testing in the initial stages of the experiment (10 - 20 min) on alumina supported iron catalysts of differing crystallite sizes ($T_{reaction}$ = 240 °C, $P_{syn-gas}$ = 10 bar, P_{water} = 6 bar, H_2/CO ratio = 2) 242
D.4 Results from Fischer-Tropsch testing in the steady state stages of the experiment (50 - 300 min) on alumina supported iron catalysts of differing crystallite sizes ($T_{reaction}$ = 240 °C, $P_{syn-gas}$ = 10 bar, P_{water} = 6 bar, H_2/CO ratio = 2) 243

Chapter 1

Introduction

Fischer-Tropsch Synthesis (FTS) is a surface polymerisation catalysed by metals such as cobalt, iron and ruthenium. For optimum catalyst performance it is important to achieve maximum metal utilisation. Principally, the smaller metal crystallites in a catalyst have a larger fraction of metal atoms on the surface, which are available to catalyse the Fischer-Tropsch reaction. However, recently published work on supported cobalt, iron and ruthenium catalysts (Bezemer et al. (2006); Barkhuizen et al. (2006)) indicate that crystallites smaller than a certain size in the nano-meter range display lower metal surface area specific activity and high methane selectivity.

Such studies can only be conducted with suitable model catalysts. Model type catalysts with uniformly sized iron crystallites evenly distributed on γ-alumina have been prepared in this work. The catalysts were produced using a novel preparation method; employing a precipitation technique using water-in-oil micro-emulsions. The method of water-in-oil micro-emulsions allows for good size control of crystallites during the preparation process and results in a catalyst sample with a narrow crystallite size distribution at a specific size within a large size range, between 2 nm to 16 nm (Barkhuizen et al. (2006)). The iron crystallites were then supported on γ-alumina, a micro-porous carrier to increase structural strength and minimise effects of sintering.

A previous study on the effect of iron crystallite size on FTS has been

performed (Mabaso (2005)). Mabaso reported similar findings to those published by Bezemer et al. (2006) on supported cobalt catalyst; ie. below a specific minimum crystallite size, both the activity and methane selectivity of the catalyst was negatively influenced. It was suggested that the results were due to the tendency of smaller crystallites to reoxidise more readily than larger crystallites. However, Mabaso's results on iron may have been influenced by the addition of a chemical promoter, namely potassium, which was loaded at constant weight loading to the catalyst. Therefore, with changing iron crystallite size, the ratio of potassium to metal surface area also changed. This remains problematic as it is known that there exists an optimum potassium to iron ratio past which the activity of the Fischer-Tropsch reaction is negatively influenced. Furthermore, the addition of potassium may have affected product selectivity in Mabaso's study.

The objective of this study is to create a model catalyst which can be used to investigate the effect of iron crystallite size on the activity and selectivity of Fischer-Tropsch synthesis without the complicating effect of potassium promotion. Furthermore, the effect of increased water partial pressure on Fischer-Tropsch synthesis is also examined, where results may indicate the reaction of catalyst samples of differing crystallite size under high synthesis-gas conversion. It is believed that this investigation may lead to a better understanding of the influence of structure sensitivity versus metal re-oxidation as potentially caused by water in iron based Fischer-Tropsch synthesis.

Chapter 2

Literature Review

2.1 Fischer-Tropsch Synthesis

Fischer-Tropsch Synthesis (FTS) has a history which spans approximately 80 years. The ability of nickel and cobalt to hydrogenate carbon monoxide was first shown by Sabatier and Senderens in 1902, however Fischer-Tropsch technology was only truly brought to prominence by the work of Franz Fischer and Hans Tropsch at the Kaiser Wilhelm Institute for Coal Research at Mülheim ad Ruhr, Germany in the 1920s (Schulz (1999)). Commercial application of Fischer-Tropsch technology for fuel production began in Germany (Dry (2002)), and by 1938 there were 9 commercial plants with a total capacity of 660 $\times 10^3$ tonnes/annum. However, these plants were closed down after the commercial viability of these plants waned with the end of the second world war. Persistent perception in the 1940s and 50s that the age of cheap oil would quickly come to an end meant that the US Bureau of Mines revived interest in Fischer-Tropsch technology and a plant was built in Brownsville, Texas, with a capacity of 360×10^3 tonnes per annum. The lifespan of this specific plant was short-lived as before its construction was completed, the oil fields of the Middle East were discovered and brought forward a new age of oil. This meant that Fischer-Tropsch technology took a back seat in world chemicals and fuel production, except in South Africa where the cheap price of coal and political sanctions made it a viable option.

Today, interest in Fischer-Tropsch synthesis has been renewed, driven by the limited reserves of crude oil shown by rocketing oil prices, leading to a perceived 'energy crisis'. Other factors driving increased interest in Fischer-Tropsch synthesis include changing environmental demands, new technological development as well as the remote nature of some natural gas reserves, all these factors increase the commercial viability of Fischer-Tropsch plants. This interest can be shown in the increase in construction of new Fischer-Tropsch plants in Quatar (SASOL and Shell) and Nigeria (SASOL) to add to the existing plants in South Africa (SASOL and PetroSA) and Malaysia (Shell). Other countries considering the possibility of new Fischer-Tropsch plants include China, USA and Australia.

2.1.1 Fischer-Tropsch Reaction

The Fischer-Tropsch reaction is a highly exothermic reaction converting synthesis gas (hydrogen and carbon monoxide) to long chained hydrocarbons over a metallic catalyst. Its stoichiometric representation is shown in Equation 2.1.

$$CO + 2H_2 \longrightarrow (-CH_2-) + H_2O \qquad \Delta H_{rxn,513K} = -153.7 kJ/mol \tag{2.1}$$

The Fischer-Tropsch reaction is thought to be a surface polymerisation reaction, leading to a broad product spectrum, with linear α-olefins and linear paraffins being the main products and water the main by-product. Some branching will also occur during synthesis leading to some branched, mainly mono-methyl branched compounds being in the product spectrum as well as some oxygenates such as alcohols and aldehydes.

The extent of chain growth and ultimately the type of product spectrum produced is heavily influenced by the catalyst used as well as the reaction conditions of temperature and pressure. Industrial Low Temperature Fischer-Tropsch Synthesis (LTFTS) takes place at $220 - 240\,^{\circ}C$ and mainly produces longer chained products and is thus predominantly aimed at production of

diesel and wax fractions. Meanwhile industrial High Temperature Fischer-Tropsch Synthesis (HTFTS) has operating temperatures ranging from $300-340\,^{\circ}C$, this increase in temperature means that chain growth is limited and more lighter products in the petrol carbon number fraction are produced (Steynberg and Dry (2004)).

Four group VIII metals; iron, cobalt, nickel and ruthenium have been found to be sufficiently active for the hydrogenation of carbon monoxide, however only iron and cobalt are used commercially. Depending on the catalyst metal chosen, further side reactions may occur. One side reaction, or consecutive reaction is the water gas shift reaction (WGS) (Equation 2.2), where produced water reacts with carbon monoxide to form hydrogen and carbon dioxide.

$$H_2O + CO \rightleftharpoons H_2 + CO_2 \qquad \Delta H_{rxn,513K} = -39.7kJ/mol \tag{2.2}$$

The water gas shift reaction is mainly catalyzed by iron catalysts, while cobalt has almost no water gas shift activity. The water gas shift is generally seen as an undesirable side reaction, however, iron's activity toward the water gas shift means that iron catalysts are more flexible toward low hydrogen to carbon monoxide ratios in the synthesis gas (Steynberg and Dry (2004)).

Another possible side reaction is the disproportionation of carbon monoxide reaction or the Boudouard reaction (Equation 2.3). This reaction is particularly problematic as it can lead to the formation of carbonaceous deposits on the surface of the catalyst, leading to deactivation.

$$2CO \longrightarrow C + CO_2 \qquad \Delta H_{rxn,513K} = -172.9kJ/mol \tag{2.3}$$

2.1.2 Fischer-Tropsch Mechanisms

The Fischer-Tropsch reaction is considered to be a surface polymerisation reaction, which is characterized by a series of key steps;

- Reactant adsorption onto the surface of the catalyst

- Generation of a chain starter
- Chain growth (Propagation step)
- Product desorption from the catalyst surface
- Re-adsorption of reactive products and further reaction

Numerous reaction pathways have been suggested to account for the variety of products present in a Fischer-Tropsch product spectrum. It is recognized that it is likely that not a single pathway exists, but rather parallel, co-existing pathways which occur during Fischer-Tropsch synthesis. The four most prominent and accepted reaction pathways have been reviewed by Claeys and van Steen (2004). They include the 'alkyl', the 'alkenyl', the 'enol' and the 'CO-insertion' mechanisms.

2.1.2.1 Alkyl Mechanism

Currently the most widely accepted mechanism for Fischer-Tropsch chain growth is the 'alkyl' mechanism (Claeys and van Steen (2004)). The proposed reaction pathway for the 'alkyl' mechanism is shown in Figure 2.1. Carbon monoxide is adsorbed onto the surface of the catalyst through dissociative chemisorption, which results in carbon and oxygen atoms attached to the metal surface. The surface oxygen results in the by-product of water, by reacting with hydrogen adsorbed on the catalyst surface. The surface carbon is sequentially hydrogenated to form CH, CH_2 and CH_3 surface species. The chain initiator species is believed to be the CH_3 surface species, while the CH_2 species is thought to be the monomer for chain propagation. The actual chain propagation occurs through the incorporation of the monomer species into a surface alkyl species. Finally species desorption occurs through three possible pathways. Firstly, through β-H-elimination resulting in α-olefins, and secondly through hydrogenation resulting in n-paraffins. The β-H-elimination reaction is reversible, thus allowing for the desorbed α-olefins to re-adsorb onto the catalyst surface and further react to result in longer chained hydrocarbons (Schulz et al. (1999)). The 'alkyl' mechanism can

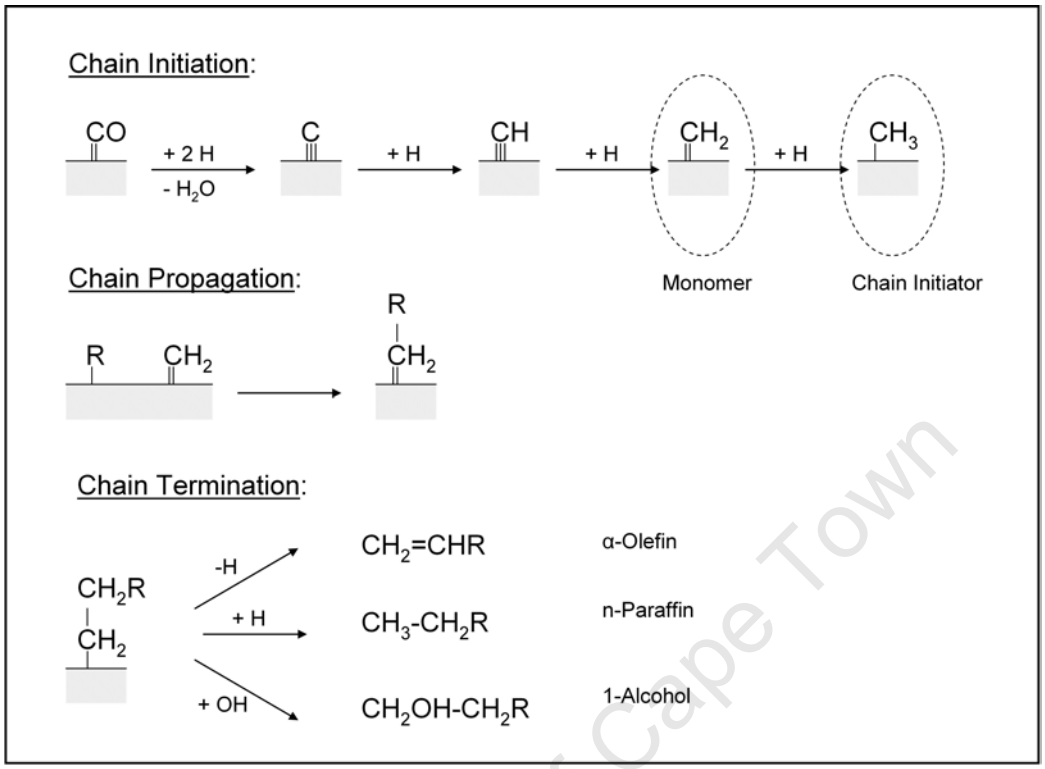

Figure 2.1: Reaction pathway for alkyl mechanism in Fischer-Tropsch synthesis (Adapted from Claeys and van Steen (2004))

explain the existence of n-paraffins and α-olefins, both of which are primary products in the Fischer-Tropsch product spectrum. However it does not explain the formation of oxygenates. It is proposed that the incorporation of surface hydroxyl groups might result in a third possible way of chain termination, resulting in the formation of alcohols, however experimental evidence for this reaction pathway does not currently exist.

2.1.2.2 Alkenyl Mechanism

An alternative reaction pathway for the formation of olefins in Fischer-Tropsch synthesis was proposed by Maitlis et al. (1999), resulting in the 'alkenyl' mechanism. This proposed reaction pathway is shown in Figure 2.2. The monomer in this mechanism is the same as for the 'alkyl' mechanism, the CH_2 surface species is proposed to be formed through the same

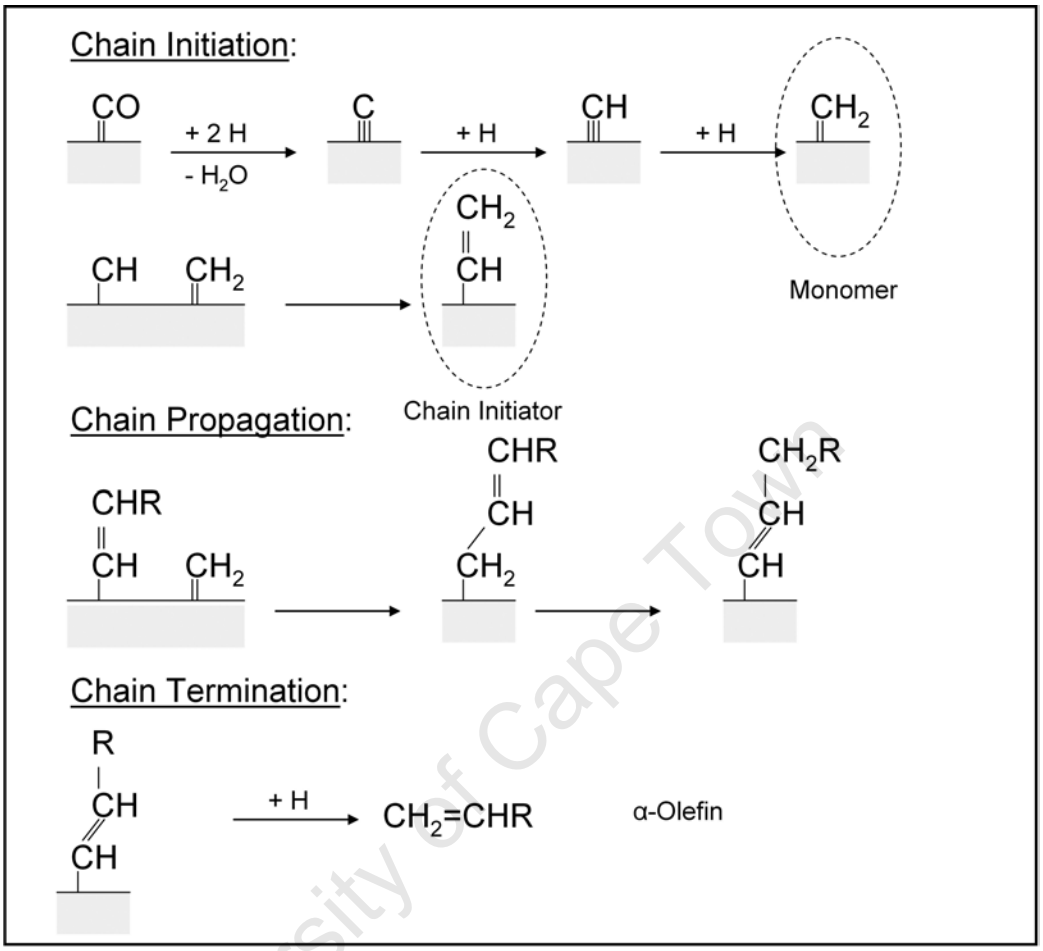

Figure 2.2: Reaction pathway for alkenyl mechanism in Fischer-Tropsch synthesis (Adapted from Claeys and van Steen (2004))

sequential hydrogenation of surface carbon. The chain initiator is a vinyl surface species ($CH = CH_2$) formed through the reaction between CH and CH_2 surface species. Chain propagation is achieved through reaction between the chain initiator species and the monomer. Finally the addition of hydrogen results in chain termination in the form of α-olefins. However, primary formation of n-paraffins cannot be explained by the 'alkenyl' mechanism, therefore an alternative co-existing reaction pathway would have to take place.

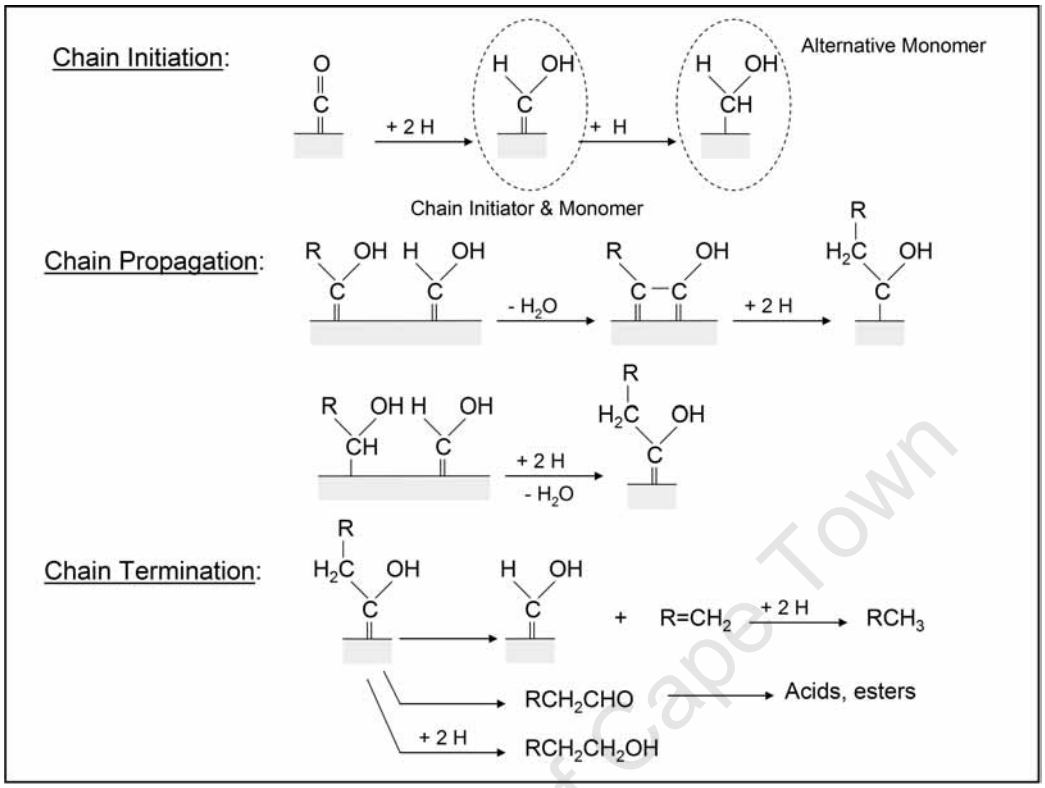

Figure 2.3: Reaction pathway for enol mechanism in Fischer-Tropsch synthesis (Adapted from Claeys and van Steen (2004))

2.1.2.3 Enol Mechanism

The 'enol' mechanism proposes a possible reaction pathway for the formation of oxygenates in Fischer-Tropsch synthesis, this mechanism is shown in Figure 2.3. For the 'enol' mechanism both the monomer and the chain initiator are the same enol surface species, formed through the hydrogenation of the chemisorbed surface CO. Two neighbouring enol surface species react in a condensation reaction, eliminating water to result in chain propagation. Chain termination can result in primary formation of oxygenates and α-olefins. However, as with the 'alkenyl' mechanism, primary formation of n-paraffins cannot be explained and an alternative reaction pathway would have to co-exist.

2.1.2.4 CO-Insertion Mechanism

The 'CO-insertion' mechanism is widely accepted as the main reaction pathway for the formation of oxygenates in Fischer-Tropsch synthesis. It was first proposed by Sternberg and Wender (1959) and fully refined to its current state by Pichler and Schulz (1970), it is shown schematically in Figure 2.4. In this mechanism the monomer is thought to be chemisorbed CO, while the chain initiator is the surface methyl species. However the formation of the surface methyl species in this mechanism is different to its formation in the 'alkyl' mechanism, though it does involve reaction with surface hydrogen and elimination of water. Reaction between the monomer and the chain initiator results in chain propagation through CO-insertion in a metal-alkyl bond leading to a surface acyl species. The formation of longer alkyl species is achieved through the elimination of oxygen. Various chain termination steps are possible; n-paraffins and α-olefins are formed in the same reaction step as in the 'alkyl' mechanism, through hydrogen addition and β-H-elimination respectively. Chain termination can also occur with oxygen containing species leading to the formation of aldehydes and 1-alcohols.

2.1.3 Fischer-Tropsch Products

A wide variety of products results from the Fischer-Tropsch reaction as it is considered to be a polymerization reaction. These products include those of different chain lengths and compositions. However in contrast to conventional polymerisation reactions, the monomer of the synthesis is only formed in-situ. The main products of Fischer-Tropsch synthesis are (Claeys and van Steen (2004));

- n-Olefins (primarily α-olefins, some olefins with internal double bond)
- n-Paraffins

While the typical side-products of Fischer-Tropsch synthesis are;

- Oxygenates (1-alcohols, aldehydes, ketones, carboxylic acids)
- Branched compounds (mainly mono-methyl branched)

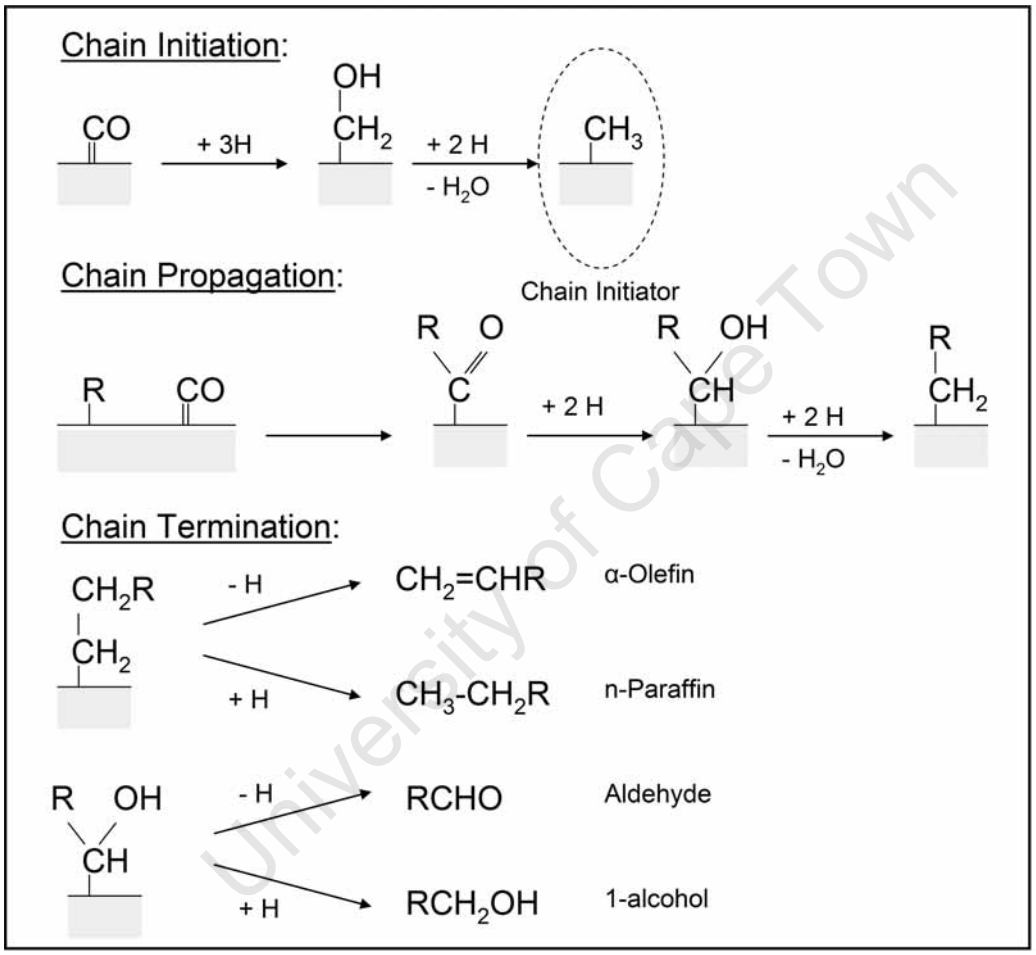

Figure 2.4: Reaction pathway for CO insertion mechanism in Fischer-Tropsch synthesis (Adapted from Claeys and van Steen (2004))

Variables which influence the composition of the product spectrum are: temperature, feed gas composition, pressure, catalyst type and promoters (Dry (2002)). However there is a constant relationship between the individual products which results in a constant variety of products irrespective of what variables are changed. The constant relationship between products is due to the fact that Fischer-Tropsch synthesis occurs through a constant stepwise growth and desorption process shown in Figure 2.5. At each stage of growth the hydrocarbon surface species has the option of either desorbing, that is forming the primary Fischer-Tropsch products, or continuing in chain growth. The probability of chain growth continuing is described by α, known as the chain growth probability in Fischer-Tropsch synthesis and is shown in Equation 2.4.

$$\alpha = \frac{r_g}{r_g - r_d} \tag{2.4}$$

Where r_g and r_d are the rates of chain growth and desorption respectively. The kinetics of product formation in Fischer-Tropsch synthesis, more commonly known as Anderson-Schulz-Flory kinetics, mathematically expresses the weight content of products of a certain carbon number (W_N) as a function of carbon number (N_C) (Shown in Equation 2.5).

$$\log \frac{W_N}{N_C} = N_C \cdot \log \alpha + \log \frac{1-\alpha}{\alpha} \tag{2.5}$$

It can be seen from Equation 2.5 that Fischer-Tropsch synthesis is very unselective, a wide variety of products will always be produced from the reaction regardless of the reaction conditions. The average chain length of the hydrocarbons produced depends on α, only methane can be produced with 100% selectivity based on an α value of zero. Generally factors which influence the Fischer-Tropsch synthesis have opposing effects on methane selectivity and chain growth. Methane selectivity increases with increasing temperature and increasing hydrogen to carbon monoxide ratio. Alternatively high pressures and potassium promotion of iron catalysts result in an increase in chain growth. The effect of the main factors on product selectivity of Fischer-Tropsch Synthesis are summarized in Table 2.1 (from Mabaso

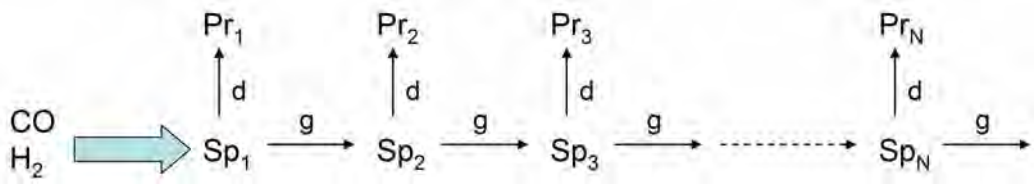

Figure 2.5: Fischer-Tropsch stepwise growth process - a series of chain growth and product desorption.

Table 2.1: Effect of reaction conditions on product selectivity in Fischer-Tropsch synthesis (Mabaso (2005))

	Temperature	**Pressure**	**H_2:CO**	**Residence Time**	**K**[a]
Methane selectivity	+	-	+	+	-
Chain growth	-	+	-	~	+
Chain branching	+	-	~	~	-
Olefin selectivity	~	~	-	-	+
Oxygenate selectivity	-	+	-	-	+
Carbon deposition	+	~	-	~	+

\+ increase with increasing parameter
\- decrease with increasing parameter
~ no clear effect

[a]Potassium loading of iron catalysts

(2005)). It can, for example, be seen that the selectivity of valuable products such as olefins and oxygenates can be increased via potassium promotion of iron based catalysts. This is mainly believed to be due to an inhibition of their readsorption and therefore a decreased secondary conversion of these reactive products (Claeys (1997), Schulz and Claeys (1999a)). These carbon number dependent secondary reactions have also been suspected to cause deviations from ideal Anderson-Schulz-Flory distributions (Iglesia (1997), Schulz and Claeys (1999a), Claeys and van Steen (2004)). It has been noted that the effect of total pressure can be a combination of individual partial pressures of H_2 and CO but also product water. The dependence of Fischer-Tropsch product selectivity on the water partial pressure, a parameter which was varied in this study, is described in detail in Section 2.3.

2.1.4 Fischer-Tropsch Catalysts

Group VIII metals; iron, cobalt, nickel and ruthenium have been shown to have the required Fischer-Tropsch activity for commercial application (Dry (2002)). However under practical application, the hydrogenation activity of a nickel catalyst is too high, producing large amounts of undesired methane. Ruthenium is the Group VIII metal with the highest activity for Fischer-Tropsch synthesis, however it is not widely available resulting in a high price and is therefore not suited to commercialization. Therefore only two metals have been successfully applied industrially; iron and cobalt (Dry (1981), Anderson (1984), Dry (2002)). Iron catalysts are known to be much more flexible than cobalt catalysts (Schulz (1999)), iron catalysts can be applied in both high (HTFT) and low (LTFT) temperature Fischer-Tropsch synthesis, while cobalt can only be applied at lower temperatures, as an increase in temperature leads to an increase in undesired methane selectivity (Dry (2002)).

When comparing iron and cobalt for Fischer-Tropsch catalysts, iron is more flexible, having a higher tolerance for sulphur, a common contaminant in the synthesis gas. It is also cheaper, and can produce a more olefinic and oxygenate-rich product spectrum compared to cobalt catalysts. However, an iron catalyst does require alkali promotion to attain high activity and stability (Schulz (1999)), the most common alkali promoter used is potassium. Copper is often also added to improve reduction of iron oxide into the active metallic form, furthermore structural supports such as alumina (Al_2O_3) or silica (SiO_2) can also be added (Dry (1981), Schulz (1999), Dry (2002), Dry (2004)). In contrast to cobalt catalysts, iron catalysts exhibit water-gas shift activity. This can be seen as a disadvantage, as an undesired byproduct, carbon dioxide is produced, or it can be seen as an advantage as water-gas shift activity means that iron catalysts can be applied to CO-rich syn-gas as derived from coal or biomass (van Steen and Claeys (2008)).

Cobalt catalysts are generally more active and have a longer lifetime on stream (5 years as compared to 8 weeks for HTFT iron catalysts, Dry (1981), Schulz (1999) and Dry (2002)). This higher activity of cobalt

means that no significant chemical promotion is required, however, due to the higher price of cobalt it is important to maximise the available surface area, therefore in cobalt catalysts, small crystallites of cobalt are generally dispersed on structural supports (Al_2O_3, SiO_2). Cobalt catalysts do not have any significant water-gas shift activity, meaning that no noticeable amount of carbon dioxide is produced, this also means that cobalt catalysts are more suitable for application in hydrogen-rich syn-gas, which is mainly produced from natural gas.

2.2 Catalyst Deactivation

It is inevitable that in catalyzed reactions, the catalyst will decay over time, losing activity as the reaction progresses, this is defined as the 'deactivation' of the catalyst. In industry the cost of catalyst deactivation is extremely high, once a catalyst has deactivated it has to be replaced, which in itself can be extremely costly. However a further cost that has to be considered is the cost of process shutdown while the catalyst is being replaced. The considerable cost associated with catalyst deactivation has meant that there is significant research going on into the topic, highlighted by three recently published review articles (Forzatti and Lietti (1999), Bartholomew (2001), Moulijn et al. (2001)). According to Bartholomew (2001) the mechanisms of catalyst deactivation can be classified into six distinct categories;

1. poisoning
2. fouling
3. thermal degradation
4. vapour-solid and/or solid-solid reactions
5. vapour compound formation accompanied by transport
6. attrition/crushing

Of these six categories of catalyst deactivation, the first four listed are the most common. There are three causes of catalyst deactivation: chemical, mechanical and thermal. Through these three causes all categories of catalyst deactivation can be explained.

2.2.1 Poisoning

Poisoning is defined as the loss of activity due to the strong adsorption of impurities on sites otherwise available for catalysis (Forzatti and Lietti (1999), Bartholomew (2001)). Reactants and products can also adsorb onto the catalyst surface, this may hinder the adsorption of reactants in the catalytic reaction in a process known as competitive adsorption. However the difference between competitive adsorption and poisoning is that inhibitors generally adsorb weakly and reversibly onto the catalyst surface while poisons have strong and permanent interaction with active sites. There are two different types of poisoning; selective and non-selective, shown in Figure 2.6. Poisons can also modify the active sites leading to a reconstruction of the active surface, meaning that catalyst performance is permanently altered.

A list of common poisons are shown in Table 2.2, these common poisons are essentially divided into four groups according to their chemical origin and type of interaction with the active metal surface. In terms of Fischer-Tropsch synthesis the most common catalyst poisons are H_2S, COS, NH_3 and metal carbonyls (Bartholomew (2001)). However the most serious poison is sulphur. Most Fischer-Tropsch synthesis gas is converted through coal gasification, which results in the reactant stream containing a significant undesired sulphur. The effect of sulphur on Fischer-Tropsch catalysts is well documented, several studies have indicated that a concentration of sulphur in the parts per billion range can cause significant loss in activity and lifetime of the catalyst (Shultz et al. (1962), Dry (1981), Bromfield and Coville (1999), Duvenhage and Coville (2006)). Therefore it should be recognized that significant and efficient sulphur removal is required after synthesis gas production, and prior to the synthesis gas reaching the Fischer-Tropsch catalyst. It is of particular importance when using the more expensive cobalt

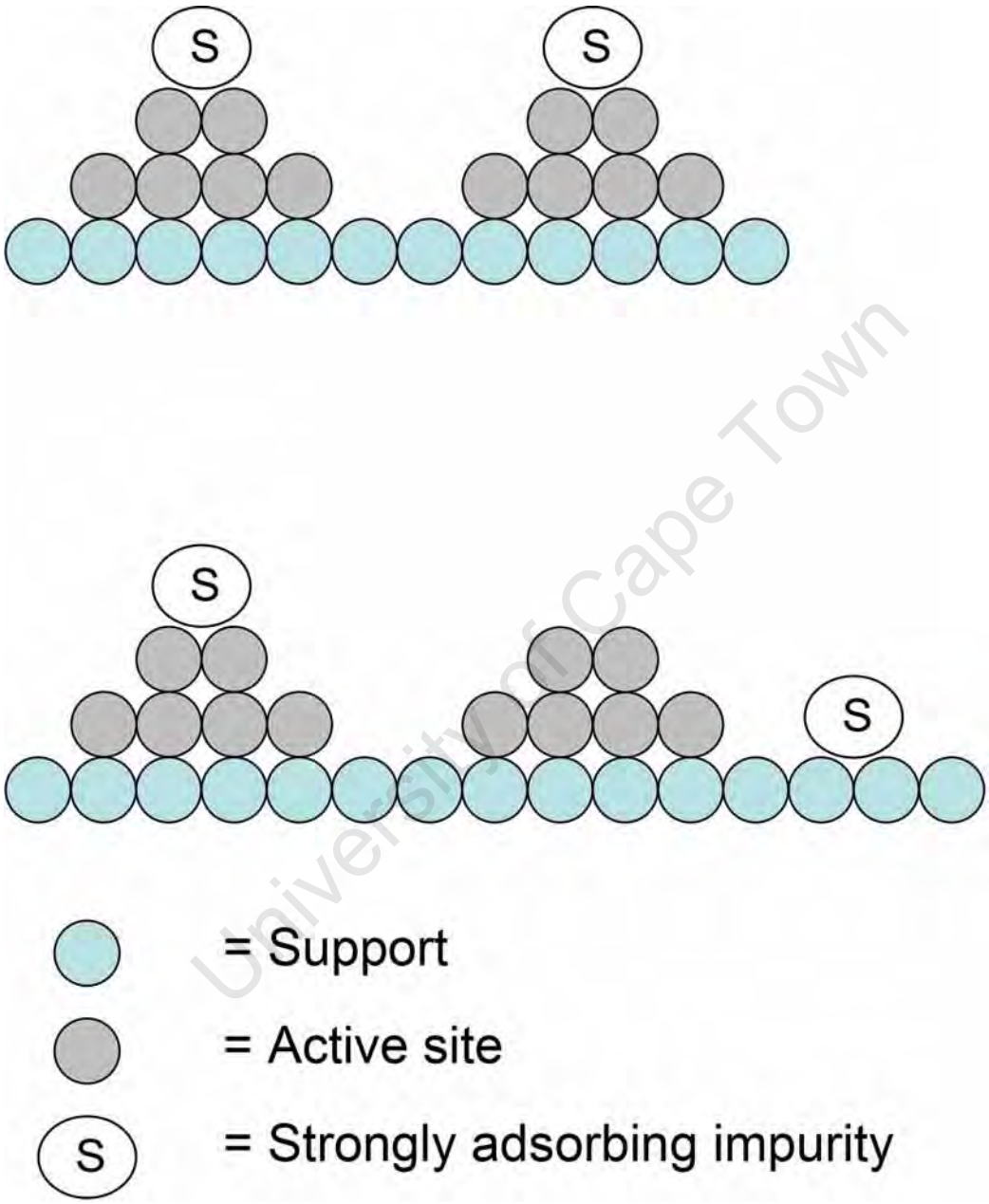

Figure 2.6: Selective (*top*) and non-selective (*bottom*) poisoning in heterogeneous catalysis.

Table 2.2: Common catalyst poisons classified according to chemical structure (Bartholomew (2001))

Chemical Type	**Examples**	**Type of Interaction with Metals**
Groups VA and VIA	N, P, As, Sb, O, S, Se, Te	Through s- and p-orbitals; shielded structures are less toxic
Group VIIA	F, Cl, Br, I	Through s- and p-orbitals; formation of volatile bases
Toxic heavy metals and ions	As, Pb, Hg, Bi, Sn, Zn, Cd, Cu, Fe	Occupy d-orbitals; may form alloys
Molecules which adsorb with multiple bonds	CO, NO, HCN, benzene, acetylene, other unsaturated hydrocarbons	Chemisorption through multiple bonds and back bonding

option (Schulz (1999)).

2.2.2 Fouling

Fouling in terms of catalyst deactivation covers all cases where a surface is covered with a deposit. This deposition onto the solid surface means that there will be a loss of active surface area due to blockage of sites and/or pores (Bartholomew (2001)). Fouling is a physical or mechanical process rather than a chemical one. The most common form of fouling is coking, which is prevalent in Fischer-Tropsch synthesis (Refer to Table 2.1). Coking is essentially the formation of carbonaceous deposits on the surface of catalysts which are involved in reactions with hydrocarbons. Coke deposits may amount to as much as 20% of the catalyst leading to deactivation through either covering of the active sites or pore blocking (Forzatti and Lietti (1999)). Coking is the result of deposition of carbonaceous material which can be made up of either carbon or coke. Carbon is traditionally thought of as the result of a carbon monoxide disproportionation reaction, while coke is the result of cracking or condensation of hydrocarbons.

Carbon deposition may affect the functionality of the catalyst through the following ways (Bartholomew (2001)):

1. Carbon chemisorbing strongly as a monolayer or physically adsorbing in multi-layers. In both cases this results in the blocking of reactant access to active sites.

2. The carbon may totally encapsulate a metal particle, thus rendering said particle totally inactive.

3. Finally, the carbon may plug micro- or meso-pores such that the access of reactants is blocked to active crystallites within these pores.

There are a number of known mechanisms through which carbon deposition may occur, one example is the dissociation of carbon monoxide over an active site to form C_α, which is an adsorbed atomic carbon. This C_α carbon can then react to form C_β, a polymeric carbon film. C_α and C_β are relatively reactive and can be formed at lower temperatures, they are however converted to less reactive, graphitic carbon over time at high temperatures. This graphitic carbon is the most stable form and therefore the most difficult to remove.

Recent work done by Moodley et al. (2009) on a cobalt catalyst supported on alumina has shown the presence of polymeric carbon located on both the metal and support material after being run at commercial Fischer-Tropsch conditions over a test period of 6 months. The authors concluded that coke formation must be one of the factors of deactivation, though other mechanisms such as sintering, poisoning and surface reconstruction cannot be ruled out.

2.2.3 Thermal Degradation

Thermal degradation is more commonly known as sintering, which is defined as the loss of active surface area through structural modification of the catalyst. This is generally a thermally driven process and is physical in nature (Forzatti and Lietti (1999)). Sintering can be caused by the following ways (Bartholomew (2001)):

1. Loss of catalytic surface area due to crystallite growth of the active phase.

2. Loss of support due to support collapse.

3. Loss of catalytic surface area due to pore collapse in crystallites of the active phase.

Initially the atoms are present as small clusters of atoms or small metal crystallites, this stage is known as momoner dispersion. Surface diffusion of the monodispersed atoms will lead sequentially to 2-dimensional clusters and then to the formation of 3-dimensional particles. These particles can further grow into larger particles through a variety of mechanisms shown in Figure 2.7 (From Moulijn et al. (2001)). Particles could travel further and coalesce with other particles, or atoms from one particle may move to another through surface migration or at higher temperature ($> 500\,^{\circ}\mathrm{C}$, Bartholomew (2001)), through volatilization.

Sintering is dependent on a variety of factors, including: temperature, metal type or dispersion, promoters/impurites and support surface area and porosity (Bartholomew (2001)). However sintering is most dependent on temperature. Sintering rates increase exponentially with temperature. The temperature at which sintering occurs are defined as the Hüttig or Tamman temperatures and are directly associated with the melting point of the metal. With increasing temperature the mobility of atoms also increase, first when the Hüttig temperature is reached the atoms located at defects become more mobile. And later when the Tamman temperature is reached the bulk atoms also exhibit mobility and finally at melting point temperature the atom mobility is so high that liquid phase behaviour is observed (Moulijn et al. (2001)). Equations 2.6 and 2.7 are semi-empirical relations for Hüttig and Tamman temperatures.

$$T_{Hüttig} = 0.3T_{melting} \tag{2.6}$$

$$T_{Tamman} = 0.5T_{melting} \tag{2.7}$$

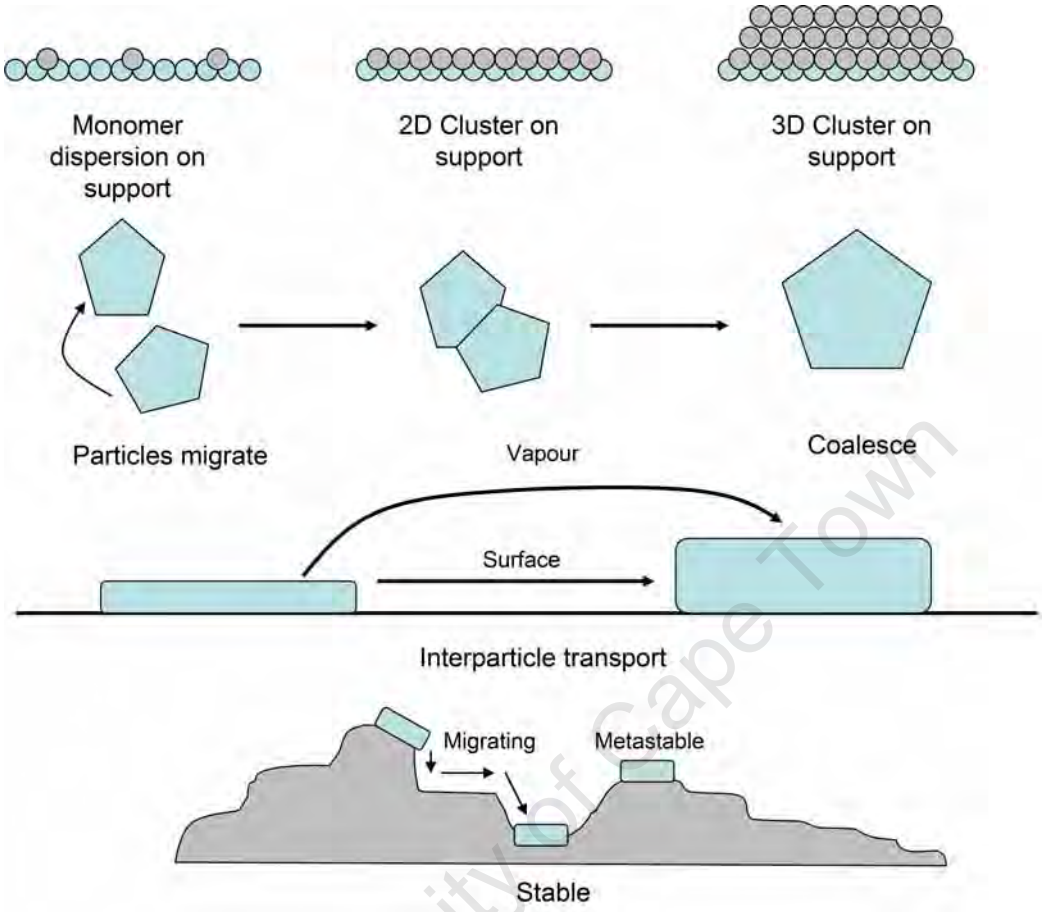

Figure 2.7: Schematic of the various stages in the formation and growth of particles from a monomer dispersion (Moulijn et al. (2001))

Table 2.3 lists the $T_{melting}$, $T_{H\ddot{u}ttig}$ and T_{Tamman} for metals and supports commonly used in Fischer-Tropsch synthesis. It is important to highlight that while in catalysis small crystallites are advantageous due to increased active surface area, they are similarly disadvantageous as it is hypothesized that with decreasing size the mobility of particles increases. Sintering is of increased importance as Dry (1981) indicated that sintering is probably the primary source of catalyst deactivation in Fischer-Tropsch synthesis.

Reaction conditions such as the water partial pressure in Fischer-Tropsch synthesis can also play a role in sintering. Satterfield et al. (1986) noted that increased water or carbon dioxide partial pressure over a prolonged pe-

Table 2.3: Hüttig, Tamman and melting temperatures of metals and supports used in Fischer-Tropsch synthesis from (Moulijn et al. (2001))

Compound	$T_{melting}$ **in K**	$T_{Hüttig}$ **in K**	T_{Tamman} **in K**
Ru	2723	817	1362
Fe	1808	542	904
Co	1753	526	877
Ni	1725	518	863
Al_2O_3	2318	695	1159
SiO_2	1986	596	993

riod causes a permanent loss of activity, the reason for which was stated as probably due to sintering. Work done on the effect of additional water on a titania-supported cobalt catalyst by Bertole et al. (2002) showed water addition reduced site activity and/or lower carbon monoxide surface inventory. While the site activity was recovered with hydrogen treatment, it did not affect surface inventory. With this observation, it was suggested by the authors that the surface loss of cobalt was due to sintering, which is facilitated by high (>4 bar) water partial pressure.

2.2.4 Vapour-Solid and Solid-Solid Reactions

Dispersed metals, metal oxides, sulphides and carbides are all known to be typical catalytic phases as their surface composition is similar to that of the bulk phase (Bartholomew (2001)). For a given reaction one or more phases may be more active than others. For example in iron catalysed Fischer-Tropsch synthesis metallic iron and carbides of iron (Fe_3C (Cementite), Fe_5C_2 (Hägg Carbide), Fe_7C_3 (Eckstrom Addock Carbide)) are known to be active, while oxides of iron are inactive (Dry (1981), Anderson (1984), Mansker et al. (1999), Li et al. (2002a), de Smit et al. (2009)). This surface modification is closely related to poisoning, however the major difference here is that instead of inactivity caused by an adsorbed species, here there is a formation of an entirely new phase.

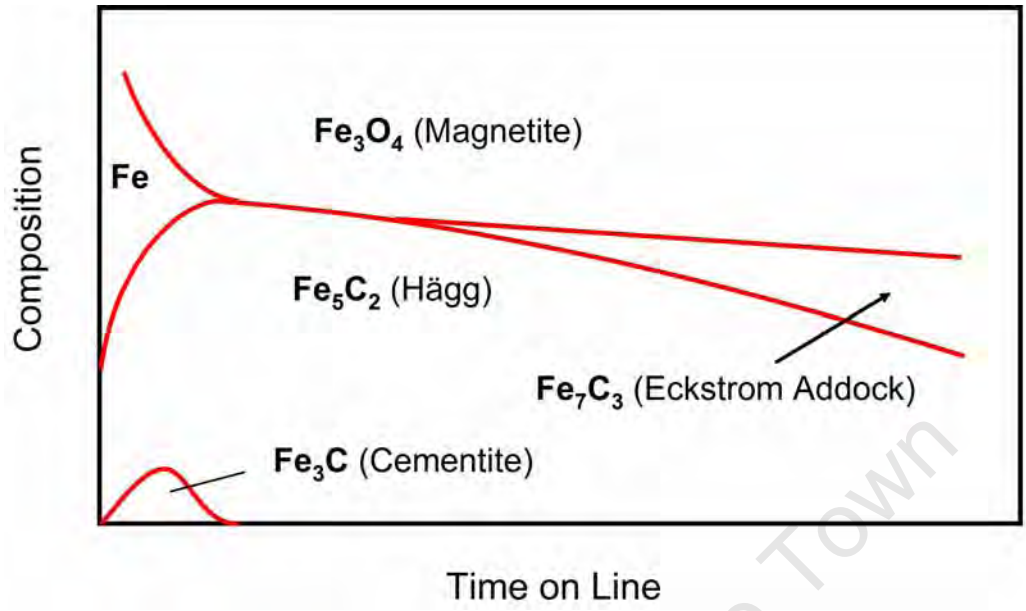

Figure 2.8: Change in composition of an iron catalyst in high temperature Fischer-Tropsch synthesis (Dry (1981))

Figure 2.8 shows the changes in the phase composition of an iron catalyst during high temperature Fischer-Tropsch synthesis (Dry (1981), Mansker et al. (1999), Schulz (1999), Li et al. (2002a), de Smit et al. (2009)). The initial composition of the iron catalyst is made up of magnetite and metallic iron however during the course of the process, there is an adsorption of atomic carbon onto the surface of the catalyst thus carbiding the surface and the bulk. Through the formation of water as a by-product the metal and the carbides will begin to reoxidize into inactive iron oxide, these changes have also been observed in other studies (Duvenhage and Coville (2006), Jager and Espinoza (1995)). Recent work done on unsupported and supported iron catalysts under Fischer-Tropsch conditions by de Smit et al. (2009) observed the presence of carbides (Fe_3C and Fe_5C_2) after 4 hours on stream, however a clear trend with respect to activity was found. The only statement that could be made was that the unsupported iron catalysts pretreated in hydrogen was found to be less active than those pretreated in syn-gas (H_2:CO = 2:1), this was thought to be due to less small clusters of Fe_3C being formed, where Fe_3C is thought to play an indirect role in the formation of coke on the

catalyst surface.

The reoxidation of metallic iron and iron carbide into iron oxide is largely attributed to water partial pressure, this was demonstrated by Espinoza et al. (1999) using a vertical fixed bed reactor divided into three sections; top, middle and bottom. The fixed bed reactor acts as a plug flow reactor, a characteristic of which is that conversion increases with distance along the reactor. Therefore the top section where the reactants enter the fixed bed reactor will generally experience a lower water partial pressure than the bottom section where the reactants and products exit. Espinoza et al. (1999) found that in the top section of the reactor the crystallite size remained nearly unchanged and reoxidation was low compared to the bottom section where the reoxidation was was significantly higher, and significant loss of active surface (sintering) was observed.

2.3 Effect of Water

Water has been shown to have a significant effect on both the selectivity and activity of Fischer-Tropsch synthesis irrespective of which active metal is used as the catalyst (Satterfield et al. (1986), Schulz et al. (1994), Schulz et al. (1997), Li et al. (2002a), Claeys and van Steen (2002), Gideon Botes (2008)). However whether this effect is positive or negative largely depends on the amount of water added and the period over which it is added. Satterfield et al. (1986) performed water addition experiments during Fischer-Tropsch synthesis on a fused magnetite catalyst containing alumina, silica and potassium; the results showed that water is largely a reversible inhibitor. With addition of up to 27 mol% water to the synthesis gas feed, upon removal of the water the reaction rate returned to 100% of its base line value. However addition of 42 mol% water showed only an 85% return to its base-line value of catalyst activity upon water removal. It was noted that water addition at a high concentration or over a prolonged time will result in a permanent loss of activity. Li et al. (2002a) similarly found on a cobalt-silica catalyst that high concentration and long time addition of water resulted in severe catalyst deactivation. However, Li et al. (2002a) found that short time addition

of water in the range of 5-25 mol% or long time addition of water below 5 mol% had a positive influence on the carbon monoxide conversion. Positive effects of water on activity in cobalt based Fischer-Tropsch synthesis were also reported by Schulz et al. (1994), while with a different precipitated cobalt catalyst, no changes of catalyst activity were observed upon water addition (Schulz et al. (1997)). Finally in experiments performed on a silica supported ruthenium catalyst, Claeys and van Steen (2002) found that for water addition of up to 24 mol% increased catalyst activity and produced significant changes in product composition.

In terms of iron catalyzed Fischer-Tropsch synthesis the widely accepted kinetic equation is given in Equation 2.8 (Huff and Satterfield (1984));

$$-r_{H_2+CO} = \frac{ab' p_{CO} p_{H_2}^2}{p_{H_2O} + b' p_{CO} p_{H_2}} \tag{2.8}$$

This equation indicates the generally inhibiting role of water in iron based Fischer-Tropsch catalysis, which is not observed in cobalt or ruthenium based Fischer-Tropsch catalysis. It has, however, been noted that the wide range of concentrations of reactants and water used in kinetic studies can lead to changes of the surface or bulk composition (e.g. oxidation) of the catalyst and/or crystallite sintering, converting it into practically a different catalyst. In addition, iron based catalysts usually display significant water-gas shift activity, which will further influence local partial pressures of H_2, CO, H_2O and CO_2, therefore further complicating micro-kinetic studies of the Fischer-Tropsch synthesis for iron catalysts (Jager and Espinoza (1995)).

Due to the difficulties surrounding the macro kinetic studies of an iron Fischer-Tropsch catalyst, several studies have attempted to relate activity and selectivity changes to the composition of the catalyst surface or bulk. However, as yet no clear cut correlations have emerged (Satterfield et al. (1986)). Other studies mentioned in Section 2.2.4 have shown that the metallic iron content decreases with time while magnetite content increases. However these changes in phase had no accompanying change in activity or selectivity in the corresponding studies (Dry (1981), Anderson (1984)). The major challenge regarding the effect of water in Fischer-Tropsch synthesis is

to decouple the kinetic and phase change effects of water and match these effects to changes in reaction activity and product selectivity.

In terms of changes in product composition upon addition of water with iron based catalysts, Satterfield et al. (1986) reported that for a water addition of up to 42 mol% there was no significant change in α, the chain growth probability, resulting in little effect on the amount of C_3 to C_6 present. Satterfield et al. (1986) further reported that upon addition of water there was a significant decrease in the methane selectivity, which was also reported by Schulz et al. (1994). However this result is opposed to that reported by Dry (1981), which showed that upon water addition to an iron Fischer-Tropsch catalyst of up to 17 mol% there was no significant change in methane selectivity. Other product selectivity changes reported by Satterfield et al. (1986) upon water addition include increase in the mole fraction of oxygenates in the C_2, C_3 and C_5 fractions, with accompanying increase in the olefin to paraffin ratios.

Even stronger effects of water in Fischer-Tropsch synthesis have been observed for cobalt (Hilmen et al. (1999), Li et al. (2002a), Bertole et al. (2002)) and ruthenium (Claeys and van Steen (2002)) catalyst. These showed a strong decrease of methane selectivity, a corresponding increase in chain growth probability and increased olefin content, indicating the important role water can play as a "moderator" in the kinetic Fischer-Tropsch regime.

2.4 Conventional Catalyst Preparation Techniques

With changing technological and environmental demands, targets for catalyst design have often changed. In terms of Fischer-Tropsch synthesis, differences in catalyst preparation can change selectivity toward either the petrol fraction or the diesel/wax fraction depending on which is desired. Catalyst preparation can also have significant effect on the activity of the resulting catalyst (Rameswaran and Bartholomew (1989)).

One technological advancement in catalyst preparation techniques is the use of an inert support material, used to achieve optimal dispersion of the active component as well as to provide stabilization for the active component. This means that most industrial catalysts used today are supported (Delmon (2008)). The use of a support material can alter the chemical reactivity of the active component depending on the preparation method used. The choice of preparation method for a supported catalyst depends on two main factors;

- Level of dispersion of the active component onto the support material.
- Interaction between the active component and the support material.

Catalyst preparation consists of three main steps; deposition of the active material onto the support, followed by immobilization of the active material onto the support material and finally, its conversion into the final desired active state (Marceau et al. (2008)). These steps can be thought of as;

- Catalyst synthesis
- Calcination
- Activation

Supported Fischer-Tropsch catalysts are prepared through two main methods; impregnation and precipitation, other less common methods include ion exchange and deposition of organometallic compounds.

2.4.1 Impregnation

For the preparation of a supported catalyst, the first step is to choose a support material based on its size, shape and chemical properties. The impregnation technique can then be used, where a solution containing the catalytically active species is introduced into the pore structure of the support material. There are two separate methods of impregnation, based on whether the pore structure of the support material is initially filled with air or with a liquid solution.

The first method of impregnation is known as capillary impregnation, where the pore volume of the support is filled with air. Capillary impregnation is usually characterized by exothermicity, caused by the replacement of a solid-gas interface by a solid-liquid interface. This rise in temperature generally does not cause any change in the quality of impregnation, but does have to be taken into account for precursor solutions that might be unstable. Another feature of capillary impregnation is the pressure that would be built up in the pore system upon impregnation, the gas in the pore system will pressurize into bubbles, which will eventually dissolve in the liquid and escape progressively. The pressure that is built up may cause degradation of the pore walls, which may in turn compromise the mechanical strength of the support material. A special case of capillary impregnation is know as 'incipient wetness' impregnation (Adesina (1996), Marceau et al. (2008)), where the volume of precursor solution introduced to the support material is equal to the pore volume of the support material, therefore no solution remains outside of the pore system.

The second method of impregnation is diffusional impregnation; the support material is first placed into contact with a pure solution of the impregnation solution, before being contacted with the actual impregnation solution containing the precursor (Marceau et al. (2008)). Using this technique means that the impregnation is no longer exothermic, nor are air bubbles built up within the pore system. Migration of the precursor into the pore system now takes place through diffusional effects, with the driving force being the concentration gradients. This means that diffusional impregnation is significantly slower than capillary impregnation.

Generally it is difficult to prepare catalysts with a high metal loading and high dispersion using the impregnation method, unless multiple impregnation steps are conducted. Furthermore the size distribution of the metal crystallites on the resulting catalyst are often wide (Anderson (1984), Dry (1981), Adesina (1996)), and therefore the method is not suitable for preparation of model catalysts.

2.4.2 Precipitation

Precipitation techniques involve the use of metal precursors dissolved into a salt solution, the metal precursor can then be precipitated in the presence of a support material or the support can be formed simultaneously via co-precipitation (Geus and van Dillen (2008)). The precipitation step is often forced through pH adjustment. Precipitation in the presence of a support material is usually used for the production of catalysts with low metal loadings, while co-precipitation usually produces catalysts with very high metal loadings. One major advantage of precipitation techniques over impregnation techniques is that the former technique results in a more homogeneous composition (Anderson (1984), Dry (1981)). Furthermore, while it is difficult to achieve high metal loadings using impregnation, precipitation techniques can achieve a fairly high metal loading with just a single preparation step. The final advantage of the precipitation technique is that the size distribution is generally much narrower, and smaller crystallites can be formed compared to conventional impregnation (Reuel and Bartholomew (1984), Fu and Bartholomew (1985)). However, the reason why the preparation technique is not suitable for the formation of model catalysts is that the adjustment of crystallite size is difficult in this case.

2.5 Microemulsion Technique

Microemulsion systems were first defined in the 1940s by Schulman and Friend (1949), however the idea of using a microemulsion system for catalyst formation was first suggested by Gault (Eriksson et al. (2004)). To this point the most widely used method of metal crystallite formation was the precipitation technique. However, synthesis of metal crystallites for catalysts, using the microemulsion technique was first reported by Boutonnet et al. (1982). This novel method can be used to make a variety of materials (Pileni (1993a), Eriksson et al. (2004)). For the synthesis of metal crystallites for catalytic use, the microemulsion method produces well-defined particles in the nano-size range. Furthermore when compared to other conventional

catalyst preparation methods, the microemulsion method allows for better control of the size of the resulting crystallites through the changing of the composition of the microemulsion.

2.5.1 Microemulsion Systems

A microemulsion system consists of three phases; water, organic and surfactant. The surfactant is a molecule with both a polar and non-polar end. The system a is thermodynamically stable and optically isotropic solution. One characteristic of a microemulsion system is on a macroscopic scale the solution appears to be homogeneous, however on a molecular scale the system is heterogeneous, the system on a molecular scale is shown in Figure 2.9, indicating that the aqueous phase can contain a metal precursor dissolved in it. At a given temperature, the internal structure of the microemulsion is determined by the ratio of its constituents, the solution can either exist as a bicontinuous phase or nano-sized spherical droplets. A ternary diagram shown in Figure 2.10 shows that at a high concentration of water, the system would consist of nano-sized oil droplets or micelles in a water phase. With increasing oil concentration, the system would move through a bicontinuous phase, and finally at a high oil phase, nano-sized water droplets (reverse-micelles) will form within an continuous oil phase (Eriksson et al. (2004)). While the solution is in a heterogeneous phase of droplets in a continuous solution, small changes in the amount of different constituents can change the size of the droplets. The internal structure of the microemulsion system is also very temperature dependent. An increase in temperature will result in the oil micelles being destroyed, while water droplets are destroyed by a decrease in temperature (Eriksson et al. (2004)).

Depending on the surfactant used the size of the micelles can vary anywhere between 1 to 100 nm. The most common surfactants used in the formation of microemulsion systems are; sodium bis-(2-ethylhexyl)-sulfosuccionate (AOT), sodium dodecyl sulphate (SDS) and cetyl trimethyl ammonium bromide (CTAB). However these ionic surfactants contain sodium and sulphur, both of which may negatively affect the resulting catalyst. Another surfac-

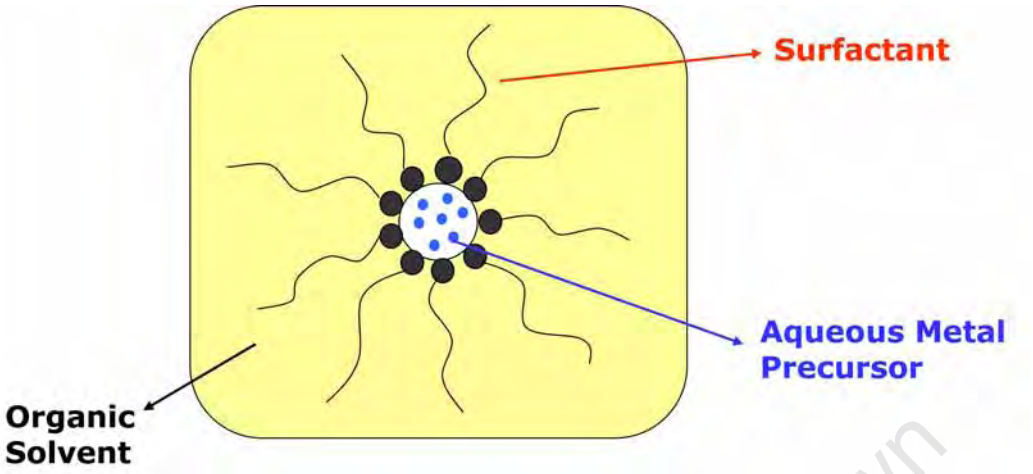

Figure 2.9: Schematic of microemulsion system

tant, penta-ethyleneglycol-dodecylether (PEGDE) is often used as an alternative, it is a non-ionic surfactant which contains no poisons to the resulting catalyst.

2.5.2 Preparation of Nano-particles

A water-in-oil microemulsion or reverse micelle solution act as tiny droplets filled with a water based solution, this is of particular interest as these droplets act as reactors which can be filled with a salt solution of a metal precursor to the final metal crystallite. As stated previously, changes in the composition of the reverse micelle solution can change the size of the droplets and ultimately the size of the final metal crystallites (Lisiecki and Pileni (1993), Eriksson et al. (2004), Mabaso (2005), Barkhuizen et al. (2006)). There exists, for example, a linear dependency of the reverse micelle, and therefore the resulting crystallite size on the water to surfactant ratio in the solution.

There are two commonly used ways of preparation to obtain nano-sized crystallites from reverse micelle solutions (Eriksson et al. (2004));

- Mix two reverse micelle solutions, one containing the metal precursor in the aqueous phase and another the precipitating or reducing agent (Figure 2.11).

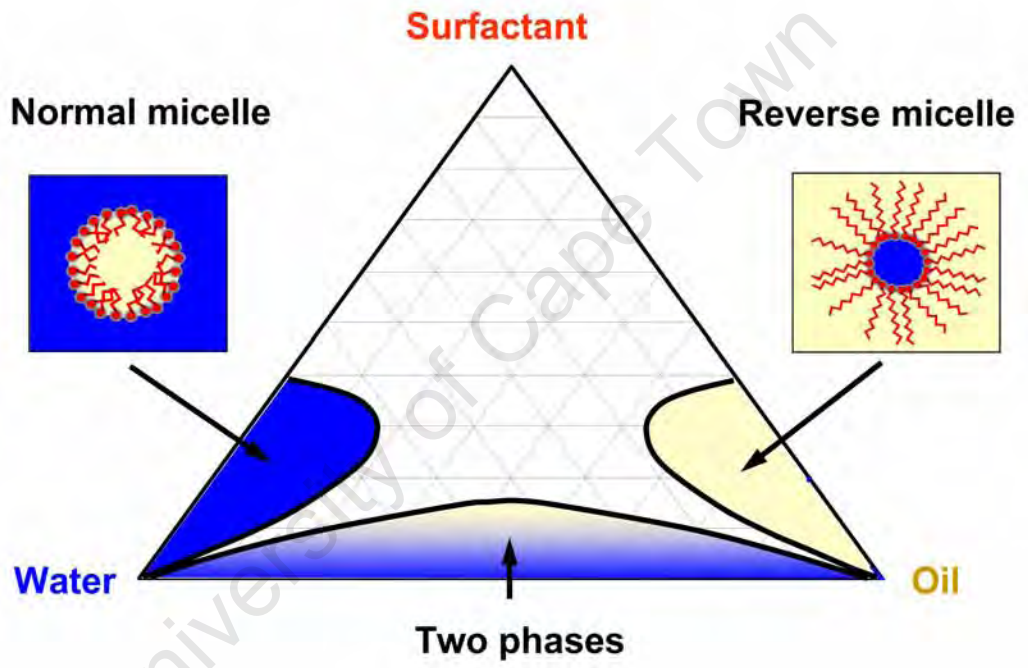

Figure 2.10: Ternary phase diagram for a surfactant-oil-water system (Mabaso (2005))

- Add the precipitating or reducing agent directly to the reverse micelle solution containing the metal precursor (Figure 2.12).

Parameters that affect the crystallite size and distribution of the resulting metal crystallites are: reaction time, chemical nature of the precursors and the composition and constituents of the microemulsion system. Furthermore, similar to conventional preparation techniques, the subsequent drying, calcination and activation steps will also play an important role in the final chemical makeup of the resulting crystallites that can be used in catalysis (Boutonnet et al. (1982), Stenius et al. (1984), Boutonnet et al. (1987), Pileni (1993b), Pileni (1993a), Pillai et al. (1995)).

In the field of catalysis, the reverse micelle technique becomes particularly important for the formation of supported catalysts with small, controllable crystallite size, a narrow size distribution and good dispersion of the metal crystallites onto the support material, that is, model catalysts that can be used to study effects of crystallite size in catalytic conversions. However, it is important to note that little work has been done on the preparation of supported catalysts using the reverse micelle method and more research is required to understand how different variables may influence the composition and structure of the final catalyst (Mabaso (2005), Welker (2007)). For model type catalysts it is important that a homogeneous distribution must be maintained while transferring the metal crystallites onto the support. Furthermore the crystallites must adhere strongly to the support material in order to avoid sintering in later preparation and reaction steps (Eriksson et al. (2004)). One possible approach is to form the support in-situ, through a co-precipitation step with a precursor of the support material (Kishida et al. (1998), Hayashi et al. (2002)). A possible problem which may arise in this technique is the undesired encapsulation of the active metal crystallites within the inactive support material. A second method is to introduce the support material to the reverse micelle solution after precipitate formation but while the reverse micelle system is still intact, this can then be followed by the breakage of the reverse micelles, causing the nano-particles to adhere to the support material (Mabaso (2005)). The final method of support addition is to add the support material directly into the reverse micelle system

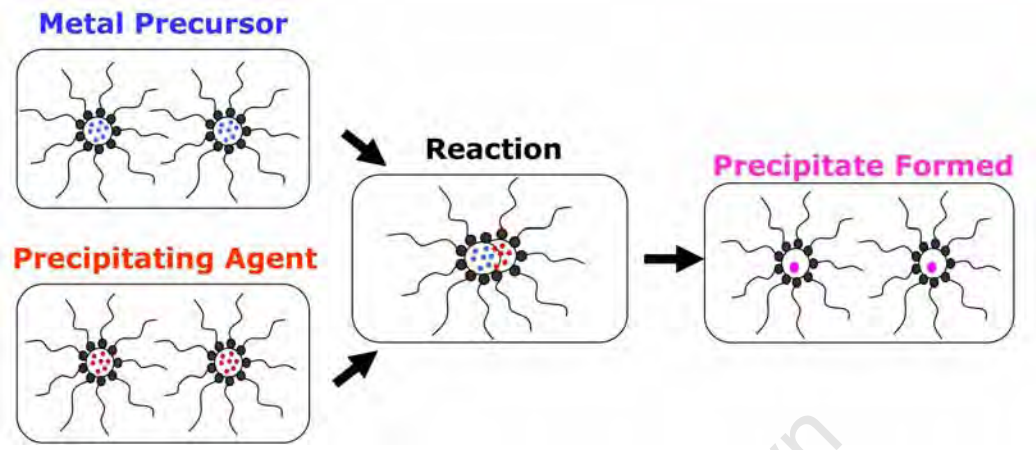

Figure 2.11: Preparation of nano-crystallites using two reverse-micelle solutions; one containing the metal precursor in the aqueous phase and another with the precipitating agent.

containing the metal precursor. In this case there is no precipitation step, the active material is deposited onto the support material through interiionic interaction, and this is followed by the break-up of the reverse micelle system (Stenius et al. (1984), Eriksson et al. (2004), Welker (2007)). The possible problem associated with the last two techniques is that some of the nano-crystallites may not be deposited onto the support material, making it difficult to attain the desired metal loadings. Nonetheless a number of model type catalysts have been successfully prepared with the latter methods which were therefore also employed for catalyst preparation to study effects of crystallite size in iron-based Fischer-Tropsch synthesis in this work.

2.6 Effect of Crystallite Size in Fischer-Tropsch Synthesis

It is common knowledge in catalysis that with smaller crystallites, more active surface area is exposed allowing for higher overall activities. However the subject of size sensitivity remains an issue as research has shown that small nano-meter sized particles can behave differently to larger particles. Bezemer et al. (2006) showed that carbon supported cobalt crystallites made

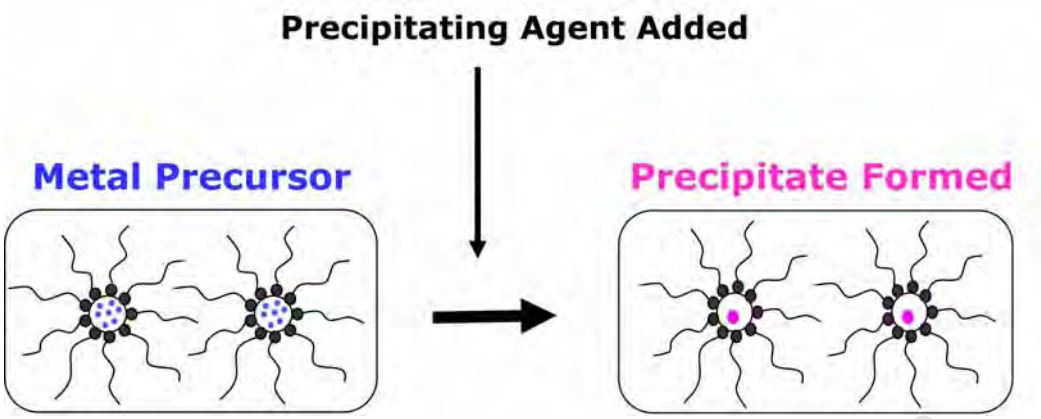

Figure 2.12: Preparation of nano-crystallites using a single reverse-micelle solution, with the precipitating agent added to the solution directly.

for the Fischer-Tropsch process showed a much lower turn-over frequency if they were smaller than 6 nm, shown in Figure 2.13. Similarly, iron supported on carbon or alumina and promoted with potassium appears to show a lower activity for crystallite sizes smaller than 7 nm (Mabaso (2005), Barkhuizen et al. (2006), Figure 2.14). The chemical background for this phenomenon is not yet fully understood (Bezemer et al. (2006)). Furthermore, it has been shown by the research of Mabaso (2005) and Bezemer et al. (2006) that size of the active metal crystallites have a significant effect on the selectivity of the Fischer-Tropsch process. Figures 2.15 and 2.16 show that the methane selectivity increases with decreasing metal crystallite size, while the opposite is true for the olefin to paraffin ratio. Similar observations were also made when using supported ruthenium (Barkhuizen et al. (2006), Welker (2007)) and rhodium (Ojeda et al. (2004)) model catalysts with varied crystallite size in carbon monoxide hydrogenation.

There are a number of different theories as to why smaller crystallites behave differently to larger ones, these include;

1. Structure sensitivity: differences in specific activity and selectivity can arise because different sites are exposed. (van Hardeveld and Hartog (1969))

2. Electronic effects: differences in activation energy required for carbon

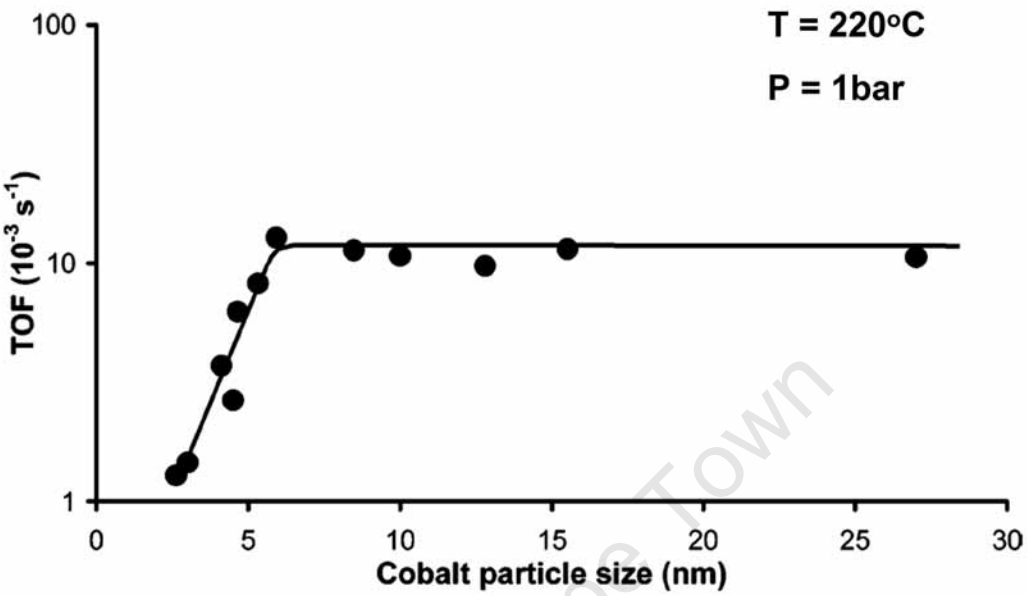

Figure 2.13: Effect of cobalt crystallite size on the turn-over frequency of Fischer-Tropsch synthesis (Bezemer et al. (2006)).

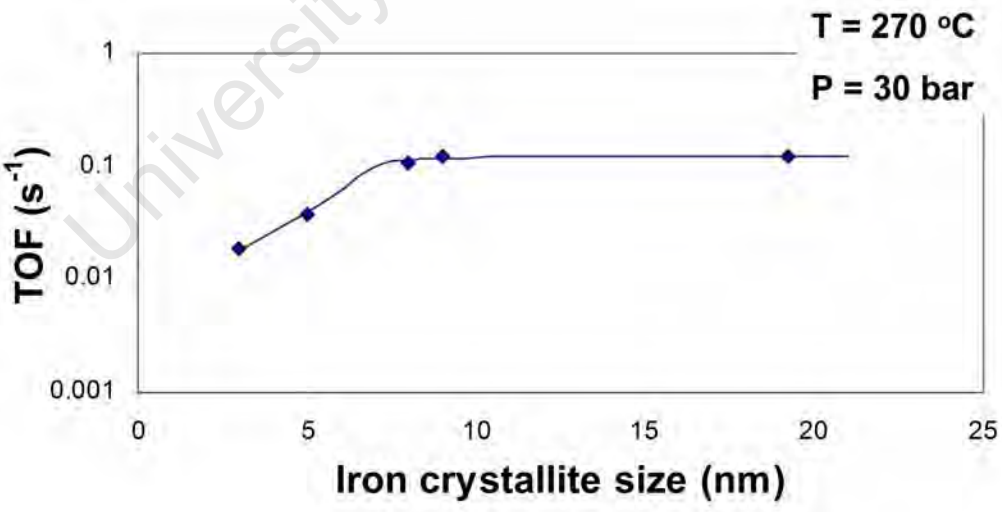

Figure 2.14: Effect of iron crystallite size on the turn-over frequency of Fischer-Tropsch synthesis (Mabaso (2005)).

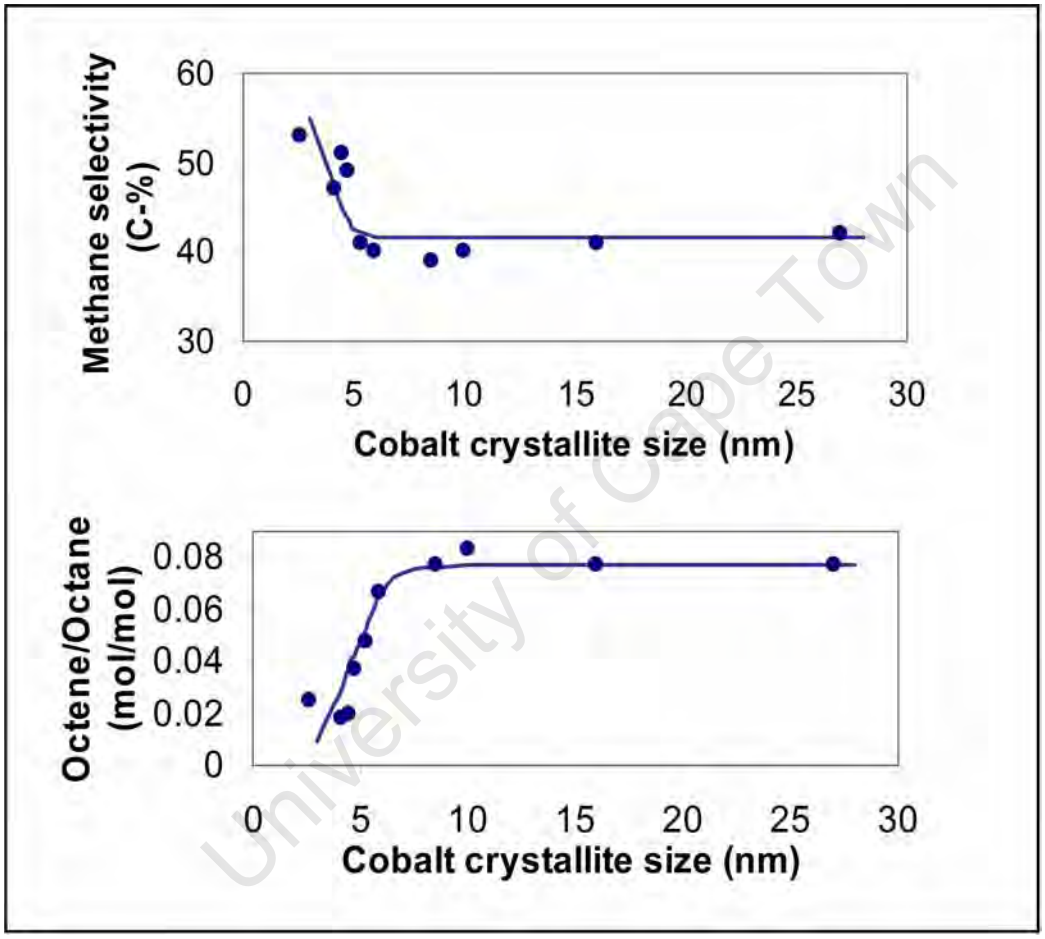

Figure 2.15: Effect of cobalt crystallite size on the methane selectivity and C_8 olefin to paraffin ratio of Fischer-Tropsch synthesis (Bezemer et al. (2006)).

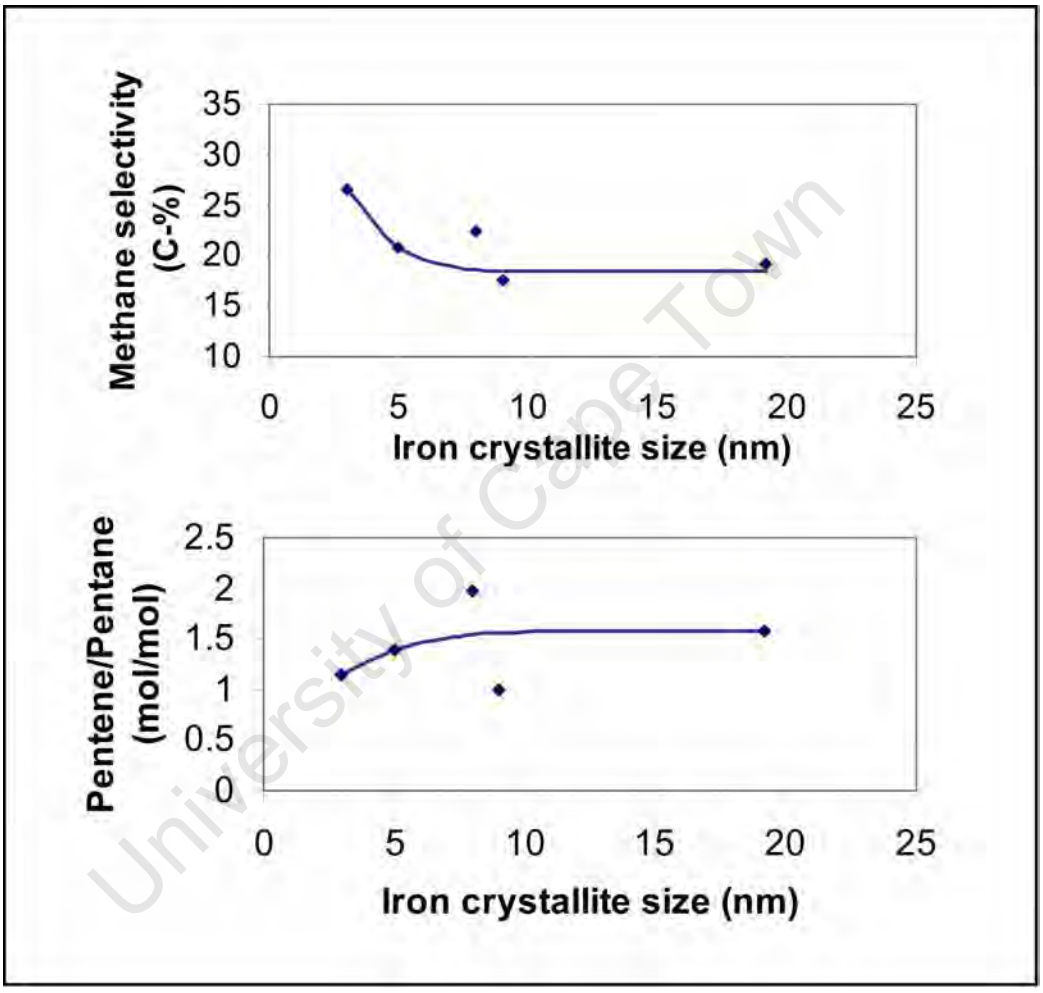

Figure 2.16: Effect of iron crystallite size on the methane selectivity and C_8 olefin to paraffin ratio of Fischer-Tropsch synthesis (Mabaso (2005)).

monoxide and hydrogen result in changes in selectivity (Phala et al. (2004), Welker (2007)).

3. Small crystallites are more susceptible to oxidation. (Iglesia (1997), van Steen et al. (2005))

The first theory is shown schematically in Figure 2.17, it expects that in Fischer-Tropsch Synthesis it takes certain minimum ensembles in order for the reaction to take place. In small crystallites there are not enough atoms available to make up the required ensembles, therefore affecting both overall activity and selectivity. Such ensembles may include specific sites on which carbon monoxide preferentially dissociates and which are mainly found along defects and steps on the crystallite surface (Ge et al. (2002), Ge and Neurock (2004), Swart et al. (2007), Shetty et al. (2008)). This theory is also known as the 'Ensemble Theory', which suggests that certain catalytic reactions require a minimum collection of neighboring sites or 'ensembles' in order to occur (Niemantsverdriet et al. (1980), Ciobica et al. (2003), Ciobica and van Santen (2003), Mabaso (2005), Bezemer et al. (2006), Welker (2007)). It is likely that a complex chemical reaction like Fischer-Tropsch synthesis that involves multiple steps would occur on ensembles rather than individual surface atoms. In contrast, methane formation is a much simpler reaction and as such can happen on a much simpler site, or a single atom.

The second theory predicts that on smaller nano-sized metal crystallites, a higher activation energy is required for carbon monoxide, while the activation energy for hydrogen remains unchanged. This would result in the hydrogen rich product spectrum found for smaller crystallites in the work done by Bezemer et al. (2006) and Welker (2007).

The final theory expects that smaller crystallites are easier to oxidize than larger crystallites. Thermodynamic calculations performed by van Steen et al. (2005) on cobalt show that at a particular water to hydrogen ratio, smaller crystallites are more likely to exist in the oxide form than larger crystallites. This is shown schematically in Figure 2.18. It is important to note that while this has been shown on a theoretical level there has been to date no experimental data to confirm the theory. It should be borne in

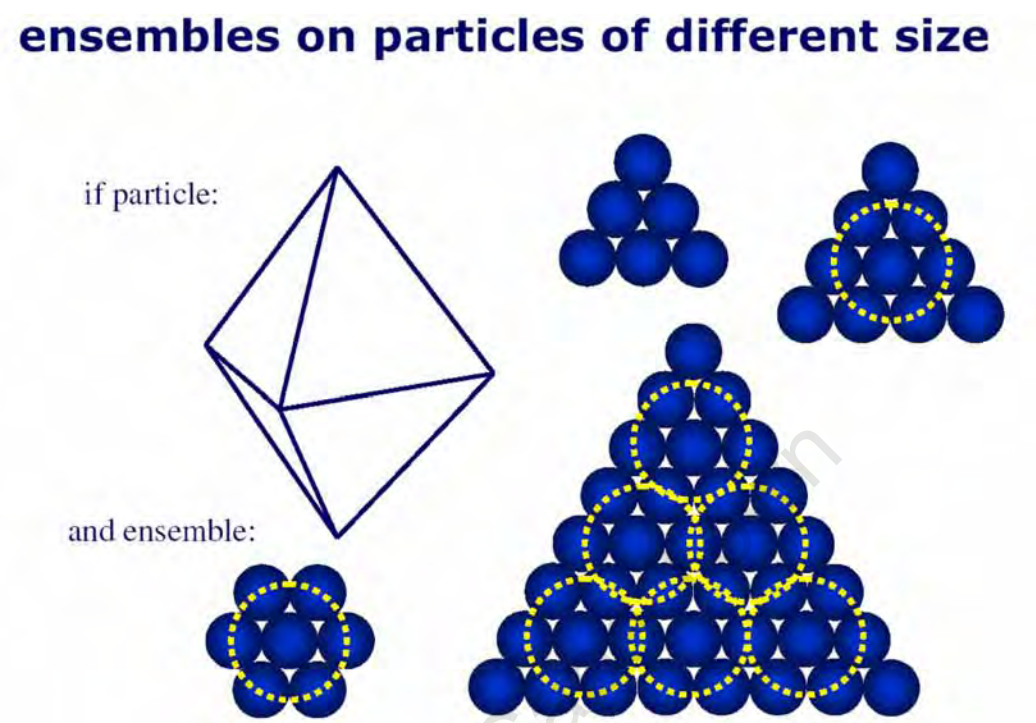

Figure 2.17: "The Ensemble Effect" explaining structure sensitivity in Fischer-Tropsch synthesis (Niemantsverdriet et al. (1980)).

mind that while oxidation with cobalt has not been directly observed yet, oxides of iron are typically found in iron-based Fischer-Tropsch catalysts. Studies dealing with effects of crystallite size require model catalysts with well defined metal crystallites of adjustable size, preferably well dispersed on the surface of an inert support (see Section 4.1).

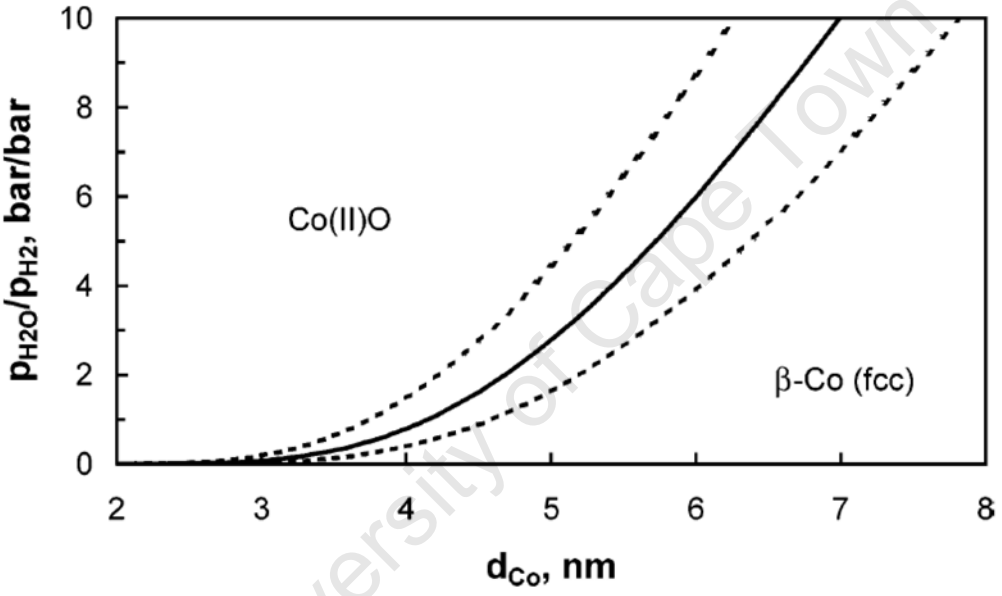

Figure 2.18: "The Oxidation Theory" stability region of spherical β-Co(fcc) and CoO crystallites in H_2O/H_2 atmosphere at 493K as a function of the cobalt crystallite size (van Steen et al. (2005)).

Chapter 3

Scope of Thesis

Fischer-Tropsch synthesis is a surface polymerisation. For optimum catalyst performance it is important to achieve maximum metal utilisation. Principally, the smaller metal crystallites in a catalyst have a larger fraction of metal atoms on the surface, which are available to catalyze the Fischer-Tropsch reaction. However, recently published work on supported cobalt, iron, ruthenium and rhodium catalysts (Bezemer et al. (2006), Mabaso (2005), Barkhuizen et al. (2006), Ojeda et al. (2004)) indicate that crystallites smaller than a certain size in the nano-meter range display lower metal surface area specific activity and high methane selectivity. Such studies can only be conducted with suitable model catalysts. Model type catalysts with uniformly sized iron crystallites evenly distributed on γ-alumina have been prepared using the reverse micelle method. Contrary to previous studies using iron and in order to simplify data interpretation (Mabaso (2005), Barkhuizen et al. (2006)), the catalysts in this work are not potassium promoted.

The aim of this study is to compare the Fischer-Tropsch activity and product selectivity of supported iron catalysts with different crystallite sizes. The first objective is to find an experimental methodology to create model type supported iron catalysts within a large range of average crystallite sizes (2-16 nm) as well as a narrow size distribution. The preparation technique is therefore chosen as the reverse micelle technique (Abrevaya and Targos (1987))

which is used to prepare a range of supported model catalysts with iron crystallites in the nano-meter range. Fresh, reduced and spent samples will be characterized using Temperature Programmed Reduction (TPR), Transmission Electron Microscope (TEM), X-Ray Diffraction (XRD) and Mössbauer Spectroscopy (MAS). Furthermore, a novel magnometer will be used to study changes of catalyst magnetisation of the working catalysts.

Supported iron catalysts with average metal crystallites ranging between 2 and 16 nm will be tested under mild Fischer-Tropsch conditions for low synthesis gas conversion and their activity and product selectivity measured as a function of time using both online and offline gas chromatography. Furthermore water will be added to the synthesis gas to investigate its effect on the model catalysts and their performance under simulated high conversion reaction conditions. Particular attention will be paid to the characterisation of spent catalysts in order to investigate the causes of small crystallites having inferior activity and selectivity when compared to larger crystallites. It is expected that these experimental runs will give insight into the effect of crystallite size and water addition on the activity and selectivity of low temperature iron based Fischer-Trospch synthesis.

Chapter 4

Experimental Methodology

4.1 Catalyst Preparation

A range of supported model catalysts were synthesized using the reverse micelle technique, resulting in catalysts with iron crystallite sizes ranging between 2 and 16 nanometers.

4.1.1 Synthesis of Supported Model Catalysts

Model catalysts were required for this research, specifically, iron crystallites evenly distributed on a porous support with a narrow crystallite size distribution. Therefore these catalysts were prepared using the reverse micelle technique. The reverse micelle technique involves the utilisation of water-in-oil micro-emulsions. These micro-emulsions are made up of three components; an aqueous phase, an organic phase and a surfactant. The surfactant used was Berol 050 (Penta-ethyleneglycol-dodecylether), and the organic phase was n-hexane.

The primary reverse micelle solution is formed by mixing the surfactant and the organic phase in an Erlenmeyer flask and left to equilibriate for 24 hours. The solution is then filtered, removing impurities in the form of a white cloudiness which may have formed overnight. The aqueous phase is then added, either in the form of the iron metal precursor (iron nitrate, $Fe(NO_3)_3.9H_2O$, 0.5$\underline{M}$) or the precipitating agent (ammonium carbonate,

$(NH_4)_2CO_3$, 2M). The solution is then left to stand for another 48 hours to allow the the reverse micelles to form and stabilize.

The amounts of surfactant, organic and aqueous phase used to create the catalyst samples were based on a ternary diagram (Figure 4.1) with a stability region for the reverse micelles. This stability region was first established by Abrevaya and Targos (1987) and again by Mabaso (2005) through a room temperature titration of Berol 050 and n-hexane mixtures with water. Keeping the amount of n-hexane constant, while varying the aqueous to surfactant ratio, the size of the reverse micelles can be changed and ultimately the size of the final metal crystallites can be controlled (Mabaso (2005).

Table 4.1 lists the compositions of the reverse micelle systems created as well as the amount of support used to get a metal loading of 13 wt%. The sample codes are listed according to the final expected crystallite sizes, i.e. the smallest expected crystallite size is 2 nm, and is therefore named '2 nm', and the largest crystallite is 16 nm, named '16 nm'. The expected sizes are based on work by Mabaso (2005), where the same reverse micelle compositions were used.

One of the objectives of this work is to create supported model iron catalysts. Using the reverse micelle technique ensure a narrow size distribution of the metal crystallites, however it is also important that the metal crystallites are evenly distributed onto the support material. To achieve this even distribution, individual steps of the catalyst preparation method were varied as described below. The steps of catalyst preparation that were varied are as follows:

1. Support addition method
2. Support material
3. Drying conditions
4. Calcination conditions

In the investigation of the variation of different catalyst steps, reverse micelle solutions were made up for the preparation of the '9 nm' catalyst.

Table 4.1: Sample codes indicating the amounts of Berol 050, n-hexane and aqueous phase used in the microemulsion solutions, and amount of support material used in preparation

Sample Code	**Anticipated crystallite size** [a]	$\mathbf{m}_{H2O}$ **(in g)**	$\mathbf{m}_{Berol050}$ **(in g)**	$\mathbf{m}_{n-hexane}$ **(in g)**	$\mathbf{m}_{Support}$ **(in g)**
'2 nm'	2	5	58	250	0.747
'3 nm'	3	5	48	250	0.747
'7 nm'	7	9	35	250	1.344
'9 nm'	9	13	50	250	1.841
'14 nm'	14	20	40	250	2.987
'16 nm'	16	20	33	250	2.987

[a]From Mabaso (2005) in nm

This particular size was chosen as it was in the middle range and therefore easy to prepare.

4.1.1.1 Variation of Support Addition Method

The first step of the catalyst preparation method to be varied, is the point at which the support material is added. Four different support addition methods were attempted:

1. No precipitation - support material added directly into the metal reverse micelle solution, i.e. no precipitation step (Figure 4.2)

2. After precipitation, using two reverse micelle solutions - as in Mabaso (2005) (Figure 4.3)

3. After drying of unsupported nano-crystallites prepared via precipitation from reverse micelle solutions (Figure 4.4)

4. After calcination of unsupported nano-crystallites prepared via precipitation from reverse micelle solutions (Figure 4.5)

In all these preparations a γ-alumina support was used.

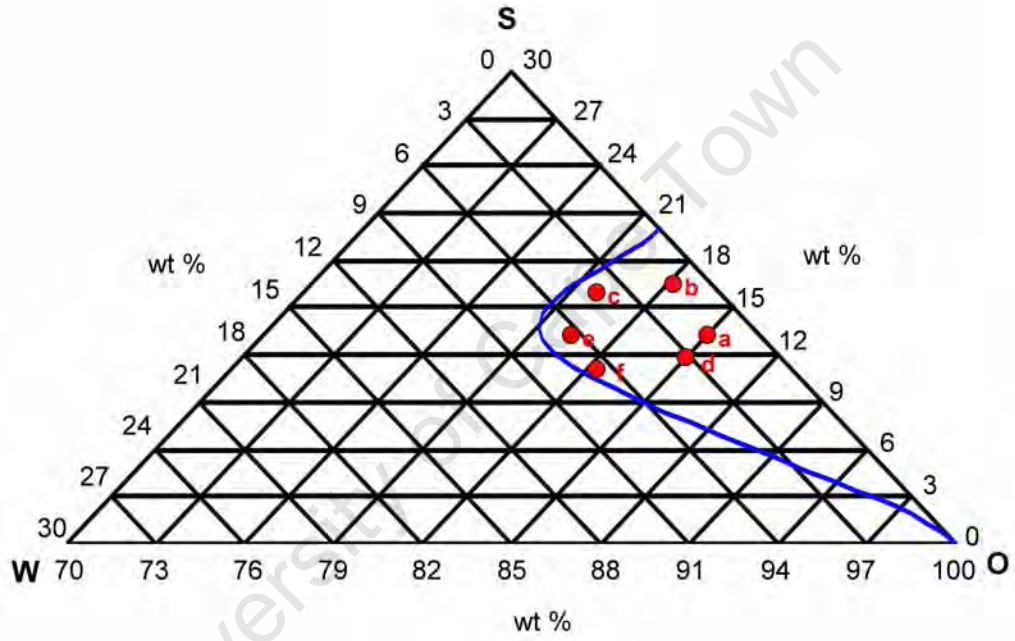

Figure 4.1: Water(W) - Berol 050(S) - n-hexane(O) ternary diagram, showing the stability region and the composition of the reverse micelle system from which the microemulsion solutions were formed (Determined by Mabaso (2005)). Sample codes: a:'2 nm', b:'3 nm', c:'7 nm', d:'9 nm', e:'14 nm' and f:'16 nm'

In the first method of support addition, one reverse micelle solution is made according to the method described in section 4.1.1, it is made with 0.5 M iron nitrate as the metal precursor. This method had been used successfully by Welker (2007) to prepare a series of alumina supported ruthenium catalysts. After allowing the reverse micelle solution to equilibrate for 48 hours, the correct amount of γ-alumina (see Table 4.1) in order to achieve a 13 wt% loading is added to the solution and mixed with an overhead stirrer at 800 rpm for 60 minutes to allow for the uptake of the iron containing reverse micelles onto the support material. At this point in the preparation sequence a slight discolouration of the iron containing solution from orange to a yellow-orange is observed visually. Acetone is then added to the solution to break the micelles and to wash out the surfactant from the solid material. The solution is then washed three or four times with acetone to remove the surfactant. Each washing step involves the addition of approximately 1.8 l of acetone to the 'impregnated' support which is then agitated for 10 minutes, after which it is allowed to settle and the excess acetone is decanted off. The resulting solid is then dried in a rotary drier at 60 °C and 350 mbar for 60 minutes. The catalyst is then calcined in air at 300 °C for 16 hours in a fluidized bed reactor (flowrate: 60 ml(NTP/min/g; heating rate: 10 °C/min). This preparation method is shown in Figure 4.2.

The second method is the one described by Mabaso (2005), here two separate water-in-oil micro-emulsions are formed, again according to the method described in section 4.1.1. One contains 0.5 M iron nitrate as the metal precursor, and another which contains 2 M ammonium carbonate as the precipitating agent. The molarities of the aqueous solutions were chosen such that there is an excess of the precipitating agent in order to achieve complete precipitation. The two reverse micelle solutions are mixed together at room temperature in a 2 l glass beaker, while being agitated by an overhead stirrer at a constant stirring speed of 800 rpm for 60 minutes. The reverse micelles will collide and bring the reactants into contact with each other. The iron nitrate reverse micelle solution has a clear orange colouration, while the ammonium carbonate solution is clear, upon mixing the resulting solution has a deep orange colouration. The precipitate forms, but will remain within

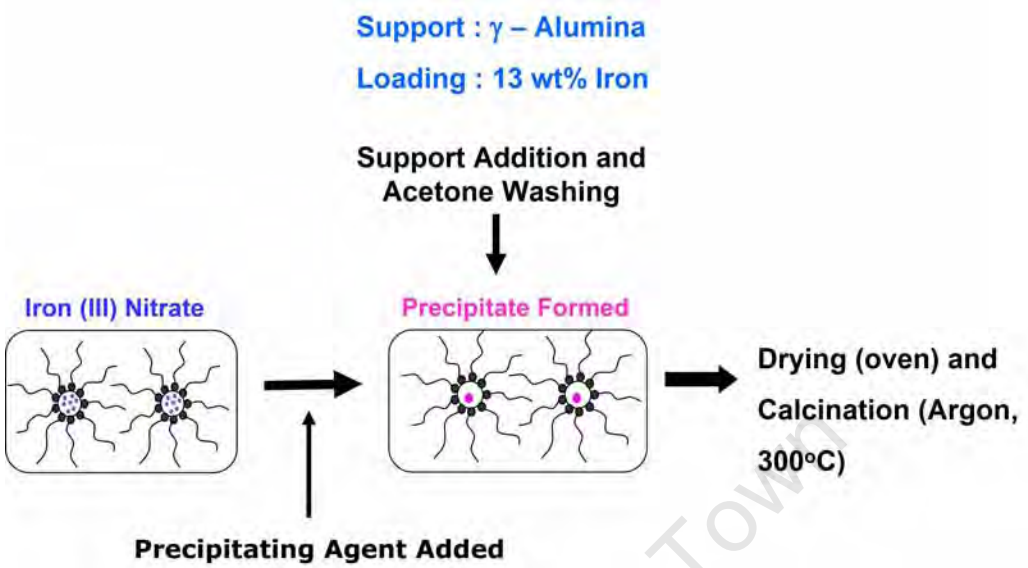

Figure 4.2: Schematic of preparation method 1, single reverse micelle solution used, no precipitation step, addition of support material directly into the reverse micelle solution

the reverse micelles, which are still intact. The γ-alumina is then added, at which point there is a slight discolouration of the solution from a deep orange to a lighter, clear orange. The stirring is continued for a further 15 minutes. Acetone is then added to de-stabilize the system and release the precipitate. Further washing, drying and calcination is the same as in method 1. Catalyst preparation via this method is shown schematically in Figure 4.3

Methods 3 and 4 involve the formation of unsupported metal crystallites first. Again this is done by making two reverse micelle solutions, one with the metal precursor and another with the precipitating agent. After allowing for equilibration, the two solutions are mixed together for 60 minutes, after which the solid precipitate is washed out with acetone.

For method 3, the precipitate is then dried in the rotary drier. After which the particles formed via precipitation and the γ-alumina are re-dispersed in 500 ml of a new solvent (see Section 4.1.1.3, within an ultra-sonic bath for 15 minutes. The suspension is then re-dried and calcined, this method is shown in Figure 4.4.

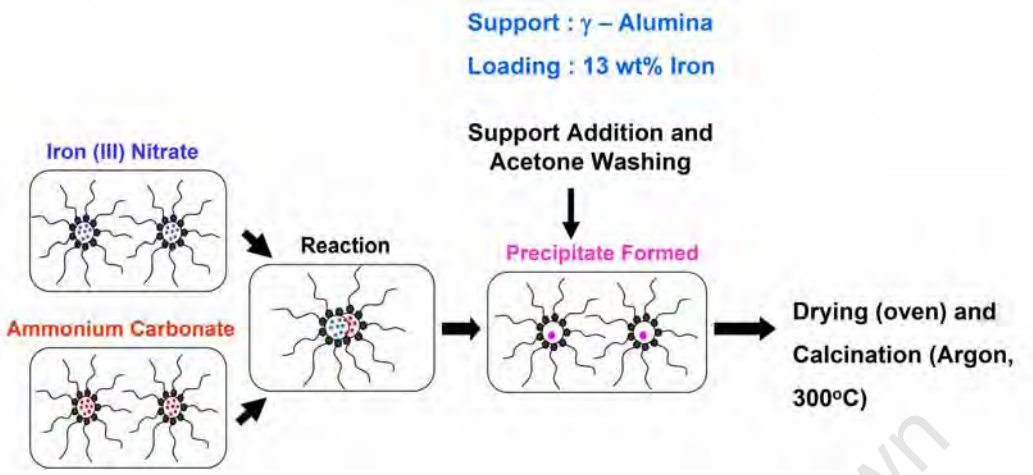

Figure 4.3: Schematic of preparation method 2, precipitation using two reverse micelle solutions. Support addition after precipitate formation as used by Mabaso (2005)

Method 4 is similar to the previous method, except the unsupported precipitate is calcinced to form nano-sized crystallites of iron oxide as evidenced by Mabaso (2005), before re-dispersion with the γ-alumina in a new solvent in the ultra-sonic bath. The solution is then re-dried and re-calcined, this method is shown in Figure 4.5.

4.1.1.2 Variation of Support Material

Three different support materials were used to test their effect on the dispersion of the metal crystallites. γ-alumina was the first support material used, but as it is difficult to view on an electron microscope, other support materials were considered. Silica was then tested, as it is known to be easier to achieve good contrast of the support and the iron crystallites on an electron microscope. A third support material of a silica modified with alumina deposited on it was also tested. This third support material had to be prepared via impregnation of the previously mentioned silica material, targeting a theoretical monolayer coverage with alumina. For 6 grams of resulting support, 15.198 g of aluminium nitrate ($Al(NO_3)_3.9H_2O$) is required, it is then dissolved in approximately 60 ml water. The solid silica is then

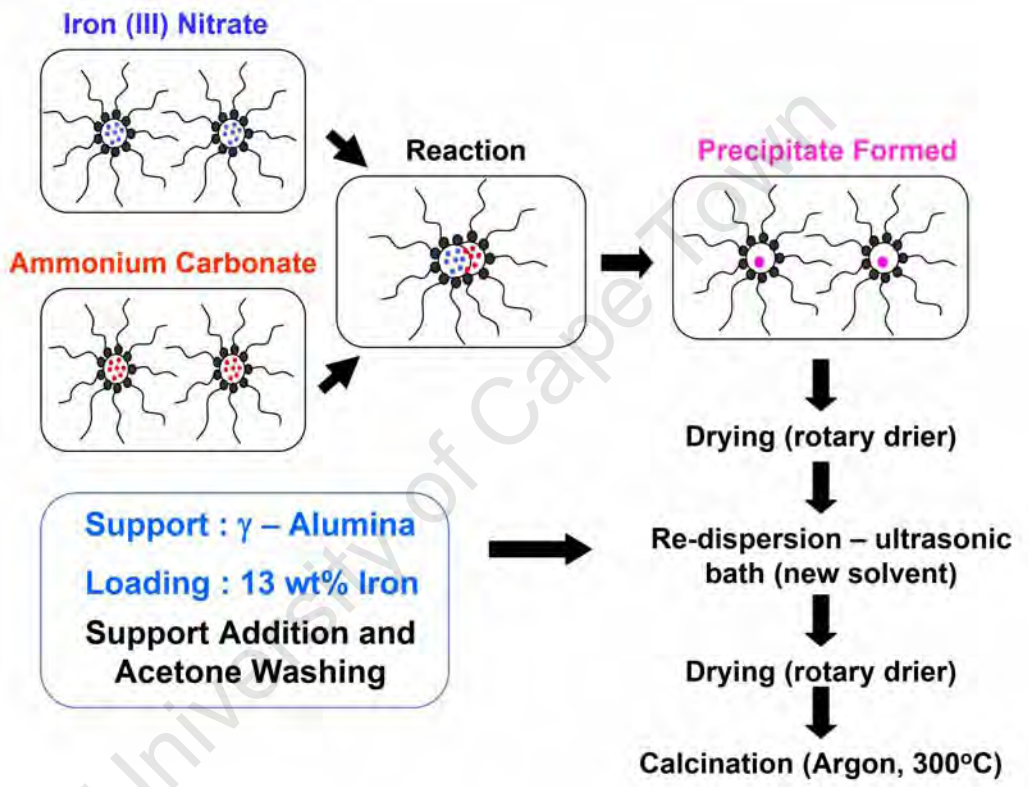

Figure 4.4: Schematic of preparation method 3, preparation of unsupported metal crystallites via precipitation of two reverse micelle solutions, followed by re-dispersion of metal crystallites and support addition in a new solvent

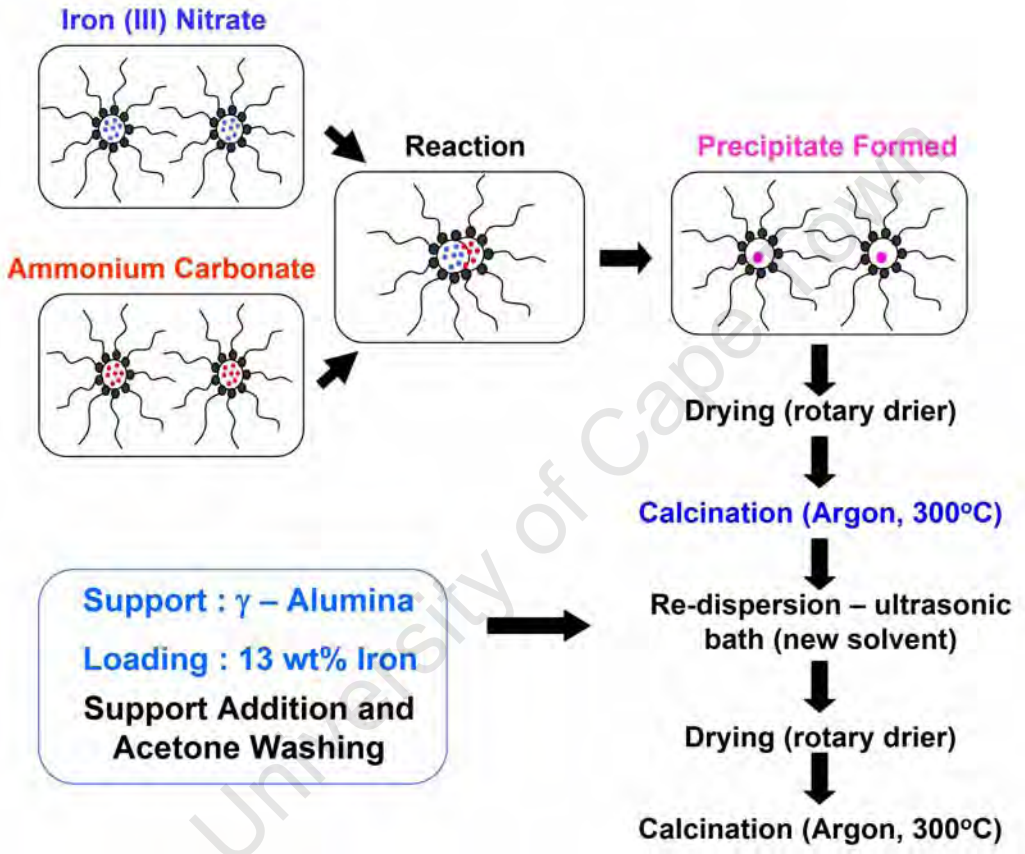

Figure 4.5: Schematic of preparation method 4, preparation of unsupported metal crystallites via precipitation of two reverse micelle solutions, followed by re-dispersion of metal crystallites and support addition in a new solvent

added to the solution and stirred for 20 minutes with an overhead stirrer at 800 rpm. After which the suspension is dried in a rotary drier at 100 °C and 250 mbar for 90 minutes. Calcination follows in air for one hour at 550 °C with a heating rate of 1 °C/min.

4.1.1.3 Variation of Solvent

For methods 3 and 4 from section 4.1.1.1, the solvent used for re-dispersion was varied. It is theorized that the polarity of the solvent may influence the dispersion of the crystallites onto the support material. Therefore 3 different solvents were used, chosen for their decreasing polarities:

1. Water
2. Ethanol
3. n-Hexane

4.1.1.4 Variation of Drying Technique

The drying method described in section 4.1.1.1 was also varied, specifically for the smaller metal crystallites (2 and 3 nm). Instead of drying in a rotary drier, the washed solution containing the metal precipitate and acetone was decanted and allowed to dry in a fume cupboard at room temperature for 24 hours. It is then moved into an oven at 120 °C for a further 3 hours of drying.

4.1.1.5 Variation of Calcination Conditions

The calcination method described in section 4.1.1.1 was also varied. The length of time the calcination procedure was carried out for was varied between 1 hr and 16 hrs (as used by Mabaso (2005). The gas used for calcination was also varied between air and argon, and finally the temperature at which the calcination took place was decreased from 350 °C to 300 °C.

Table 4.2: Experimental procedures carried out for the investigation of variations in method during the preparation of supported catalysts

Variation in support addition					
Method	**Support**	**Precipitation**	**Solvent**	**Drying**	**Calcination**
1	γ-alumina	no	~	x1/oven	x1/Argon/300 °C/16 hrs
2	γ-alumina	yes	~	x1/oven	x1/Argon/300 °C/16 hrs
3	γ-alumina	yes	~	x2/oven	x1/Argon/300 °C/16 hrs
4	γ-alumina	yes	~	x2/oven	x2/Argon/300 °C/16 hrs
Variation in support material					
Method	**Support**	**Precipitation**	**Solvent**	**Drying**	**Calcination**
2	γ-alumina	yes	~	x1/oven	x1/Argon/300 °C/16 hrs
2	Silica	yes	~	x1/oven	x1/Argon/300 °C/16 hrs
2	Modified silica	yes	~	x1/oven	x1/Argon/300 °C/16 hrs
Variation in solvent					
Method	**Support**	**Precipitation**	**Solvent**	**Drying**	**Calcination**
4	γ-alumina	yes	n-hexane	x1/oven	x1/Argon/300 °C/16 hrs
4	γ-alumina	yes	ethanol	x1/oven	x1/Argon/300 °C/16 hrs
4	γ-alumina	yes	water	x1/oven	x1/Argon/300 °C/16 hrs
Variation in drying technique					
Method	**Support**	**Precipitation**	**Solvent**	**Drying**	**Calcination**
2	γ-alumina	yes	~	x1/rotary drier	x1/Argon/300 °C/16 hrs
2	γ-alumina	yes	~	x1/oven	x1/Argon/300 °C/16 hrs
Variation in calcination conditions					
Method	**Support**	**Precipitation**	**Solvent**	**Drying**	**Calcination**
2	γ-alumina	yes	~	x1/oven	x1/Air/350 °C/16 hrs
2	γ-alumina	yes	~	x1/oven	x1/Air/350 °C/1 hr
2	γ-alumina	yes	~	x1/oven	x1/Air/300 °C/16 hrs
2	γ-alumina	yes	~	x1/oven	x1/Argon/300 °C/16 hrs

4.2 Characterisation of Support Material

The different support materials (see Section 4.1.1.2 were characterized by zeta potential and ultimately their isoelectric points. The instrument used is a Malvern Zetasizer Nano-series (Malvern Instruments Ltd., England). The zeta potential indicates the total surface charge of a specific material. By measuring the zeta potential of the support material at different pH values, the isoelectric point of the material can be isolated. The support material is first crushed and sieved until it is below 5 μm, 0.1 g of the material is then suspended in 100 ml of 0.1 M KCl solution. Some of the solution is loaded into a measuring cell and placed into the instrument, three separate readings are then taken. Drops of either 0.1 M HCl or 0.1 M KOH solution is then added to the suspension to adjust the pH. Readings are then taken at different pH settings. A graph of the zeta potential versus the pH of the solution can then be plotted and the isoelectric point of the material isolated.

4.3 Characterisation of Supported Model Catalyst

4.3.1 Transmission Electron Microscopy (TEM)

The size distributions of the calcined, reduced and spent model catalysts were determined using Transmission Electron Microscopy (TEM). The TEM photos can also be used to determine whether the iron-containing crystallites are evenly distributed onto the support material.

Sample preparation for TEM analysis begins by placing a small amount of sample in a plastic vial, which was then filled with a liquid resin. The liquid resin is then stirred around in order to avoid the formation of air bubbles. The sample is then allowed to solidify in an oven for 24 hours at 60 °C. The solid sample is then cut into 0.1 μm slices using an Ultramicrotome Leica UltracutS cutting machine. The samples could then be transferred onto copper grids.

The copper grids are then loaded into the electron microscope and photos

are taken of the sample. Two different TEM instruments were used, a LEO 912 operated at 120 kV and a JEM200CX operating at 200 kV. The photos are later analyzed using freeware IMAGEJ, a minimum of 300 crystallites per sample were measured to establish representative size distributions.

4.3.2 Atomic Absorption Spectroscopy (AAS)

Atomic Absorption Spectroscopy (AAS) was used to determine whether the pre-determined catalyst metal loading was achieved. From the results of AAS the percentage of iron, alumina or silica in a sample can be determined. The sample is first ground up, and then 0.1 g is weighed out and placed into a wide-mouthed 250 ml Erlenmeyer flask. For sample digestion, 10 ml of a 4:1 HCl/HF mixture is then added to the flask and brought to boiling, after which 10 ml of HNO_3 is then added to the flask and further heated until the sample volume is approximately 2 ml, upon which 5 ml of $HClO_4$ is added and again boiled until approximately 2 ml of sample is left. At this point a white cloud will form which indicates that a reaction has taken place. The solution is then allowed to cool before transferring the sample into a 100 ml volumetric flask and make up to 100 ml with distilled water. The liquid sample is then filtered through a Whatman No. 1 filter paper into a sample bottle. The sample can then be read on the AA instrument.

4.3.3 Temperature Programmed Reduction (TPR)

Temperature Programmed Reduction (TPR) was used to investigate the reduction behaviour of the catalyst samples, it was also used to determine the degree of reduction of the samples. The reduction was carried out in a u-tube reactor on a Micromeritics AutoChem2910 (Micromeritics Instrument Corp., USA). An amount of 0.03 g of sample was loaded into the reactor and dried under argon at 120 °C for 30 minutes, after which the sample was cooled back to room temperature and the gas changed from argon to the reducing gas of 5% hydrogen in argon. The sample is heating under the reducing gas from room temperature to 1000 °C at a heating ramp of 10 °C/min. The hydrogen consumption is measured by a Thermal Conductivity Detector (TCD) which

was calibrated at regular intervals with NiO which has a known reduction behaviour.

The degree of reduction was carried out by first submitting the sample to the same reduction procedure as applied on the catalyst prior to Fischer-Tropsch testing (see Section 4.1.1.1), entailing of reduction of 16 hours at 300 °C under pure hydrogen with a ramping rate of 1 °C/min. After this the sample is cooled back down to room temperature and a the TPR program described above is carried out. Should further reduction be observed, it is assumed that this is due to unreduced Fe_3O_4, the corresponding degree of reduction can be calculated.

4.3.4 X-Ray Diffraction (XRD)

The calcined, reduced and spent samples were tested in the XRD instrument, which was used to analyse the crystalline phases and the average crystallite sizes of the samples. Three separate instruments were used for the measurements, a Philips X-ray diffractometer with Cu-Kα radiation of wavelength 1.540 $\mathring{A}$ at 40 kV and 25 mA was used to analyse the calcined and reduced samples. The scan range for these measurements was between 20 ° and 80 ° using a step scan mode. The spent catalysts were analyzed using two separate, more advanced instruments as their crystalline phases were more complex. The first instrument used for the spent catalysts was located at ITEMBA Labs (Stellenbosch), it was a Bruker AXS diffractometer, with Cu-Kα radiation of wavelength 1.540 $\mathring{A}$ at 40 kV and 40 mA. The scan range for this instrument was between 15 ° and 80 ° using a step scan mode. The second instrument used was located at Sasol Ltd. (Sasolburg), the instrument was a Philips X'Pert Pro diffractometer, with cobalt source at 1.789 $\mathring{A}$ at 40 kV and 40 mA. The scan range for this final instrument was between 5 ° and 105 °, again using a step scan mode. The resulting diffraction peaks were compared against those of standard powder compounds reported in the JCPDS[1] data file.

The average crystallite sizes of the sample were calculated using the Scher-

[1]Joint Committee for Powder Diffraction Standards

rer formula:

$$L_{hkl} = \frac{k\lambda}{\beta \cos\theta_0} \tag{4.1}$$

L_{hkl} is the thickness of a crystallite, k is a constant, λ is the wavelength of the X-ray used and θ_0 is the angular position of the peak maximum. Finally β is expressed in radians and is the integral breadth (total area under the line profile divided by the line intensity at maximum).

A correction factor is required for β to account for any errors introduced by the apparatus itself, this is done according to the following equation:

$$\beta^2 = \beta^2_{observed} - \beta^2_{apparatus} \tag{4.2}$$

The correction factor of $\beta_{apparatus}$ is obtained by running a reference sample of sodium chloride in the X-Ray diffractometer.

Associated Rietveld analysis could not be done on the catalyst samples as the alumina support contains some δ-alumina as well as γ-alumina. The complete crystallographic structure of δ-alumina is not known and as such Rietveld refinement to obtain the full phase composition of the catalyst samples would not be possible.

4.3.5 Mössbauer Spectroscopy (MAS)

The crystalline phases of calcined and spent catalysts were further determined using Mössbauer spectroscopy (MAS). Constant acceleration spectrometers were utilized, with ^{57}Co/Rh as the radiation source. The data was recorded at room temperature over a velocity range of approximately 12 mm/s. The spectra obtained from the Mössbauer spectroscopy were then analyzed using a least squares program "Normos" which models the spectra as a combination of quadruple doublets and sextets based on a Lorentzian line-shape profile (Cairns (2009)). The individual absorption features of various doublets and sextets were then identified to specific crystalline phases based on their isomer shift (δ), quadrupole splitting (Δ) and magnetic hyperfine field (B_{hf}) values. Finally the amounts of each phase present were

determined from the relative areas of the absorption spectra. Metallic iron (α-Fe) was used to calibrate the velocity scale and the isomeric shift values are reported relative to it.

4.3.6 Magnetic Measurements

Measurement of the total magnetisation is a suitable method to study the properties of metals such as iron, cobalt or nickel as the metals, the oxides, and the carbides have different and distinguishable properties. For example, metallic iron is ferromagnetic, hematite (α-Fe_2O_3) is antiferromagnetic, maghemite (γ-Fe_2O_3) and magnetite (Fe_3O_4) are ferromagnetic, and wuestite (FeO) is antiferromagnetic.

The carbides of iron are ferromagnetic with different Curie temperatures, deviating from the Curie/Néel temperatures of the iron oxides. All the different phases of iron display different saturation magnetisation. Due to these differences, measuring the total saturation magnetisation of an iron containing catalyst will enable the study of changes in the composition of the phases during Fischer-Tropsch synthesis. These measurements provide information about the bulk phases present.

The total magnetisation as a function of an external magnetic field can give information on crystallite sizes in a sample (Dalmon (1994)). In purely superparamagnetic samples no magnetism is present upon removal of an external field, whereas remnant magnetisation after removal of an external field indicates the presence of crystallites larger than a certain temperature dependent critical size, believed to be around 23 to 25 nm for metallic iron at room temperature (Bonneviot and Olivier (1994)).

The weight percentage of crystallites larger than this critical size, i.e. the percentage of ferromagnetic material, can be calculated as being (Dalmon (1994), Barbier et al. (1998), Barbier et al. (2001)):

$$\gamma = \frac{2M_{rem}}{M_{sat}} \tag{4.3}$$

Where M_{rem} is the remnant magnetisation and M_{sat} is the saturation magnetisation.

Table 4.3: Magnetic properties of iron compounds (van de Loosdrecht (1994))

Compound	**Magnetism**	**Curie/Néel Temperature (K)**	**Saturation Magnetisation (Am^2/kg)**
Fe (metallic iron)	ferromagnetic	1043	222
α-Fe_2O_3 (hematite)	antiferromagnetic	963	0.4
γ-Fe_2O_3 (maghemite)	ferromagnetic	873	80
Fe_3O_4 (magnetite)	ferromagnetic	853±15	90-92
FeO (wuestite)	antiferromagnetic	188	-
θ-Fe_3C (cementite)	ferromagnetic	485±8	128
χ-Fe_5C_2 (Häag)	ferromagnetic	530±10	140 [a]
Fe_7C_3	ferromagnetic	523±3	110 [b]
ε-$Fe_{2.2}C$	ferromagnetic	723±10	130
ε-Fe_2C	ferromagnetic	653±10	-

[a] Hofer and Cohn (1950)
[b] Tajima and Hirano (1990)

Magnetic measurements were performed on a novel magnometer specifically developed at the University of Cape Town for in-situ catalyst characterisation at fully relevant reaction conditions of temperature, pressure and gas environment (up to 50 bar and 500 °C).

4.4 Fischer-Tropsch Synthesis Experiments

4.4.1 Test Unit Set-up

The schematic set-up of the experimental test unit used to perform the Fischer-Tropsch runs is shown in Figure 4.6. During operation, hydrogen, carbon monoxide and argon are supplied through mass flow controllers MC-1 to 3 (Brooks Instruments) into the test unit. The pressure of the system is controlled via a dome loaded back pressure regulator I-7, argon is fed via a pressure regulator to the back chamber of the back pressure regulator, therefore setting the pressure. The pressure of the entire experimental test unit is kept at the set pressure, only past the back pressure regulator does the pressure return to atmospheric pressure.

The reactor used is a U-tube fixed bed reactor made from 1/4" stainless steel tubing (see Section 4.4.2). Flow of gas to the reactor is controlled through two three way valves V-17 and V-18. The inert argon fed to the system is used as the internal standard for gas analysis. Liquid products are collected at two points, a wax trap T-1 for the longer-chained hydrocarbons and a cold-trap T-3 to collect water and liquid, lower hydrocarbon products. The wax trap is kept at 180 °C, 10 °C less than the temperature of the rest of the lines to ensure efficient wax collection. The cold trap is maintained at room temperature, ensuring that any water in the product stream is effectively knocked out of the product stream before it enters the online gas chromatograph.

4.4.2 Reactor Set-up

The reactor set-up used for Fischer-Tropsch synthesis is shown schematically in Figure 4.7, the reactor is a U-tube fixed bed reactor made from stainless steel (d_{out}=6.35 mm[2], d_{int}=4.4 mm[3]). The isothermal region of the reactor (determined by Mabaso (2005)) is packed with 0.5 g of catalyst diluted with 1.2 g of silicon carbide (mesh size = 200-250 μm). The outlet end is tightly

[2]outer diameter
[3]internal diameter

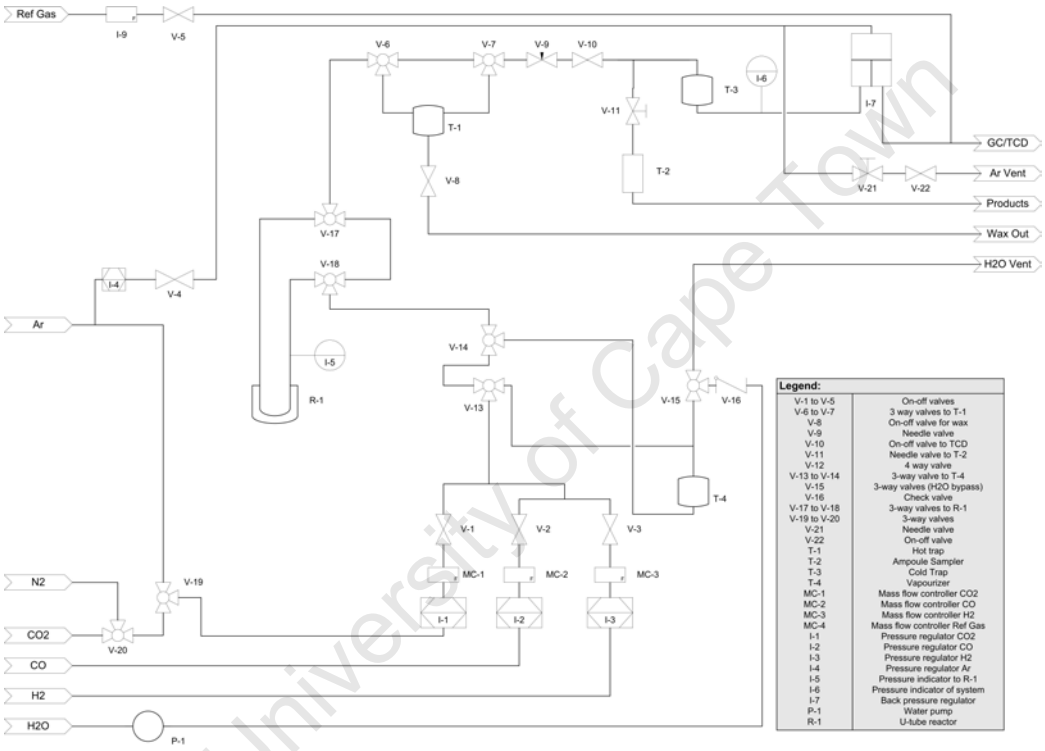

Figure 4.6: Schematic set-up of experimental test unit for Fischer-Tropsch synthesis

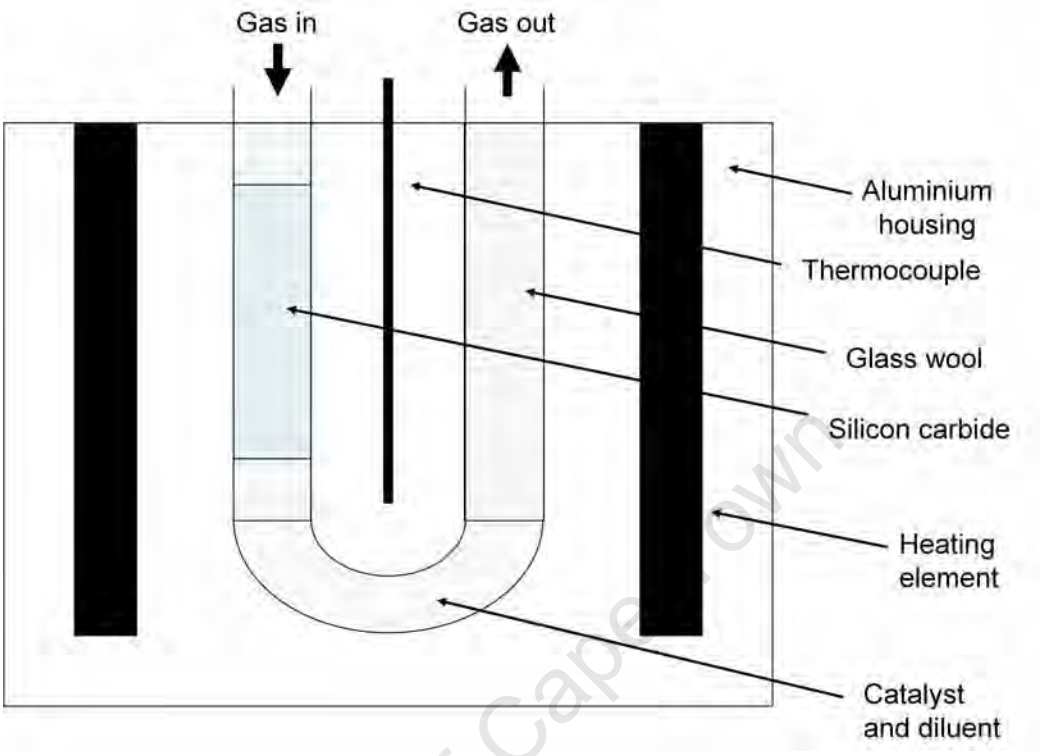

Figure 4.7: Schematic set-up of fixed-bed U-tube reactor used for Fischer-Tropsch synthesis

packed with silane treated glass wool to the top, the inlet end is first tightly packed with a small amount of glass wool, followed by silicon carbide, used to pre-heat and fully mix the reaction gases before they reach the catalyst bed, the end of the inlet side is finally plugged to the top with glass wool. It is important to tightly pack the ends of the u-tube with glass wool such that the catalyst bed does not move during reaction and is kept within the isothermal region, i.e. the region where the temperature is within $\pm 1\,^{\circ}\mathrm{C}$ of the desired temperature. The reactor is then placed within an insulated block aluminium housing which provides controlled heating through an electric heating elements. A thermocouple is also placed centrally in an axial position within the aluminium housing.

4.4.3 Experimental Procedure

4.4.3.1 Base Case Runs

Prior to a Fischer-Tropsch experiment the catalyst is reduced *in-situ* in 30 ml/min of H_2 to its metallic form at 300 °C for 16 hrs with a temperature ramp of 1 °C/min.

After reduction, gas flow is changed from hydrogen to an inert gas nitrogen and a temperature of 240 °C is maintained for Fischer-Tropsch reaction, total pressure is preset at 12 bar, and maintained with a back-pressure regulator using an auxiliary argon flow. The reactor is then isolated via two three-way valves V-17 and V-18 in order to maintain the catalyst in its reduced form. Once the reactor is isolated, gas flows bypassing the reactor are set to achieve reaction conditions, $m_{H_2} = 30$ ml/min, $m_{CO} = 15$ ml/min and $m_{Ar} = 9$ ml/min, which correspond to partial pressures of: $P_{H_2} = 6.66$ bar, $P_{CO} = 3.33$ bar, $P_{Ar} = 2$ bar within the reactor. The resulting space velocity at normal temperature and pressure is 831 $ml/g_{Fe}.min$. These mild operating conditions and relatively high space velocities were chosen in order to maintain a low conversion, i.e. negligible water partial pressures, to avoid concentration and temperature gradients within the reactor system.

Once the reaction gases have stabilized the positions of the two three way valves are changed such that the reaction gases flow through the reactor. Product sampling is achieved through two methods; online gas chromatography of the cold effluent gas was performed using a micro-gas chromatograph employing Thermal Conductivity Detectors (TCD), using argon as the reference gas, conversion levels of hydrogen and carbon monoxide could be calculated, as well as yields of methane and carbon dioxide. Offline gas chromatography was also performed, utilising the ampoule sampling technique (see Section 4.4.4). The flow of the hot effluent gas to the ampoule sampler is controlled through the needle valve V-11. The contents of the ampoules were analysed using a gas chromatograph employing a Flame Ionisation Detector (FID) for detection of organic products. This detection technique has a higher sensitivity than the TCD which allowed for product detection of very low levels, with products ranging from C_1 to C_9. Methane was used

as a reference component to tie together the TCD and FID analyses. The online gas sampling is performed every 5 minutes (analysis time: 3 minutes) for the first hour, then every 15 minutes of the second hour, and finally every 30 minutes until a total reaction time of 5 hours. Ampoules are taken and eight different points in the 5 hour period; at 10, 20, 90, 150, 240 and 300 minutes, details on gas-chromatographic procedures are give in Section 4.6.

Upon completion of the experimental run the temperature program controlling the reactor temperature is switched off and the auxiliary argon flow to the back pressure regulator switched off and the pressure within the experimental test unit released through valves V-21 and V-22, until atmospheric pressure is reached. The flow of hydrogen and carbon monoxide are switched off, leaving only inert argon flowing. When the temperature of the reactor is back to room temperature, two three way valves V-19 and V-20 are switched such that carbon dioxide flows through mass flow controller MC-1. The carbon dioxide is then allowed to flow for 60 minutes to ensure passivation of the catalyst sample. The catalyst sample can then be removed from the reactor and post run analyses can be conducted.

4.4.3.2 Runs with Water Co-feeding

To test the effect of water addition on the activity and selectivity of Fischer-Tropsch synthesis, runs with water co-feed were performed to compare against the basecase runs. Water is fed into the system by a pump in 1/16" tubing, through a check valve V-16 and a three-way valve V-15. The check valve is used to ensure that there is no back flow of water from the system towards the pump, and the three-way valve allows the pump to be primed without the priming water running into the system. The water then runs through a vapourisor packed with silicon carbide and set at the temperature of 200 °C, which ensures that the water is vapourized before entering the reactor together with the feed gas. The line between the water vaporizer and the reactor is heated to avoid condensation.

The start up of the runs with water addition is the same procedure as described in Section 4.4.3.1, the only difference is that two three-way valves

V-13 and V-14 are switched such that the water vapour enters into the reactor system. Also the total pressure of the system is increased to account for the addition of water vapour in the reaction gas, for example; if three bar of water is added, the total pressure of the system would be increased by 3 bar, meaning that the partial pressure of syn-gas (hydrogen and carbon monoxide) in the reactor will always remain constant at 10 bar. A negligible conversion of synthesis gas (<10%) is assumed, so that the partial pressure of water formed can also be assumed to be negligible ($P_{H_2O} \backsimeq 0$ bar). Product sampling remains the same for the runs with water addition as with the base case runs.

4.4.4 Offline Sampling Technique

Offline sampling was done using the ampoule technique developed by Schulz et al. (1984). Glass ampoules are made from standard Pasteur pipettes and used as sample containers. The glass ampoules are evacuated using a pump, and then sealed. The capillary end of the evacuated glass sample is then inserted into the heated ampoule sampler through the air-tight septum into the product stream. The breaking fork is used to break the end of the capillary and a sample of the product vapour is drawn into the ampoule, this is shown schematically in Figure 4.8. The ampoule is then immediately sealed using a butane flame. These samples are now airtight and can be stored and analyzed at a later stage using a special ampoule breaker connected to a gas chromatography system with a flame ionization detector (FID) which allows for the analysis of organic gases (see Section 4.6.2).

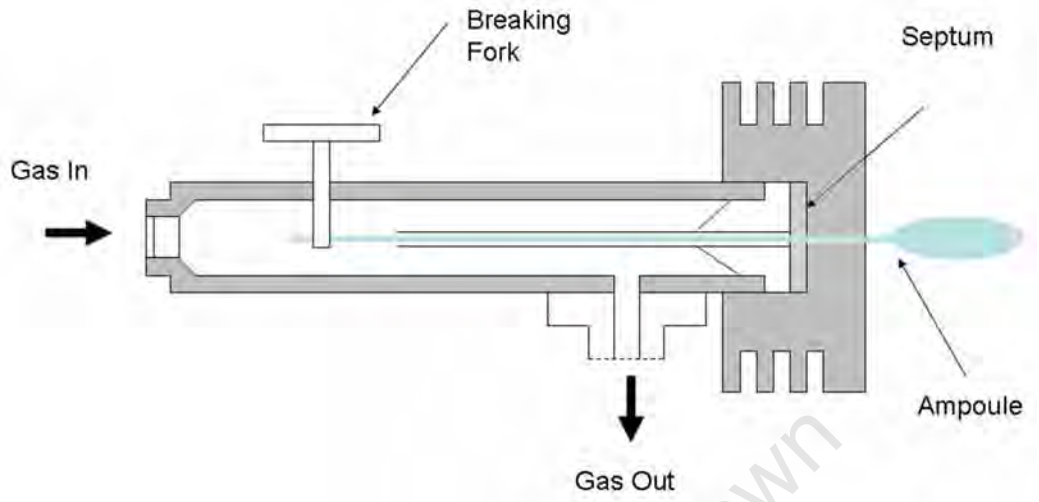

Figure 4.8: Schematic of offline amouple sampling set-up

4.5 Fischer-Tropsch Synthesis Experiments in Set-up for Magnetic *in-situ* Characterisation

4.5.1 Test Unit Set-up

A separate experimental test unit is used to carry out *in-situ* characterisation of magnetic properties of the model catalysts, this experimental test unit is shown schematically in Figure 4.9. During operation, a pre-mixed combination of hydrogen, carbon monoxide and argon at a 6:3:1 ratio is fed into the system through mass flow controller MC-M1 (Brooks Instruments) into the test unit. The pressure of the system is controlled via a spring loaded back pressure regulator I-M7. The tightness of the spring sets the total pressure of the system, the pressure of the entire experimental test unit is kept at the set pressure, only past the back pressure regulator does the pressure return to atmospheric pressure.

The reactor used is a straight fixed bed reactor made from 1/2" stainless steel tubing. Flow of gas to the reactor is controlled through two three way valves V-M9 and V-M10. The inert argon fed to the system is used as the in-

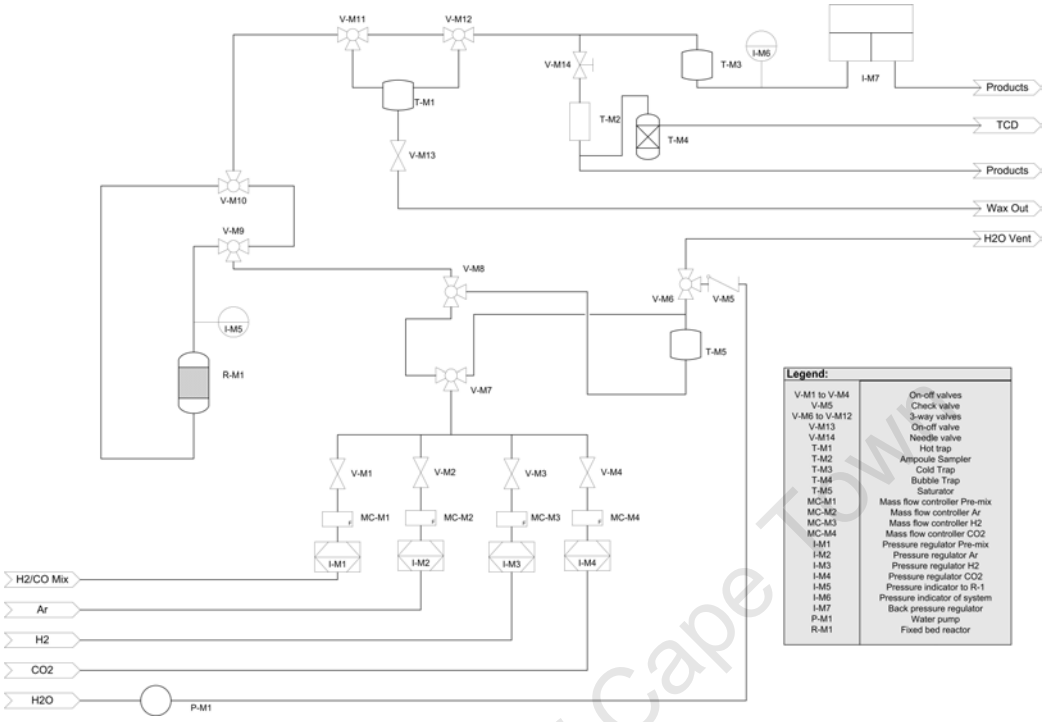

Figure 4.9: Schematic set-up of experimental test unit for magnetic *in-situ* characterisation during Fischer-Tropsch synthesis

ternal standard for gas analyses. Liquid products are collected at two points, a wax trap T-M1 for the longer-chained hydrocarbons and a cold-trap T-M3 to collect water and lower hydrocarbon liquid products. The wax trap is kept at 180 °C, 10 °C less than the temperature of the rest of the lines to ensure efficient wax collection. The cold trap is maintained at room temperature, ensuring that any water in the product stream is effectively knocked out of the product stream. A gas bubbler T-M4, bubbles the product gas through water, showing that there is constant gas flow through the ampoule sampler. The gas stream after the bubbler is sent to the gas chromatography system employing Thermal Conductivity Detectors (TCD), during operation the gas bubbler is used to knock out the water in the product stream as the cold trap has a volume of 250 ml meaning the lag time to the TCD would be too great for the purpose of the short term experiments of this study.

4.5.2 Reactor Set-up

The reactor set-up used for the *in-situ* characterisation of magnetic catalyst properties is shown schematically in Figure 4.10, the reactor is a 1/2" straight fixed bed reactor made from stainless steel (d_{out}=6.35 mm[4], d_{int}=4.4 mm[5]). The isothermal region of the reactor is packed with 0.5 g of catalyst diluted with 1.2 g of alumina, alumina is used as the diluent with these studies instead of silicon carbide in order to minimise the effect of catalyst segregation from the diluent upon applying an external magnetic field. A non-magnetic mesh is placed in the reactor two thirds of the way down to ensure that no catalyst escapes from the reactor. Glass wool is then packed into the reactor, the temperature probe (a non magnetic Pt 100 element) is placed into the reactor, with a metallic star to maintain the central radial position of the thermocouple in the catalyst bed, with the tip of the temperature probe in the center of the catalyst bed. The catalyst is then packed into the reactor followed by a layer of glass wool and silicon carbide filled to the top of the reactor. The axial position of the reactor within the magnetic field is adjustable, it is important to adjust the reactor such that the catalyst bed is centralized between the signal pick up coils in the homogeneous magnetic field, allowing for maximum strength of magnetic readings. The reactor itself is held by an aluminium bracket, which is moved up and down via a computer controlled electromotor (amplitude: 4 cm, frequency: 2 Hz), to induce a signal from the magnetised sample in the detection coils, this is shown in Figure 4.10.

The induced signal is proportional to the magnetisation of the sample, and the system is calibrated with known amounts of metallic cobalt powder. The reactor is heated with external infrared heaters, so as to minimise effects of signal interference. Flexible heated 1/16" tubing is connected to the reactor to allow for gas downward flow through the reactor.

[4]outer diameter
[5]internal diameter

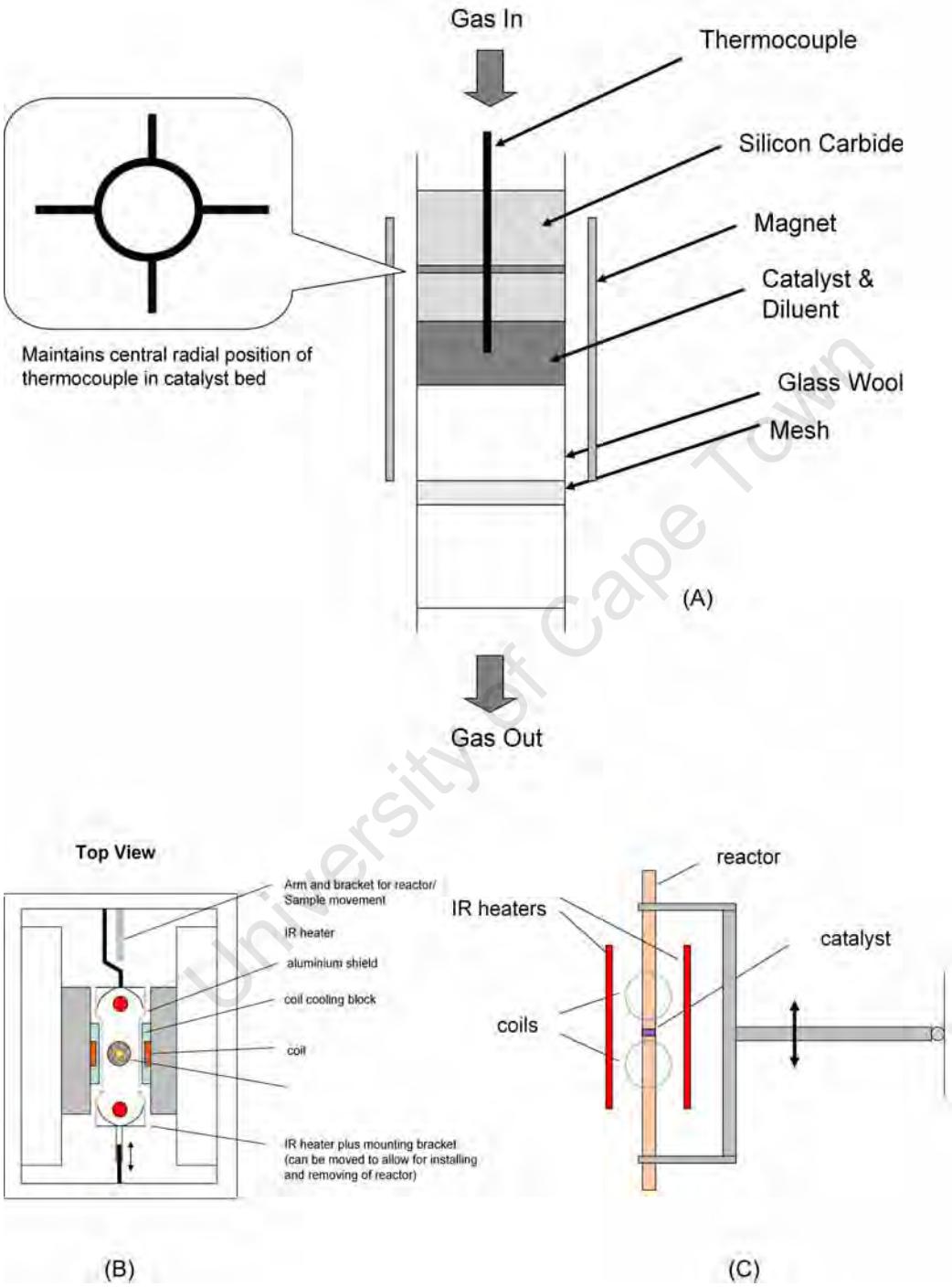

Figure 4.10: (A): Drawing of fixed bed reactor set-up for *in-situ* characterisation of magnetic properties. (B) Top view of magnetic reactor set up. (C): Side view of magnetic reactor set up, showing position of infrared heaters.

4.5.3 Experimental Procedure

The reaction conditions applied in the *in-situ* experiments for the characterisation of the magnetic catalyst properties were identical to the conditions used in the U-tube fixed bed reactor. The catalyst is reduced *in-situ* in 30 ml/min of H_2 fed through mass flow controller MC-M3 to its metallic form at 300 °C for 16 hrs with a temperature ramp of 1 °C/min.

After reduction, gas flow is changed from hydrogen to an inert gas argon, fed through mass flow controller MC-M2 and a temperature of 240 °C is maintained for Fischer-Tropsch reaction, total pressure is preset at 12 bar, and maintained with the back-pressure regulator. The reactor is then isolated via two three-way valves V-M9 and V-M10 in order to maintain an inert atmosphsere and keep the catalyst in its reduced form. Once the reactor is isolated, gas flow is changed to achieve reaction conditions, 50 ml/min of the a pre-mixed combination of hydrogen, carbon monoxide and argon is fed, which corresponds to partial pressure of; $P_{H_2} = 6.66$ bar, $P_{CO} = 3.33$ bar, $P_{Ar} = 2$ bar within the reactor. These conditions mimic the conditions run in the U-tube experimental test unit, although only three of the model catalysts were studied in this set-up, comprising of the smallest ('2 nm'), the largest ('16 nm') and an intermediate crystallite size ('9 nm').

In a first series of experiments, the three catalysts were tested at base case conditions, i.e. without water co-feed. Once the reaction gases have stabilized the positions of the two three way valves are changed such that the reaction gases flow through the reactor. Product sampling is the same as described in Section 4.4.3.1, through two methods; online gas chromatography was performed using Thermal Conductivity Detectors (TCD), and offline gas chromatography utilising the ampoule sampling technique described in section 4.4.4. The online gas sampling is performed every 5 minutes for the first hour, then every 15 minutes of the second hour, and finally every 30 minutes until a total reaction time of 5 hours. Ampoules are taken and eight different points in the 3 hour period; at 10, 20, 60, 90, 150 and 180 minutes. Freshly loaded and pre-calcined catalysts were then tested, again for 180 minutes, at conditions of 6 bar water partial pressure via water co-feeding.

The procedure for these runs with a 6 bar water co-feed is very similar to the procedure for the base case runs. Prior to the start of the experiment, while the reactant gases are on reactor by-pass, the pressure of the system is set at 18 bar to account for the additional water partial pressure. The two three way valves V-M7 and V-M8 are switched such that the water vapour is mixed in with the other reactant gases. Once steady state is reached, the procedure followed for the runs with 6 bar water co-feed from the start of the experiment is the same as that for a base case run.

In the first set of experiments, the 3 model catalysts were first tested at base case conditions for 180 minutes, after which they were exposed for 2 hrs, to different water partial pressures (3 bar, 6 bar; and 9 bar for the catalyst with the largest crystallites ('16 nm')). Between the different reaction conditions of different water partial pressures, base case conditions without water co-feed were revisited for 2 hrs to investigate reversibility of the observed effects. The procedure that was followed in order to attain the conditions of these additional water co-feed runs are as follows: upon the completion of the base case run, the gas flow is switched back to argon, and the pressure increased to 15 bar to account for an addition of 3 bar of water. The reactor is once again isolated using valves V-M9 and V-M10, while valves V-M7 and V-M8 are switched such that water vapourized in T-M5 is fed into the system, gas flow is also changed from argon back to the pre-mix. The experimental run is performed at these conditions for 3 hours, at the end of which the gas flow is changed back to argon and the system depressurized back to the basecase condition of 12 bar and the valves V-M7 and V-M8 are switched back such the the saturator is on bypass. The reactor is isolated again, after which mixed gas is allowed to flow, and another basecase is run for 2 hours. This procedure is repeated for an addition of 6 bar water (and 9 bar water for the '16 nm' catalyst).

Upon completion of the experimental runs the temperature program controlling the reactor temperature is switched off and the pressure within the experimental test unit released, until atmospheric pressure is reached. The flow of the pre-mixed gas is switched off and flow of argon is switched on. When the temperature of the reactor is back to room temperature, carbon

dioxide is fed through mass flow controller MC-M4. The carbon dioxide is allowed to flow for 60 minutes to ensure passivation of the catalyst sample.

4.5.4 Magnetic Sampling Procedure

After loading of the catalyst into the reactor a full hysteresis reading is taken prior to reduction. This reading involves taking 53 readings starting at negative 2 Tesla and step-wise increasing to 2 Tesla before returning to negative 2 Tesla.

During reduction saturation and remnant magnetisation is measured every 5 minutes for the duration of the ramp to 300 °C. These measurements involve a reading of the magnetisation at 2 Tesla followed by another reading at 0 Tesla. During the isothermal portion of the reduction, readings are taken every 5 minutes for the first hour, once the magnetisation of the readings stabilizes the frequency of readings is decreased. After reduction is completed, the temperature is decreased by intervals of 25 °C, and further readings are taken at each step until room temperature is reached. At room temperature another full hysteresis reading is taken.

Once reaction is started, saturation and remnant magnetisation are measured every 5 minutes for the first 30 minutes and then at 10 minute intervals for the remainder of the run. After reaction, when the gas flow is first switched to argon, three magnetic readings are taken at 2 minute intervals to ensure that the magnetisation remains constant. The same sampling procedure is followed for the water addition periods.

At the end of the experimental run, the temperature is again stepwise decreased at 25 °C intervals, with saturation and remnant magnetisation being measured at every step. Upon reaching room temperature, one last full hysteresis reading is taken. After the catalyst is passivated (see Section 4.4.3.1), and argon flow is applied, the temperature is dropped to approximately −180 °C using liquid nitrogen, which is poured over the reactor outside wall and magnetic readings are taken during this decrease in temperature as well as during the return to room temperature. Finally the temperature is step-wise increased in 25 °C intervals to a maximum temperature of approxi-

mately 360 °C with a magnetic readings taken at each step. The variation of temperature was done to obtain the temperature dependency of saturation and remnant magnetisation, which can be used to identify different phases present in the catalyst samples. This information can be further used to obtain qualitative information on crystallite size distributions.

4.6 Product Analysis

4.6.1 Analysis of Permanent Gases

An on-line gas chromatograph employing Thermal Conductivity Detectors (TCD) was used to analyse permanent gases in the feed or product stream. The gas is sampled by the gas chromatograph (GC) and analysis is performed on the reactants hydrogen and carbon monoxide as well as products of methane, carbon dioxide, ethene, ethane, propene and propane. Argon was used as the internal standard for this on-line analysis. The use of this technique allows for the monitoring of reactant conversions and rate of product formation. The conditions under which the analysis takes place are listed in Table 4.4.

The GC used for TCD analysis is a micro GC with 3 different channels. Channel A, which used hydrogen as a carrier gas, was used to separate and analyse argon, methane and carbon monoxide. Channel B performs analysis on carbon dioxide, ethene, ethane, propene and propane, channel B also provides a more sensitive analysis on methane for experimental runs using catalysts of very low activity, hydrogen is also used as a carrier gas on this channel. Finally channel C gives analysis on hydrogen and carbon monoxide using argon as a carrier gas.

The GC is calibrated periodically using a standard calibration gas mix, with a known composition of hydrogen, carbon monoxide, nitrogen, argon, methane and carbon dioxide. Peak areas A_i corresponding to individual gases are then obtained from the TCD trace, these are used to calculate calibration factors, C_i relative to the internal standard of argon.

Table 4.4: Conditions for on-line gas chromatographic analysis using Thermal Conductivity Detectors (TCD)

Micro Gas Chromatograph Varian CP-4900	
Channel A	
Detector	Thermal Conductivity Detector (TCD)
Column Type	Molsieve 5 $\AA$ Plot Column, 20 m
Carrier Gas	Hydrogen
Analysis Temperature	80 °C
Analysis Pressure	150 kPa
Analysis Time	220 s
Channel B	
Detector	Thermal Conductivity Detector (TCD)
Column Type	Pora PLOT Q Column, 10 m
Carrier Gas	Hydrogen
Analysis Temperature	60 °C
Analysis Pressure	100 kPa
Analysis Time	220s
Channel C	
Detector	Thermal Conductivity Detector (TCD)
Column Type	Molsieve 5 $\AA$ Plot Column, 10 m
Carrier Gas	Argon
Analysis Temperature	80 °C
Analysis Pressure	150 kPa
Analysis Time	220 s

$$\left(\frac{n_i}{n_{Ar}}\right) = C_i \left(\frac{A_i}{A_{Ar}}\right) \tag{4.4}$$

where n_i/n_{Ar} is the molar ratio of component i relative to argon.

4.6.2 Analysis of Organic Products

A Gas Chromatograph (GC) with a Flame Ionization Detector (FID) was used for offline analysis of organic products in the gas phase under reaction conditions. The glass ampoules collected during the experimental run is

placed into a heated ampoule breaker device where it is broken under a flow of nitrogen, this flow with the gas sample is then introduced into the split injector of the gas chromatograph through a system of valves, where the carrier gas is switched to hydrogen after 2 minutes.

The FID is carbon specific in its response, however the response of all carbon atoms are not equal. For example carbon atoms bonded to an oxygen atom givess a weaker response than other carbon atoms. To account for this variation in response, theoretical incremental response factors suggested by Kaiser (1969) are used. Using this approach, all carbon atoms not attached to an oxygen atom has a response factor of 1. For a carbon atom with a single bond to oxygen, the response factor is 0.55 and finally a carbon atom with a double bond to oxygen has no response. Therefore the response factor of a specific compound can be calculated according to Equation 4.5.

$$f_i = \left(\frac{N_{C,i}}{N_{C(noO)} + 0.55(N_{C(CO)})} \right) \tag{4.5}$$

Where f_i is the response factor for compound i, $N_{C,i}$ is the total number of carbon atoms, $N_{C(noO)}$ is the number of carbon atoms not bonded to an oxygen atom and $N_{C(CO)}$ is the number of carbon atoms with a single bond to oxygen.

4.6.3 Data Work-up

The data collected from both on-line and off-line analysis using the different GC's need to be quantitatively worked up to result in the molar flow rates of all reactants and products. In order to quantify the measurements internal standards are used. For the measurements using the TCD detector, argon, which was co-fed during the experiments, was the internal standard. Product methane is used as the reference component to tie together the analysis done on the two gas chromatographs (TCD and FID).

For the measurements using the TCD detector, the molar flow rates are obtained according to Equation 4.6.

Table 4.5: Conditions for off-line gas chromatographic analysis using a Flame Ionization Detector (FID)

Gas Chromatograph Varian CP-3800	
Detector	Flame Ionization Detector (FID)
Column Type	25 m x 0.15 mm Capillary Column
	2 μm film thickness CP-SIL 5CB
Oven Temperature	200 °C
Ampoule Breaker Temperature	170 °C
Injector	Split Injector
	Split ratio 1:15 to 1:50
	(depending on sample)
Carrier Gas	Hydrogen
Introduction Gas	Nitrogen
Oven Coolant	Carbon Dioxide
Hydrogen Flow	30 ml/min
Nitrogen Make-up Flow	25 ml/min
Pressure Program	
	1.79 bar, 25 min isobar
	at 0.03 bar/min to 2.41 bar, 0 min isobar
Total time	45 min
Temperature Program	
	-55 °C, 1.50 min isothermal
	at 20 °C/min to 0 °C, 0 min isothermal
	at 14 °C/min to 100 °C, 0 min isothermal
	at 16 °C/min to 280 °C, 22.36 min isothermal
Total time	45 min

$$\dot{n}_i = C_i \cdot \left(\frac{A_i}{A_{Ar}} \right) \cdot \dot{n}_{Ar} \tag{4.6}$$

Where;
$\dot{n}_i$ is the molar flow rate of compound i.
C_i is the response factor for compound i relative to the reference argon.
A_i is the peak area of compound i in the TCD chromatogram.
A_{Ar} is the peak area of the reference gas argon in the TCD chromatogram.
$\dot{n}_{Ar}$ is the molar flow rate of the reference gas argon.

Once the molar flow rate of methane $\dot{n}_{CH_4}$, as measured with the TCD set-up is determined, it is used as the internal standard for the FID measurements. Therefore the molar flow rates of the volatile organic compounds can now be determined using Equation 4.7.

$$\dot{n}_i = \left(\frac{N_{CH_4}}{N_i} \right) \cdot \left(\frac{f_i \cdot A_i}{f_{CH_4} \cdot A_{CH_4}} \right) \cdot \dot{n}_{CH_4} \tag{4.7}$$

Where;
$\dot{n}_i$ is the molar flow rate of compound i.
N_{CH_4} is the number of carbon atoms in methane (=1).
N_i is the number of carbon atoms in compound i.
A_i is the peak area of compound i in the FID chromatogram.
f_i is the response factor for compound i described in Equation 4.5.

Once the molar flow rates of the various reactants and products have been determined, further calculations can then be performed. The conversion X_i of a reactant i, can be determined using Equation 4.8.

$$X_i = \frac{\dot{n}_{i,in} - \dot{n}_{i,out}}{\dot{n}_{i,in}} \tag{4.8}$$

The yield, $Y_{i,C}$ and selectivity $S_{i,C}$ of compound i on a carbon basis are expressed by the following;

$$Y_{i,C} = \frac{\dot{n}_{i,out}}{\dot{n}_{CO,in}} \tag{4.9}$$

$$S_{i,C} = \frac{Y_{i,C}}{X_{CO} - Y_{CO_2}} \tag{4.10}$$

While the selectivity of carbon dioxide $S_{CO_2,C}$ can be determined by the following expression;

$$S_{CO_2,C} = \frac{Y_{CO_2,C}}{X_{CO}} \tag{4.11}$$

Finally the Fischer-Tropsch rate r_{FT} can be determined according to Equation 4.12.

$$r_{FT} = \frac{\dot{n}_{CO,in} - \dot{n}_{CO,out} - \dot{n}_{CO_2}}{SA_{total}} \tag{4.12}$$

Where;
$\dot{n}_{CO,in}$ is the molar flow rate of carbon monoxide entering the experimental system.
$\dot{n}_{CO,out}$ is the molar flow rate of carbon monoxide exiting the experimental system.
$\dot{n}_{CO_2}$ is the molar flow rate of carbon dioxide produced.
SA_{total} is the total surface area of iron in the catalyst, this can be calculated according to Equation 4.13.

$$SA_{total} = N_{cryst} \cdot SA_{cryst} \tag{4.13}$$

Where;
N_{cryst} is the number of crystallites in the catalyst sample and can be calculated according to Equation 4.14.
SA_{cryst} is the surface area of a single crystallite in the catalyst sample (πd^2).

$$N_{cryst} = \frac{V_{total}}{V_{cryst}} \tag{4.14}$$

Where;
V_{total} is the total volume of all iron crystallites in the catalyst sample (m_{Fe}/ρ_{Fe}).

V_{cryst} is the volume of a single crystallite in the catalyst sample($(1/6)\pi d^3$).

All volumes and surface areas are calculated according to equations relating to a sphere. Crystallite diameters can be obtained by means of XRD or TEM analysis. The latter was used for the calculation of SA_{total} in this study. For this study, SA_{total} refers to the initial iron surface area of the freshly reduced catalyst (taking the degree of reduction into account); unless otherwise noted. For further data work up associated with the use of Anderson-Schulz-Flory distributions see Appendix B.

Chapter 5

Model Catalyst Synthesis Results

5.1 Method Variation

In performing an investigation into the effect of different support addition methods, the four different methods used are described in Section 4.1.1 and are also shown below:

1. No precipitation - support material added directly into the metal reverse micelle solution, i.e. no precipitation step (Figure 4.2)
2. After precipitation, using two reverse micelle solutions - as in Mabaso (2005) (Figure 4.3)
3. After drying of unsupported nano-crystallites prepared via precipitation using two reverse micelle solutions (Figure 4.4)
4. After calcination of unsupported nano-crystallites prepared via precipitation using two reverse micelle solutions (Figure 4.5)

The targeted crystallite size for the investigation into a method for creating a model catalyst is 9 nm. The support material used for all methods was γ-alumina and the solvent used in Methods 3 and 4 is n-hexane. The characterisation results of some of the samples prepared in this investigation

are shown in Figures 5.1 and 5.2. Figure 5.1 shows the XRD patterns for the four methods investigated, it is easy to see that three of the patterns are similar (a, b and d) while pattern c is different. This is due to the fact that Methods 1, 2 and 4 resulted in the iron phase hematite (α-Fe_2O_3), while Method 3 resulted in maghemite (γ-Fe_2O_3). Hematite and maghemite represent two different physical phases of the chemical formula Fe_2O_3. It is known that maghemite has a very similar XRD pattern to magnetite (Fe_3O_4), in this case the two were differentiated between using TPR (Temperature Programmed Reduction), which resulted in a reduction behaviour with a 11%, 89% usage of hydrogen of the two peaks respectively, this is indicative of the two step reduction of Fe_2O_3. The TPR profile of iron crystallite supported on alumina with n-hexane as the solvent using Method 3 is shown in Figure 5.3. This two peak system shown in Figure 5.3 is representative of Fe_2O_3 first reduced to Fe_3O_4 (magnetite), using 11% of the total hydrogen before the Fe_3O_4 is further reduced to iron metal using the remaining 89% of the total hydrogen (Lin et al. (2003)).

Figure 5.2 shows the TEM micrographs of samples prepared via the four different methods used. Here again a difference can be seen between Method 3 and the other methods. The TEM micrograph shows that the iron crystallites prepared via Method 3 are not well dispersed onto the support material, the iron crystallites have clustered together, this characteristic is not desired as one cannot discern whether the iron crystallites are acting as individual particles or as a cluster, furthermore the metal crystallites might be more prone to sintering. Methods 2 and 4 show very good dispersion of iron crystallites on the alumina. Method 1 shows good dispersion, but with some particles which are larger than expected, which may have been caused by sintering during the preparation process. It is clear from these results that the phase of the iron oxide plays an important role in how well the iron crystallites will be dispersed onto the support material. It is assumed that the calcination step in the preparation process is the critical one where maghemite is converted to hematite, as Method 3 is the only method where the iron crystallites are re-dispersed without a calcination step.

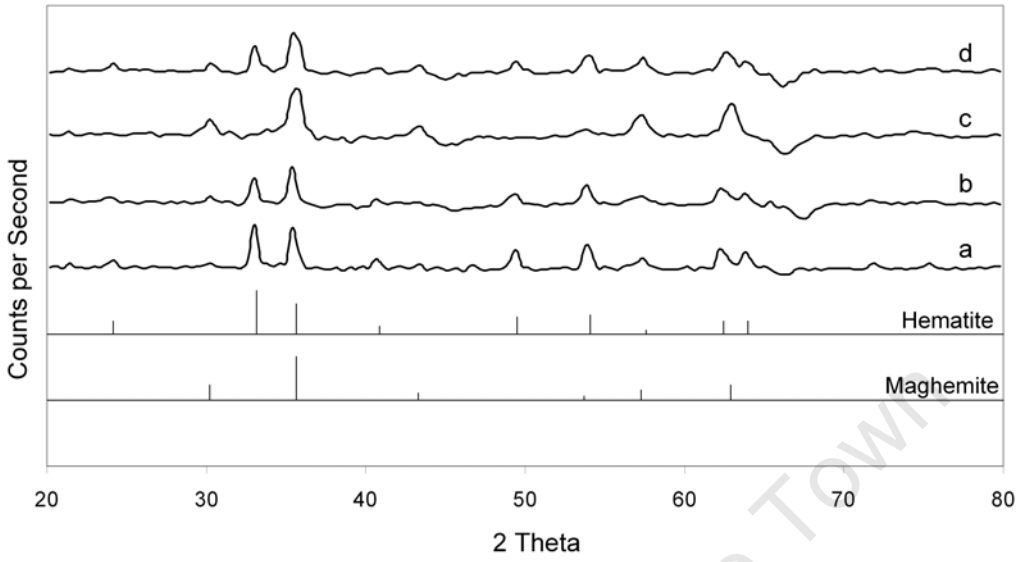

Figure 5.1: XRD patterns of iron crystallites on alumina (a) Method 1 - Hematite, (b) Method 2 - Hematite, (c) Method 3 - Maghemite and (d) Method 4 - Hematite

From these results it can be seen that in order to prepare a model type catalyst, Methods 2 and 4 result in the samples with the best dispersion of iron crystallites onto the support material. Method 2 would be the preferred method of support addition due to two reasons; firstly, according to Figure 5.2 Method 2 shows excellent dispersion of metal crystallites onto the support material, while Method 4 also shows similar dispersion there appears to be some larger crystallites present. Secondly Method 2 has less preparation steps as compared to Method 4 which is desirable.

5.2 Support Variation

This work also looked at the influence different support materials would have on the dispersion of iron crystallites on said support material. Three support materials were chosen for this work; alumina, silica and silica modified with alumina. Figure 5.4 shows the zeta potentials of the 3 different support materials. It can be seen that silica does not have a point of zero charge in the investigated pH range, and its zeta potential is always negative. The

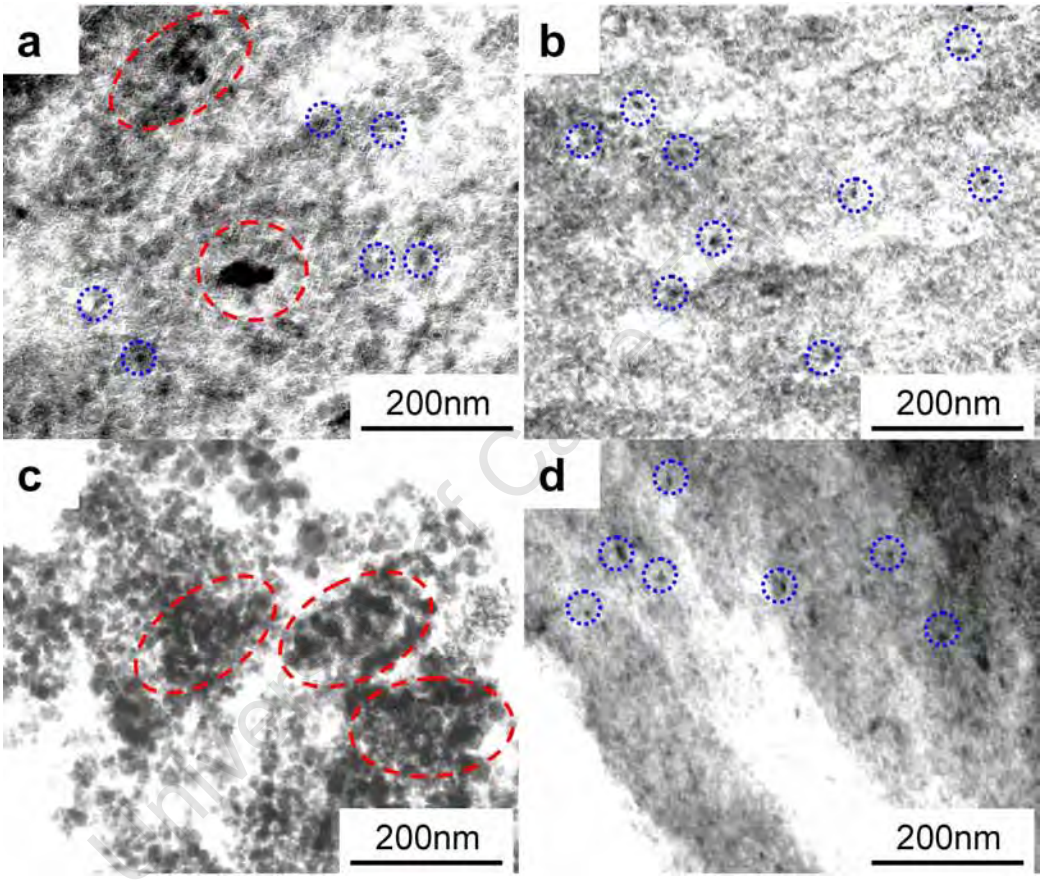

Figure 5.2: TEM images showing the effect of method of support addition on iron crystallite dispersion on alumina (a) Method 1, (b) Method 2, (c) Method 3 and (d) Method 4. Where the red circles indicate clustering of iron crystallites and blue circles indicate individual crystallites well dispersed onto the support material

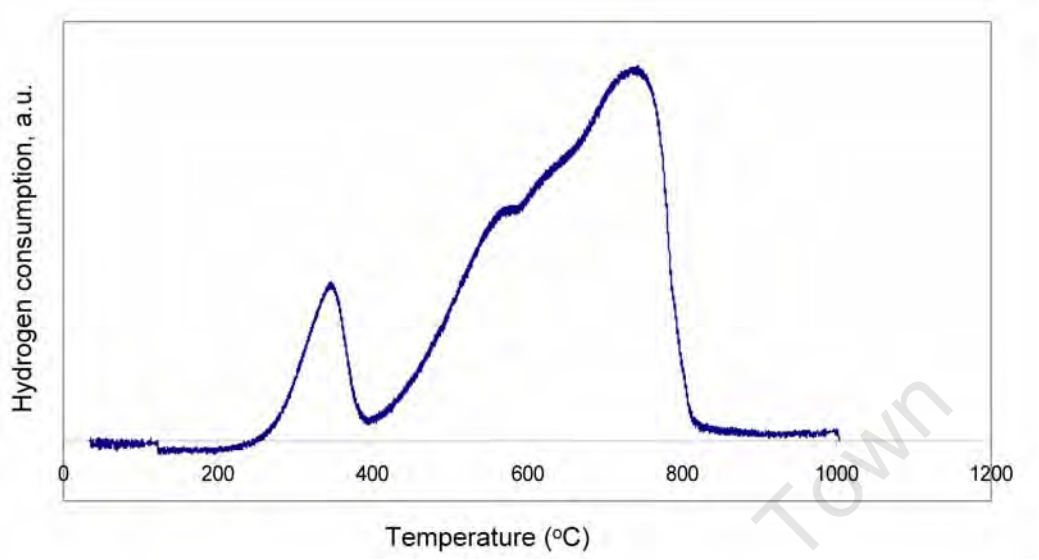

Figure 5.3: TPR profile for a Method 3 loading of iron crystallites on alumina with n-hexane as the solvent

γ-alumina support has a point of zero charge at around pH 7-8, and finally the modified silica has a point of zero charge above a pH of 8, which is very similar to the γ-alumina support possibly indicating that the modification of the silica aiming for an alumina mono-layer was indeed successful. The zeta potential curves associated with silica ((a) on Figure 5.4) and alumina ((c) on Figure 5.4) are similar to the expected curves found in literature. However the zeta potential curve associated with the modified silica support ((b) on Figure 5.4) is unusual due to the fact that it's zeta potential curve reaches a maximum at an approximate pH of 5. A decrease in the zeta potential from pH 5 to pH 2 can be explained by the alumina monolayer dissolving at a low pH resulting in the modified silica support performing like pure silica at low pH values.

In this section of the work the method of support addition was kept constant at Method 2, which meant that no separate solvent was required. Method 2 was chosen, as the results from Section 5.1 show that it is the method of support addition that results in the best dispersion of the iron crystallites onto the support material. Figure 5.5 shows the XRD patterns of the catalysts prepared using the three different support materials used. It

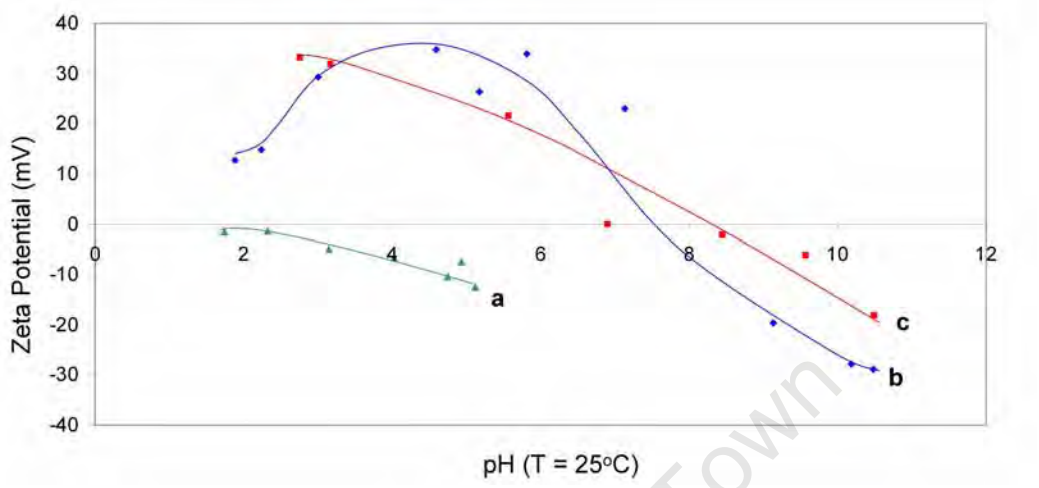

Figure 5.4: Zeta potential of different support materials (a) Silica, (b) Silica modified with alumina and (c) Alumina

can be seen that on alumina the iron oxide is still hematite, however when it comes to the other two supports, the iron oxide is predominately maghemite. However on the modified silica one can still see some hematite peaks, but on silica the iron oxide is almost completely in the form of maghemite.

The TEM micrographs in Figure 5.6 show that there is fairly good dispersion of the iron oxide crystallites when alumina is used as the support material. However on silica extensive clustering of the crystallites is observed. Finally the modified silica support is shown to not be homogeneous. It is therefore evident that the support material does influence how well the iron crystallites are dispersed onto the support, it also effects the phase of the iron oxide. The physical properties of the support material, such as surface area and pore volume may play important roles in the distribution of the metal crystallites. For example, the pore volume of the support will determine the size of the metal crystallites that can enter the port system. Therefore the best support material to use in the case of iron oxide is the alumina support, this may be due to alumina's zeta potential, which would affect the surface of the alumina, making it easier for the iron crystallites to load independently onto the support surface.

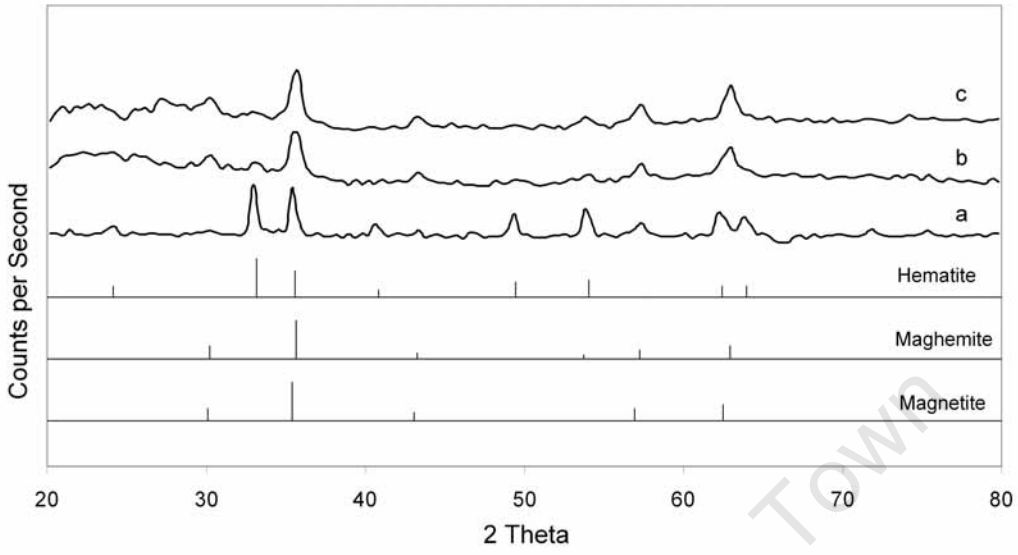

Figure 5.5: XRD patterns of iron crystallites on alumina using Method 4: (a) Alumina - Hematite, (b) Silica modified with alumina - Hematite/Maghemite and (c) Silica - Maghemite

5.3 Solvent Variation

Further investigation was done on the effect of different solvents on the dispersion of the pre-made crystallites on the support material, in order to justify the comparison the method used was kept constant at Method 4, while the support used was alumina. Method 4 was the preferred method of support addition as it produced a better dispersion of metal crystallites onto the support material than Method 3 (see Section 5.1), where both Methods 3 and 4 include the use of a new solvent. Method 4 includes the preparation of unsupported crystallites via two reverse micelle solutions followed by the drying and calcination of the unsupported metal crystallites, these crystallites are then redispersed in a new solvent with a support material by applying ultra-sound followed by further drying and calcination. Three different solvents were chosen for this investigation; ethanol, water and n-hexane. These solvents were chosen for their differing polarity, decreasing from ethanol to n-hexane.

Figure 5.7 shows the XRD patterns for the catalysts prepared using the

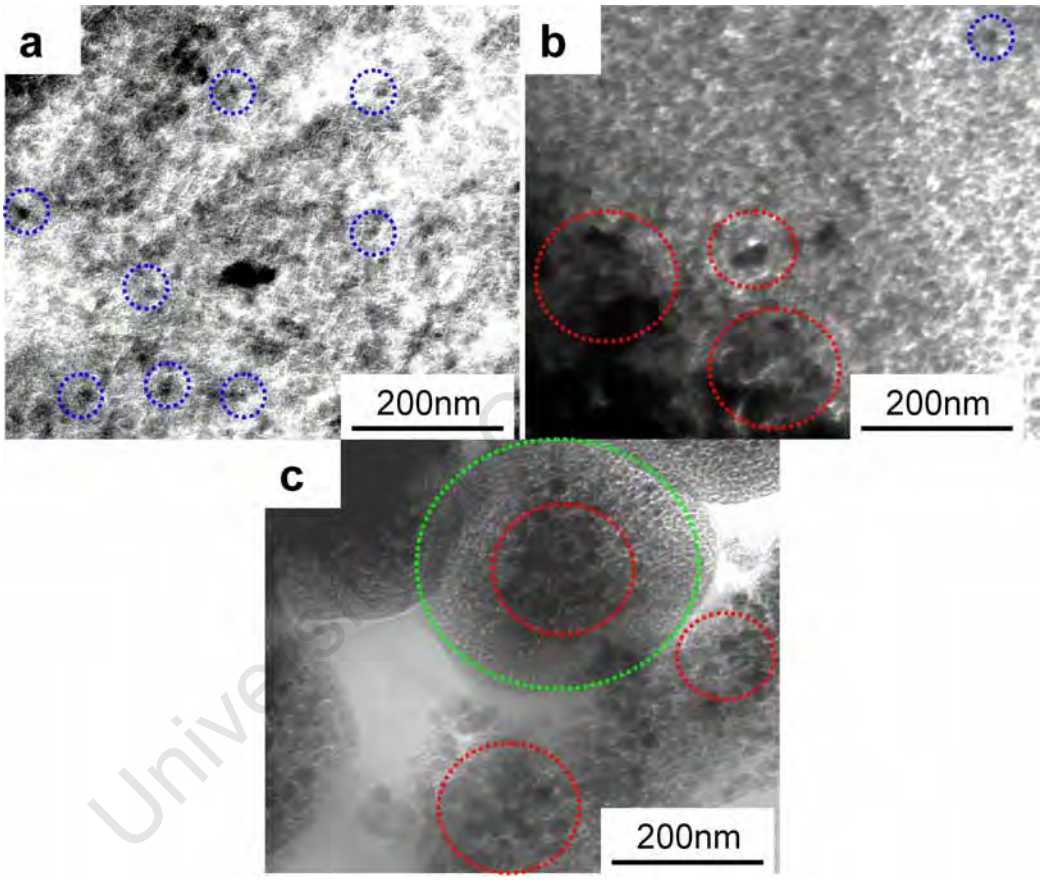

Figure 5.6: TEM images showing the effect of solvent on dispersion of iron crystallites on alumina (a) Alumina, (b) Silica modified with alumina and (c) Silica

different solvents, while it appears that the XRD pattern for water as a solvent is different to the others, it is not the case, the pattern is still that of hematite, however the loading of iron crystallites onto the support material was extremely low in this case, therefore the peaks are not big. Therefore all three patterns are that of hematite, which is expected as the same method for crystallite preparation was used and all were exposed to a calcination step during the preparation process.

The TEM micrographs for the solvent investigation are shown in the Figure 5.8, here it can be seen that n-hexane as the solvent produced the most satisfactory result where the iron crystallites are well dispersed onto the alumina support. When ethanol was used as the solvent the result was excessive clustering. With water as the solvent clustering was also observed, furthermore the loading of the iron crystallites onto the support using water as a solvent was extremely low, which is also not desired. The inefficient loading associated with using water as a solvent resulted from when the unsupported metal crystallites were re-dispersed with the support material in an ultrasonic bath. During this re-dispersion step the metal crystallites are expected to attach to the support material. However using water as the solvent, the unsupported metal crystallites did not attach to the support material and these unsupported nano-crystallites are lost during decanting, drying and calcination of the resulting catalyst. It can hypothesized that with a high polarity solvent, the unsupported metal crystallites are more attracted to each other than to the support material, resulting in clustering of metal crystallites for ethanol and water used as solvents shown in Figure 5.8. This also results in the low metal loading associated with the catalyst produced with water used as the re-dispersion solvent.

From these results it can be seen that the solvent used does have an influence on how well the pre-made iron crystallites are dispersed onto the support material. A solvent with low to no polarity is desired, where with increasing polarity, and increase in the tendency for the iron crystallites to cluster together is observed.

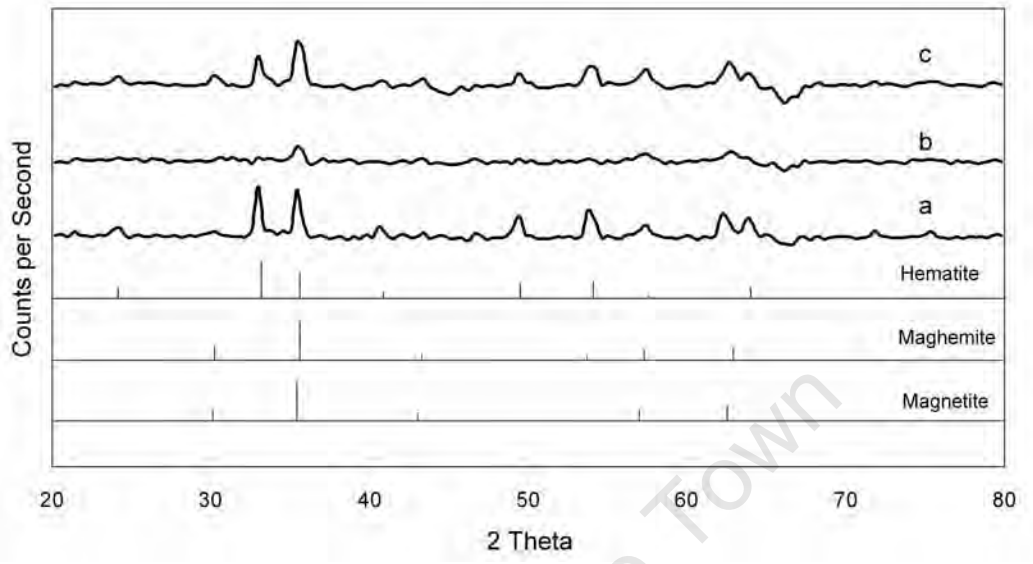

Figure 5.7: XRD patterns of iron crystallites on alumina using Method 4: (a) Ethanol - Hematite, (b) Water - Hematite and (c) n-Hexane - Hematite

5.4 Variation of Drying and Calcination Conditions

The drying and calcination conditions were also varied to investigate their effect on the dispersion and final metal crystallite size. This was particularly important for the smallest metal crystallites prepared ('2 nm', '3 nm' - anticipated sizes after calcination, Mabaso (2005)) as they were the most susceptible toward agglomeration and sintering. The method used while testing the effects of drying and calcination conditions was Method 2, which consisted of the preparation of supported metal crystallites via the precipitation of two reverse micelle solutions. Method 2 was chosen due to the fact that this particular method of support addition resulted in the best dispersion of metal crystallites onto the support material (see Section 5.1). The support used in this section of the investigation was alumina, chosen again because it resulted in the best dispersion of metal crystallites onto the support addition (see Section 5.2). Figure 5.9 shows the effect of two different drying conditions on a '3 nm' catalyst. The catalyst sample shown in (a) was dried

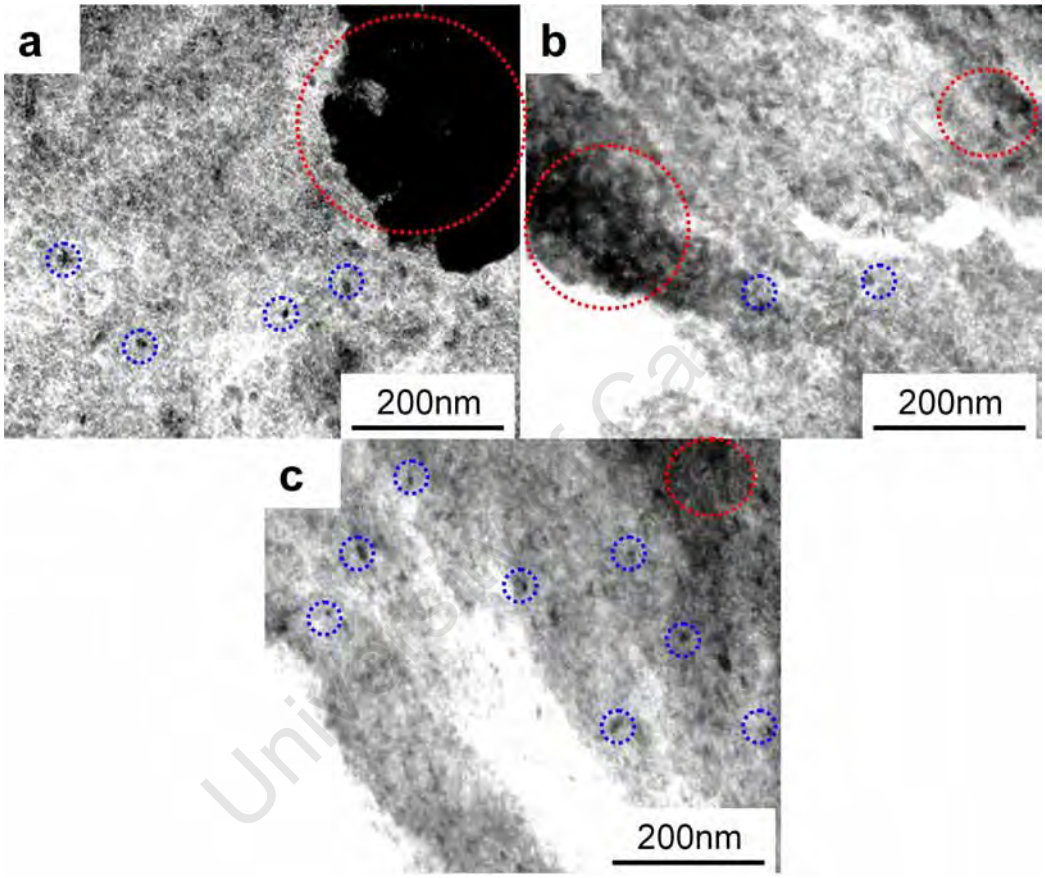

Figure 5.8: TEM images showing the effect of solvent on iron crystallite dispersion on alumina: (a) Ethanol, (b) Water and (c) n-Hexane

in a rotary drier as compared to the sample (b) which was dried for 24 hours at room temperature followed by one hour in an oven at 120 °C. Following these varied drying procedures, the samples produced were calcined in argon at 300 °C for 16 hrs.

It can be seen that the sample shown in (a) dried in the rotary drier has much larger crystallites than the sample shown in (b). The rotary dried sample not only has larger crystallites but also shown significant agglomeration of crystallites resulting in an uneven distribution of the crystallites onto the support material. In contrast, the catalyst sample in (b) shows significantly smaller crystallites (avg. size: 1.7 nm), approximately one order of magnitude smaller and these metal crystallites are better dispersed onto the support material. There is some clustering shown in sample (b) however not to the extent seen in sample (a).

In terms of the calcination procedure, both the time for which the catalyst sample was calcined and the temperature at which it was done at were varied. The time for which the catalyst sample was calcined and the temperature at which it was calcined were considered to be the two most important factors involving sintering and dispersion of the metal crystallites during the calcination procedure. Figure 5.10 shows TEM pictures of different '2 nm' catalyst samples which were calcined at varying conditions, these samples had been previously dried using a rotary drier for 60 min at 60 °C and 350 mbar. Sample (a) was calcined for one hour at 350 °C, sample (b); was calcined for 16 hours at 350 °C and finally sample (c) 16 hours at 300 °C. Sample (a) shows fairly small crystallites, however there is also significant clustering of the crystallites on the support material. Sample (c) appears to show the best dispersion of crystallites on the support material, furthermore the sample also shows small crystallites. Sample (b) was calcined using the conditions described by Mabaso (2005), however these conditions result in a catalyst sample with significantly larger crystallites than samples (a) and (c). Sample (b) also shows significant clustering of the crystallites on the support material.

It can be seen from the results of varying the drying and calcination conditions that these steps in the catalyst preparation procedure play very

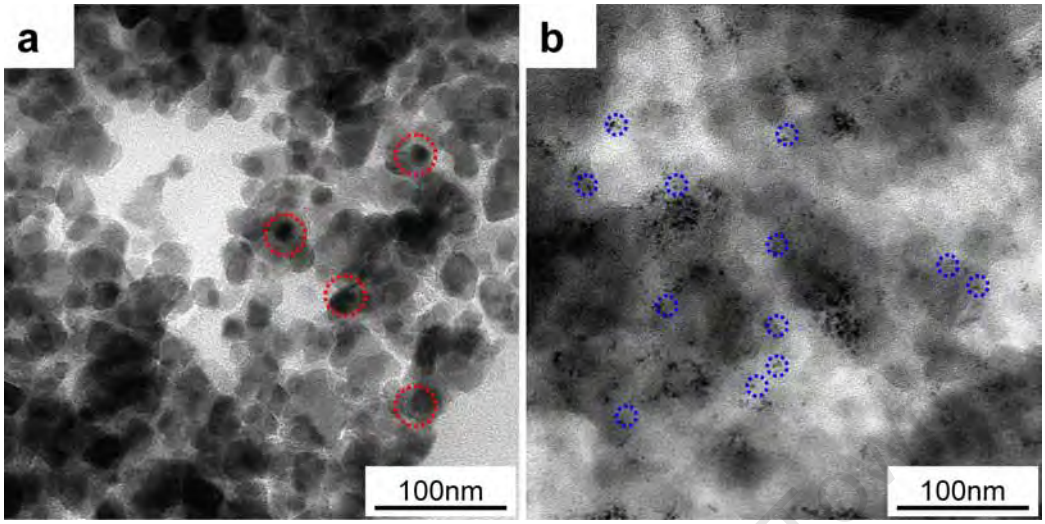

Figure 5.9: TEM images showing the effect of different drying conditions on the metal crystallite size and dispersion on support: (a) '3 nm' catalyst dried in a rotary drier, (b) '3 nm' catalyst dried in oven for 3 hours at 120 °C

important roles in the outcome of the final catalyst. For smaller crystallites it is important to dry the catalyst in an oven rather than a rotary drier, in essence making use of a higher temperature to dry the sample rather than using and decreasing pressure to drive the liquid solution from the solid catalyst sample. Furthermore, from the results of varying the calcination conditions of the catalyst sample it can be seen that the time for which the catalyst is calcined for is not as important as the temperature at which it is calcined. Calcining a sample for just an hour still resulted in clustering of the metal crystallites, however, the sample calcined at a lower temperature did not show any significant sintering. This suggests that sintering occurs fairly rapidly once a threshold temperature has been attained. However due to the much larger crystallite size found in sample (c) of Figure 5.10 compared to the crystallite size found in sample (a) of the same Figure shows that the sintering may start rapidly, but does continue throughout the length of the calcination.

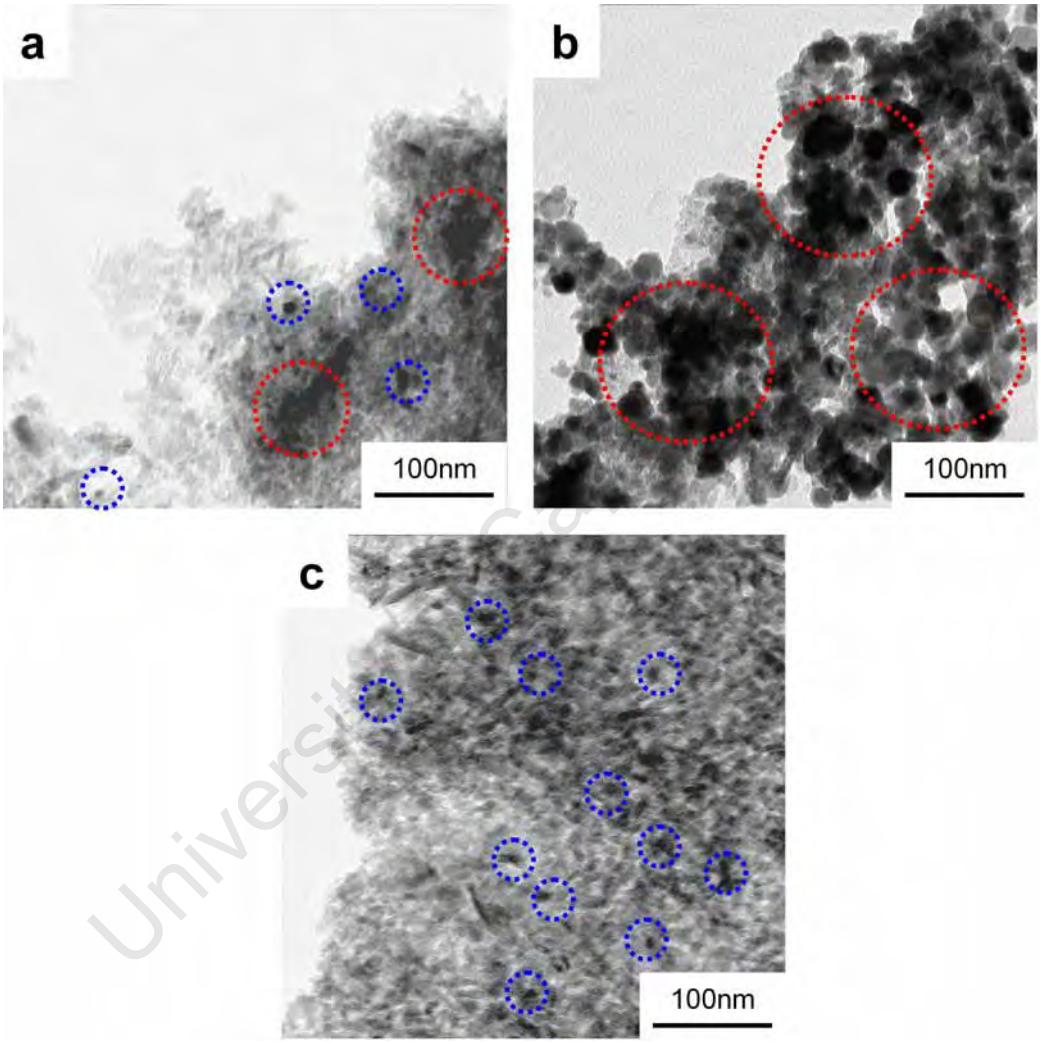

Figure 5.10: TEM images showing the effect of different calcination conditions on the metal crystallite size and dispersion on support: (a) '2 nm' catalyst calcined for 1hr at 350 °C, (b) '2 nm' catalyst calcined for 16 hours at 350 °C and (c) '2 nm' catalyst calcined for 16 hours at 300 °C

.

5.5 Summary of Model Catalyst Synthesis Results

It is important to note that there are many different steps to the successful preparation of model type catalysts with well dispersed nano-crystallites; any variation in one step may result in significant changes to the structure of the final catalyst. During the synthesis of a model catalyst five different conditions were varied:

1. Different support addition methods
2. Use of different supports (Method 2: preparation of supported crystallites via precipitation from 2 reverse micelle solutions)
3. Different solvents (Methods 3 and 4: preparation of unsupported crystallites via precipitation followed by re-dispersion in a new solvent)
4. Different drying conditions (Method 2: preparation of supported crystallites via precipitation from 2 reverse micelle solutions)
5. Different calcination conditions (Method 2: preparation of supported crystallites via precipitation from 2 reverse micelle solutions)

For even distribution of the metal crystallites onto the support material it was conceived that introducing the support material at different stages of the catalyst preparation process may impact the final distribution. From experimentation of four separate methods it was found that Method 2, the one used by Mabaso (2005), was the most efficient at maintaining specific crystallite size and attaining even distribution. This method consisted of the preparation of supported metal crystallites via the precipitation of two reverse micelle solutions followed by drying and calcination.

It was further hypothesized that different support materials may also influence the metal crystallite dispersion. Three different supports were investigated, two were commercially available, γ-alumina and a silica gel. The final one was a specifically made resulting in a silica gel coated with alumina. It was shown that the different support materials have very different

zeta potential graphs, therefore a different point of zero charge. However, the similarity that was shown by the zeta potential method in the commercially available alumina and the modified silica gel (with a monolayer of alumina) suggested that the modification method resulted in a support material that was comparable with the commercially available alumina. This influenced the distribution of the metal crystallites on the support material, it was concluded that the best support material to use was γ-alumina, it is more difficult to discern in TEM characterisation, but it does result in the best dispersion of metal crystallites onto the support material. In the same way the supports affect the final distribution of metal crystallites on the support material, different solvents may have a significant effect in terms of Methods 3 and 4. Method 3 consisted of the preparation of unsupported metal crystallites via the precipitation of 2 reverse micelle solutions, these unsupported metal crystallites are dried and re-dispersed with a support material in a new solvent, followed by drying and calcination. Method 4 is the same as Method 3 except that the unsupported metal crystallites are both dried and calcined before re-dispersion in a new solvent. Solvents of differing polarities were investigated, with the hypothesis being; depending on the polarity of the solvent metal crystallites may be more influenced by each other or by the support material. The results show that a non-polar solvent works better than a polar solvent.

Finally the drying and calcination conditions were varied. The method used in these cases was Method 2, where supported crystallites were prepared using two reverse micelle solutions followed by drying and calcination, this was the method used in Mabaso (2005). It was shown that these conditions affect smaller crystallites more significantly than larger ones. Therefore for smaller crystallites (2nm-4nm) the drying procedure used is drying in the oven rather than rotary drier. In terms of the calcination procedure, the results showed that the temperature at which the calcination took place has a major influence on both the size of the metal crystallites as well as the distribution on the support material. Therefore the calcination temperature was dropped to 300 °C for preparation of all catalyst samples. Ultimately Method 2 was used for the preparation of the model catalysts used in this

work.

Chapter 6

Results of Characterisation of Model Catalysts

From the results shown in Section 5, model catalysts were prepared in six discrete nanometer sizes ranging between 2 and 16 nm, using the experimental procedure described in Section 4.1.1. The method used was Method 2 (Mabaso (2005)) which consisted of the preparation of supported metal crystallites via precipitation of two reverse micelle solutions followed by drying and calcination (Figure 4.3). Crystallites size variation was targeted via variation of the water-to-surfactant ratio of the reverse micelle system they were prepared from. The characterisation results of calcined and reduced catalysts are presented in the following section. Calcined catalysts refer to catalysts which have been prepared and calcined in argon for 16 hours with a heating ramp of 10 °C/min at 300 °C. Reduced catalysts are further reduced in hydrogen for another 16 hours with a heating ramp of 1 °C/min, again at 300 °C. The final step is the passivation procedure, which happens after the catalyst is allowed to cool to room temperature, after which pure CO_2 is fed at 25 ml/min for an hour.

6.1 TEM Analysis

TEM images of calcined and reduced samples are shown in Figures 6.1, 6.2 and 6.3. The names of the catalyst samples refer to the expected crystallite size from work by Mabaso (2005), i.e. '2 nm' refers to the catalyst sample prepared using a water-to-surfactant ratio from Mabaso (2005) which resulted in an average crystallite size of 2 nm post calcination. The crystallite size distributions of all samples are shown in Figure 6.4, and the average sizes of the metal crystallites are summarized in Table 6.1. The metal crystallites are shown as the darker spots on the images in Figures 6.1, 6.2 and 6.3, selected crystallites are circled for clarity. The three figures show that using the reverse micelle technique was successful in creating catalyst samples with differing metal crystallite sizes. Figure 6.1 shows TEM micrographs of catalyst samples with the smallest metal crystallite sizes, these samples are the ones which seem to be the most prone to agglomerization and sintering during the preparation process. The calcined samples show extremely small crystallite sizes, which do show some clustering of crystallites, however the reduced samples show that the metal crystallites are larger than previously and have increased in clustering (see Table 6.1).

Figure 6.2 shows TEM images of catalyst samples with medium sized iron crystallites. These micrographs show that the crystallites in this size range do not show any significant clustering, resulting in good dispersion onto the support material. Furthermore there are no major increases in crystallite size. Similar results are shown in Figure 6.3, which shows the TEM micrographs of the catalyst samples with the largest crystallite sizes when considering the reduced samples.

Figure 6.4 shows the crystallite size distributions of the prepared catalyst samples. The histograms are prepared by counting a minimum of 300 iron crystallites from corresponding TEM micrographs. The prepared catalyst samples have generally narrow crystallite size distributions with standard deviations ranging between 11 and 32% for the calcined samples and 14 and 32% for the reduced samples (Table 6.1). A general trend that can be observed is that the standard deviations increase with decreasing crystallite

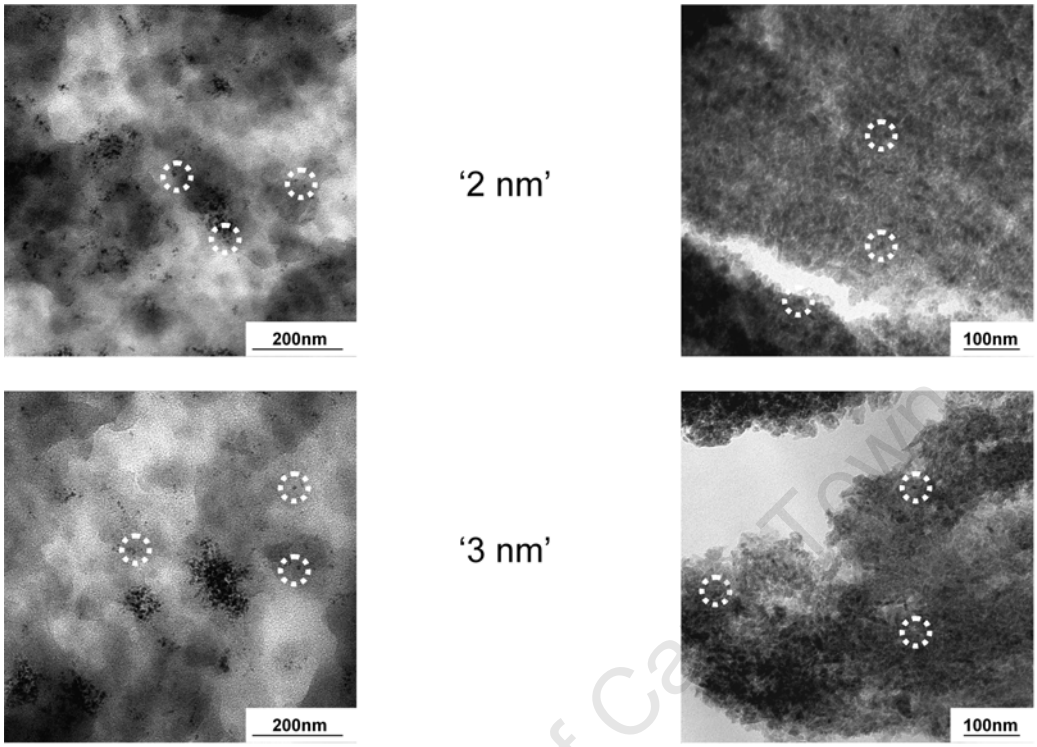

Figure 6.1: TEM images of catalyst samples with the smallest metal crystallites of '2 nm' and '3 nm': *(left)*: Calcined samples, *(right)*: Reduced samples

size, this is an expected result as the smaller crystallites are more difficult to prepare with more acetone washes required to remove the surfactant, and general inaccuracies in the sizing of crystallites increase with decreasing crystallite size. It is generally expected that the reduced samples would have smaller average crystallite sizes than the calcined samples as the density of metallic iron (ρ_{Fe} = 7.87 g/cm^3) is greater than that of iron oxide ($\rho_{Fe_2O_3}$ = 5.24 g/cm^3), that is, shrinkage during reduction. However this was not the case as shown by the histograms in Figure 6.4 and the average crystallite sizes summarized in Table 6.1. The iron crystallites in the reduced samples have a greater average crystallite size when compared to the corresponding calcined samples, it is expected that this is due to some degree of sintering or agglomeration taking place during the reduction process as the Hüttig Temperature (Section 2.2.3) of iron is exceeded.

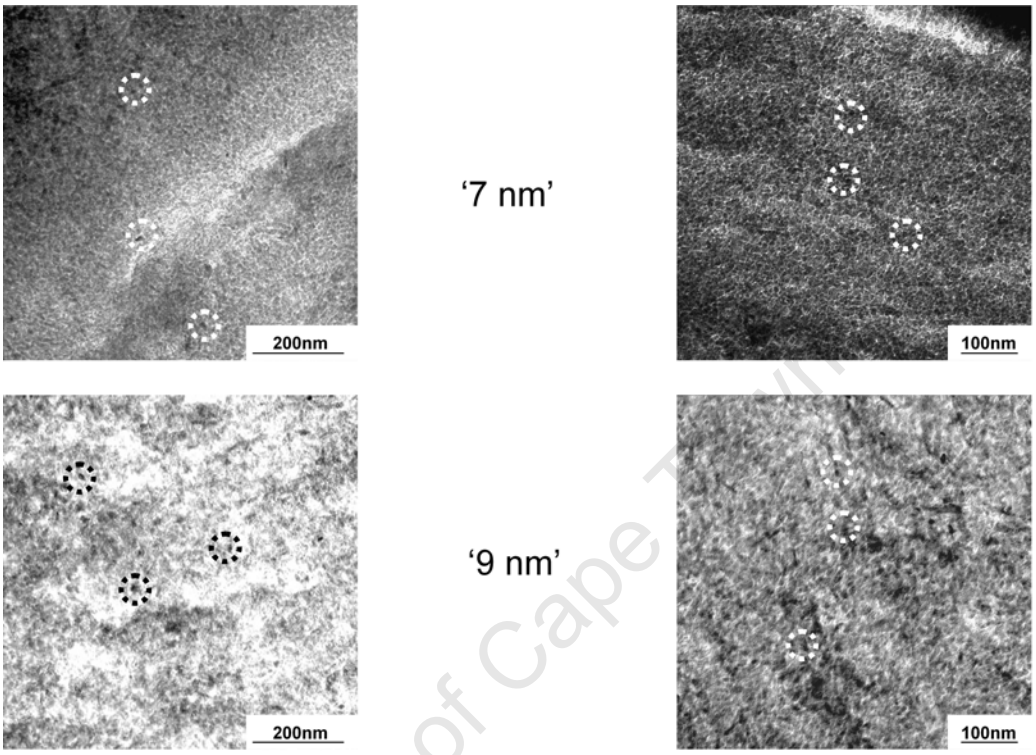

Figure 6.2: TEM images of catalyst samples with medium metal crystallites of '7 nm' and '9 nm': *(left)*: Calcined samples, *(right)*: Reduced samples

Table 6.1: Average crystallite sizes (d_{cryst}) and variance (σ) observed by means of TEM analysis for calcined and reduced alumina supported iron catalysts

Expected crystallite size (nm)	Calcined Sample		Reduced Sample	
	$\bar{d}_{cryst} \pm \sigma$	std dev (%)	$\bar{d}_{cryst} \pm \sigma$	std dev (%)
'2 nm'	2.4 ± 0.8	32.1	4.2 ± 1.3	32.2
'3 nm'	2.7 ± 0.8	29.8	3.8 ± 1.0	26.2
'7 nm'	6.7 ± 1.2	17.8	6.9 ± 1.7	25.2
'9 nm'	7.9 ± 1.4	18.3	8.8 ± 1.5	16.8
'14 nm'	12.0 ± 1.9	16.0	12.6 ± 1.8	14.1
'16 nm'	15.40± 1.7	11.0	15.7 ± 2.3	14.7

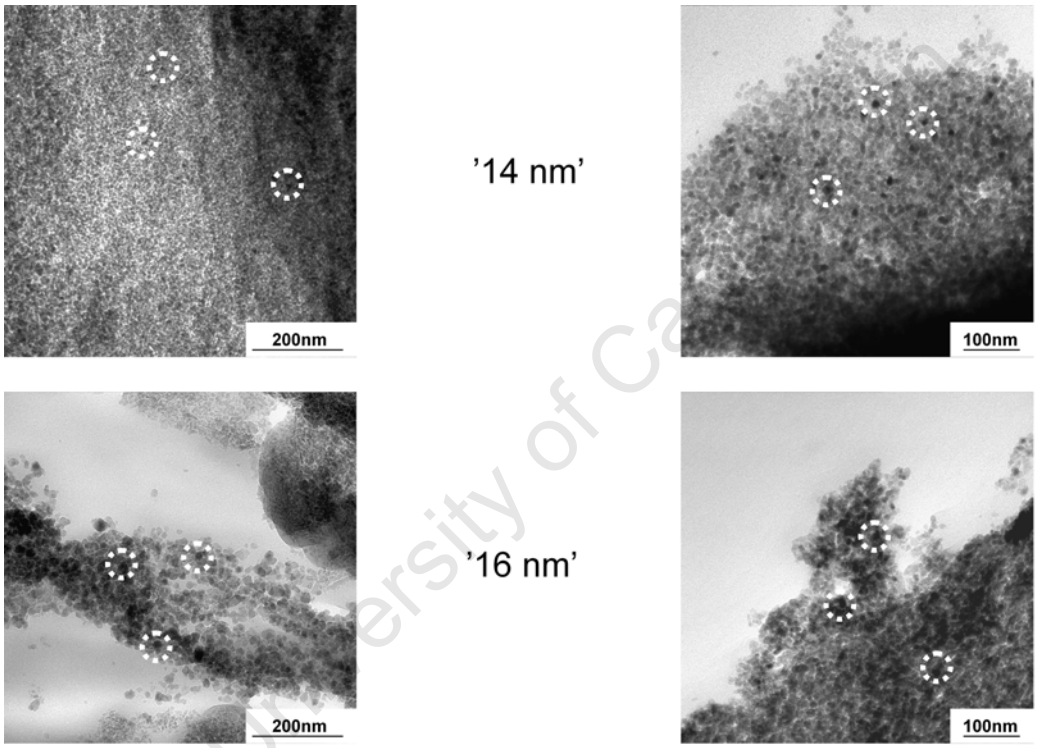

Figure 6.3: TEM images of catalyst samples with the largest metal crystallites of '14 nm' and '16 nm': *(left)*: Calcined samples, *(right)*: Reduced samples

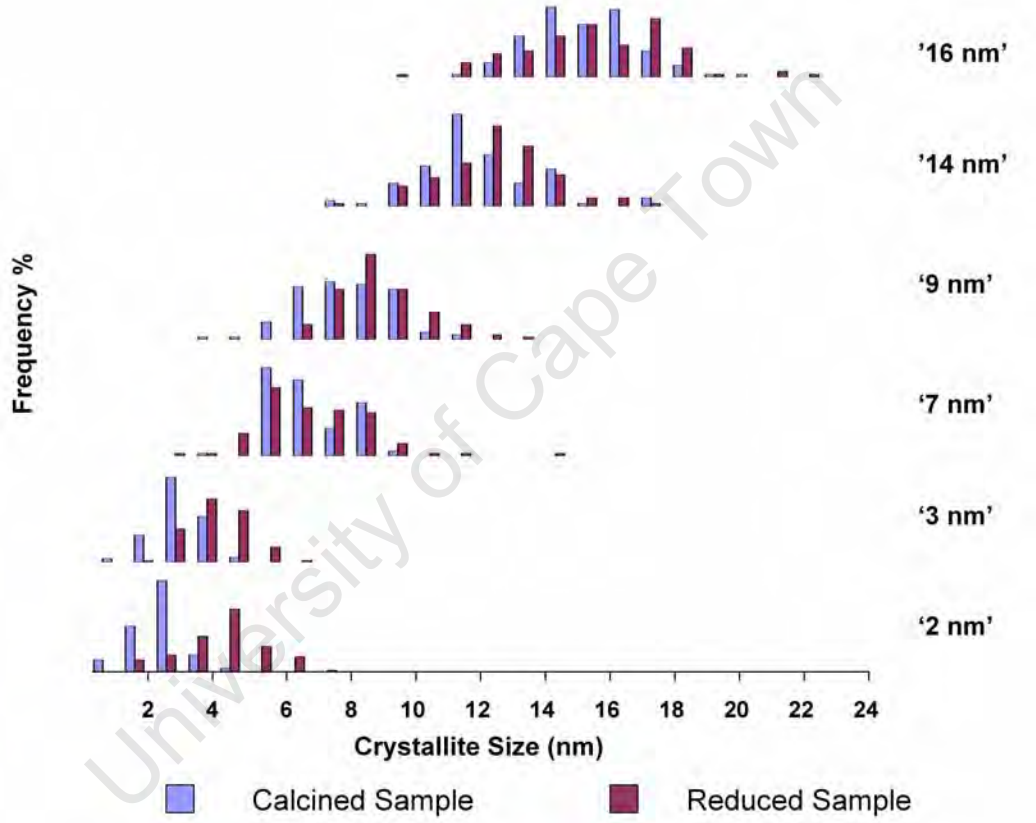

Figure 6.4: Crystallite size distributions of calcined and reduced samples of all six alumina supported tested catalysts as determined by TEM analysis
.

6.2 XRD Analysis

XRD analysis was used to analyse the iron phases of the catalyst sample after calcination and again after reduction. Figure 6.5 shows an example of XRD traces for a '9 nm' calcined and reduced catalyst. The catalyst sample consists of an alumina support as well as iron crystallites in various phases. A XRD trace for a pure alumina support is also included in Figure 6.5.

The calcined sample shows that the iron phase after the calcination procedure is an iron oxide, mainly made up of maghemite, i.e. γ-Fe_2O_3. However it is impossible to eliminate the existence of magnetite (Fe_3O_4), due to very similar diffraction patterns of the two phases. Another difficulty in analysing the phase composition of the calcined sample is the inclusion of the alumina peaks which are very broad and exist in a wide range of 2Theta values, therefore any reference peaks that are in the same 2Theta range cannot be analyzed with any accuracy. Moreover, the alumina support contains some δ-alumina in addition to γ-alumina which is the major phase. The complete crystallographic structure of the support is not known, therefore no Rietveld refinement analysis of the samples could be done to obtain the phase composition. Generally it is expected post calcination the iron crystallites exist as Fe_2O_3, mainly in the form of maghemite though some hematite would also be present.

After reduction the XRD trace is significantly different to that of the samples post calcination. The reduced sample depicted in Figure 6.5 shows one significant peak matching the reference iron metal peak. This result shows that the chosen reduction conditions produced the required reduction from iron oxide to metallic iron. No size determination of the reduced samples using the Scherrer formula was possible as the single metallic iron peak fell on a wide alumina peak and true separation of the two was not possible. However, the Scherrer formula could be applied to the three maghemite peaks which could be found away from the alumina support peaks. The XRD traces for all six prepared catalysts are shown in Figure 6.6. It can be seen that as the expected crystallite size increases, the peak widths dcreases, i.e. the peak width become narrower, this essentially indicates an increase in the average

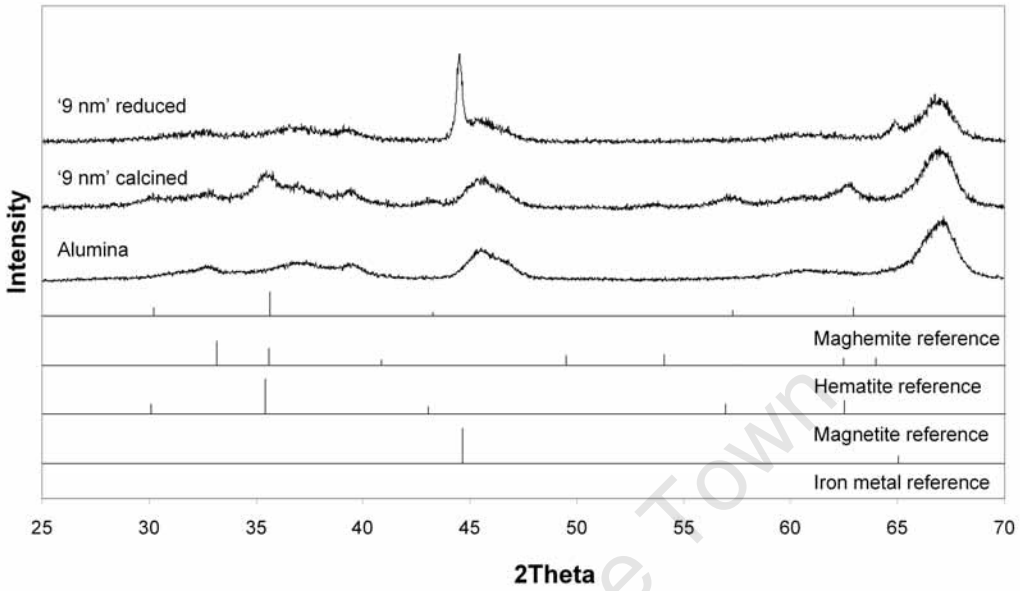

Figure 6.5: XRD patterns of a reduced and calcined '9 nm' catalyst and a pure alumina support. Reference patterns for hematite, maghemite, magnetite, and metallic iron are also shown

iron crystallite size.

The average crystallite sizes as calculated using the Scherrer formula and XRD traces shown in Figure 6.6 can be found in Table 6.2. Average crystallite sizes measured from the XRD traces are in the correct order of magnitude and follow the trend of increasing crystallite size. However, they are not considered completely accurate as the iron crystallites might not be in a completely crystalline phase, and some may exist as an amophorous phase.

6.3 TPR Analysis

The reduction behaviour of the catalyst samples were investigated using TPR analysis. The hydrogen consumption as a function of temperature for the six catalyst samples are shown in Figure 6.7. There are two distinct peaks, which represent the two phases of reduction of Fe_2O_3. The first phase of reduction is represented by Equation 6.1 and the second by Equation 6.2. As mentioned previously in Section 5 the two peaks have a 11 to 89% division,

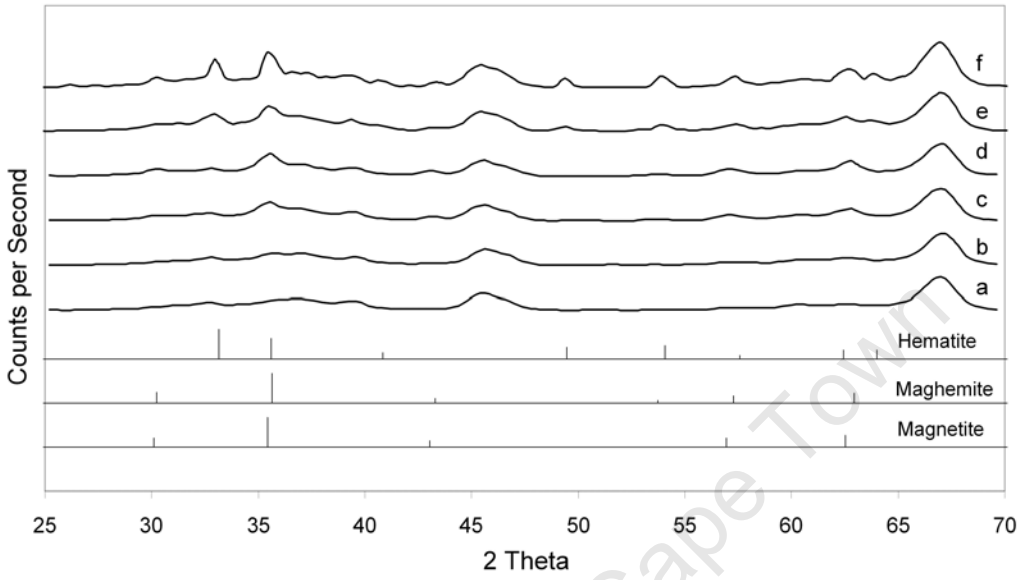

Figure 6.6: XRD patterns of calcined iron catalysts on an alumina support. Reference patterns for hematite, maghemite and magnetite are also included. (a) '2 nm' (b) '3 nm' (c) '7 nm' (d) '9 nm' (e) '14 nm' (f) '16 nm'

Table 6.2: Calculated average metal crystallite size according to the Scherrer formula with respect to XRD traces

Expected crystallite size (nm)	Calculated crystallite size (nm)
'2 nm'	4.6
'3 nm'	4.3
'7 nm'	7.2
'9 nm'	8.3
'14 nm'	11.2
'16 nm'	11.6

Table 6.3: Degree of reduction of alumina supported iron catalysts of differing crystallite sizes calculated from TPR characterisation

Sample	Degree of Reduction (%)
'2 nm'	98
'3 nm'	98
'7 nm'	83
'9 nm'	84
'14 nm'	72
'16 nm'	79

which indicates that the original iron phase of the crystallites was Fe_2O_3.

The first reduction peak occurs between 315 °C and 420 °C, the second peak occurs between 430 °C and 1000 °C. There is a shift of the second reduction peak towards higher temperatures for the larger crystallites. This shift of reduction peak may indicate more significant metal-support interactions (Welker (2007)) occuring for the larger crystallites and the alumina support. Another possible explanation for this shift in the second reduction peak is that there may be diffusional limitations constraining hydrogen transport in the reducing crystallites during reduction. Ultimately the shift in the second reduction peak indicates that complete reduction would be more difficult for the catalyst samples with the larger crystallite size. This result is confirmed by the degree of reduction calculations which were obtained via complete reduction of reduced catalysts samples (see Section 4.3.3) and which are summarized in Table 6.3, the larger crystallites have a lower degree of reduction indicating that it was more difficult to achieve complete reduction.

$$3Fe_2O_3 + H_2 \longrightarrow 2Fe_3O_4 + H_2O \tag{6.1}$$

$$Fe_3O_4 + 4H_2 \longrightarrow 3Fe + 4H_2O \tag{6.2}$$

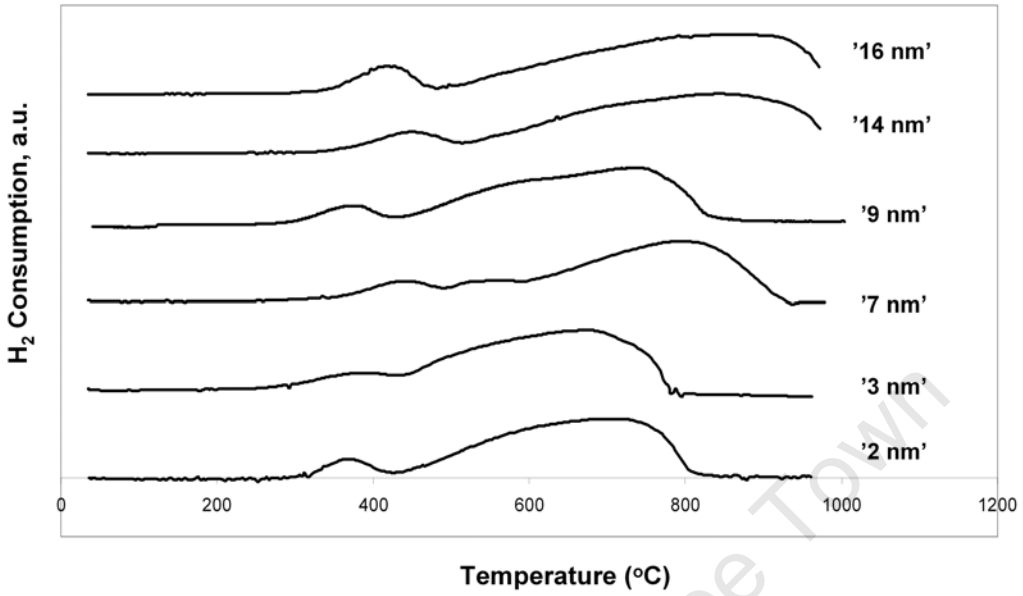

Figure 6.7: TPR traces for all six different catalysts, measuring H_2 consumption as a function of temperature

6.4 AAS Analysis

Acid digestion was performed on the catalyst followed by AAS analysis to determine the metal loading of the catalyst sample. The theoretical iron loading of the calcined samples (assuming Fe_2O_3 as the iron phase) was 13.1 wt%, however a lower actual loading was expected due to some loss of iron during the catalyst preparation process. AAS analysis indicated a general 10 wt% loading of iron on the support material. However metal loading calculated from the total hydrogen consumption obtained from TPR characterisation appears to increase with increasing crystallite size. This might be expected given that the catalyst samples with the smallest crystallites are the most difficult to prepare, thus requiring more washing steps, resulting in more opportunites for iron to be lost. The results from both analysis are represented in Table 6.4.

Table 6.4: Metal loading of calcined alumina supported iron catalysts determined by means of AAS and TPR analysis

Sample	wt% Fe	
	AAS	TPR
'2 nm'	10.3%	11.3%
'3 nm'	10.0%	11.6%
'7 nm'	10.3%	11.6%
'9 nm'	12.0%	12.3%
'14 nm'	10.5%	12.5%
'16 nm'	10.5%	13.1%

6.5 Summary of Characterisation Results for Supported Crystallites

Characterisation results indicate that the reverse micelle method can be successfully used to create supported catalysts with metal crystallites of sizes varying between 2 and 16 nm. The metal crystallites generally exhibit narrow size distributions, and are well dispersed over the support material. It is expected that the procedure of dispersing the metal crystallites onto the support material can still be improved upon as there is some clustering observed, especially for the catalyst samples with the smallest crystallites. However it can be concluded that the current catalyst preparation procedure is sufficient to create model catalysts for the investigation of effect of crystallite size on Fischer-Tropsch selectivity and activity.

TEM analysis also showed that the reduction procedure does result in an increase of the average crystallite size, indicating some sintering may occur, however the increase in crystallite size is not sufficient to be considered problematic. TPR and XRD analysis show that in a calcined catalyst the iron is in the form of iron oxide (Fe_2O_3), mainly maghemite, though some hematite may also be present. TPR analysis also showed that catalyst samples with larger crystallites tend to be more difficult to reduce, degree of reduction results confirmed this, showing the lowest degree of reduction for the largest crystallites, while the smallest crystallites show a high degree of reduction,

i.e. they are almost fully reduced. Finally both AAS and TPR analysis were used to confirm the iron loading on the support material. AAS showed a general iron loading of approximately 10 wt%, however TPR results show that a higher loading is achieved for the catalysts with larger crystallites. Both the changes in loading and degree of reduction as well as the actual crystallite sizes in the reduced samples will have to be accounted for in the evaluation of the Fischer-Tropsch test results.

Chapter 7

Fischer-Tropsch Testing

7.1 Dependence on Crystallite Size

Investigation into the performance of catalysts with different metal crystallite size in Fischer-Tropsch synthesis was carried out in a fixed bed reactor. The calcined catalyst was reduced *in-situ* in 30 ml(NTP)/min of pure hydrogen (300 °C for 16 hrs at a heating rate of 1 °C/min). The catalysts were tested at a reaction temperature of 240 °C and a total pressure of 12 bar (10 bar of synthesis gas with a hydrogen to carbon monoxide ratio of 2.0, 2 bar of argon as a reference gas). The experiments were run over 5 hours with steady state being attained after approximately 1 hour. Passivation of the spent catatlyst took place at room temperature under CO_2 for an hour.

7.1.1 Fischer-Tropsch Activity and Characterisation of Spent Catalysts

The Fischer-Tropsch activity is defined as a rate of carbon conversion to hydrocarbon products per time and exposed metal surface area post-reduction. The exposed metal surface area used during calculations took into account the crystallite size distribution in the catalyst, either after reduction of the metal crystallites (reduced catalyst size for initial results) or after Fischer-Tropsch reaction of the metal crystallites (spent crystallite size for steady state results), the degree of metal reduction as well as the total metal load-

ing. Two separate analysis methods were used in the determination of the Fischer-Tropsch rate. Carbon monoxide conversion as well as methane and carbon dioxide production were measured directly from the online GC with TCD detection. The second analysis method used was an offline GC with FID detection. The FID analysis method was especially important for experimental runs involving the smaller crystallite samples, as the conversion is expected to be low ($< 5\%$) and at these conversion levels the TCD no longer has the required accuracy. Eight ampoule samples were taken from the hot product gas at specific intervals during the five hour experimental test. These product samples were then analyzed and product formation rates of the volatile organic compounds (C_1 - C_9) were determined using calculated methane production rates from the TCD as the internal standard. From the results of the FID analysis an Anderson-Schulz-Flory distribution can be calculated and extended to high carbon numbers (in this study to C_{100}) assuming carbon number independant chain growth probability to obtain a total product formation rate on a carbon basis, which equals the rate of carbon monoxide conversion to Fischer-Tropsch products (see Appendix B). Carbon monoxide conversion to Fischer-Tropsch product can then also be back calculated. The carbon that resulted in carbon dioxide was not considered as part of the Fischer-Tropsch rate as carbon dioxide is not considered as part of the Fischer-Tropsch product spectrum, it is rather produced via the water-gas shift reaction. It should be noted that steady state carbon monoxide conversion for all 6 catalysts tested were below 10%, the reaction conditions had been chosen specifically to maintain a low conversion in order to compare the catalysts in activity and selectivity directly and in the absence of concentration profiles. Conversions of below 10% (actual conversion levels are listed in Appendix C) were desirable as the activities and selectivities of catalysts with different crystallite sizes could be compared directly.

The general trend that emerged for all catalysts tested was that there was no maximum conversion reached in the initial stages of reaction time unlike the trends observed with a ruthenium catalyst in the study by Welker (2007). This trend can be observed in Figure 7.1, there is a steady increase in the rate of formation of Fischer-Tropsch products over the first hour, an

episode during which catalyst crystallites reconstruction including carbide formation occurs (Dry (1981), Schulz et al. (1997)). Please note that the three catalysts indicated in Figure 7.1 and for other figures in the results sections are named according to the expected crystallite sizes associated with the water to surfactant ratios used to create the metal crystallites in the calcined catatlyst from Mabaso (2005), i.e. '16 nm' refers to the catalyst made with a water to surfactant ratio expected to result in 16 nm metal crystallites. Steady state activity is reached at approximately 100 minutes. Figure 7.1 also shows that as metal crystallite size decreases, so does the surface area specific Fischer-Tropsch rate and this is found throughout the duration of the experiments; that is, initially when the exact metal surface area is known and at the end of the runs, at steady state, at which the crystallite sizes may have changed and phase changes may have occurred. This trend is further highlighted in Figure 7.2, which shows the specific Fischer-Tropsch rate as a function of initial metal crystallite size, furthermore the figure also shows that smaller metal crystallite sizes result in an increase in methane selectivity, similar results have been shown in previous studies on ruthenium catalysts (Welker (2007)), rhodium catalysts (Ojeda et al. (2004)) as well as on potassium promoted iron (Mabaso (2005), and cobalt catalysts (Bezemer et al. (2006)). However, studies on potassium promoted iron (Mabaso (2005), Barkhuizen et al. (2006)) and on cobalt (Bezemer et al. (2006)) have shown that the specific Fischer-Tropsch rate or turnover frequency respectively leveled out above a certain crystallite size, namely 7-8 nm for iron and 5-6 nm for cobalt, this trend was not observed in this study. The trend observed in this study is similar to the findings using ruthenium by Welker (2007), a steady increase of activity with crystallite size was found. It is known and to be expected that the catalyst may undergo changes during exposure to Fischer-Tropsch conditions. In order to be able to interpret some of the temporal changes and crystallite size dependencies the characterisation of the spent catalysts is therefore crucial and discussed below.

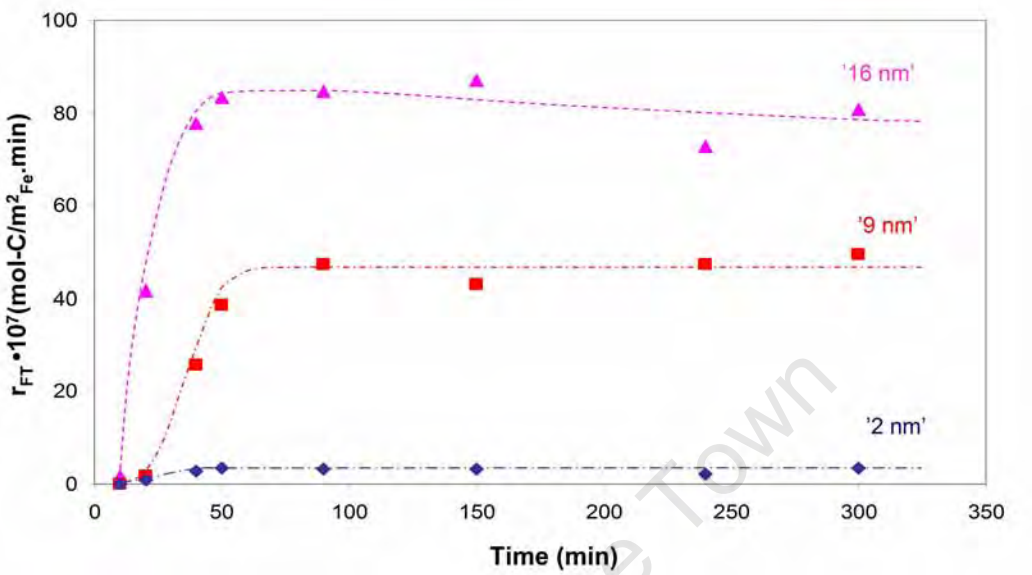

Figure 7.1: Specific Fischer-Tropsch rate as a function of time for three selected catalysts ('2 nm', '9 nm', '16 nm') at initial (reduced) crystallite size (T = 240 °C, P = 12 bar, $P_{syn-gas}$ = 10 bar, H_2/CO ratio = 2)

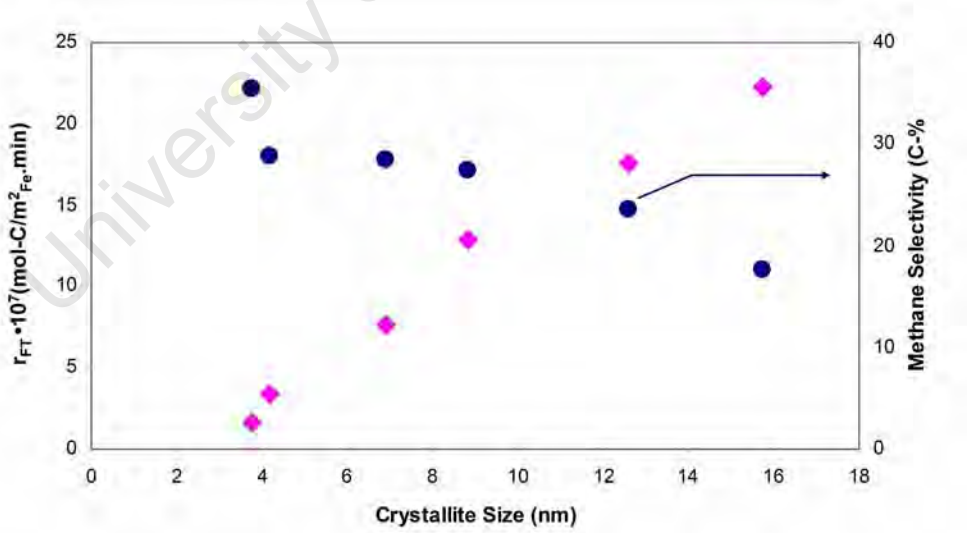

Figure 7.2: Specific Fischer-Tropsch rate and methane selectivity as a function of initial (reduced) crystallite size at steady state for all 6 alumina supported iron model catalysts (T = 240 °C, P = 12 bar, $P_{syn-gas}$ = 10 bar, H_2/CO ratio = 2)

Table 7.1: Average crystallite sizes and standard deviations (in nm) of calcined, reduced and spent catalyst as determined by means of TEM analysis

Sample Code	Expected crystallite size	Calcined Sample $\bar{d}_{cryst} \pm \sigma$	Reduced Sample $\bar{d}_{cryst} \pm \sigma$	Spent Sample $\bar{d}_{cryst} \pm \sigma$
'2 nm'	2	2.4 ± 0.8	3.8 ± 1.3	5.6 ± 2.0
'3 nm'	3	2.7 ± 0.8	4.2 ± 1.0	5.6 ± 1.4
'7 nm'	7	6.7 ± 1.2	6.9 ± 1.7	7.9 ± 1.8
'9 nm'	9	7.9 ± 1.4	8.8 ± 1.5	10.8 ± 3.4
'14 nm'	14	12.0 ± 1.9	12.6 ± 1.8	13.3 ± 2.1
'16 nm'	16	15.4 ± 1.7	15.7 ± 2.3	16.8 ± 2.6

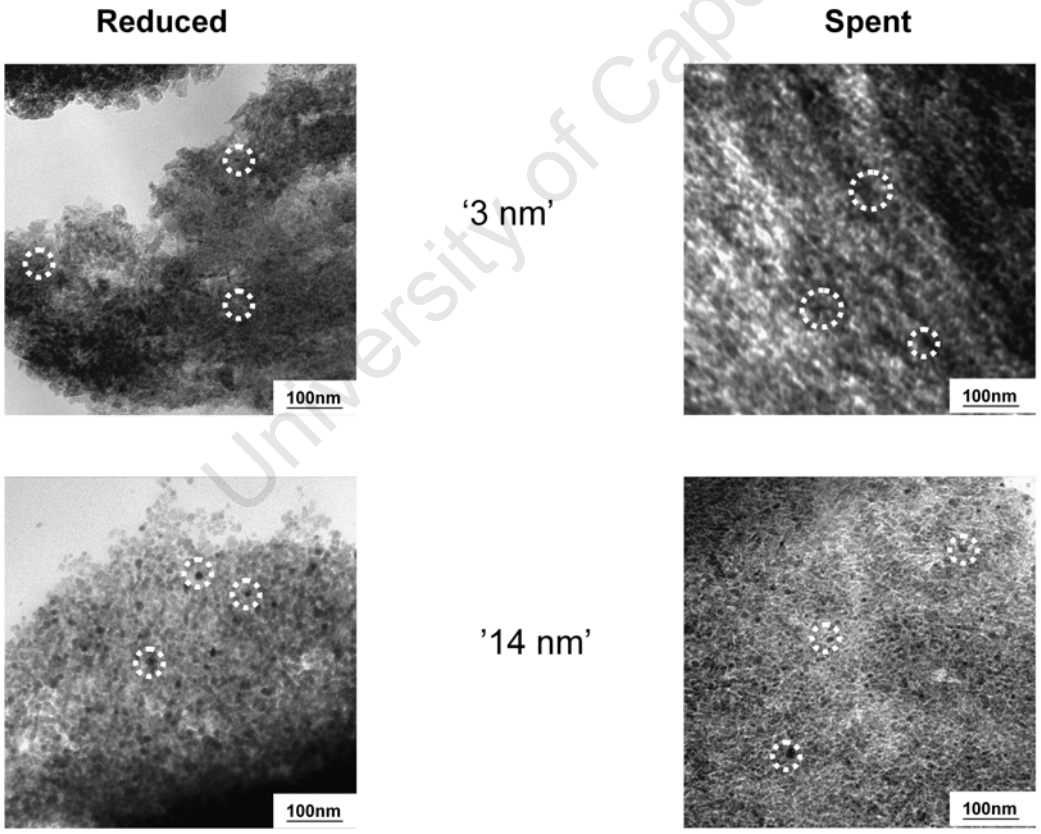

Figure 7.3: TEM micrographs of reduced *(left)* and spent *(right)* samples of two selected alumina supported model iron catalysts ('3 nm' and '14 nm')

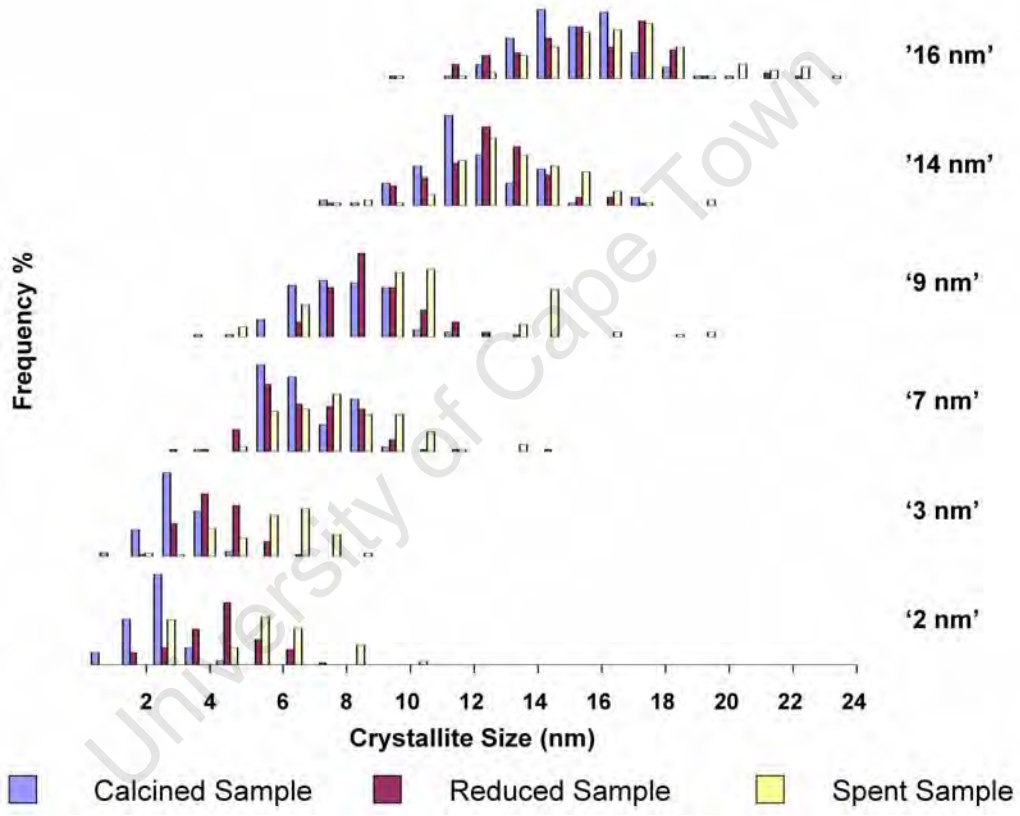

Figure 7.4: Crystallite size distributions of calcined, reduced and spent samples of all six alumina supported model iron catalysts.

Table 7.2: Percentage crystallite growth of spent catalysts from reduced catalysts

Sample	Growth,%
'2 nm'	33.0
'3 nm'	48.5
'7 nm'	14.2
'9 nm'	22.7
'14 nm'	5.6
'16 nm'	6.6

7.1.1.1 Characterisation of Spent Catalysts

Figure 7.3 shows TEM micrographs comparing spent samples of catalyst with anticipated crystallite sizes of 3 and 14 nm corresponding to the reduced samples. The TEM micrographs of the spent catalysts were taken after 5 hours of test time at reaction conditions of 240 °C and 12 bar (10 bar syn-gas), and a further 1 hour passivation with carbon dioxide at room temperature. On comparison, the spent samples of the '14 nm' catalyst did not show any significant change after reaction, the metal crystallites are roughly the same size and are still well dispersed over the support material. However, the smaller '3 nm' catalyst did show some sintering and clustering, resulting in some crystallite growth. Table 7.1 lists the average metal crystallite sizes of all six tested samples after reaction and Figure 7.4 shows the size distributions of the samples after calcination, after reduction and after reaction. It can be seen from these results that metal crystallite growth occurs to a greater extent on the smaller crystallites than on larger crystallites, this is further highlighted in Table 7.2 which shows the percentage growth of the metal crystallites from reduced sample to spent sample. Nonetheless, the observed trend with respect to catalyst activity as function of crystallite size still holds even if taking the slight growth of the crystallites into account.

There are three different theories as to why smaller crystallites are less active than larger ones; electronic effects, the 'Oxidation Theory' (Figure 2.18) and the 'Ensemble Effect Theory' (Figure 2.17) which are described in

detail in Section 2.6. Metal oxides have long been considered either to be inactive or less active in Fischer-Tropsch synthesis (Mansker et al. (1999), Li et al. (2002b), Bian et al. (2002)). During Fischer-Tropsch synthesis α-iron, iron carbides and magnetite have all been found in the catalyst. In the fresh catalyst α-iron is predominant, and the formation of both iron carbides and magnetite from metallic iron is possible under Fischer-Tropsch conditions (Dry (1981), Iglesia et al. (1993), de Smit et al. (2009)).

$$3Fe + 4H_2O \rightleftharpoons Fe_3O_4 + 4H_2 \tag{7.1}$$

$$3Fe + 2CO \rightleftharpoons Fe_3C + CO_2 \tag{7.2}$$

Considering Equations 7.1 and 7.2, the assumption could be made that iron carbides would form more rapidly at the start of the experimental run as magnetite would require product water in order to form, while the carbides form with the reactant carbon monoxide. Therefore it has been suggested that magnetite would form through a further reaction of iron carbide with product water. However it has been shown by Mabaso (2005) that this bulk transformation is not thermodynamically feasible under low temperature Fischer-Tropsch conditions. Considering that nano-sized crystallites have a much higher surface energy, the assumption can be made that the oxidation of nano-sized iron carbide would be more feasible than the oxidation of bulk iron carbide (Mabaso (2005)). The same has been shown theoretically for nano-sized cobalt by van Steen et al. (2005). Therefore the 'Oxidation Theory' suggests that the more straightforward transformation of nano-sized iron carbide crystallites to magnetite could account for the lower activity observed for smaller crystallites, however substantial experimental proof is still outstanding and the characterisation data of the spent catalysts do not provide clear evidence for this. Alternatively, surface oxygen formed via carbon monoxide dissociation could react with the metallic surface to form iron oxide phases, in competition with the reactions of oxygen to form water, carbon dioxide and organic oxygen containing products.

The second theory is the 'Ensemble Theory', which suggests that certain

catalytic reactions require a minimum collection of neighboring atoms or 'ensembles' in order to occur (Niemantsverdriet et al. (1980), Ciobica et al. (2003), Ciobica and van Santen (2003), Mabaso (2005), Barkhuizen et al. (2006), Bezemer et al. (2006), Welker (2007)). It is likely that a complex chemical reaction like the Fischer-Tropsch synthesis that involves multiple steps (reactant adsorption onto the surface of the catalyst, generation of a chain starter, chain growth (propagation step), product desorption from the catalyst surface, re-adsorption of reactive products and further reaction (Section 2.1.2)) would occur on ensembles rather than individual atoms. It can further be assumed that these ensembles would be present in a higher concentration on larger crystallites than on smaller ones, furthermore a minimum size would exist below which no Fischer-Tropsch activity would be present. This could explain the decrease in Fischer-Tropsch activity with decreasing crystallite size, at least over a certain range of crystallite sizes. Further experimental data that reinforce this theory is the increase in methane selectivity with decreasing crystallite size shown below in Section 7.1.2.2, the more simplistic nature of the methane formation reaction in comparison to that of the Fischer-Tropsch reaction would suggest that it would require less atoms or different ensembles in order to occur. Therefore on smaller crystallites in the absence of required ensembles of Fischer-Tropsch synthesis, methane formation occurs instead. However, concrete experimental proof is again lacking, therefore it would be prudent to consider that the observed decrease in Fischer-Tropsch activity with decreasing crystallite size is due to a combination of both the 'Oxidation Theory' and the 'Ensemble Effects Theory'. Furthermore, size dependent electronic effects man be considered in addition, as it has for example been reported that adsorption or activation of carbon monoxide is strongly dependent on size of gold crystallites, while hydrogen adsorption can be assumed to be crystallite size independent (Phala and van Steen (2007))

7.1.2 Product Formation

Products formed during Fischer-Tropsch testing at the basecase conditions of 240 °C and 12 bar (10 bar syn-gas, $H_2/CO = 2$) were analyzed using a combination of online TCD detection and offline FID detection using the ampoule method. Detailed results of activity and selectivity of catalysts of varying crystallite sizes can be found in Appendix C, these results are separated into two categories; initial state (10 - 20 minutes) and steady state (50 - 300 minutes)[1]. All reported hydrocarbon and oxygenate selectivities are calculated from off-line FID analysis of volatile organic compounds (VOCs C_1 - C_9), longer chained hydrocarbons could not be considered as they were not present on the FID chromatograph in large enough concentrations. Due to this limitation, the methane in this fraction is an overestimate of the true methane selectivity, while the selectivity of C_5+ compounds are underestimated. However, this could be corrected for by taking longer chained hydrocarbons into account (by extrapolating to C_{100} for example, assuming carbon number independent chain growth). Such a correction was not done as the presented data should provide a good reflection of the true trends. Furthermore, only one chain growth probability is reported for each crystallite size, the second, greater chain growth probability at higher carbon numbers was not observed as described by others (Satterfield et al. (1986), Mabaso (2005), Cairns (2009)) for any of the catalysts tested in this study. The chain growth probability reported here was obtained from Anderson-Schulz-Flory plots in the carbon number range C_3 - C_9. Note that results of initial and steady-state selectivities are plotted against their respective crystallite sizes during this stage of no water addition as size changes were relatively small. However in the next section investing the effect of water co-feed both initial and steady state data are plotted against initial crystallite sizes, this is done purely for comparison purposes, and means that more emphasis has to be put onto the inital state results as at this stage the size of the crystallites is assumed to be fairly unchanged as well as composition of the iron catalyst.

[1] All values are averaged values for 10 to 20 minutes and 50 to 300 minutes, any obvious outliers have been ignored during calculations

7.1.2.1 Carbon Dioxide Formation

Iron catalyzed Fischer-Tropsch synthesis always results in the formation of carbon dioxide (CO_2) as an undesired by-product. Carbon dioxide is formed through the water-gas shift reaction (Equation 2.2), which is seen as a consecutive reaction to the Fischer-Tropsch reaction where produced water reacts with carbon monoxide to form carbon dioxide and hydrogen. Figure 7.6 shows the change carbon dioxide formation rates normalized for initial metal surface area as a function of time for 3 selected catalysts of varying crystallite size. It can be seen in the figure that there appears to be a trend with respect to metal crystallite size, similar to what was shown in Figure 7.1, where with an increase in metal crystallite size, there is an associated increase in the specific rate of formation of carbon dioxide. However, Figure 7.5 depicts initial and steady state carbon dioxide selectivity as a function of crystallite size shows that a minimum carbon dioxide selectivity is actually attained with the middle crystallite sizes, this trend is repeated with other product selectivities and will be discussed in detail in the following sections. With respect to time, steady state is again reached after approximately 100 minutes, after which there are no significant changes in the carbon dioxide formation rate (Figure 7.6). Figure 7.7 shows carbon dioxide selectivity as a function of time on stream, here the trend associated with metal crystallite size is no longer present, and the scatter shown in the '2 nm' sample is due to the extremely low conversion levels, resulting in less accurate TCD readings. It is expected that the increase shown in the first hour of testing is due to the series-like nature of the two reactions (Fischer-Tropsch and Water-Gas Shift), however another possible explanation is the change in the phases of the catalyst during the initial stages of the reaction (Figure 2.8, Dry (1981), Schulz et al. (1997), Riedel et al. (2001)). It has been previously stated that water-gas shift on an iron Fischer-Tropsch catalyst is catalyzed by the oxide phase (Satterfield et al. (1986)), however no experimental proof has been given for this statement. Furthermore, if smaller crystallites are preferentially oxidized as is hypothesized by the 'Oxidation Theory' it would be expected that the smallest crystallites would produce the highest amount of

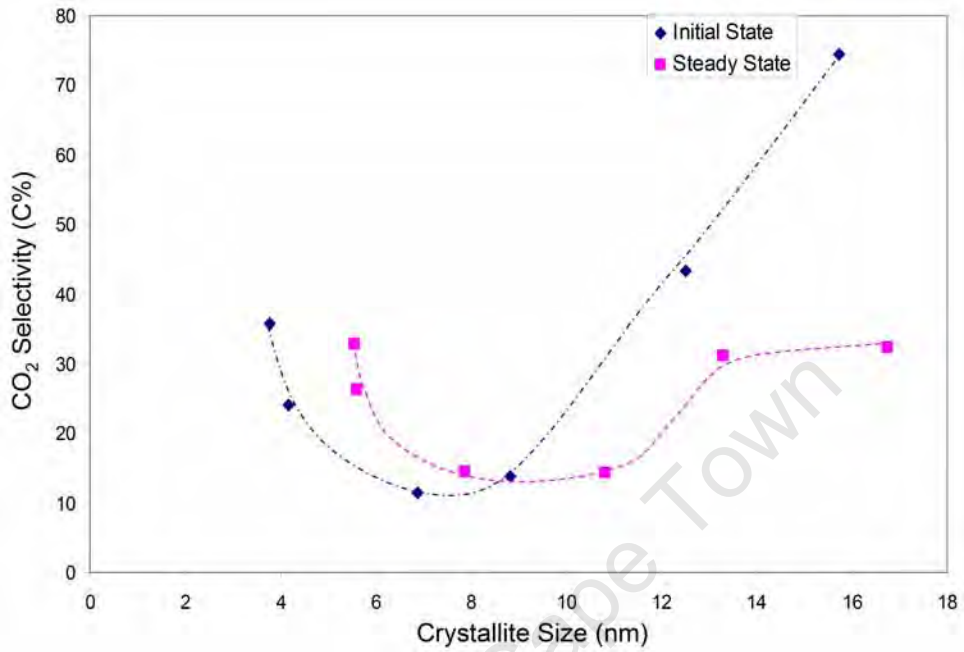

Figure 7.5: Selectivity of carbon dioxide as a function of crystallite size for both initial state (10 - 20 min with reduced crystallite sizes) and steady state (50 - 300 min with spent crystallite sizes) (T = 240 °C, P = 12 bar, $P_{syn-gas}$ = 10 bar, H_2/CO ratio = 2)

carbon dioxide, however it can be seen in Figure 7.6 that this is not the case. Therefore it has to be stated from the results of this work that there is no clear trend involving crystallite size and the selectivity to carbon dioxide at conditions of low synthesis gas conversion. Furthermore, the characterisation of the spent catalysts do not show any evidence for enhanced oxidation of small crystallites (see Section 7.2.1.1).

7.1.2.2 Methane Formation and Chain Growth Probability

The most thermodynamically stable product in Fischer-Tropsch synthesis is methane (Anderson (1984)), this is unfortunate as methane is arguably the least economically viable product, therefore inhibition of methane production has often been a requirement of a good Fischer-Tropsch catalyst. Methane is formed through the associative desorption of a methyl species and surface

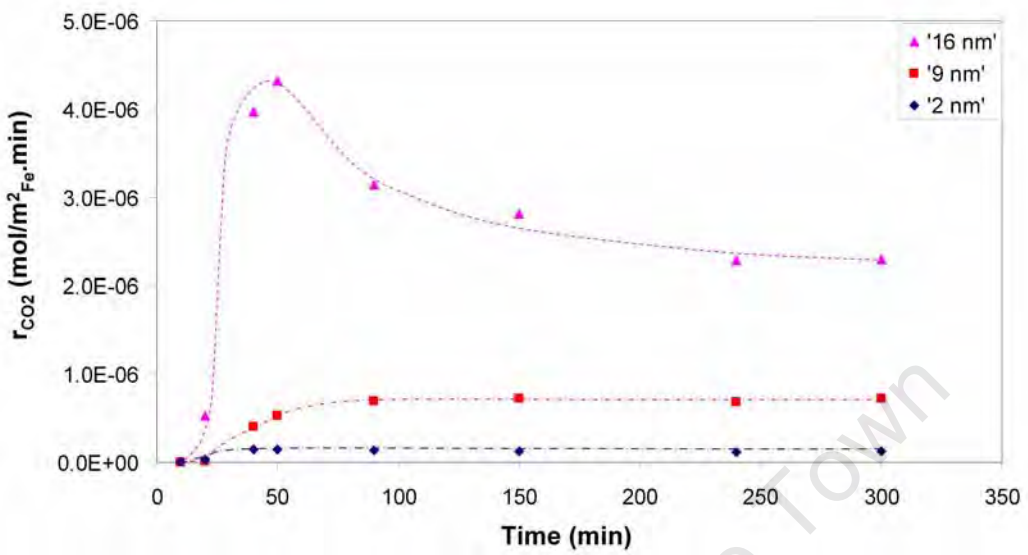

Figure 7.6: Rate of formation of carbon dioxide normalized to initial metal surface area as a function of time of three selected catalysts ('2 nm', '9 nm', '16 nm') (T = 240 °C, P = 12 bar, $P_{syn-gas}$ = 10 bar, H_2/CO ratio = 2)

hydrogen, alternatively and more desirably the methyl species can act as a chain starter leading to chain growth.

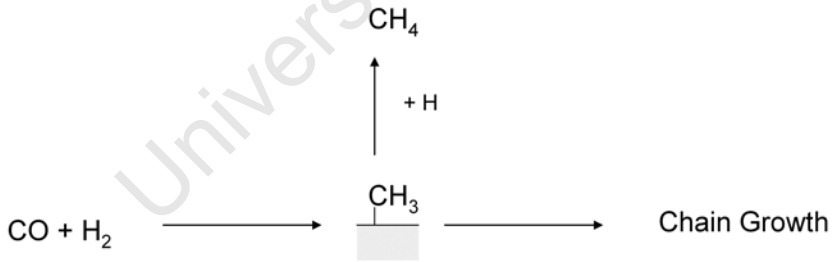

The methane selectivities both during the initial stages of the experiment (10 - 20 min) and steady state (50 - 300 min) for all six model catalysts can be found in Figure 7.8, the trend shown is that methane selectivity increases with decreasing crystallite size. Figure 7.9 further shows the methane selectiviy calculated from FID data as a function of time on stream for 3 selected catalysts also shows a similar trend. Furthermore, it can be seen that higher methane selectivities result during the initial stages (10 - 20 minutes) of the test run compared to steady state (50 - 300 minutes). This could be

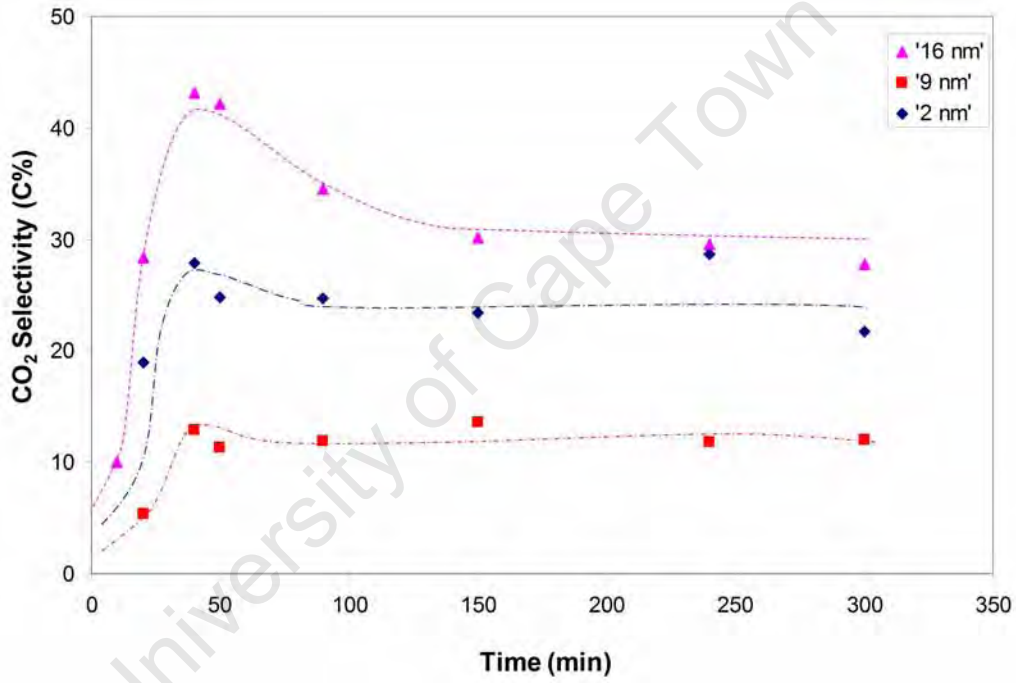

Figure 7.7: Carbon dioxide selectivity as a function of time for three selected catalysts ('2 nm', '9 nm', '16 nm') (T = 240 °C, P = 12 bar, $P_{syn-gas}$ = 10 bar, H_2/CO ratio = 2)

attributed to the effects of catalyst reconstruction from metallic iron to the active carbide phase (Schulz et al. (1994), Schulz et al. (1999), Riedel et al. (2001)). Previous work by Mabaso (2005) also found this trend in potassium supported iron catalysts, however in that work it could not be said whether this trend was due to crystallite size effects or the enhanced effect of potassium in larger crystallites due to an increased potassium to metal surface area. As no potassium promoters were added to the iron catalyst in this work, it can be said that the trend of increasing methane selectivity with decreasing crystallite size is due to the crystallite size effect. It must be emphasized again that the observed effects were not complicated by effects of sintering as crystallite sizes of the initial and spent samples remained largely unchanged (see Table 7.1). This trend has also been reported in work on rhodium (Ojeda et al. (2004)), cobalt (Bezemer et al. (2006)) and ruthenium (Welker (2007)). As mentioned previously, this observation of methane selectivity increasing with decreasing metal crystallite size can be attributed to the more simplistic nature of methane formation in comparison to the Fischer-Tropsch reaction. As such, the methane reaction would require less atoms or ensembles in order to occur. Therefore, on smaller crystallites where the required ensembles for Fischer-Tropsch synthesis are absent, methane formation occurs instead. It is very interesting to note that the observed methane selectivities with respect to each independent crystallite size sample are not affected while several phase changes are believed to have occured.

The chain growth probabilities of all six catalysts at steady state are reported in Table C.2 and shown in Figure 7.10. Chain growth probability values are calculated from Anderson-Schulz-Flory distributions in the carbon number range between C_3 and C_9. The values range between 55 and 59% at steady state, which is very low when compared to, for example, industrial operation, however this was an expected result as the catalysts were unpromoted. It appears that the chain growth probability at steady state is not greatly affected by crystallite size, this result combined with the crystallite size trend for methane selectivity supports the 'Ensemble Effect Theory' mentioned in Section 7.1.1. These results suggest that there are more methane formation sites present on smaller crystallites relative to

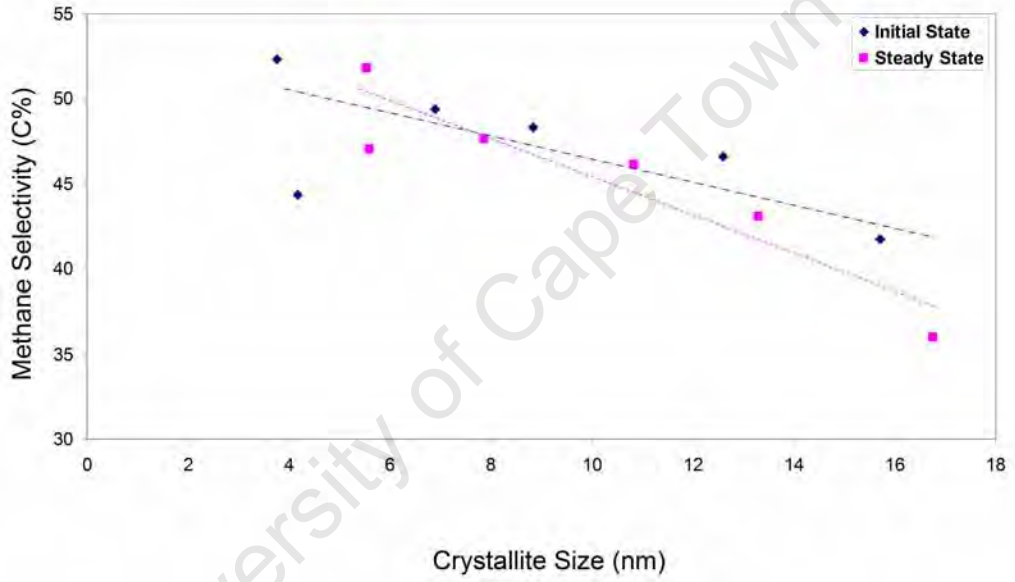

Figure 7.8: Methane selectivity as a function of crystallite size of all six alumina supported iron model catalysts calculated both during initial state (10 - 20 min with reduced crystallite sizes) and steady state (50 - 300 min with spent crystallite sizes) (T = 240 °C, P = 12 bar, $P_{syn-gas}$ = 10 bar, H_2/CO ratio = 2)

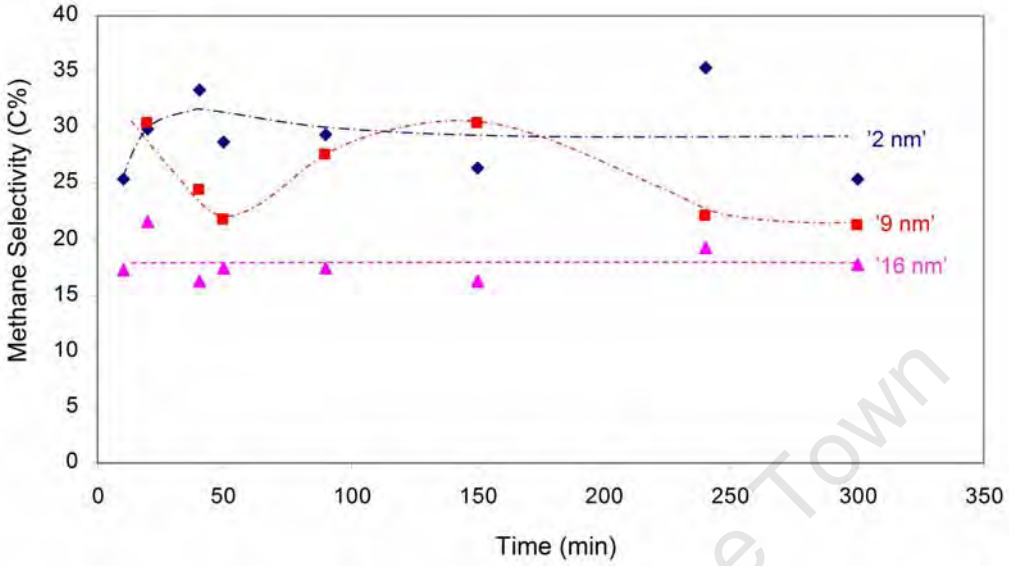

Figure 7.9: Methane selectivity as a function of time for three selected alumina supported model iron catalysts ('2 nm', '9 nm', '16 nm') (T = 240 °C, P = 12 bar, $P_{syn-gas}$ = 10 bar, H_2/CO ratio = 2)

Fischer-Tropsch growth sites, and chain growth itself, at least at steady state is not affected. Chain growth does however seem to be affected by crystallite size during the initial stages of the experiment, when lower chain growth probabilities can be found on small crystallites. A similar observation concerning this time dependent effect was made by Welker (2007) when testing ruthenium crystallites of differing sizes. It was proposed that the effects of surface reconstruction may have played a role, where after the initial stages of the experiment surface reconstruction takes place, and more Fischer-Tropsch ensembles become available on the small metal crystallites, thereby increasing the chain growth probability at steady state. Another possible factor is the surface coverage; surface coverage is low during the initial stages of the experiment, however this changes as the Fischer-Tropsch kinetic regime is fully established at steady state. This may indicate that after surface reconstruction and the establishment of the kinetic Fischer-Tropsch regime on the catalyst surface the chain growth step is unaffected by crystallite size. However, in the case of the freshly reduced catalyst, insufficient surface re-

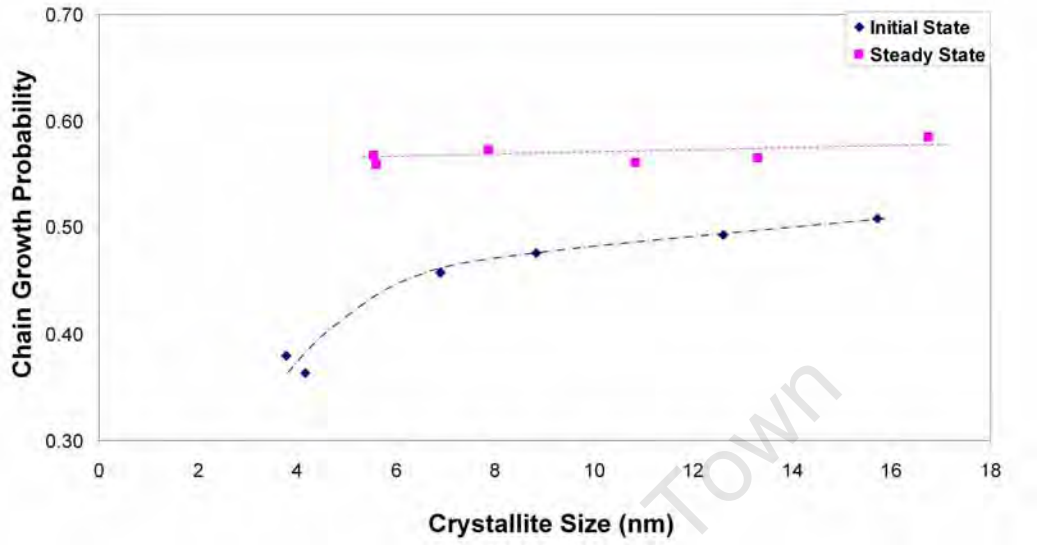

Figure 7.10: Chain growth probability as a function of crystallite size of all six alumina supported model iron catalysts during both initial state (10 - 20 min with reduced crystallite sizes) and steady state (50 - 300 min with spent crystallite sizes) (T = 240 °C, P = 12 bar, $P_{syn-gas}$ = 10 bar, H_2/CO ratio = 2)

construction has taken place and low coverage is expected, the chain growth step becomes crystallite size dependent.

7.1.2.3 Olefin Formation

Olefins are known to be the main primary products of Fischer-Tropsch synthesis (Schulz (1999)). α-olefins are formed through β-H-elimination from an alkyl surface species, alternatively the alkyl species could be hydrogenated resulting in n-paraffins. The β-H-elimination reaction is reversible, thus allowing for the desorbed α-olefins to re-adsorb onto the catalyst surface and further react in secondary reactions to result in longer chained hydrocarbons (Figure 2.1, Schulz and Claeys (1999a), Claeys and van Steen (2004)), however paraffin desorption is irreversible. In the case of no secondary reactions, i.e. primary selectivity, then the hydrogenation of the alkyl species to a paraffin is strongly inhibited resulting in 70 - 90 mol% olefins in each carbon fraction (Schulz and Claeys (1999b)).

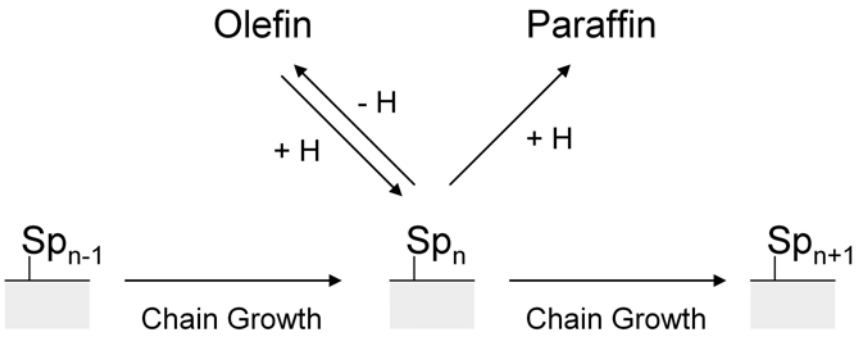

By plotting the mole fraction of linear olefins in linear hydrocarbons as a function of carbon number, one can determine the extent of secondary reactions that may have occurred. Figure 7.11 is such a plot of the steady state values of 3 selected catalysts (in this case '3 nm' catalyst is chosen instead of '2 nm' as the '2 nm' catalyst only showed values up to C_6, it should be noted however, that alpha values were calculated for the '2 nm' sample using only C_3 to C_6, this was considered to not contain the necessary accuracy). In the case of primary selectivity (no secondary reactions), a horizontal line at a mole fraction of 0.7 - 0.9 is expected. However, for most working catalysts this is not the case as shown in Figure 7.11, the trend is that there is a particularly low value at C_2 showing the relatively high reactivity of ethene, while a maximum exists at C_3 with decreasing values as the carbon number increases (this has previously been attributed to the carbon number dependent diffusivity (Iglesia et al. (1993)), solubitility (Schulz and Claeys (1999b))) and physisorption (Kuipers et al. (1996)). This is the expected trend as ethene has often been shown to be the most reactive olefin (Iglesia et al. (1993), Schulz and Claeys (1999b)). It should also be noted that despite this set of catalysts not being potassium promoted a relatively 'primary' product fraction was obtained. Potassium promotion is generally used on iron catalysts to suppress secondary reactions, an un-promoted iron catalyst generally results in poor product quality, with high methane selectivity and low olefin contents, with much higher fractions of olefins with internal double bonds and branched products from secondary reactions (Schulz et al. (1997)). This was not the case here, more features of the product content will be discussed further in the following sections,

however, it should be noted that these experimental runs were carried out at a relatively low temperature of 240 °C and low conversion levels where increased secondary reactions were not expected.

Another observation from the plots of the mole fraction of olefins in linear hydrocarbons against carbon number in Figure 7.11 is that there isn't a clear trend of these olefin contents with respect to crystallite size. Instead it appears that while the smallest and largest crystallite sizes show mostly primary selectivity, the middle crystallite size of '9 nm' appears to show an increased propensity toward secondary reactions. This trend can be highlighted by selecting a single carbon number such as carbon number 5 and plotting the mole fraction of olefins in linear C_5 hydrocarbon fraction as a function of the actual crystallite size, as shown in Figure 7.12. This graph shows the initial (10 - 20 minutes) selectivities, as well as data collected at stead state (50 - 300 minutes). Comparing the initial values has the advantage that at this stage of testing, one can be sure that sintering and major phase changes have not yet occured. It is interesting to note that regardless of the stage (initial or steady state) within an experiment the same trends with respect to the actual crystallite size (freshly reduced or spent respectively) were found, that is, regardless of any differences in phases present in the differently sized crystallites. In Fischer-Tropsch synthesis, primary selectivity is classified as between 70 and 90 mol-% olefins in the corresponding linear hydrocarbon fraction. This is illustrated in Figure 7.12 highlighted in blue. It can be seen that the smallest and largest crystallites all fall within this range, while the middle sized crystallites fall into the range of increased secondary reactions as illustrated by the area shaded in red.

Figures 7.13 and 7.14 show the mole percent of ethene or propene in the corresponding C-fraction as a function of time. Here again, steady state is reached fairly quickly after approximately one hour of time on-stream. Steady state is also reached independently of crystallite size, which is a result contrary to those presented by Welker (2007) on a ruthenium catalyst, where it was suggested that larger crystallites would reach steady state faster and also result in a higher olefin content, the latter was also reported by Bezemer et al. (2006) on cobalt based catalysts with crystallites of vary-

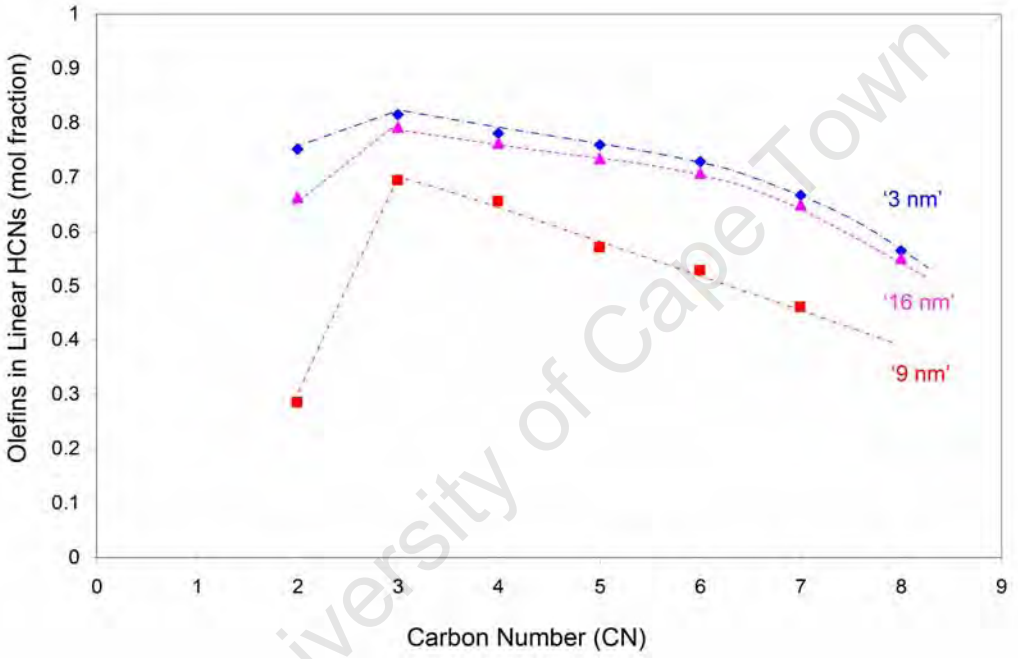

Figure 7.11: Mole fraction of olefins in the corresponding carbon fraction of linear hydrocarbons as a function of carbon number at steady state (50 - 300 min) of three selected alumina supported model iron catalysts ('2 nm', '9 nm', '16 nm') (T = 240 °C, P = 12 bar, $P_{syn-gas}$ = 10 bar, H_2/CO ratio = 2)

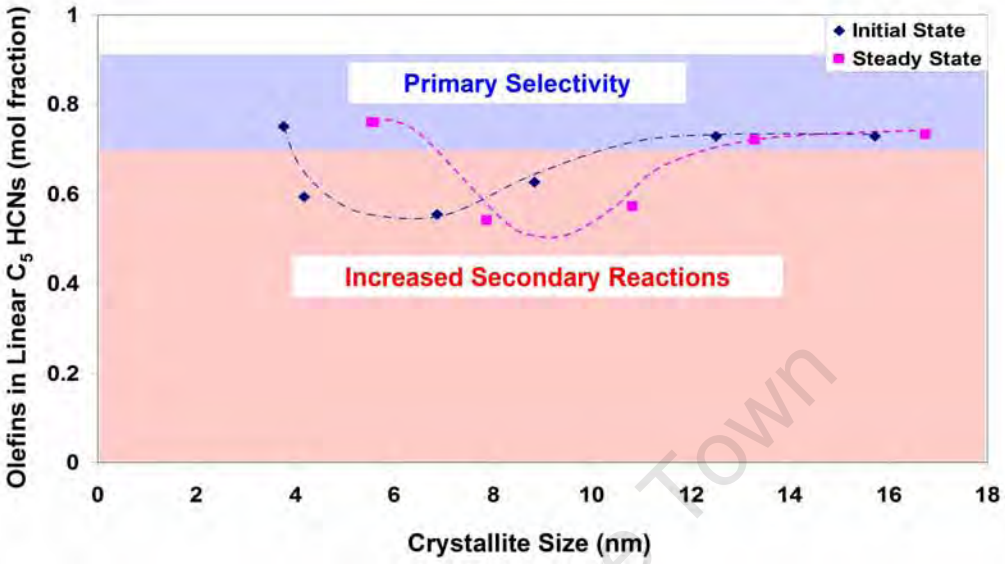

Figure 7.12: Mole fraction of olefins in the C_5 fraction of linear hydrocarbons as a function of crystallite size at both initial (10 - 20 min reduced crystallite sizes) and steady state (50 - 300 min spent crystallite sizes) (T = 240 °C, P = 12 bar, $P_{syn-gas}$ = 10 bar, H_2/CO ratio = 2)

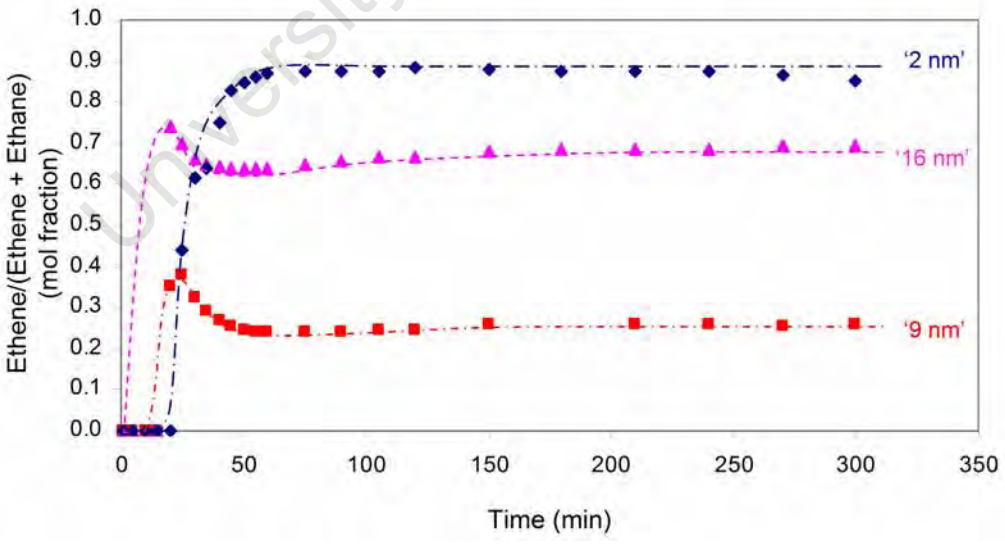

Figure 7.13: Molar olefin content of the C_2 fraction as a function of time of 3 selected alumina supported model iron catalysts ('2 nm', '9 nm', '16 nm') (T = 240 °C, P = 12 bar, $P_{syn-gas}$ = 10 bar, H_2/CO ratio = 2)

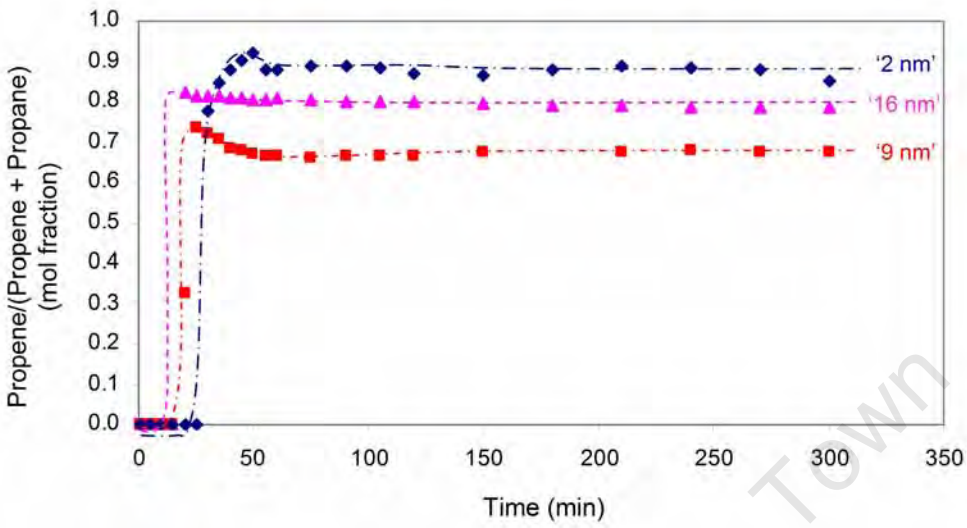

Figure 7.14: Molar olefin content of the C_3 fraction as a function of time of 3 selected alumina supported model iron catalysts ('2 nm', '9 nm', '16 nm') (T = 240 °C, P = 12 bar, $P_{syn-gas}$ = 10 bar, H_2/CO ratio = 2)

ing size. This was not seen here, in fact results from this work show the highest olefin contents result from the smallest crystallites followed by the largest crystallites, while the catalysts with a middle range crystallite size lead to the lowest olefin contents (see Appendix C for results of all 6 tested catalysts). Furthermore, there is less spread in the C_3-fraction than in the C_2-fraction; the olefin content in the C_3-fraction ranges between 65 and 90 mol-% compared to 25 and 90 mol-% in the C_2-fraction. This result again highlights the higher relative reactivity of ethene compared to other olefins.

Another secondary reaction in which olefins may participate is that of isomerisation to form olefins with internal double bonds. It has been suggested that primarily formed α-olefins can re-adsorb onto the catalyst surface and form olefins (Schulz and Claeys (1999b)). A graph of the molar content of α-olefins in linear olefins as a function of carbon number at steady state (50 - 300 minutes) is shown in Figure 7.15. As seen in previous results, the smallest and largest crystallites do not seem prone to promote much secondary reaction, leading to a high content of α-olefins (>90 mol-%). However, this is not the case for the middle range crystallite size catalysts, high levels of

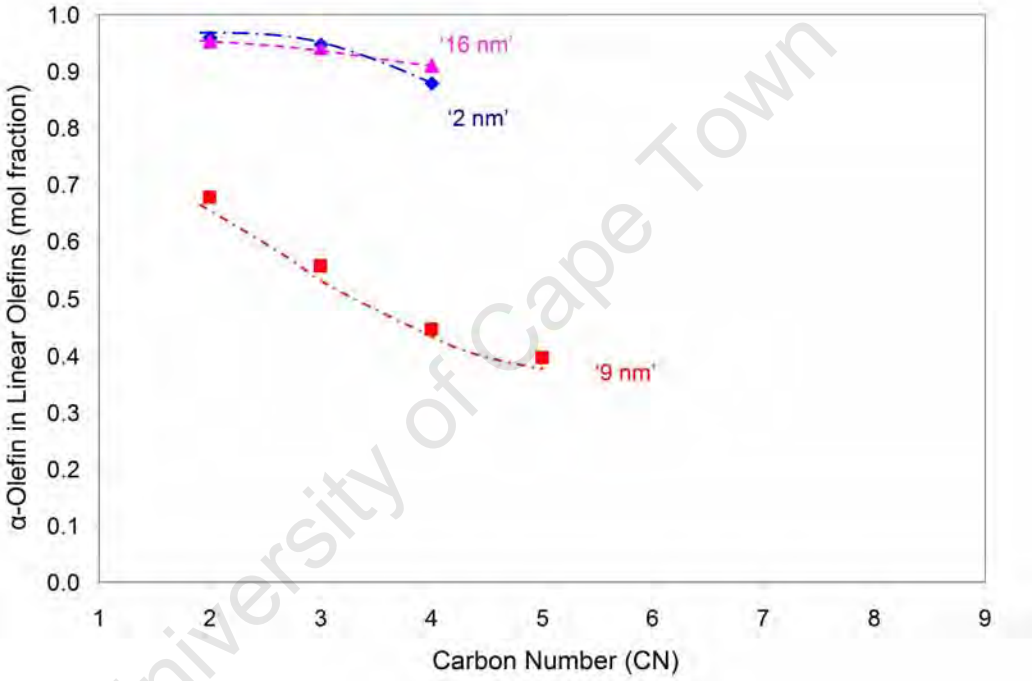

Figure 7.15: Mole fraction of α-olefins in linear olefins during the steady state (50 - 300 minutes) for 3 selected alumina supported model iron catalysts ('2 nm', '9 nm', '16 nm') (T = 240 °C, P = 12 bar, $P_{syn-gas}$ = 10 bar, H_2/CO ratio = 2)

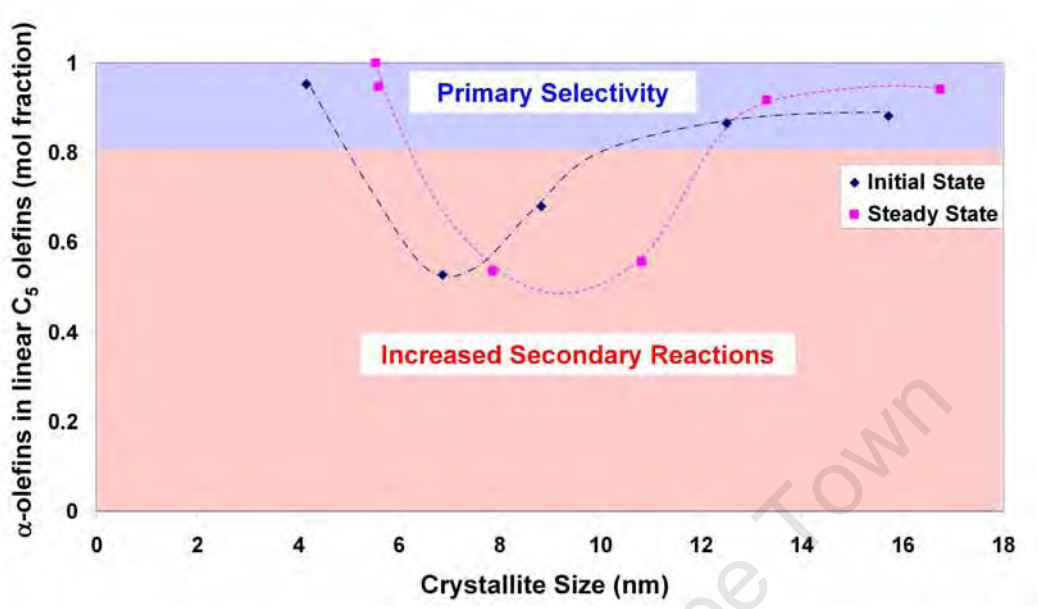

Figure 7.16: Mole fraction of α-olefins in linear olefins during the initial state (10 - 20 minutes) as a function of initial crystallite size ((T = 240 °C, P = 12 bar, $P_{syn-gas}$ = 10 bar, H_2/CO ratio = 2)

secondary reactions lead to a low content of α-olefins (35 - 65 mol-%) (See Figures C.6 and C.7 in Appendix C for both initial and steady state graphs of all six tested catalysts). This result can again be highlighted by taking a single carbon number (Carbon number 5) and plotting the mole fraction of α-olefins in linear olefins against initial crystallite size as shown in Figure 7.16. Primary selectivity (>90 mol-%) is illustrated by the blue box, while an increased propensity towards secondary reactions is highlighted by the red box. Results pertaining to olefin formation and its resultant secondary reactions do suggest a possible trend where catalysts with the middle range crystallite sizes ('7 nm' and '9 nm') are more prone to secondary reactions than other catalysts tested. This trend was obtained at inital stages of catalyst testing and at steady state. Possible explanations for this behavious are given in Section 7.1.3

7.1.2.4 Oxygenate Formation

Oxygenates are minor products of Fischer-Tropsch synthesis, consisting mainly of alcohols and aldehydes, with a small amount of ketones and acids (see Tables C.1 and C.2). Little is known about the formation routes of the oxygenate species, Pichler and Schulz (1970) suggested that oxygenates can be formed through a CO insertion step, while Johnson and Joyner (1993) proposed that another formation pathway could be through the addition of hydroxyl groups to an alkylidene species. Desorption of this species then leads to the formation of alcohols or aldehydes respectively.

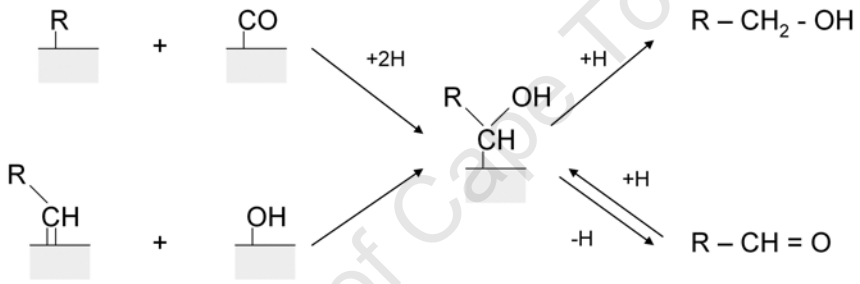

Figure 7.17 shows the molar content of alcohols and aldehydes in corresponding fraction of linear hydrocarbons and oxygenates as a function of carbon number at steady state for 3 selected catalysts. It can be seen here that no methanol was found in the product spectrum, and all alcohols and aldehydes are found in the C_2+ fractions. In an analogy with the results obtained regarding olefins, it can again be seen that the catalysts with mid-range crystallite sizes ('7 nm' and '9 nm') shows lower alcohol and aldehyde contents than the smallest and largest crystallite sizes (For full results see Figures C.10 and C.11 in Appendix C).

It has been prostulated that CO-insertion reactions may preferentially occur on metal sites with low co-ordination (Schulz et al. (2002), Schulz (2003)), which is to say, sites with low numbers of neighbours, normally found on the corners and edges of crystallites. Increased oxygenate selectivity has been previously reported in Fischer-Tropsch synthesis studies with small crystallites on rhodium (Ojeda et al. (2004)), cobalt (Bezemer et al. (2006)) and iron (Mabaso (2005)). The reverse trend was observed in work

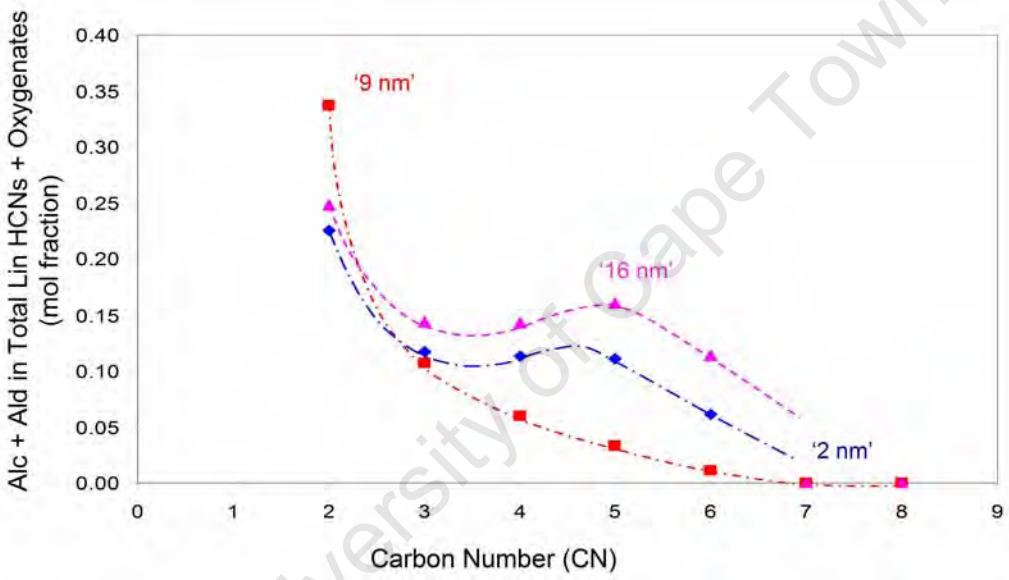

Figure 7.17: Mole fraction of alcohols and aldehydes in linear products during steady state (50 - 300 minutes) on 3 selected alumina supported model iron catalysts ('2 nm', '9 nm', '16 nm') (T = 240 °C, P = 12 bar, $P_{syn-gas}$ = 10 bar, H_2/CO ratio = 2)

on ruthenium by Welker (2007), who suggested that this decrease in oxygenate selectivity with decreasing crystallite size may be due to either formation of the oxygenates through the reaction pathway suggested by Johnson and Joyner (1993) or that the primarily formed oxygenates are consumed in secondary reactions. A combination of these results were found in this work, where both the smallest and largest crystallite sizes resulted in high oxygenate selectivity, with the mid-range crystallite sizes resulting in the lowest oxygenate selectivity. A full discussion of this and previous result will be given in Section 7.1.3, which gives a full summary of all Fischer-Tropsch results dependent on crystallite size.

7.1.2.5 Branched Product Formation

All previous discussion of product formation results has been concerned with linear products, however small amounts of branched products have also been detected in the product spectrum. Formation of branched products are believed to take place through both primary and secondary reaction pathways, through either a combination of an alkylidene and methyl surface species or through secondary incorporation of α-olefins.

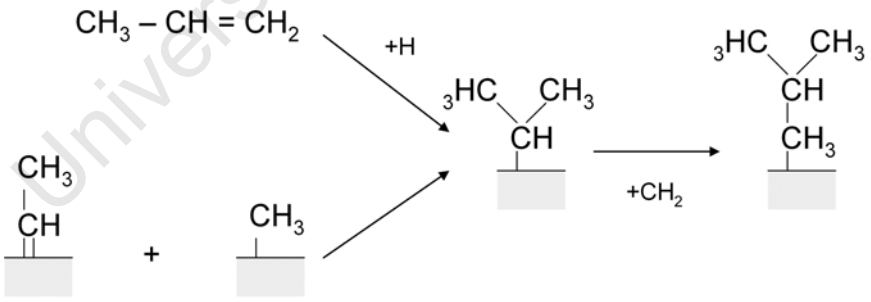

The formation of branched products is thought to be more spatially demanding than linear chain growth, therefore branching reactions are considered to be the ideal probe reaction to investigate spatial constraints on different reaction pathways in Fischer-Tropsch synthesis (Schulz et al. (1994), Schulz et al. (1995)). Figure 7.18 shows the iso to n ratio of products in the C_5 hydrocarbon fraction, considered to be representative of all other carbon fractions. Previous work on iron (Mabaso (2005)) and ruthenium (Welker

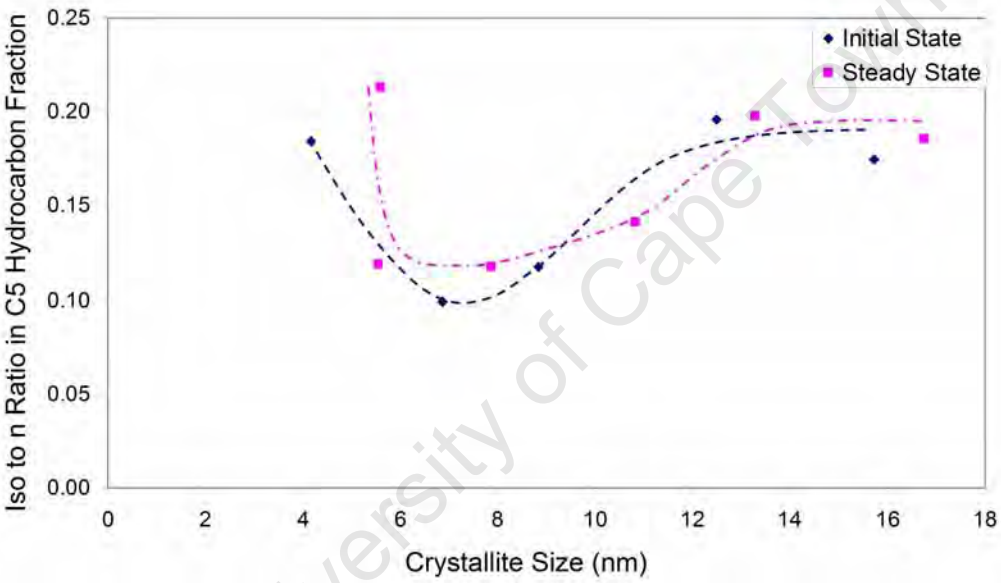

Figure 7.18: Molar ratio of iso(branched) to n(straight) compounds in the C_5 hydrocarbon fraction as a function of crystallite size during both initial state (10 - 20 minutes with reduced crystallite sizes) and steady state (50 - 300 minutes with spent crystallite sizes) on alumina supported model iron catalysts (T = 240 °C, P = 12 bar, $P_{syn-gas}$ = 10 bar, H_2/CO ratio = 2)

(2007)) have shown that there is an increase in branching reactions with a decrease in crystallite size, it was suggested that this was due to secondary reactions occuring preferentially on smaller crystallites. This result was not found in this case, where increased branching was found on the smallest and largest crystallites. This result combined with previous results on olefin isomerisation and oxygenate formation suggests that the reaction pathway for the formation of branched products is a primary reaction.

7.1.3 Summary and Discussion of Results for Fischer-Tropsch Dependency on Crystallite Size

The effect of metal crystallite size on the activity and selectivity of Fischer-Tropsch synthesis was investigated on an unpromoted iron catalyst supported on alumina at reaction conditions of; $T_{reaction}$ = 240 °C, $P_{syn-gas}$ = 10 bar and H_2/CO ratio = 2. Changes of activity and selectivity with respect to crystallite size were largely unaffected throughout the tests. Some sintering was found to occur, predominantly of the smaller crystallites, but sizes remained largely intact and no clear differences in the phase composition of the spent crystallites were found. In terms of activity, a metal surface area specific Fischer-Tropsch rate was calculated, which showed that the rate increases with increasing crystallite size, which corresponds with results from previous studies. However one difference seen here is that the levelling out of the Fischer-Tropsch rate above approximately '7 nm' seen in previous work on iron (Mabaso (2005)) and cobalt (Bezemer et al. (2006)) was not observed.

Methane selectivity was shown to decrease with time on-stream, initial methane selectivities were higher than steady state values. Furthermore, the methane selectivity was shown to increase significantly with decreasing crystallite size. This result coupled with the result that steady state chain growth probability for all six tested catalysts were very similar points to the fact that on a relative basis, there are more methane formation sites on smaller crystallites than on the larger ones. These results, including catalyst characterisation of spent samples suggests that the 'Ensemble Effects Theory'

may be more relevant than the 'Oxidation Theory'. The 'Ensemble Effects Theory' suggests certain ensembles of atoms are required in order for chain growth to occur, while the more simplistic nature of the methanation reaction means that less atoms would be required. Therefore it can be said from the above results that while the required chain growth ensembles are present on the smaller crystallites, there appears to be more methanation sites available resulting in a lower overall Fischer-Tropsch rate as well as a higher methane selectivity. It is however important to note that absolute formation rates of methane also decrease significantly with decrease in crystallite size.

Other selectivity results show that the catalyst samples in the middle size range (7 - 9 nm) show an increased propensity toward secondary reactions. The secondary reactions in this work are considered to occur when readsorption of α-olefins are required such as double bond isomerisation and hydrogenation of the α-olefins. There are two possible explanations for this; an extension of the 'Ensemble Effects' theory or electronic effects between the adsorbate and the metal surface.

It has been considered by previous authors who have done investigations into Fischer-Tropsch product spectrums that secondary reactions are more likely to occur on edge atoms, if this is the case it would be expected that the highest propensity towards secondary reactions would be found on the catalyst samples with the smallest crystallite sizes. However, this was not the case, instead it was found that selectivity towards α-olefins was minimized in the middle crystallite size range, or secondary reactions were maximized respectively. This type of behaviour resulting in a minimum or maximum usually points to two opposing trends. Figure 7.19 shows two possible opposing trends; the first being the frequency of edge atoms and the second being the frequency of flat area atoms available on the metal crystallite. As the size of the crystallite decreases more edge atoms can be found, whereas on larger crystallites the flat area atoms dominate. An extension of the 'Ensemble Effects' theory could be that secondary reactions do in fact occur preferentially on edge atoms as previously suggested, however ensembles of flat area atoms are also required for said secondary reactions to occur. Therefore it is only the crystallite sizes in the middle size range that would feel the effects of both

edge and flat area atoms and as such increase the probability of secondary reactions.

The second possible explanation lies with the electronic effects that occur between the readsorbing α-olefin and the metal surface. The two species interact to form a π-adsorbed complex, and the interaction can be considered to be a classic HOMO-LUMO (Highest Occupied Molecular Orbital - Lowest Unoccupied Molecular Orbital) interaction (van Steen (2008)), where the HOMO of the olefin would interact with the LUMO of the surface (Fermi-level). The strength of the interaction between the olefin and the metal surface depends on the degree of overlap which exists between the HOMO of the olefin and the orbitals closest to the Fermi-level on the metal surface. The strength of the interaction will increase when the energy difference between the HOMO and the Fermi-level decreases. Figure 7.20 shows the absolute energy difference between the HOMO of the olefin and the Fermi-level of the metal (iron) as a function of crystallite size, a minimum can be seen here for C_5 at approximately 3 nm, this is where the strength of the interaction of the olefin and the metal surface would be maximized, and this would explain the increased propensity at the size range for the olefin to readsorb and participate in further reactions. It should however be noted that the functions are extrememly sensitive to the position of the Fermi-level, and for Figure 7.20 the Fermi-level was taken as the reported iron Fermi-level of 4.7 eV.

7.2 Dependence on Water Partial Pressure

Upon the completion of the investigation into the performance of catalysts with different metal crystallite size, a second parameter was varied, that of water partial pressure. This condition was chosen to be varied as a higher water partial pressure simulated conditions at a higher Fischer-Tropsch conversion, therefore conditions potentially conducive to oxidation of the iron crystallites. The Fischer-Tropsch conversion had to be kept below 10% such that the activities and selectivities of the different catalysts could be directly compared, however this meant that no knowledge of how nano-sized crys-

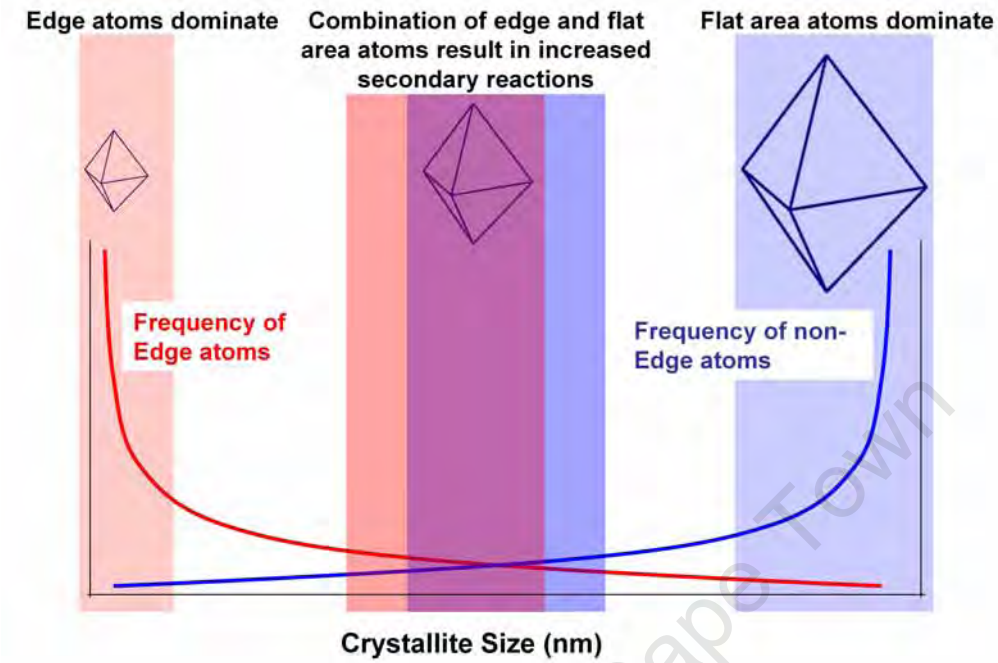

Figure 7.19: Simplified schematic showing the effect of crystallite size on ensembles of atoms available for Fischer-Tropsch synthesis.

tallites would react to conditions of high conversion would be collected. In order to remedy this, conditions of 3 and 6 bar water partial pressure, as realized via water co-feeding, were also tested, with these higher water partial pressure conditions simulating conditions that might be caused by higher Fischer-Tropsch conversion. These experimental runs were conducted in the same u-tubed fixed bed reactor as used previously and the test reported in the previous section can be seen as base case tests with 'no water' in this series. Again an amount of 0.5 g of the catalyst was loaded into the u-tube reactor with 1.2 g of silicon carbide acting as a diluent. The calcined catalyst was reduced *in-situ* in 30 ml/min of pure hydrogen (300 °C for 16 hrs at a heating rate of 1 °C/min). The catalysts were tested at a reaction temperature of 240 °C and a total pressures of either 15 or 18 bar (10 bar of synthesis gas with a hydrogen to carbon monoxide ratio of 2, 2 bar of Argon as a reference gas and 3 or 6 bar water partial pressure respectively). The effect of water partial pressure experiments were run over 5 hours with steady state

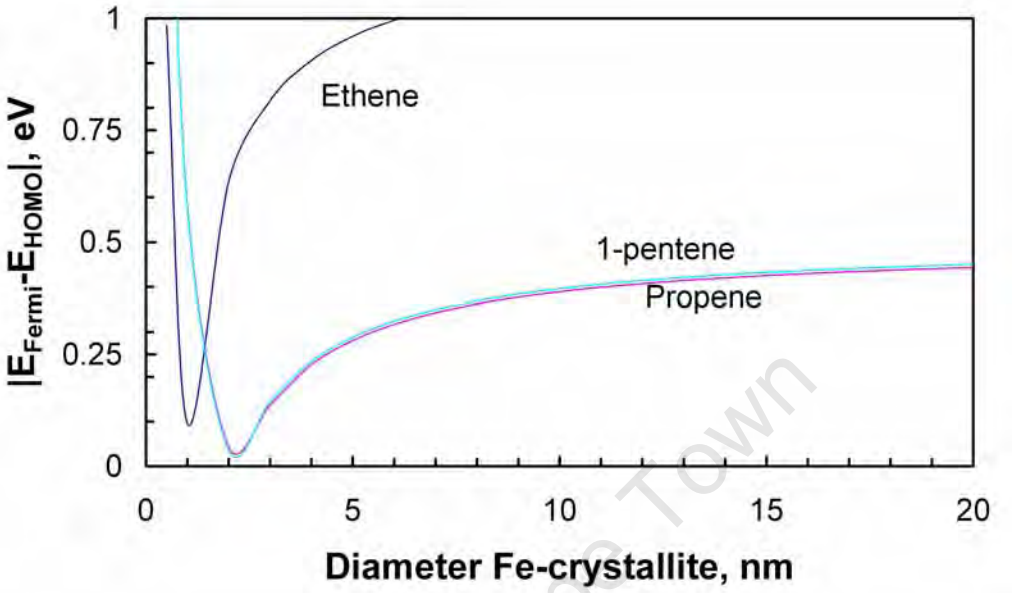

Figure 7.20: Difference between the HOMO energy level of the olefin and the Fermi-level of the metal as a function of the crystallite size (From van Steen (2008)).

being attained at approximately 2 hours.

7.2.1 Fischer-Tropsch Activity and Characterisation of Spent Catalysts

The same definitions and methods of obtaining Fischer-Tropsch activity were used in this part of the experimental method as previously (See Section 7.1.1). Again the data obtained through the FID linked with the methane formation rate obtained on the online TCD, was considered to be more accurate than that of the straight conversion measurement on the TCD. In the presentation of the data on the dependence on water partial pressure, emphasis will be placed on the initial state (10 - 20 minutes) of the experimental run, as at this point there is more confidence on both the crystallite size as well as the iron phase present. As time increases, both crystallite size and phase will change, and at this point it becomes increasingly difficult to separate which

effects are due to which causes.

There was no significant change upon the addition of water in the approach to steady state in terms of Fischer-Tropsch activity. The same trend, shown previously in Section 7.1.1, of no maximum activity reached in the initial stages of the reaction time still holds true here. Furthermore, it can also be shown that the same trend of decreasing crystallite size resulting in a decrease in Fischer-Tropsch rate also remains the same, this is shown in Figures 7.21 for 3 bar water and 7.22 for 6 bar water. While Figures 7.21 and 7.22 only shows three selected catalysts, the trend can be further emphasized by plotting the Fischer-Tropsch rate (initial) against crystallite size, as shown in Figure 7.23. Figure 7.23 shows that upon the addition of 3 bar water there is a large decrease in the Fischer-Tropsch rate, however an addition of 6 bar water from the start of the experimental run does not result in much more of a decrease in comparison to the addition of 3 bar water. This seems to suggest that there is a threshold water partial pressure that exists between no addition of water and 3 bar addition of water past which there is no longer such a large effect. However it should be noted that there are only 3 data points here in terms of the water partial pressure and as such many more data points would have to be collected in order for a trend to truly emerge. It can further be noted that the same observation is made for steady state data regardless of crystallite size and phase change that may have occured.

By looking at the plots for the smallest crystallite sized catalyst ('2 nm') in Figures 7.21 and 7.22, one can see that compared to other, larger crystallite sizes, the '2 nm' catalyst is most prone to permanent deactivation due to the addition of water, and most pronounced at high levels of water addition when almost no activity could be detected for this sample. Similar results have been seen in previous studies on the effect of water addition on Fischer-Tropsch synthesis on iron (Satterfield et al. (1986)) and on cobalt (Li et al. (2002a), Jacobs et al. (2004)). Both Satterfield et al. (1986) and Li et al. (2002a) noted that the addition of water over a long time period would cause the deactivation of the catalyst, and Jacobs et al. (2004) further noted that smaller sized crystallites of cobalt would be more sensitive to permanent deactivation due to water. However the cause of this deactivation

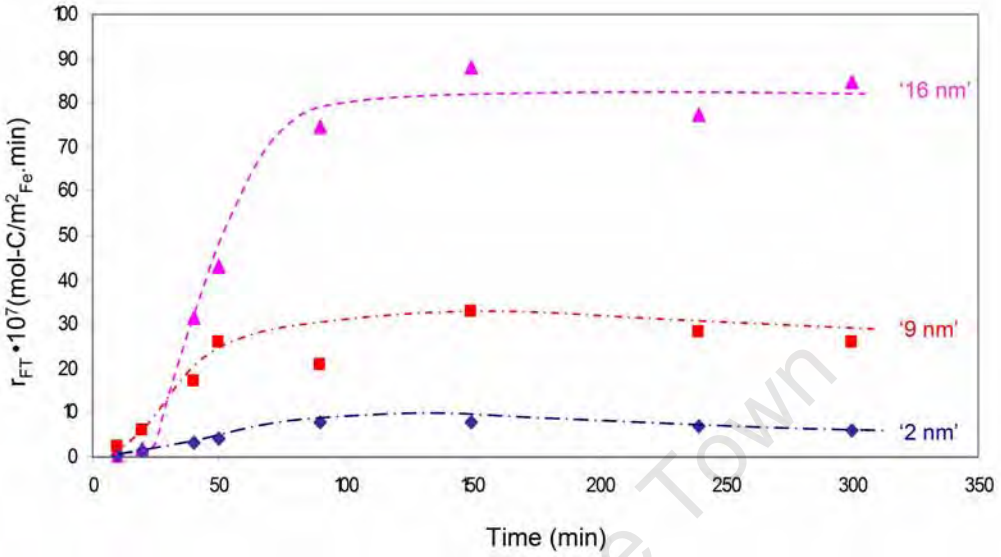

Figure 7.21: Specific Fischer-Tropsch reaction rate as a function of time at initial (reduced) crystallite size for three selected catalysts ('2 nm', '9 nm', '16 nm') (T = 240 °C, P = 15 bar, $P_{syn-gas}$ = 10 bar, P_{water} = 3 bar, H_2/CO ratio = 2)

is unknown, or at this point has not been shown conclusively Satterfield et al. (1986) suggested that the most probable cause of the deactivation would be sintering, though it is just as possible that a change of phase, such as oxidation due to the addition of water would be the cause of such deactivation. Theoretical thermodynamic calculations done on cobalt by van Steen et al. (2005), shows that as water partial pressure increases, the thermodynamically stable phase for small sized crystallites becomes the oxide phase (Figure 2.18). Though this calculation was done on cobalt, it can be expected that a similar trend is true for iron, and iron is known to oxidize fairly easily during Fischer-Tropsch synthesis. In order to gain insight into the reasons behind the deactivation caused by the addition of water, the catalysts were characterized post-run.

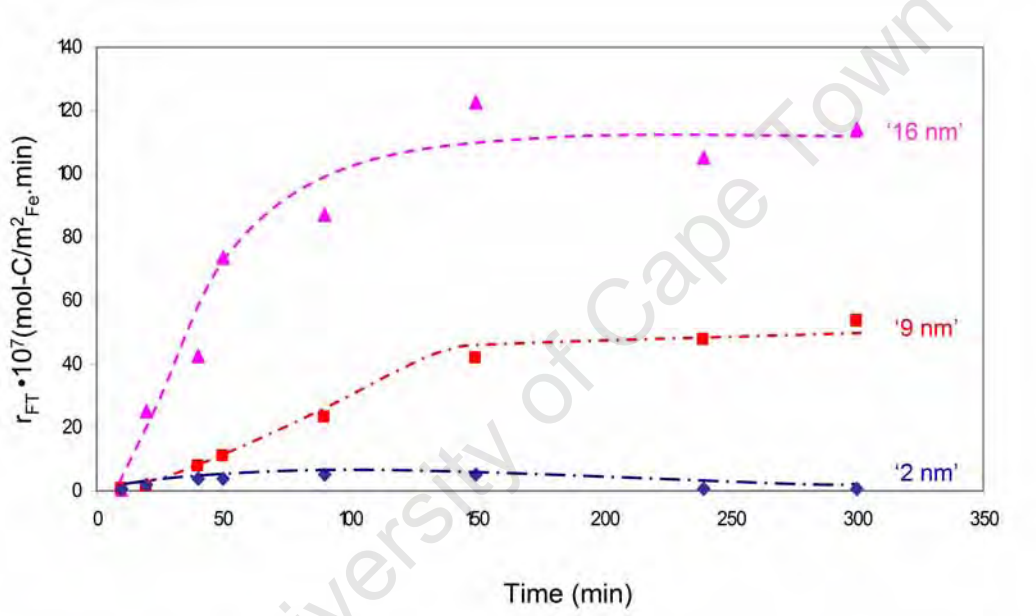

Figure 7.22: Specific Fischer-Tropsch reaction rate as a function of time at initial (reduced) crystallite size for three selected catalysts ('2 nm', '9 nm', '16 nm') (T = 240 °C, P = 18 bar, $P_{syn-gas}$ = 10 bar, P_{water} = 6 bar, H_2/CO ratio = 2)

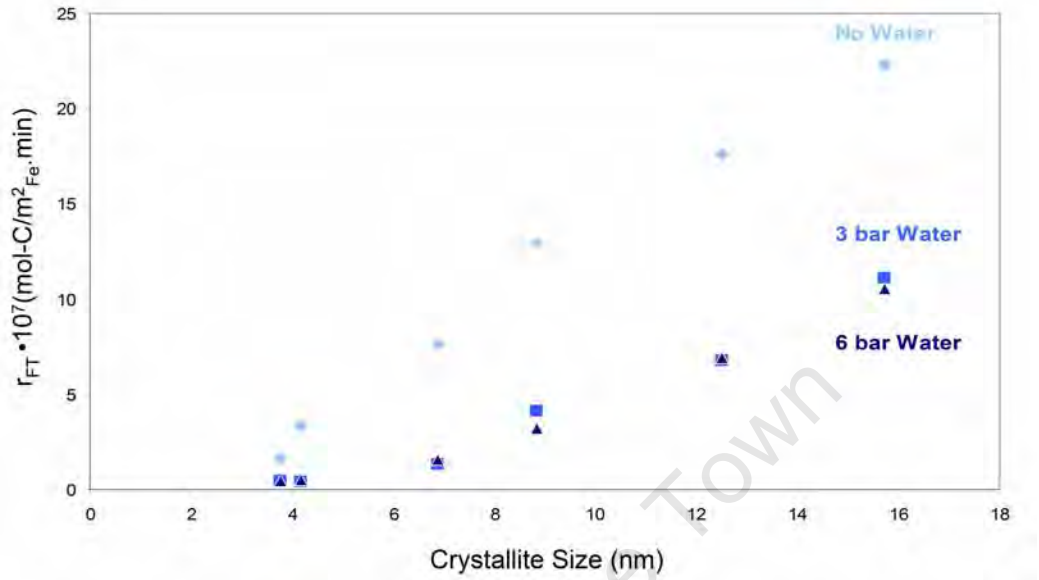

Figure 7.23: Specific Fischer-Tropsch reaction rate as a function of initial crystallite size (T = 240 °C, P = 15 bar, $P_{syn-gas}$ = 10 bar, P_{water} = 3 bar, H_2/CO ratio = 2)

7.2.1.1 Characterisation of Spent Catalysts - Water Series

Upon the completion of the experimental runs done with the addition of water, the catalyst was passivated at room temperature using carbon dioxide, after which the spent catalyst was removed from the reactor system and characterized. The main characterisation methods used were TEM (Transmission Electron Microscopy), XRD (X-Ray Diffraction) and Mössbauer Spectroscopy, crystallite sizes determined by means of TEM characterisation. Table 7.3 shows the average sizes of the catalyst samples at different stages, first, after calcination, then after reduction and finally after the completion of the experimental runs conducted at different water partial pressure levels. It can be seen from Table 7.3 that without the addition of water, there is some growth of the crystallites, which is expected due to the high energy nature of nano-sized crystallites. Therefore, with a decrease in crystallite size, there is an expected increase in the percentage growth of the crystallites, and this was successfully shown in Table 7.2. However, upon the addition of water, there is significantly more growth and clustering, shown numerically in Table

7.4 and pictorially in Figures 7.24 and 7.25.

Figure 7.24 shows the effect that the addition of water has on the crystallite size distribution of the various catalyst samples. This figure combined with the results presented in Table 7.4 shows that with the addition of 3 bar water, there is a significant growth in the size of the crystallites and on addition of 6 bar of water there is slightly a higher increase in size, though not significantly more than what was caused by 3 bar water addition. However, surprisingly the smallest crystallites were not most prone to sintering as suggested previously by Jacobs et al. (2004), it is instead the middle crystallites of '7 nm' and '9 nm' that underwent the highest percentage growth. In fact these two catalyst samples ended up with average crystallite sizes higher than the final sizes of the largest starting crystallite samples ('14 nm' and '16 nm'). This large size increase obtained with crystallites of all sizes does seem to suggest that there is credence in the idea that Satterfield et al. (1986) put forward of sintering being the major cause of deactivation upon the addition of water. Figure 7.25 shows how the sintering might take place on a '14 nm' catalyst sample. It can be seen that upon reduction there are still small crystallites that are well dispersed over the support material, similarly after an experimental run involving no addition of water. However upon addition of water there is en masse movement of the crystallites over the support material resulting in clustering of crystallites and ultimately sintering of smaller crystallites into larger ones. It is these characterisation results showing large increases in the crystallite size that mean the analysis of initial activity and selectivity must gain more importance as in the initial stages there is more confidence on the crystallite size and phase. From these results, it might be suggested that with water addition there is a lessening of the metal-support interaction, resulting in the increased ability of metal crystallites to move over the support material. This lessened interaction might be a result of chemical support surface changes caused by increased water partial pressures.

It is however still possible despite the obvious sintering that phase change could be a contributing factor in the loss of activity, as such XRD and Mössbauer analysis were carried out on the spent samples. The results of 3 catalysts with different crystallite sizes are presented here; the smallest

Table 7.3: Average crystallite sizes and standard deviations (in nm) of calcined, reduced and spent (no water addition, 3 bar water addition, 6 bar water addition) catalyst as determined by means of TEM analysis

Calcined Sample $\bar{d}_{cryst} \pm \sigma$	Reduced Sample $\bar{d}_{cryst} \pm \sigma$	Spent Sample No Water $\bar{d}_{cryst} \pm \sigma$	Spent Sample 3 bar Water $\bar{d}_{cryst} \pm \sigma$	Spent Sample 6 bar Water $\bar{d}_{cryst} \pm \sigma$
2.4 ± 0.8	3.8 ± 1.3	5.6 ± 2.0	8.6 ± 2.3	11.0 ± 3.3
2.7 ± 0.8	4.2 ± 1.0	5.6 ± 1.4	8.2 ± 2.5	11.4 ± 3.3
6.7 ± 1.2	6.9 ± 1.7	7.9 ± 1.8	24.6 ± 3.6	30.0 ± 3.7
7.9 ± 1.4	8.8 ± 1.5	10.8 ± 3.4	25.1 ± 4.6	29.3 ± 4.8
12.0 ± 1.9	12.6 ± 1.8	13.3 ± 2.1	20.0 ± 5.5	22.8 ± 5.7
15.4 ± 1.7	15.7 ± 2.3	16.8 ± 2.6	18.9 ± 4.4	21.6 ± 4.9

Table 7.4: Percentage crystallite growth of spent catalysts from reduced catalysts upon addition of water

Sample	Percentage Growth 'No Water'	Percentage Growth '3 bar Water'	Percentage Growth '6 bar Water'
'2 nm'	33.0%	128.4%	190.2%
'3 nm'	48.5%	96.2%	173.6%
'7 nm'	14.2%	257.5%	334.4%
'9 nm'	22.7%	184.3%	232.0%
'14 nm'	5.6%	58.5%	81.3%
'16 nm'	6.6%	20.2%	37.1%

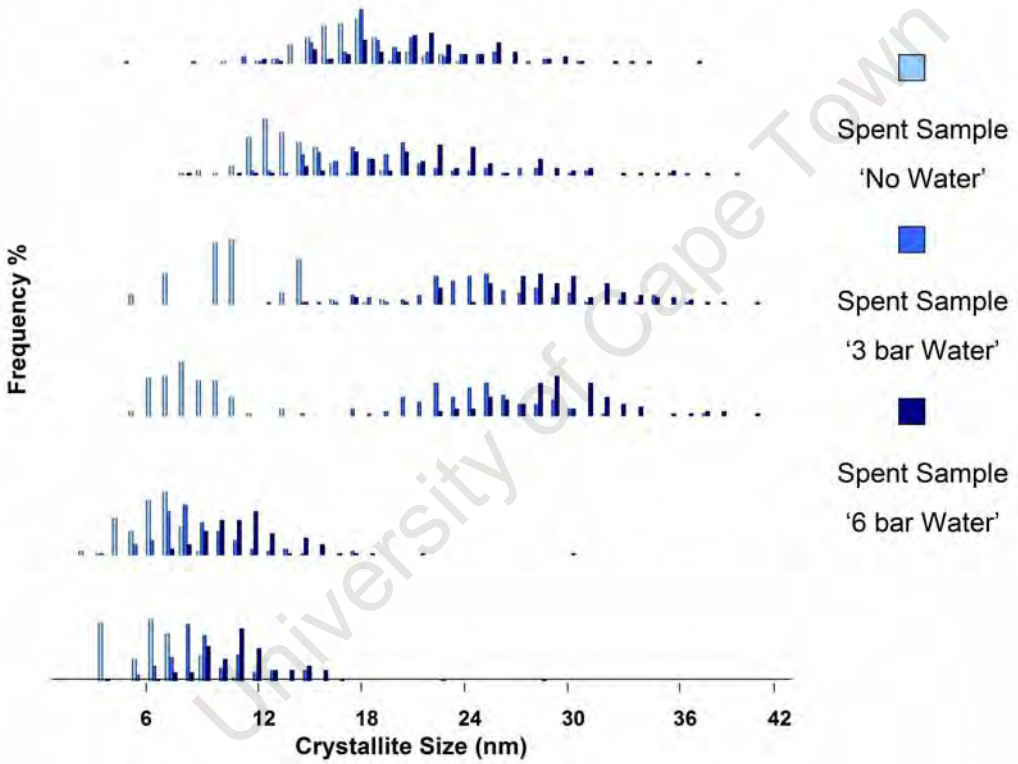

Figure 7.24: Crystallite size distributions of spent samples all six alumina supported model iron catalysts at conditions of no water addition, 3 bar water addition and 6 bar water addition

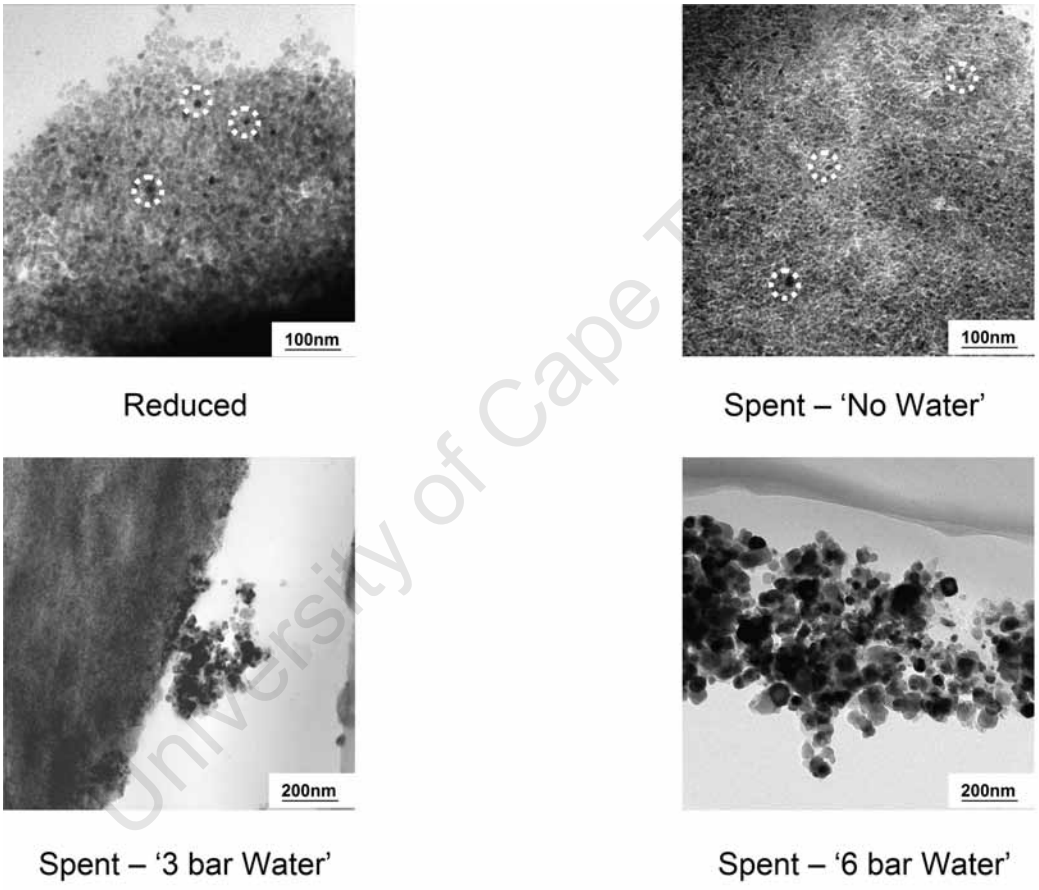

Figure 7.25: TEM micrographs of reduced and spent (no water, 3 bar water and 6 bar water addition) samples of the '14 nm' catalyst

('2 nm'), largest ('16 nm') and one middle ('9 nm') sized sample. Complete results of all 6 different sized samples can be found in Appendix D. The XRD patterns are shown in Figures 7.26, 7.27 and 7.28. The smallest sized crystallite sample is the '2 nm' sample shown in Figure 7.26, with no addition of water there are no readily identifiable iron peaks (all other peaks seen are alumina peaks related to the support), which is the expected result as XRD is not really sensitive enough to crystallite sizes of under approximately 5 nm. However upon the addition of water to the experimental run, one begins to see some different peaks emerging, particularly one at a 2theta position of 50.5°. This peak can be identified as a Hägg Carbide peak (χ-Fe_5C_2). At a water partial pressure of 6 bar, even more peaks emerge, particularly those associated with Magnetite (Fe_3O_4). However, it is important to note that even with the emergence of the magnetite peaks, the hägg carbide peak still remains, leading to the conclusion that the spent sample still contains a combination of both iron carbides and oxides. These XRD results can be combined with the Mössbauer results for the '2 nm' sample which are shown numerically in Table 7.5 and pictorially in Figure 7.29.

Table 7.5 presents the results obtained from Mössbauer Spectroscopy relating to the '2 nm' sample after experimental runs where no water was added, 3 bar water and finally 6 bar water was added. For the 'no water' addition sample, it can be seen that full phase identification was not possible, this is because the sample is superparamagnetic which is due to the crystallite size of the sample being below 8 nm, this can only be resolved by running the Mössbauer analysis under cryogenic conditions. This result corresponds to that obtained from XRD. With 3 bar water addition and an observed increase in crystallite size, the resulting phases are iron carbides and oxides, with 72% of the sample being iron carbides in the form of hägg carbide and cementite (Fe_3C). Again due to some crystallites still being in the superparamagnetic state the phase identification was not fully resolved, though 13% of the sample is expected to be some form of iron oxide, most likely magnetite which was observed in the XRD results. Finally upon the addition of 6 bar water the sample is now expected to be in the form of magnetite (96%), though again the sample is not fully identified and it is expected

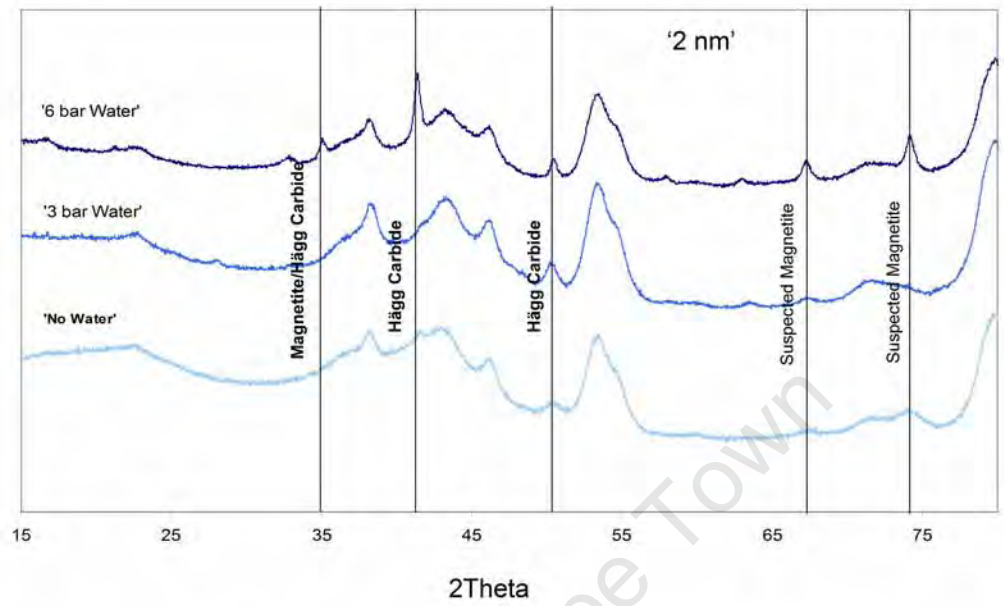

Figure 7.26: Comparison of XRD pattern of '2 nm catalyst at three different water partial pressure conditions (no water *(bottom)*, 3 bar water *(middle)* and 6 bar water *(top)*)(T = 240 °C, $P_{syn-gas}$ = 10 bar, H_2/CO ratio = 2)

that some iron carbide does still exist in the superparamagnetic state. These Mössbauer results do correspond to that found in XRD, however the surprising result here is that there was no en masse phase change into the iron oxide phase upon first addition of 3 bar water, which was the result most expected at the smallest crystallite size, despite this, at a water addition of 3 bar, a decrease of Fischer-Tropsch activity was observed (Figure 7.23). However upon addition of 6 bar water the majority of the catalyst was converted into an oxide phase, this suggests that there is a threshold water partial pressure after which oxidation occurs. The combination of these results suggests that oxidation does not appear to play as large a role in the deactivation of the catalyst as initially expected. Instead, the observed increase in crystallite size (Figure 7.24), or the sintering of the catalyst could be the main cause of deactivation. The role of phase change and size effects as deactivation mechanisms will be discussed in more detail in this section.

With larger crystallite sizes such as the samples with '9 nm' and '16 nm' crystallites, XRD analysis becomes more useful. The results from the XRD

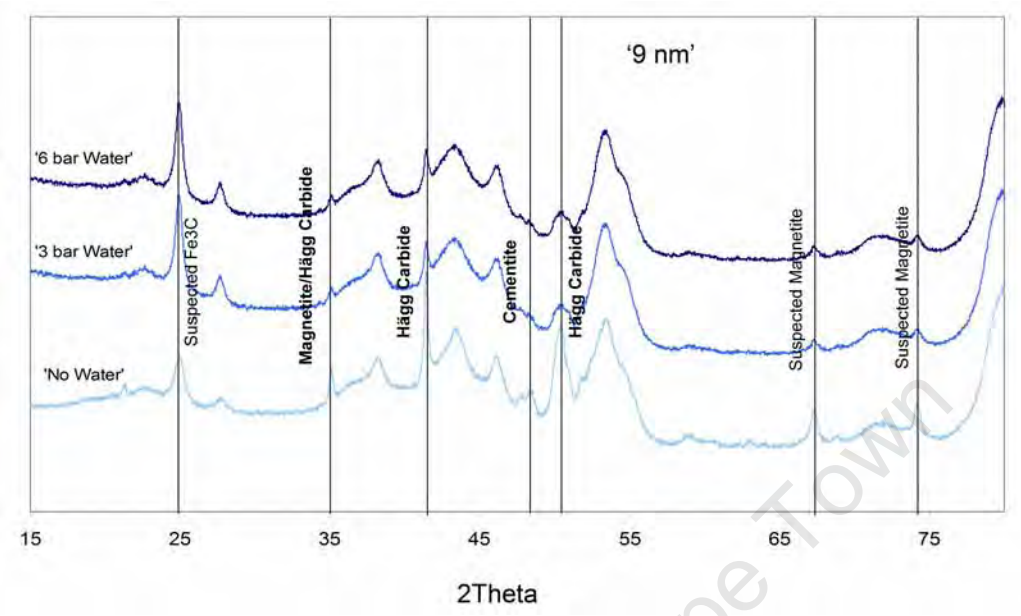

Figure 7.27: Comparison of XRD patterns of '9 nm' catalyst at three different water partial pressure conditions (no water *(bottom)*, 3 bar water *(middle)* and 6 bar water *(top)*) (T = 240 °C, $P_{syn-gas}$ = 10 bar, H_2/CO ratio = 2)

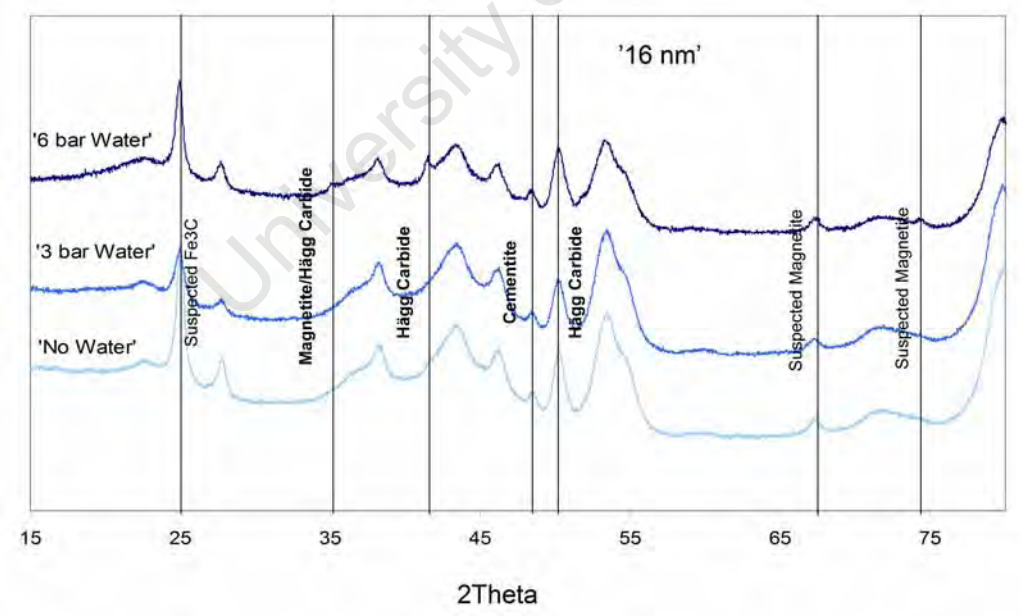

Figure 7.28: Comparison of XRD patterns of '16 nm' catalyst at three different water partial pressure conditions (no water *(bottom)*, 3 bar water *(middle)* and 6 bar water *(top)*),(T = 240 °C, $P_{syn-gas}$ = 10 bar, H_2/CO ratio = 2)

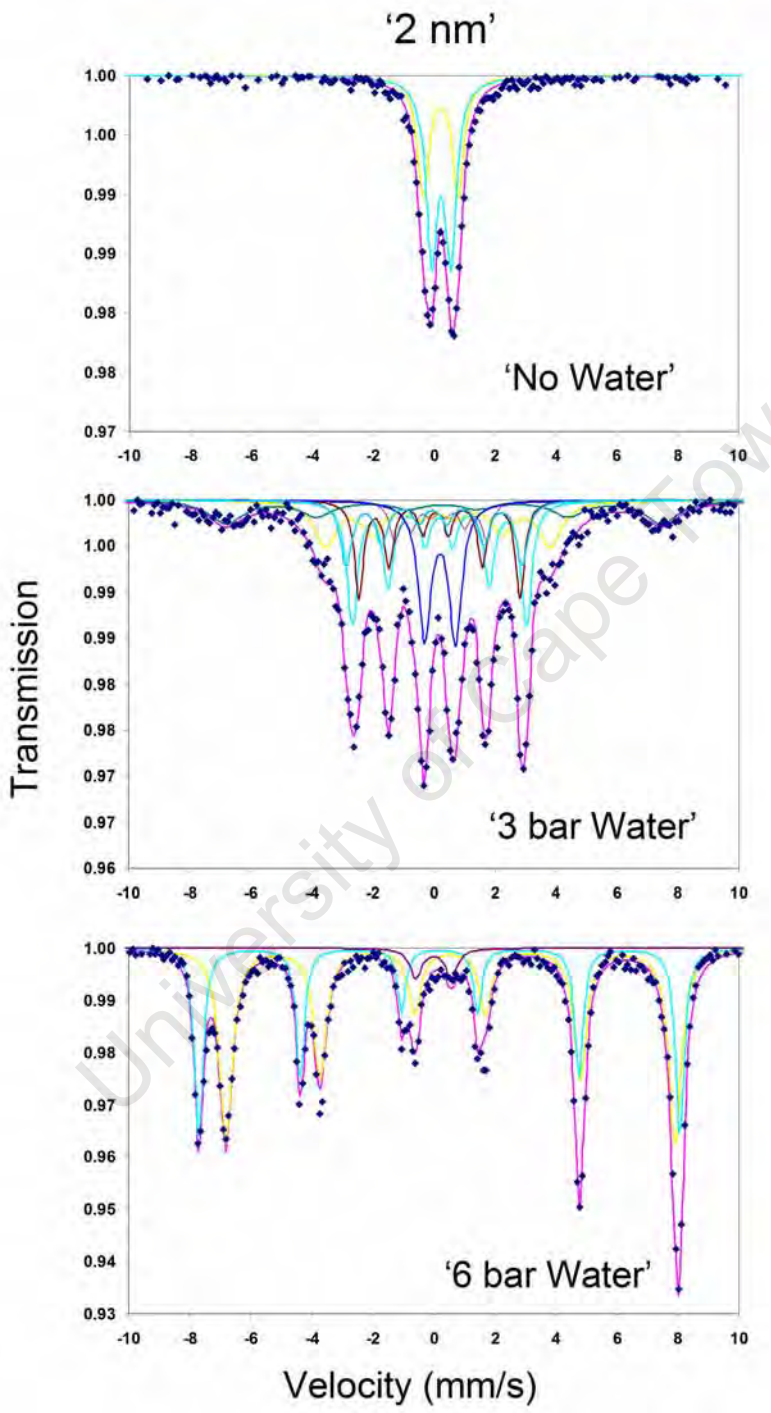

Figure 7.29: Comparison of Mössbauer spectra of '2 nm' catalyst at three different water partial pressure conditions (no water *(top)*, 3 bar water *(middle)* and 6 bar water *(bottom)*) (T = 240 °C, $P_{syn-gas}$ = 10 bar, H_2/CO ratio = 2)

Table 7.5: Hyperfine splitting parameters of '2 nm' catalyst series and phase determination by means of both Mössbauer spectroscopy and XRD analysis

Condition	δ [a] mm/s	Δ mm/s	B_{hf} T	Relative Area %	Identified Iron Phase	XRD Phases
No Water	0.34	1.15	-	41	Fe^{3+}	
	0.36	0.62	-	59	Fe^{3+}	
3 bar Water	0.24	0.02	22.8			
	0.10	0.04	17.9	35	χ-Fe_5C_2	
	0.29	0.08	9.3			
	0.29	0.02	17.7	37	ε-$Fe_{2.2}C$	
	0.24	0.02	16.4			
	0.41	0.05	44.2	13	Fe-oxide	
	0.31	1.01	-	15	Fe-oxide	
6 bar Water	0.65	0.01	45.6	96	Fe_3O_4	χ-Fe_5C_2
	0.30	-0.01	48.9			
	0.10	1.15	-	4	Fe^{3+}	Fe_3O_4

[a]Error: ± 0.02mm/s

for these samples are shown in Figures 7.27 and 7.28. It can be seen in these diffractograms that more iron related peaks are visible, the main peaks identified are those of magnetite, hägg carbide and cementite. In comparing the different water addition conditions to each other, the general trend that can be seen is a decrease in the prominence of the iron carbide peaks as water partial pressure increases, while at the same time the magnetite peaks increase in prominence. These results are then tied to Mössbauer results presented in Tables 7.6 and 7.7 and pictorially in Figures 7.30 and 7.31.

For both the '9 nm' and '16 nm' samples it can be seen that there is very little loss of iron carbides upon the addition of water. In fact for the '16 nm' samples the iron carbide content remains largely unchanged; for an increasing water partial pressure the iron carbide content decreases from 80% for no water addition to 79% for 3 bar water addition and finally to 78% for 6 bar water addition. The trends of the 9 nm samples are not as clear, due to the fact that the sample exposed to 3 bar water addition was not fully identified with as much as 50% of the sample in the superparamagnetic

phase, however if this part of the sample is assumed to be iron carbide, then the trend is a slight decrease in percentage iron carbides as water increases of; 64% to 60% to 57%. As iron carbides are the expected active phases in iron based Fischer-Tropsch synthesis it can be said that oxidation cannot be the overriding factor for any changes of activity upon the addition of water.

Table 7.8 shows crystallite sizes and iron carbide content with varying water co-feed. This data is used to calculate the Fischer-Tropsch rate per surface area of carbides, assuming that the carbides are the active phases in Fischer-Tropsch synthesis. This calculation in undertaken to try and separate the effects of sintering and oxidation on overall deactivation. The results of this calculation are shown in Figure 7.32. The Fischer-Tropsch rate per surface are of carbides is calculated on the spent catalyst size determined from TEM, assuming that TEM sizing is representative of the carbide phase, however in Figure 7.32 these results are plotted against the expected sample sizes, to give a clearer picture of deactivation, as the initial middle sized crystallites ('7 nm' and '9 nm') underwent severe sintering to result in larger spent crystallites than the largest initial sizes ('14 nm' and '16 nm'). Figure 7.32 can be compared against Figure 7.23 which showed a decrease of rate as water co-feed increases. In contrast, Figure 7.32 shows that the smallest ('2 nm' and '3 nm') and middle ('7 nm' and '9 nm') crystallites undergo loss of rate, however the largest crystallites do not. These larger crystallites do not undergo severe sintering even under conditions of 6 bar water addition, and it is shown by Mössbauer spectroscopy that the percentage of carbides in the spent samples also does not change. However, the cause of deactivation in the smallest and middle crystallites may be different. For the middle crystallites, it is shown that the carbide content does not change significantly, however, severe sintering occurs, therefore it can be assumed that the deactivation is due to sintering. However in the smallest crystallites, both oxidation and sintering occurs, and it is impossible to decide which is the major cause of deactivation, though for these smallest crystallites oxidation is much more of a factor, as oxides are the thermodynamically more stable phase at these small crystallites.

The characterisation of the spent samples combined with the result pre-

sented in Figure 7.23 shows that for the loss of activity resulting from the addition of 3 bar water, the overriding cause must be due to agglomeration and sintering of the metal crystallites as suggested by Satterfield et al. (1986), rather than the expected oxidation theory put forward by van Steen et al. (2005).

7.2.2 Product Formation

Products formed during Fischer-Tropsch testing at the base case conditions of 240 °C and 12 bar (10 bar syn-gas, $H_2/CO = 2$) were analyzed using a combination of online TCD detection and offline FID detection using the ampoule method. Detailed results of activity and selectivity of catalysts of varying crystallite sizes can be found in Appendix D, these results are separated into two categories; initial state (10 - 20 minutes) and steady state (50 - 300 minutes)[2]. For a complete description of methods used in determining product formation, please see Section 7.1.2. Although mostly both initial and steady state data are given, emphasis is placed on initial selectivity where initial crystallite sizes should still be largely intact.

7.2.2.1 Carbon Dioxide Formation

It is well known that the undesired formation of carbon dioxide (CO_2) as a by-product in iron based Fischer-Tropsch synthesis is unavoidable. Carbon dioxide is formed through the water-gas shift reaction (Equation 2.2), which is seen as a consecutive reaction to the Fischer-Tropsch reaction where product water reacts with carbon monoxide to form carbon dioxide and hydrogen gas. It has been previously suspected that the water-gas shift is catalyzed by the oxide form of iron (magnetite) during Fischer-Tropsch synthesis, however it has also been stated by Satterfield et al. (1986) that: "The nature of the active form of an iron catalyst for the water-gas shift is still speculative and much of the evidence is circumstantial." In fact in the work done by Satterfield et al. (1986) on the effect of water on iron based Fischer-Tropsch

[2]All values are averaged values for 10 to 20 minutes and 50 to 300 minutes, any obvious outliers have been ignored during calculations

Table 7.6: Hyperfine splitting parameters of '9 nm' catalyst series and phase determination by means of both Mössbauer spectroscopy and XRD analysis

Condition	δ [a] mm/s	Δ mm/s	B_{hf} T	Relative Area %	Identified Iron Phase	XRD Phases
No Water	0.27	0.02	21.1	50	χ-Fe_5C_2	Fe_3O_4 χ-Fe_5C_2 ε-$Fe_{2.2}C$ Fe_3C
	0.22	0.02	18.2			
	0.19	0.08	11.8			
	0.26	0.02	15.2	14	ε-$Fe_{2.2}C$	
	0.26	0.02	16.8			
	0.33	0.05	49.2	18	Fe_3O_4	
	0.64	-0.03	45.8			
	0.32	1.01	-	16	Fe^{3+}	
	0.13	-0.14	33.5	2	Fe^{3+}	
3 bar Water	0.69	-0.04	45.5	41	Fe_3O_4	Fe_3O_4 χ-Fe_5C_2 ε-$Fe_{2.2}C$ Fe_3C
	0.33	-0.01	49.0			
	0.24	0.06	17.7	10	ε-$Fe_{2.2}C$	
	0.35	0.78	-	50	Fe^{3+}	
6 bar Water	0.24	0.02	21.9	31	χ-Fe_5C_2	Fe_3O_4 χ-Fe_5C_2 ε-$Fe_{2.2}C$ Fe_3C
	0.11	0.02	18.8			
	0.26	0.08	11.0			
	0.23	0.07	17.7	26	ε-$Fe_{2.2}C$	
	0.31	-0.01	48.7	24	Fe_3O_4	
	0.64	0.00	45.7			
	0.31	-0.05	50.9	5	γ-Fe_2O_3	
	0.37	0.02	36.0	1	Fe Oxide	
	0.30	0.96	-	13	Fe Carbide	

[a]Error: ± 0.02mm/s

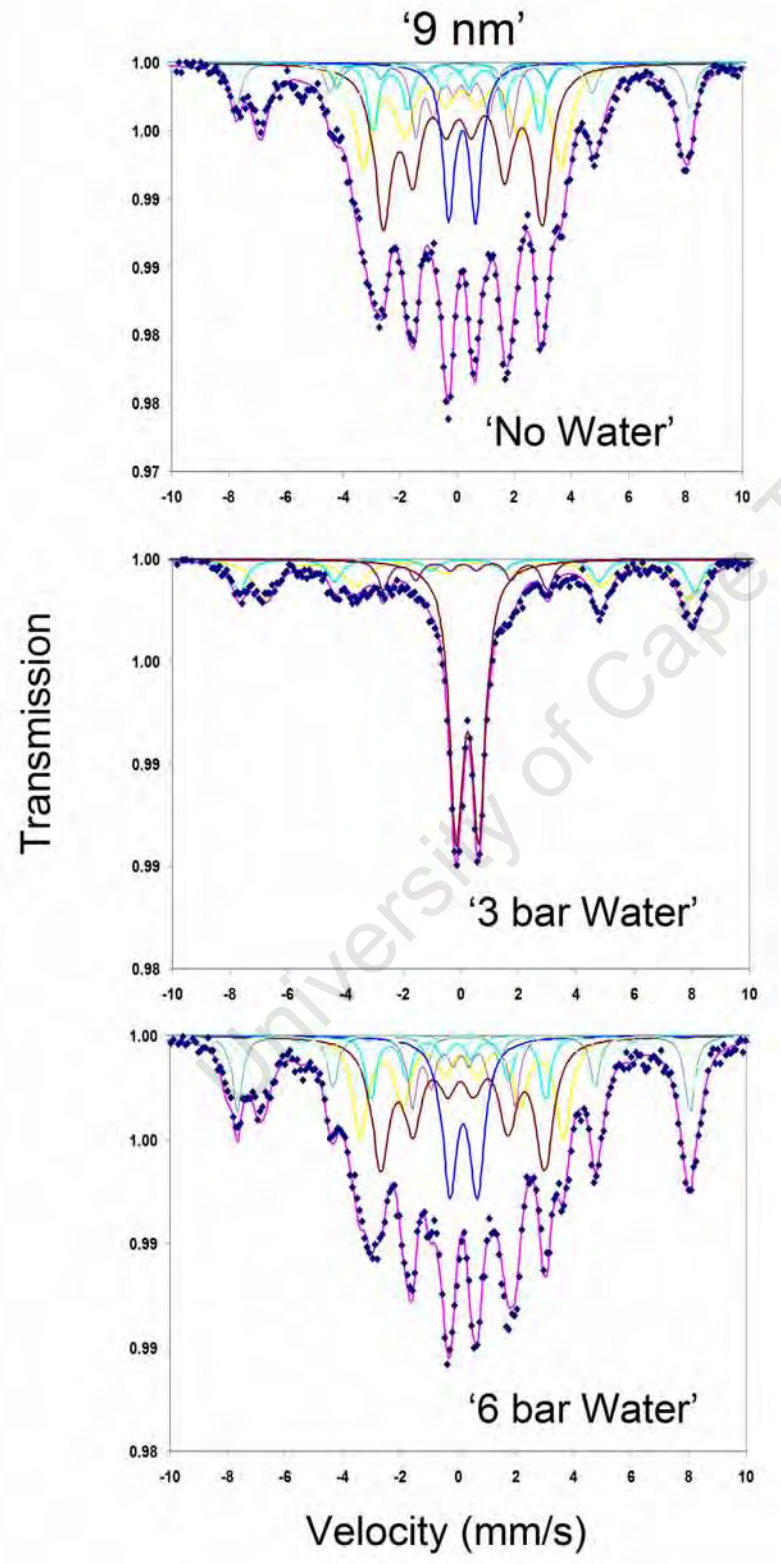

Figure 7.30: Comparison of Mössbauer spectra of '9 nm' catalyst at three different water partial pressure conditions (no water *(top)*, 3 bar water *(middle)* and 6 bar water *(bottom)*) (T = 240 °C, $P_{syn-gas}$ = 10 bar, H_2/CO ratio = 2)

Table 7.7: Hyperfine splitting parameters of '16 nm' catalyst series and phase determination by means of both Mössbauer spectroscopy and XRD analysis

Condition	δ [a] mm/s	Δ mm/s	B_{hf} T	Relative Area %	Identified Iron Phase	XRD Phases
No Water	0.24	0.02	21.7			
	0.10	0.02	18.5	40	χ-Fe_5C_2	Fe_3O_4
	0.39	0.08	9.7			χ-Fe_5C_2
	0.23	0.08	16.5	34	ε-$Fe_{2.2}C$	ε-$Fe_{2.2}C$
	0.30	0.05	47.5	3	Fe Oxide	Fe_3C
	0.33	0.99	-	17	Fe^{3+}	
	0.25	0.02	17.7	6	ε-$Fe_{2.2}C$	
3 bar Water	0.25	0.02	22.0			
	0.20	0.02	18.6	29	χ-Fe_5C_2	Fe_3O_4
	0.43	0.08	10.1			χ-Fe_5C_2
	0.30	0.23	16.7	50	ε-$Fe_{2.2}C$	ε-$Fe_{2.2}C$
	0.22	0.02	17.0			Fe_3C
	0.34	0.99	-	18	Fe Carbide	
	0.36	0.05	49.0	2	Fe Oxide	
6 bar Water	0.24	0.02	21.3			
	0.19	0.02	18.2	48	χ-Fe_5C_2	Fe_3O_4
	0.40	0.08	10.0			χ-Fe_5C_2
	0.23	0.09	16.8	30	ε-$Fe_{2.2}C$	ε-$Fe_{2.2}C$
	0.33	0.96	-	13	Fe Carbide	Fe_3C
	0.35	0.04	49.1	9	Fe_3O_4	
	0.55	0.00	45.4			

[a]Error: $\pm$ 0.02mm/s

Table 7.8: Spent catalyst characterisation by Mössbauer Spectroscopy - Total carbide content with varying water co-feed

Sample	'No Water'		'3 bar Water'		'6 bar Water'	
	$\bar{d}_{cryst}$	Carbide %	$\bar{d}_{cryst}$	Carbide %	$\bar{d}_{cryst}$	Carbide %
'2 nm'	5.6	-	8.6	72%	10.9	'4'%
'9 nm'	10.8	64%	25.1	60%	29.3	57%
'16 nm'	16.8	80%	18.9	79%	21.6	78%

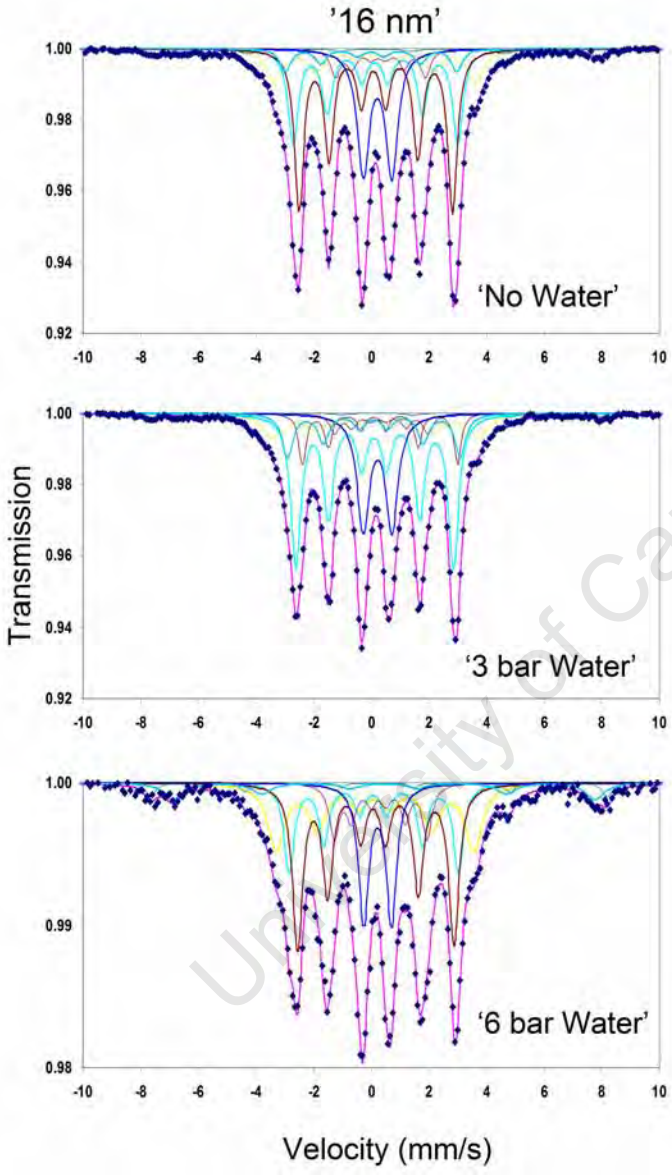

Figure 7.31: Comparison of Mössbauer spectra of '16 nm' catalyst at three different water partial pressure conditions (no water *(top)*, 3 bar water *(middle)* and 6 bar water *(bottom)*) (T = 240 °C, $P_{syn-gas}$ = 10 bar, H_2/CO ratio = 2)

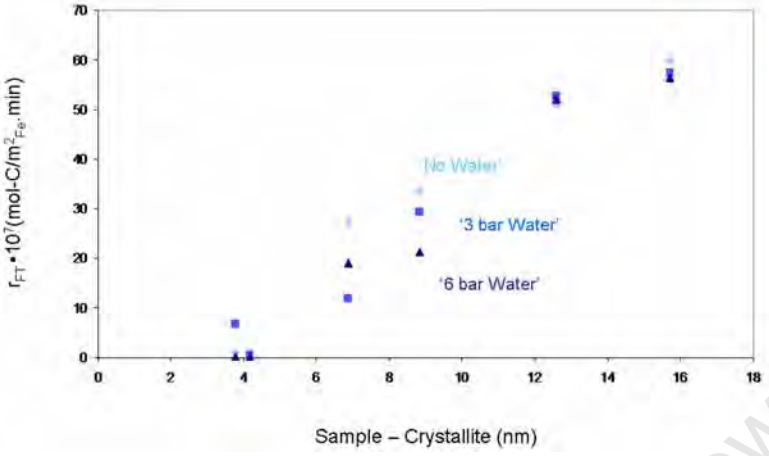

Figure 7.32: Specific Fischer Tropsch reaction rate as a function of initial crystallite size of all six alumina supported model iron catalysts at varying water partial pressures (no water addition, 3 bar water addition, 6 bar water addition) (T = 240 °C, $P_{syn-gas}$ = 10 bar, H_2/CO ratio = 2)

synthesis, results show that there is no correlation between the carbon dioxide selectivity and the amount of magnetite found in the catalyst. As such the conclusion drawn would be that any increase in carbon dioxide selectivity due to an increase in water partial pressure would be entirely kinetically based.

In the previous chapter, results presented in Section 7.1.2.1 showed that there was no clear trend regarding the crystallite size and the selectivity of carbon dioxide. This statement still holds true despite the addition of water. Figure 7.33 shows the change in carbon dioxide selectivity as a function of time for 3 selected catalysts of varying crystallite size at a condition of '3 bar' additional water partial pressure. Based on the assumption that magnetite is the active phase for iron-based Fischer-Tropsch synthesis and that smaller crystallites would be preferentially oxidized, it should be expected that the smallest crystallite sized sample would result in the highest selectivity of carbon dioxide. However, this is not the case, and as such a definitive conclusion can be reached that there exists no correlation between crystallite size and carbon dioxide selectivity.

Finally, Figure 7.34 shows the change in carbon dioxide selectivity as a

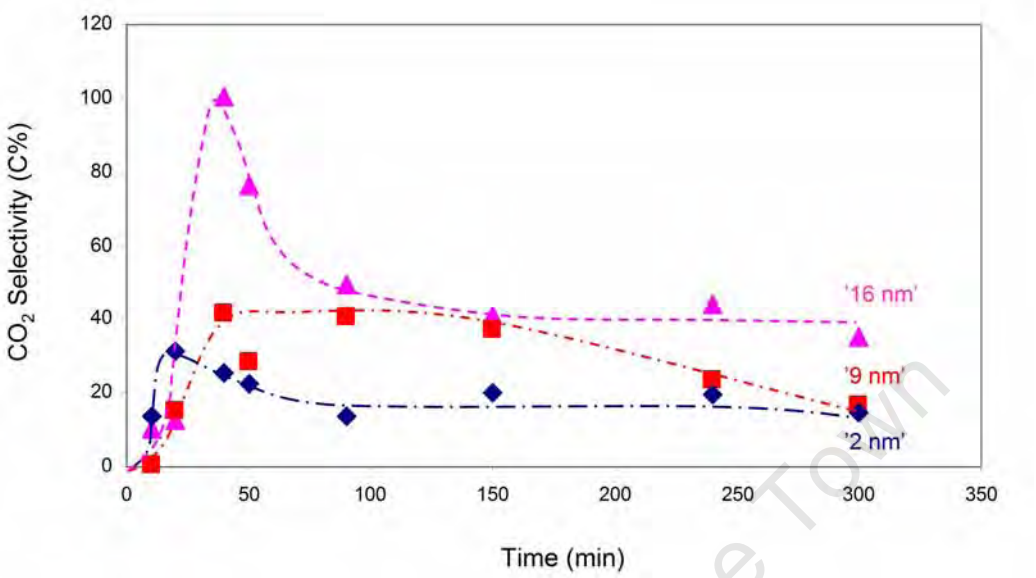

Figure 7.33: Carbon dioxide selectivity as a function of time of three selected catalysts ('2 nm', '9 nm', '16 nm') (T = 240 °C, P = 15 bar, $P_{syn-gas}$ = 10 bar, P_{water} = 3 bar, H_2/CO ratio = 2)

function of time at increasing water partial pressures for a 9 nm catalyst. It is expected that that an increase in the water partial pressure will result in increased carbon dioxide selectivity. This is shown in Figure 7.34, with the samples exposed to additional water showing an increased carbon dioxide selectivity in comparison to the sample with no water addition. However, based on previous characterisation results done on the 9 nm catalyst it can be said that this change is more likely due to kinetic effects rather than oxidation of iron carbide into iron oxide. It is interesting to note that while at steady state similar carbon dioxide selectivities were found, at initial stages of testing large differences of carbon dioxide selectivity are observed with enhanced selectivity at high water levels.

7.2.2.2 Methane Formation and Chain Growth Probability

Methane is the most abundant product in Fischer-Tropsch synthesis, however it is the product with the lowest commercial value, therefore it is important for a good Fischer-Tropsch catalyst to inhibit the formation of methane.

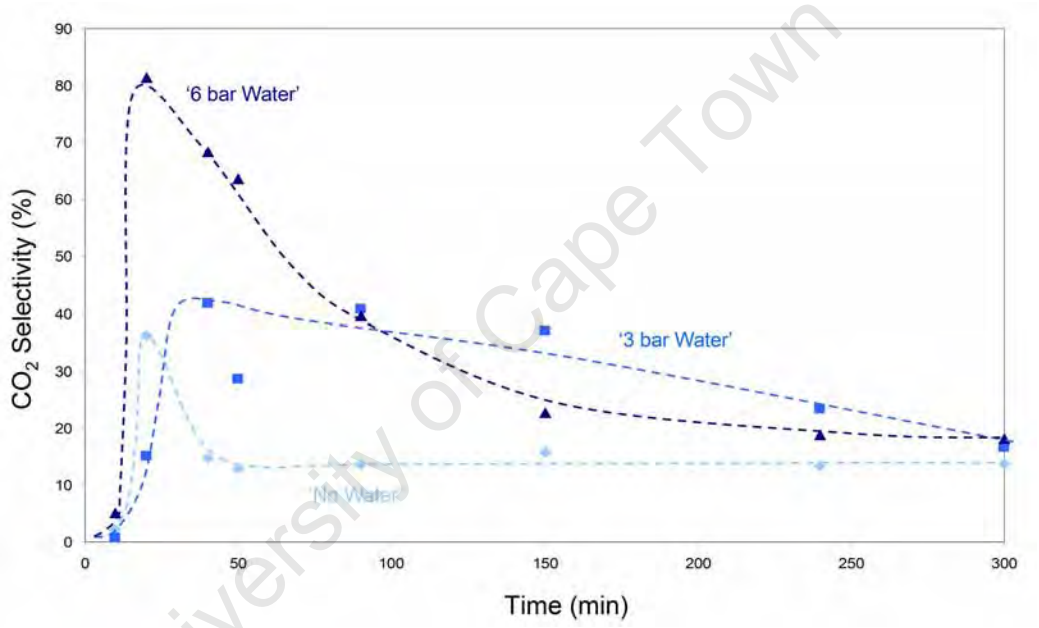

Figure 7.34: Carbon dioxide selectivity as a function of time of '9 nm' alumina supported model iron catalysts at 3 different conditions of water addition (no water addition, 3 bar water addition, 6 bar water addition) (T = 240 °C, $P_{syn-gas}$ = 10 bar, H_2/CO ratio = 2)

However, this is not an easy process as methane is the most thermodynamically stable product under normal Fischer-Tropsch synthesis conditions.

The trend of increasing methane selectivity with decreasing crystallite size has been found in this work, for base case conditions, and by other previous work on iron by Mabaso (2005). This trend has also been reported by Ojeda et al. (2004) on rhodium, Bezemer et al. (2006) on cobalt and Welker (2007) on ruthenium. However, upon the addition of water this trend no longer holds true with this study. Figures 7.35 and 7.36 show the effect of water addition on methane selectivity as a function of (initial) crystallite size at initial and steady state conditions respectively. There is a general trend which exists between water addition and methane selectivity, where upon the addition of water the methane selectivity is decreased. This result has also been shown for iron (Satterfield et al. (1986)), Schulz et al. (1997), cobalt (Li et al. (2002a)) and ruthenium (Claeys and van Steen (2002)). However, with respect to crystallite size, a rather surprising result is obtained, where the addition of water partial pressure has the greatest effect on the smallest particle sizes, resulting in a loss of the linear trend of increasing methane selectivity with decreasing crystallite size. In fact the water addition has such a strong effect on the smallest crystallites, or indeed the crystallites that exist in the superparamagnetic state that at both initial and steady state the initially smallest crystallites have now got the lowest methane selectivity. Once past these small, superparamagnetic crystallites, the linear trend is once again established. It is unclear why exactly water has such a marked effect on the small crystallites, but one possible explanation is the ability of water to inhibit product desorption leading to increased chain growth. As discussed earlier, the 'Ensemble Effects' theory could explain why methane is the predominant product for smaller, nano-sized crystallites. Therefore when water is added, the C_1 intermediates are inhibited from desorbing leading to a marked decrease in the methane selectivity in the smallest crystallite sizes.

Figures 7.37 and 7.38 show the effect water addition has on the chain growth probability at initial (10 - 20 minutes) and steady state (50 - 300 minutes) respectively. It can be seen that upon the addition of water during the initial stage of the experimental run, the general trend is an increase in the

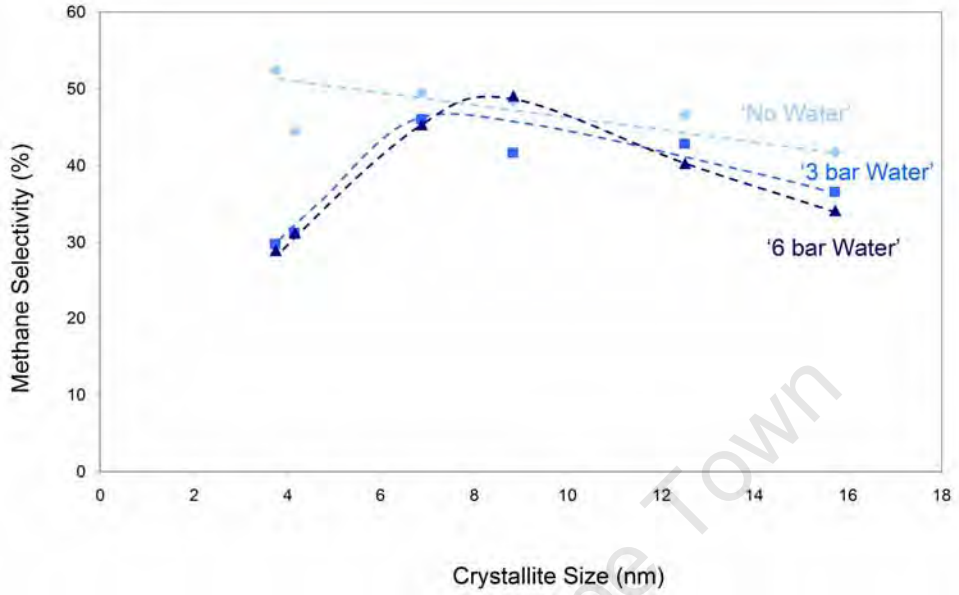

Figure 7.35: Methane selectivity as a function of crystallite size at initial state (10 - 20 min) for all six alumina supported model catalysts at varying water addition conditions (no water addition, 3 bar water addition, 6 bar water addition) (T = 240 °C, $P_{syn-gas}$ = 10 bar, H_2/CO ratio = 2)

chain growth probability. This is the expected result as it has been previously hypothesized that the addition of water would lead to the inhibition of the desorption step, therefore promoting chain growth (Schulz et al. (1997)). However, once steady state is reached, water addition does not seem to have any effect on the final chain growth probability.

7.2.2.3 Olefin Formation

As described previously in Section 7.1.2.3, linear α-olefins and paraffins are the main primary products of Fischer-Tropsch synthesis. However, at reaction conditions α-olefins can re-absorb onto the catalyst surface and undergo further reaction such as hydrogenation or double bond isomerisation, these reactions are classified as secondary reactions (Schulz and Claeys (1999a)). It has been shown in the previous Chapter (Section 7.1.2.3) that there isn't a linear relationship in terms of degree of secondary reactions undergone with respect to crystallite size. This trend still holds true with addition of water.

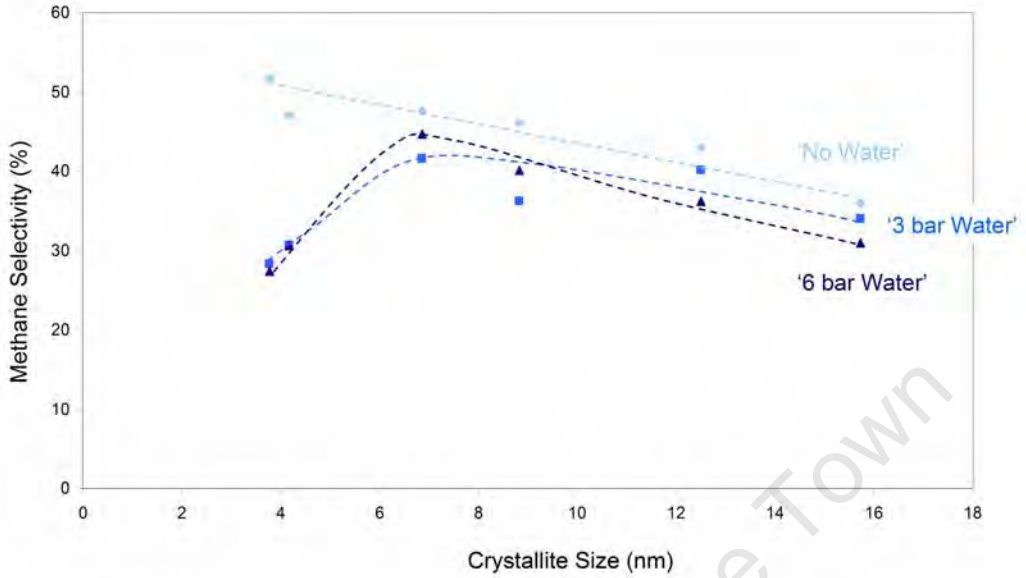

Figure 7.36: Methane selectivity as a function of crystallite size at steady state (50 - 300 min) for all six alumina supported model catalysts at varying water addition conditions (no water addition, 3 bar water addition, 6 bar water addition) (T = 240 °C, $P_{syn-gas}$ = 10 bar, H_2/CO ratio = 2)

However, for each individual crystallite size, the addition of water results in an increase in the overall olefin content, this is shown in Figures 7.39, 7.40 and 7.41 for the C_2 fraction as a function of time as shown for 3 selected catalysts. This same result has been found previously for iron (Dry (1981), Satterfield et al. (1986)), cobalt (Schulz et al. (1997), Li et al. (2002a)) and ruthenium (Claeys and van Steen (2002)). For complete results for all 6 catalysts please see Appendix D and Figures D.10, D.11 and D.12 for the effect on the C_3 fraction as well as the carbon number dependency of the molar olefin contents. In the C_2 fraction it can be seen that with an addition of 3 bar water there is a marked increase in the olefin content across all crystallite sizes tested, however, upon the addition of 6 bar water there is also an increase in the olefin to paraffin ratio, however not as much as that induced by the addition of 3 bar water. As mentioned previously, this could point to the existence of an optimal water partial pressure, where the production of methane is minimized and olefins maximized. This increase in

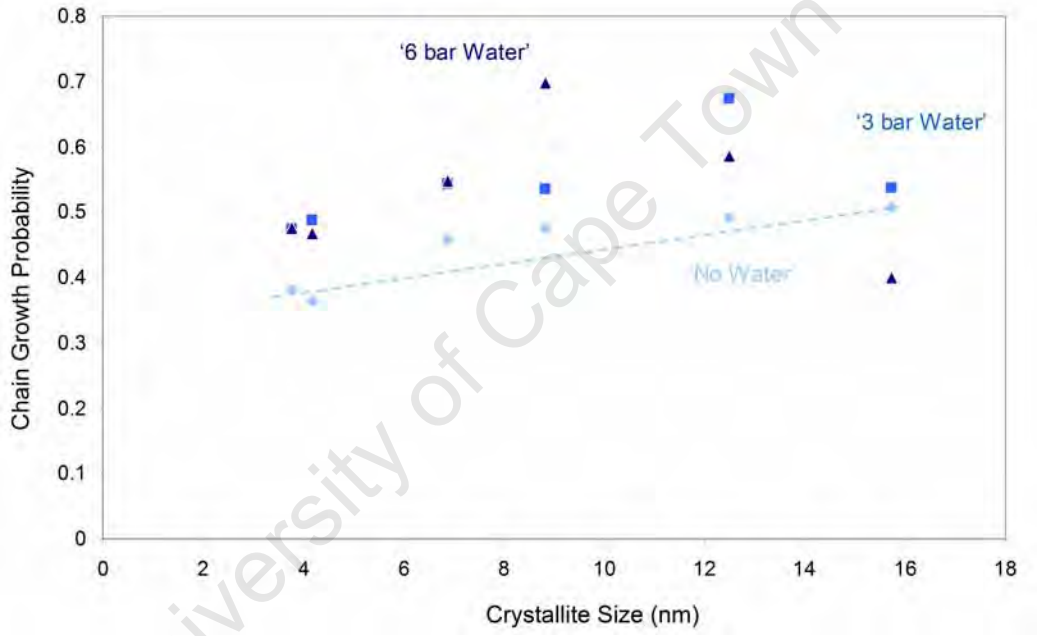

Figure 7.37: Chain growth probability as a function of crystallite size at initial state (10 - 20 min) for all six alumina supported model catalysts at varying water addition conditions (no water addition, 3 bar water addition, 6 bar water addition) (T = 240 °C, $P_{syn-gas}$ = 10 bar, H_2/CO ratio = 2)

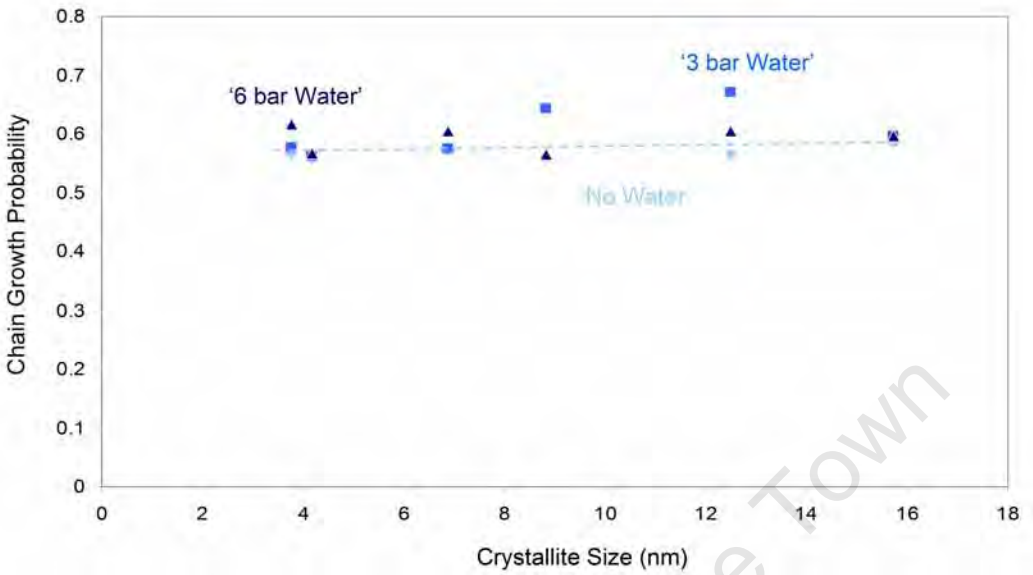

Figure 7.38: Chain growth probability as a function of crystallite size at steady state (50 - 300 min) for all six alumina supported model catalysts at varying water addition conditions (no water addition, 3 bar water addition, 6 bar water addition) (T = 240 °C, $P_{syn-gas}$ = 10 bar, H_2/CO ratio = 2)

the olefin to paraffin ratio can be attributed to the suppression of secondary reactions (Satterfield et al. (1986), Schulz et al. (1997), Claeys and van Steen (2002)).

For primary olefin selectivity in Fischer-Tropsch synthesis, a 70 - 90 mol-% content of olefins in linear hydrocarbons and more than 90 mol-% α-olefins in linear olefins are expected. Figures 7.42 and 7.43 show these percentages with respect to crystallite size of the C_5 fraction at initial stages of Fischer-Tropsch testing. Both of these figures show that upon the addition of water, there is a shift towards primary selectivity due to the inhibition of the readsorption of α-olefins. Schulz et al. (1997) suggested that the changes in selectivity observed due to variations in the water partial pressure can be attributed to inhibition of individual reaction routes by water, for example, inhibition of product desorption and olefin readsorption. However the mechanism by which these inhibitions may take place are still unknown.

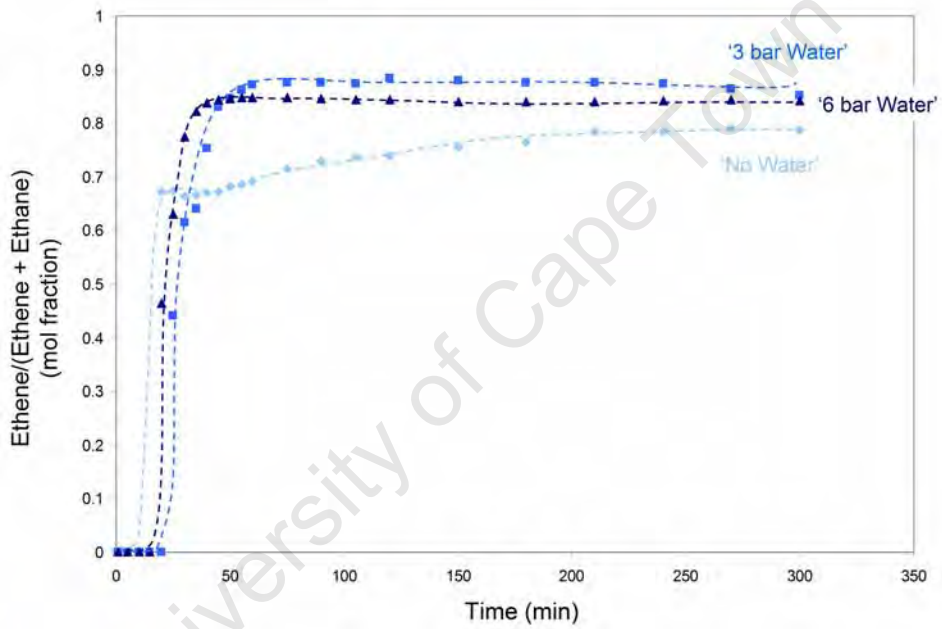

Figure 7.39: Molar olefin content of the C_2 fraction as a function of time of the '2 nm' catalyst at varying water partial pressure conditions (no water addition, 3 bar water addition, 6 bar water addition) (T = 240 °C, $P_{syn-gas}$ = 10 bar, H_2/CO ratio = 2)

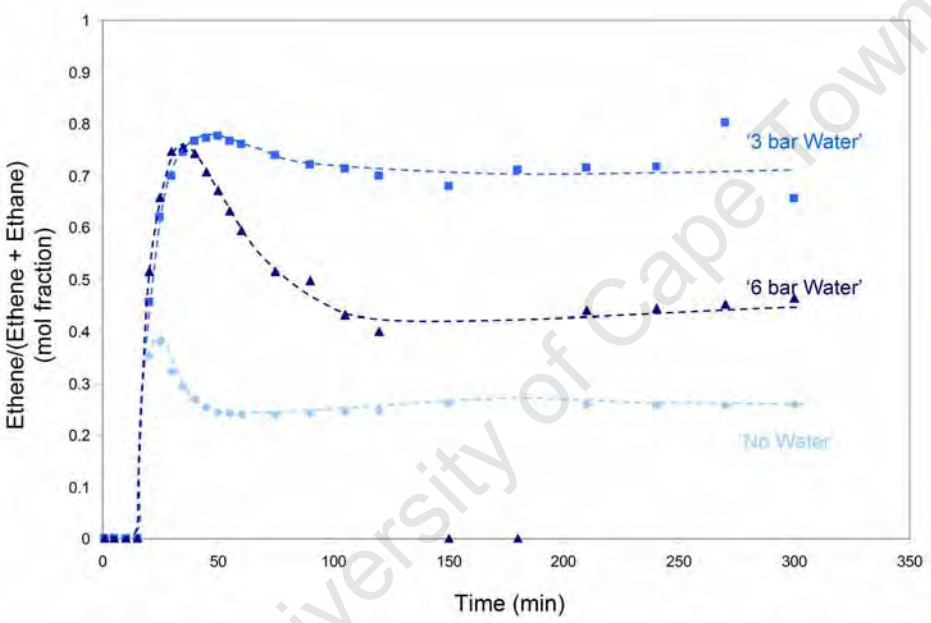

Figure 7.40: Molar olefin content of the C_2 fraction as a function of time of the '9 nm' catalyst at varying water partial pressure conditions (no water addition, 3 bar water addition, 6 bar water addition) (T = 240 °C, $P_{syn-gas}$ = 10 bar, H_2/CO ratio = 2)

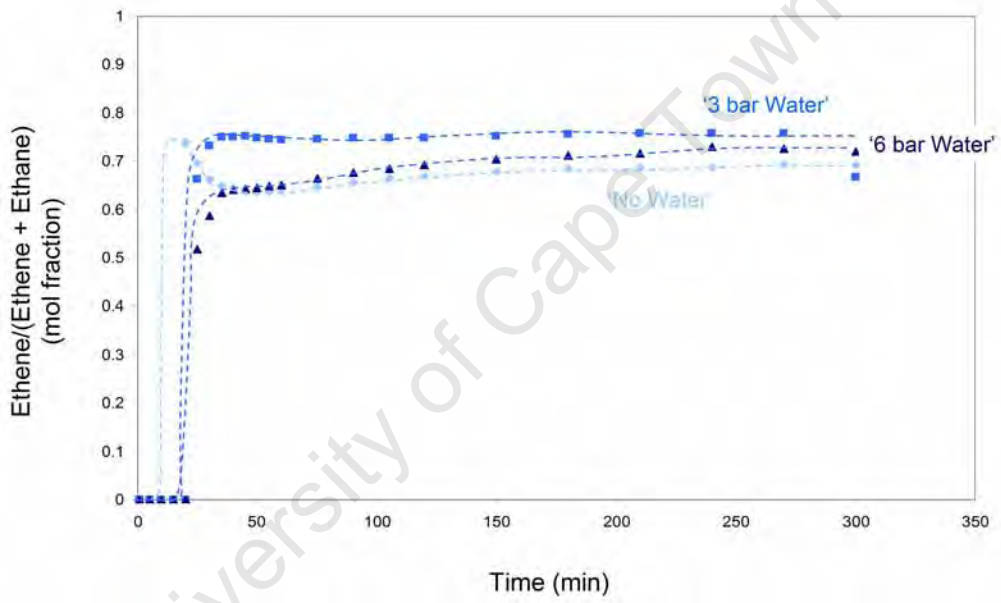

Figure 7.41: Molar olefin content of the C_2 fraction as a function of time of the '16 nm' catalyst at varying water partial pressure conditions (no water addition, 3 bar water addition, 6 bar water addition) (T = 240 °C, $P_{syn-gas}$ = 10 bar, H_2/CO ratio = 2)

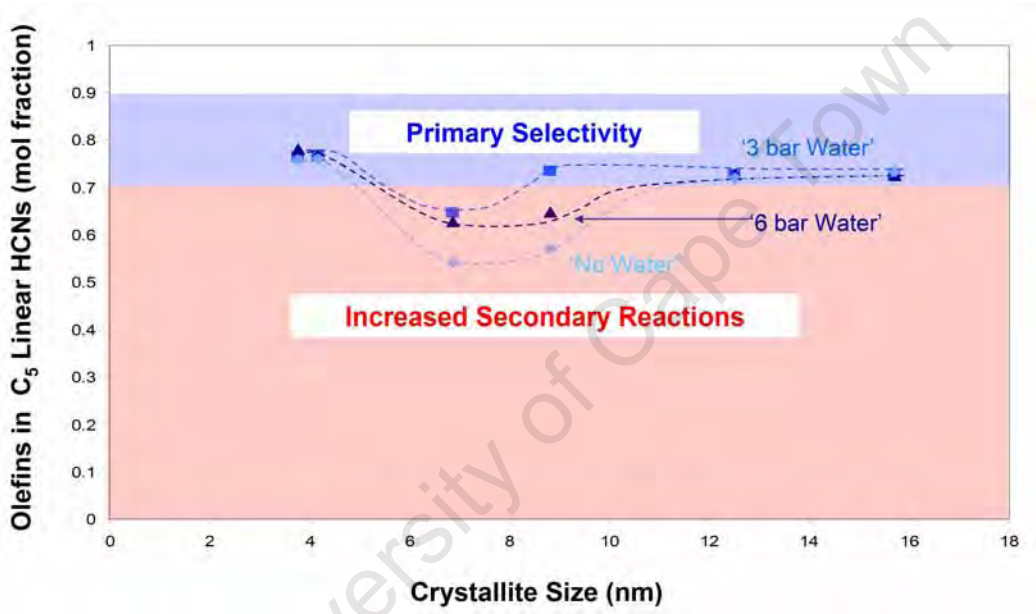

Figure 7.42: Mole fraction of olefins in the C_5 fraction of linear hydrocarbons as a function of crystallite size during the initial state (10 - 20 minutes at reduced crystallite sizes) at varying water partial pressure conditions (no water addition, 3 bar water addition, 6 bar water addition) (T = 240 °C, $P_{syn-gas}$ = 10 bar, H_2/CO ratio = 2)

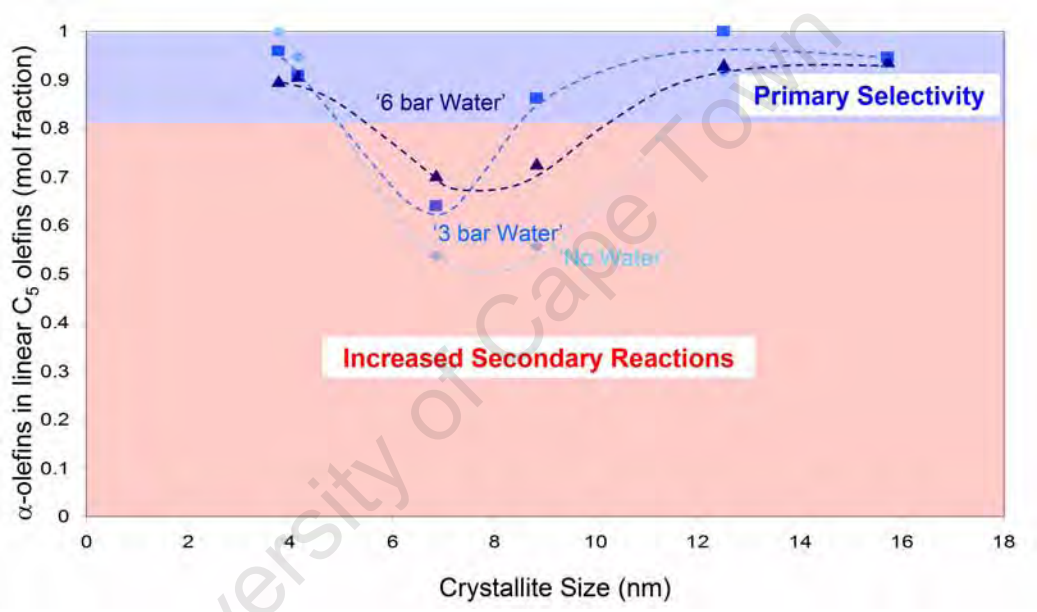

Figure 7.43: Mole fractionof α-olefins in linear olefins as a function of crystallite size during the initial state (10 - 20 minutes at reduced crystallite sizes) at varying water partial pressure conditions (no water addition, 3 bar water addition, 6 bar water addition) (T = 240 °C, $P_{syn-gas}$ = 10 bar, H_2/CO ratio = 2)

7.2.2.4 Oxygenate Formation

The effect of water partial pressure on oxygenate formation during Fischer-Tropsch synthesis is less easy to anticipate than previous results presented. It was shown in the previous chapter (Section 7.1.2.4) that the mid-sized metal crystallites show the least formation of oxygenates, this trend is continued here as shown in Figure 7.44 which shows the initial alcohol and aldehyde content in total linear hydrocarbons plus oxygenates with respect to carbon number for 3 selected catalysts of differing crystallite size at '3 bar' water addition. Again the mid-sized crystallite ('9 nm') shows a lower ratio of alcohols and aldehydes in comparison to those of smaller ('3 nm') and larger ('16 nm') crystallites. While this trend is continued, the actual effect of water addition on the production of oxygenates is more complicated. Figure 7.45 shows that while water partial pressure certainly seems to have an effect on the initial production of oxygenates, there is too much scatter in the data to actually ascertain what the effect may be. The scatter in the data may be partially due to the extremely small amounts of alcohols and aldehydes actually produced, leading to larger errors during data work-up of FID chromatograms.

7.2.3 Summary of Results for Fischer-Tropsch Dependence on Water Partial Pressure

The effect of increasing water partial pressure via co-feeding on the the activity and selectivity of Fischer-Tropsch synthesis was investigated on unpromoted alumina supported iron crystallites of varying size at reaction conditions of; $T_{reaction}$ = 240 °C, $P_{syn-gas}$ = 10 bar and H_2/CO ratio = 2. In terms of activity, a specific Fischer-Tropsch rate was calculated, the same trend of increasing activity with increasing crystallite size as obtained in the series reported in the previous section without water co-feeding is still true with the addition of water. However, with increasing water partial pressure, there is a decrease of activity at all crystallite sizes, with the addition of 3 bar water a significant decrease is observed, however with the increase of an additional 3 bar water to 6 bar water total no big difference in activity

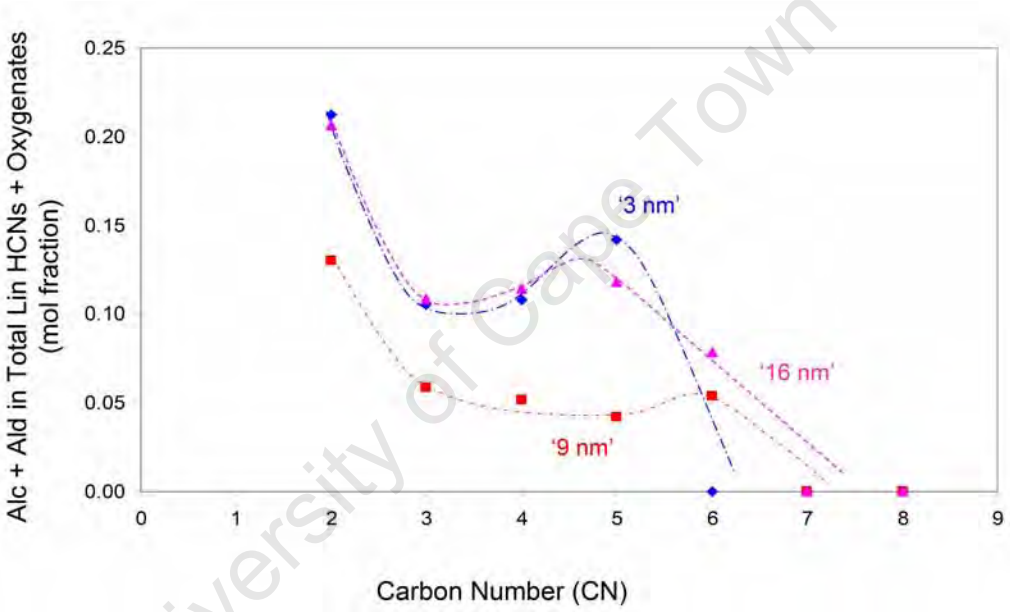

Figure 7.44: Mole fraction of alcohols and aldehydes in linear products as function of carbon number during steady state (50 - 300 minutes) for 3 selected alumina supported model iron catalysts of varying crystallite sizes (T = 240 °C, P = 15 bar, $P_{syn-gas}$ = 10 bar, P_{water} = 3 bar H_2/CO ratio = 2)

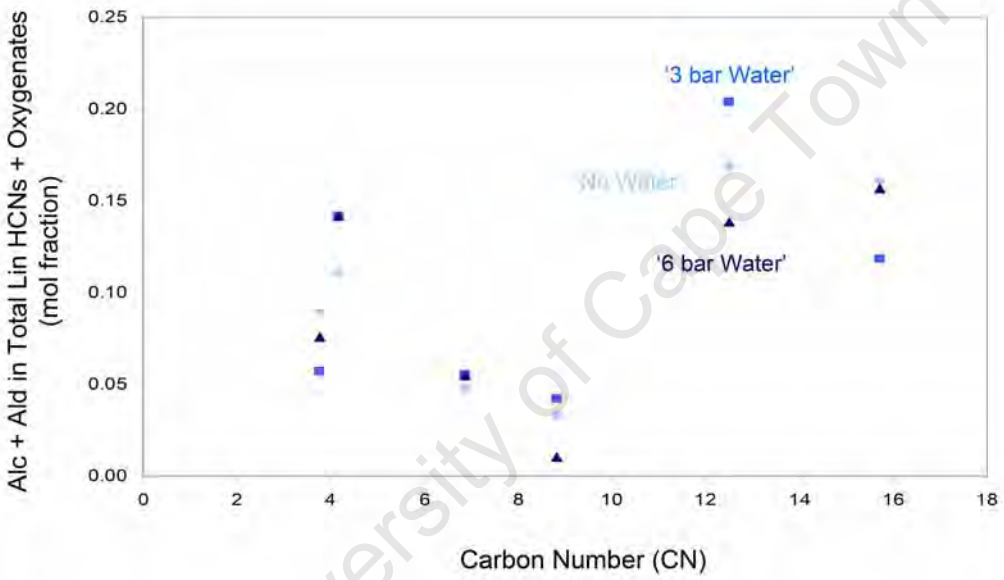

Figure 7.45: Mole fraction of alcohols and aldehydes in linear products as function of crystallite size in the C_5 fraction at initial state (10 - 20 min at reduced crystallite sizes) at varying water addition conditions (no water addition, 3 bar water addition, 6 bar water addition) (T = 240 °C, $P_{syn-gas}$ = 10 bar, H_2/CO ratio = 2)

was observed. This loss in activity upon water addition can be attributed to either oxidation of the iron crystallites or sintering of the iron crystallites. From characterisation results of the spent catalyst, it can be seen that there is no bulk oxidation observed except in the smallest crystallites ('2 nm' and '3 nm'), though massive sintering is seen. Therefore the lower activity of the catalyst samples upon addition of water can be attributed to sintering, although it should be stated thta kinetic effects cannot be completely ruled out. The further deactivation of initially small sized crystallites at very high water partial pressures (i.e. '2 nm'/'6 bar') may be due to additional effects of oxidation.

In terms of product formation, the addition of water decreased the methane selectivity and increased olefin selectivity. However, the basic trends with respect to crystallite size that were observed at the 'base case' condition of no water addition are still carried through here. It has been suggested that the decrease in both methane selectivity and secondary reactions can be put down to the inhibition effect that water has on the desorption and readsorption mechanisms respectively.

7.3 Magnetic in-situ Characterisation of Catalysts

The final set of experimental runs were done on a magnetometer developed specifically for $in-situ$ catalyst characterisation which potentially allows for the tracking of phase changes and crystallite size changes. The magnetometer utilized an induction method of magnetic measurement whereby the position of the sample was adjusted leading to an observable voltage induced in the detection device upon movement of the sample due to the variation in the flux. The schematic set-up of the Weiss extraction method utilized by the magnetometer is shown in Figure 4.10 and the reactor position in the set-up is again highlighted in Figure 7.46. The sample is placed in a reactor system, which is then positioned in the geometric center of the pole gap. Two pairs of signal pick-up sensing coils are located on either side of the sample, these

make up the detection device. The sample can then be mechanically moved in the vertical orientation, and as it moves, the magnetic flux through the coils is altered, resulting in a voltage induction. This voltage is directly proportional to the magnetisation of the sample.

The magnetometer can be operated at field strengths of between -2 and 2 Tesla, and allows for measurement of saturation magnetisation, remnant magnetisation as well as measurement of full hysteresis at reaction conditions as a function of time on stream, therefore allowing for the measurement of compositional and crystallite size changes of the catalyst during Fischer-Tropsch testing and catalyst pre-treatment. More detail on the overall setup is given in Section 4.5 as well as in Claeys (2008a), Claeys (2008b) and Claeys et al. (2009).

The magnetometer can be used to give indications of whether phase change has occured during the experimental run. This is particularly useful in terms of the water addition experiments as one potential theory associated with the cause of deactivation upon addition of water is the bulk oxidation of the iron crystallites. The iron phases expected during a Fischer-Tropsch run are metallic iron, iron carbides and iron oxides. The relative magnetisation of these phases at a temperature of $T_{reaction} = 240\,°C$ can be found in Table 7.9 (only carbide phases which were observed by means of Mössbauer spectroscopy in the spent samples are included here. Note that Hägg carbide and cementite have Curie/Néel temperatures which are close to the Fischer Tropsch reaction temperature and they should therefore not display any magnetism at $in-situ$ conditions, $Fe_{2.2}C$ is still magnetic at this condition, however it is lower than the magnetism expected for metallic iron). Therefore according to previous work and Figure 2.8, it would be expected that at the beginning of the experimental run the catalyst would be mainly in the α-iron phase and as such show the highest magnetisation. After the start of the run there would be a rapid decrease in the magnetisation due to a phase change into the carbide phase and/or magnetite. However if water is added and oxidation is the cause of the catalyst deactivation of a working catalyst, a change in the saturation magnetisation would be expected as the iron oxides have a different relative magnetisation when compared to the

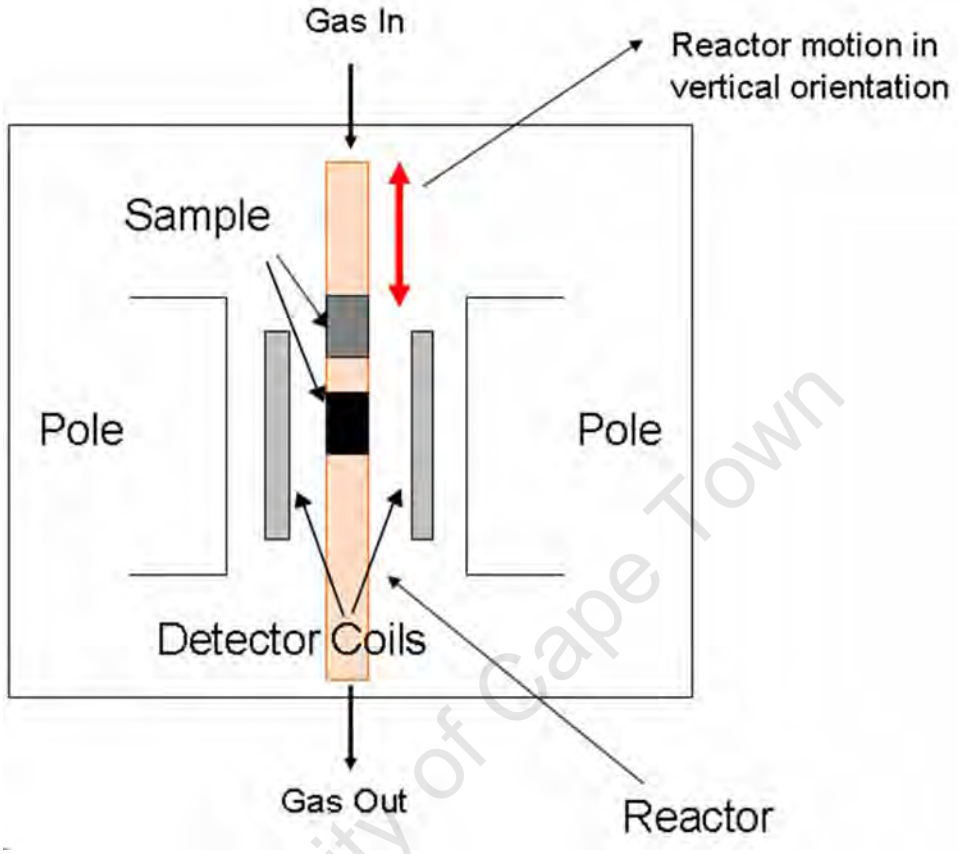

Figure 7.46: Simplified schematic for the reactor placement and movement in $in-situ$ magnetometer. Adapted from Claeys (2008a)

carbides at $T_{reaction} = 240\,^{\circ}C$.

7.3.1 Phase Changes in FT Synthesis as followed by an $in-situ$ Magnetometer

Due to time constraints only 3 selected catalysts were tested in the magnetometer ('2 nm', '9 nm' and '16 nm'). An amount of 0.5 g of the catalyst sample was loaded into the fixed bed reactor (Figure 4.10), with 1.2 g alumina as the diluent, silicon carbide was not used in this case as separation of the catalyst from silicon carbide might occur upon applying external magnetic fields. The experimental and sampling procedure are fully listed in Sections 4.5.3 and 4.5.4 respectively.

Table 7.9: Relative magnetisation of iron phases found during Fischer-Tropsch synthesis at $T_{reaction} = 240\,^{\circ}C$

Metallic	
α-iron	1.00
Oxides	
Magnetite	0.40
Maghemite	0.36
Hematite	0.00
Carbides	
Hägg Carbide	0.00
Cementite	0.00

Two sets of experiments were conducted, in the first one, water levels were varied stepwise with basecase conditions being revisited, while in a second series, freshly reduced catalysts were subjected from the start to additional water, that is, '6 bar water'. Figure 7.47 shows the saturation magnetisation for the first series of experiments plotted against time in minutes, where the changes in the water partial pressure are also shown. It can be seen that the saturation magnetisation (shown in normalized form here) for all 3 samples remains fairly constant despite the addition of high levels of water, up to 9 bar, the only major change was at the start of the experimental run, where a sharp decrease is seen, as mentioned previously, this is expected due to the change of phase from α-iron to iron carbide and/or magnetite. The unchanged nature of the saturation magnetisation upon water addition is not the expected result, if bulk oxidation takes place upon water addition it is expected to lead to a change in the saturation magnetisation. A close inspection of the data obtained at 6 bar water addition however indicates a slight increase of magnetisation at 450 minutes runtime, which may be due to carbide oxidation. This 'oxidation' was not reversed upon removal of the externally added water. At this point the question arose whether the difference between the experimental procedures used during the runs with the magnetometer and runs conducted with conventional test set-up reported in the previous sections could have led to different results. During the runs in

the conventional set-up water was added at the start of the run, however in the first series of runs in the magnetometer the run was started in the 'basecase' condition of no water addition and then water was added in a step-wise manner with a return to 'basecase' after each water addition. It was theorized that perhaps starting the experiment in the 'basecase' condition led to more iron carbide being allowed to form, and perhaps the carbides were more resistant to oxidation due to water addition than metallic iron in a freshly reduced catalyst. To test this theory more runs were conducted in the magnetometer where the experimental procedure used for the runs conducted in the conventional set-up were followed, as such 6 bar water was added from the start of the experiment. The duration of these runs was 3 hours.

Figure 7.48 shows the comparison of normalized saturation magnetisations of runs started in the 'basecase' condition and runs that started with '6 bar' water addition. Again it can be seen that the steady state saturation magnetisation of all 3 samples at both water addition conditions are very similar, and no major changes were observed during the run except for the initial strong decrease in magnetisation. The only difference between the two conditions is the time taken for steady state saturation magnetisation being reached, this is delayed in the second series of runs with direct initial water addition. This result can only lead to the conclusion that no bulk phase change or more specifically, no bulk oxidation occurred during the experimental runs despite the addition of water. Previous results suggested that the deactivation of the catalyst upon water addition is not due to oxidation but rather kinetic effects, and the results obtained from the magnetometer seem to correspond. In addition to the saturation magnetisation data shown for the first series of magnetic runs in Figure 7.47, carbon monoxide conversion as a function of time for the same series of experiments can be found in Figure 7.49 (The greyed out areas on this graph show initial data which are due to residence time effects). The reversibility of the effects of water additions on iron catalysts with crystallites of varying size can be analyzed from these results. For all crystallite sizes, upon the addition of 3 bar water, lower activity was shown, however, upon removal of the addition water

partial pressure, the samples all showed some return to 'basecase' conversion levels, with the '2 nm' and '9 nm' crystallites showing moderate reversibility and the '16 nm' sample showing almost complete reversibility from the addition of 3 bar water. Upon the addition and removal of 6 bar water, the '2 nm' and '9 nm' crystallites showed no reversibility, while the '16 nm' crystallites showed only moderate reversibility. Because the '16 nm' showed some reversibility at 6 bar water addition, the experimental run was continued with the addition of 9 bar water, at this point no reversibility was shown. These results suggest that there is a threshold water partial pressure level above which no reversibility is possible, furthermore this threshold level differs with crystallite size, where larger crystallites can withstand a higher water partial pressure level. The reversibility of water addition that was shown suggests that the effects of water addition is largely kinetic in nature. It is interesting to note though, even at water levels which lead to irreversible deactivation, no bulk transformation of the catalyst was observed with the largest crystallites.

Another interesting result that can be observed from the experimental runs conducted in the magnetometer is that the steady state saturation magnetisation of all samples is higher than that expected for magnetite present, that is approximately 0.4. This is an unexpected result, as for this value to be possible it means that some material with a relative magnetisation of higher than 0.4 must still be present in the sample. And from all previous characterizations including those done on spent samples using Mössbauer spectroscopy and XRD show that the only phases present are those of oxides and carbides which according to Table 7.9 have relative magnetisation of 0.4 and below. As α-iron cannot be detected by Mössbauer, which is the most sensitive characterisation technique utilized, it points to the existence of α-iron throughout the entire run. This is a possibility which has not been considered in detail in literature. It should also be noted however that $Fe_{2.2}C$ may show higher magnetism than iron oxides at the reaction conditions, therefore it may also contribute to the higher than expected magnetisation observed. An indication of different phases present in a catalyst can also be obtained via characterisation of the spent catalysts at different temperatures using the

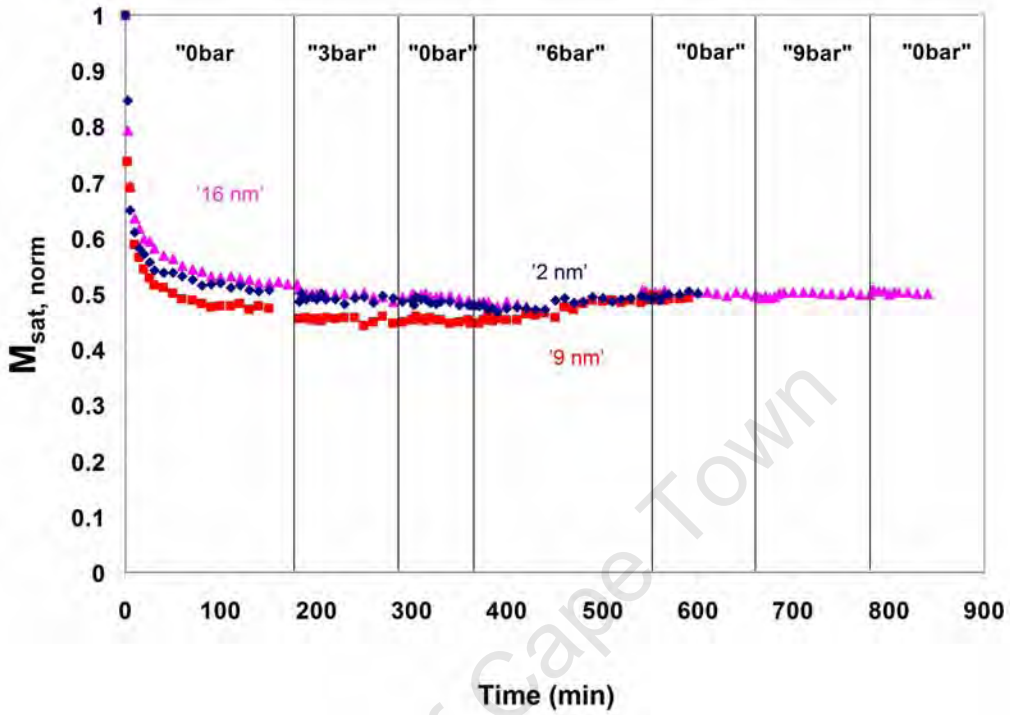

Figure 7.47: Saturation magnetisation as function of time for 3 selected alumina supported iron catalysts ('2 nm', '9 nm', '16 nm') (T = 240 °C, $P_{syn-gas}$ = 10 bar, H_2/CO ratio = 2)

magnetometer. The different contributions of the different phases according to their relative saturation magnetisation and their Curie/Néel termperatures can give a qualitative or even quantitative phase composition (Hofer and Cohn (1950)). The cooling below room temperature was achieved using liquid nitrogen poured over the outside of the reactor. The results are shown in Figure 7.50 for the experiments of the '9 nm' series with and without water addition, but no significant differences of the saturation magnetisation as a function of temperature was seen, suggesting that the phase compositions of the spent catalysts were relatively similar. It can also be noted that no significant changes of the magnetisation was observed upon the cooling down suggesting that only small amounts or no Fe_3C and $Fe_{2.2}C$ was present.

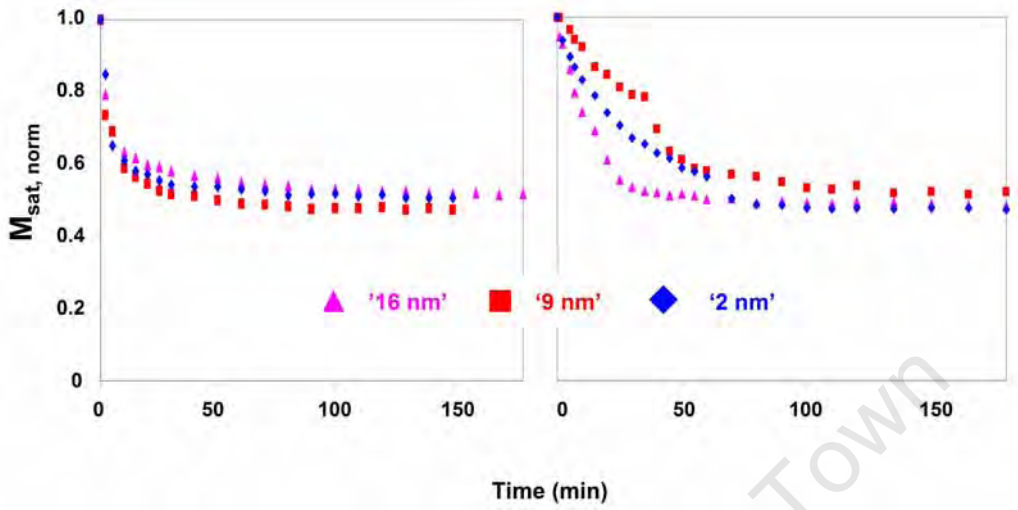

Figure 7.48: Saturation magnetisation as a function of time for 3 selected alumina supported iron catalysts ('2 nm', '9 nm', '16 nm') (no water *(left)*, 6 bar water *(right)* (T = 240 °C, $P_{syn-gas}$ = 10 bar, H_2/CO ratio = 2)

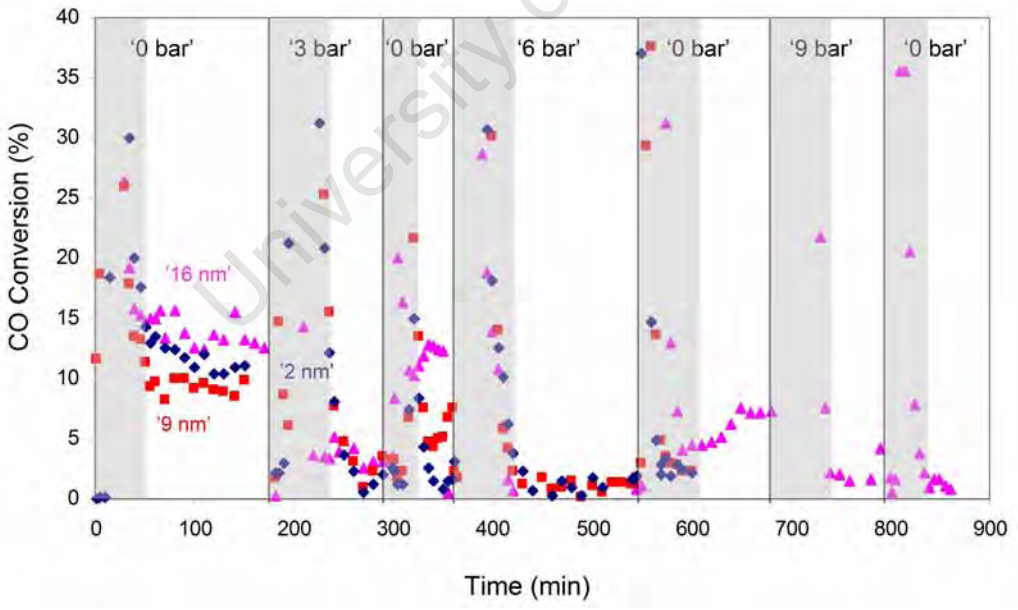

Figure 7.49: CO conversion as function of time for 3 selected alumina supported iron catalysts at varying stepwise water addition conditions (T = 240 °C, $P_{syn-gas}$ = 10 bar, H_2/CO ratio = 2)

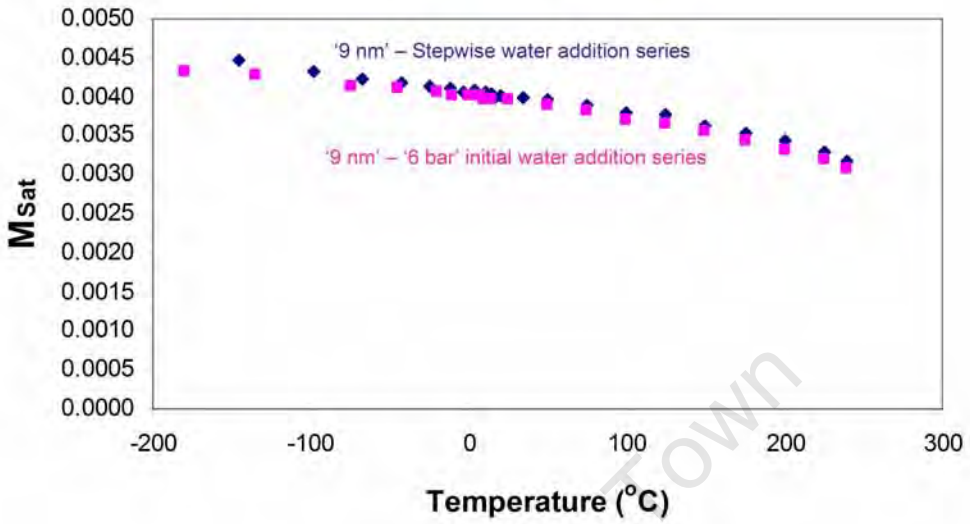

Figure 7.50: Saturation magnetisation as a function of temperature for '9 nm' alumina supported model iron catalyst at different water addition procedures (stepwise addition of water - starting with no water and 6 bar water addition) (T = 240 °C, $P_{syn-gas}$ = 10 bar, H_2/CO ratio = 2)

7.3.2 Crystallite Size changes in FT Synthesis as followed by an $in-situ$ Magnetometer

The magnetometer can also provide information on crystallite size and changes thereof (Claeys et al. (2009)). Small crystallites can behave as single magnetic domains, which upon removal of an external field show random magnetic orientation, and the net effect is such that a sample does not show any lasting magnetisation. This behaviour is called super-paramagnetism and it is restricted to crystallites below a certain size only, which is temperature dependent; at room temperature for metallic iron this diameter is up to 25 nm according to Bonneviot and Olivier (1994), and it is even larger for magnetic oxidic iron phases of magnetite and maghemite.

Crystallites above this critial size will display a lasting, 'remnant' magnetisation, that is, ferro-magnetic behaviour. The weight fraction of ferromagnetic or larger particles can be directly obtained from magnetic measurements using the saturation magnetisation and the remnant magnetisation at

2 Tesla and 0 Tesla respectively, according to Equation 7.3.

$$\%FM = \frac{2M_{rem}}{M_{sat}} \tag{7.3}$$

It should be noted that at higher temperatures this critical diameter is even larger, and the percentage of ferro-magnetic material therefore lower. Characterizing a sample at different temperatures over a wide range can therefore be used to obtain information on size distributions from magnetic measurements (remnance or 'Weil' method, Dalmon (1994)). However, in the case of iron this is complicated by the fact that several phases may be present (Claeys et al. (2009)).

Figures 7.51 and 7.52 shows the hystereses observed before and after the temperature programmed reductive pre-treatment of the 3 model catalysts used. It can be seen that the fresh catalysts already display magnetic behaviour, however, no remnant magnetisation was obtained here, that is super-paramagnetism, while the catalyst after reduction all show remant magnetism, with about 50-60 wt% ferro-magnetic crystallites. This is not in line with the critical diameter for iron (23 nm) reported by Bonneviot and Olivier (1994) and TEM characterisation clearly provides evidence that the crystallites after temperature programmed reduction are smaller than 23 nm. Therefore the conclusion may be drawn that ferro-magnetic behaviour of supported iron is observed at much smaller crystallite sizes than previously thought. The percentage of ferro-magnetic material at 240 °C during Fischer-Tropsch experiments in the magnetometer set-up is shown in Figure 7.53. A strong initial increase is obtained at the start, which may indicate crystallite growth, but the percentage of ferro-magnetic material present stays constant until the addition of 6 bar water where a decline is seen. This remains an experimental observation at this point, as it is not known why such a decrease would occur at the addition of 6 bar water and not at 3 bar water. A possible explanation for this decrease is oxidation, as it is exactly at this time of the run where a slight increase in magnetisation had occured. The oxidized crystallites then display super-paramagnetic behaviour, and as a net effect, the total percentage of ferro-magnetic material decreased. However

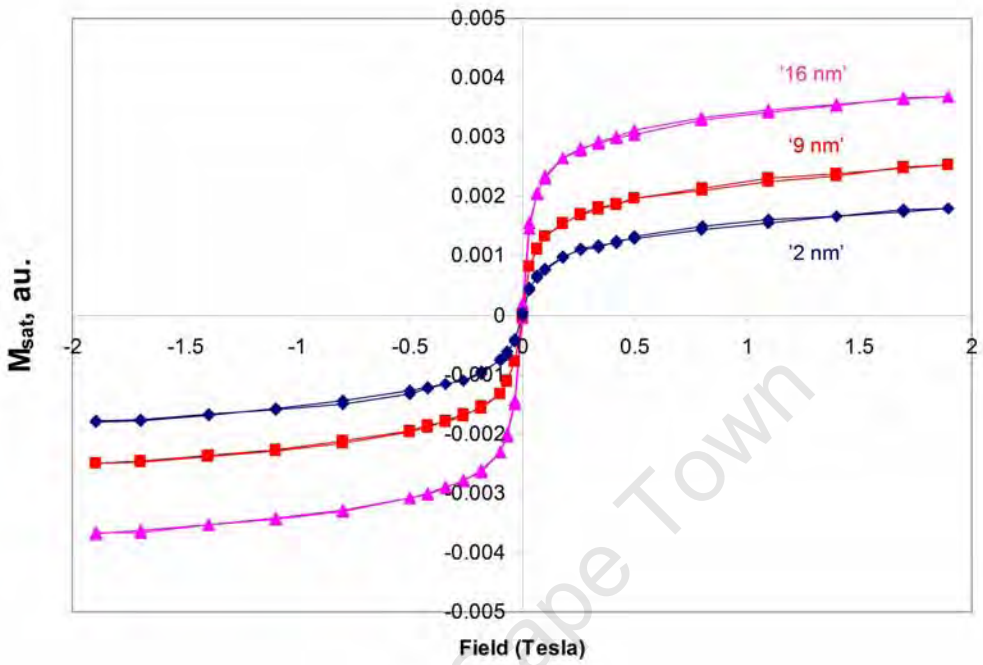

Figure 7.51: Hysteresis measurement for 3 selected alumina supported model iron catalysts prior to reduction conditions

no marked differences could be obtained for the differently sized crystallites.

Figure 7.54 shows that should 6 bar water be added from the start of the experiment, a decrease in the ferromagnetic material present would also occur. However this decrease is sharper and lower levels of ferro-magnetic fractions were obtained (30 wt% compared to 40 wt%) than those shown when 'base case' was the starting condition. This result may lend credence to the idea that iron carbides are less susceptible to bulk oxidation upon the addition of water.

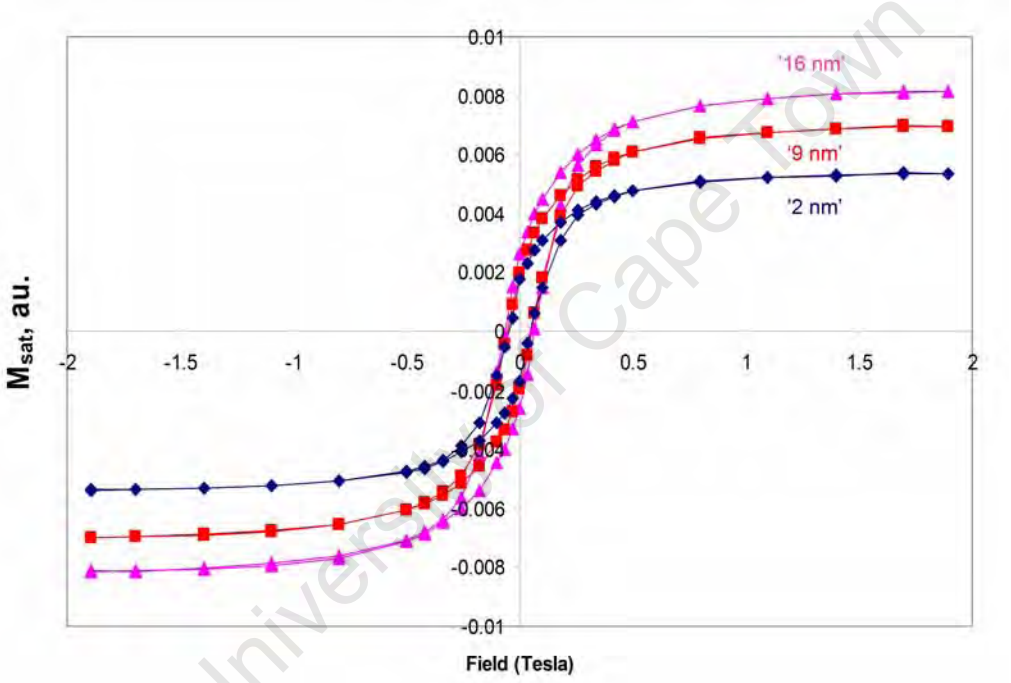

Figure 7.52: Hysteresis measurement for 3 selected alumina supported model iron catalysts post reduction conditions

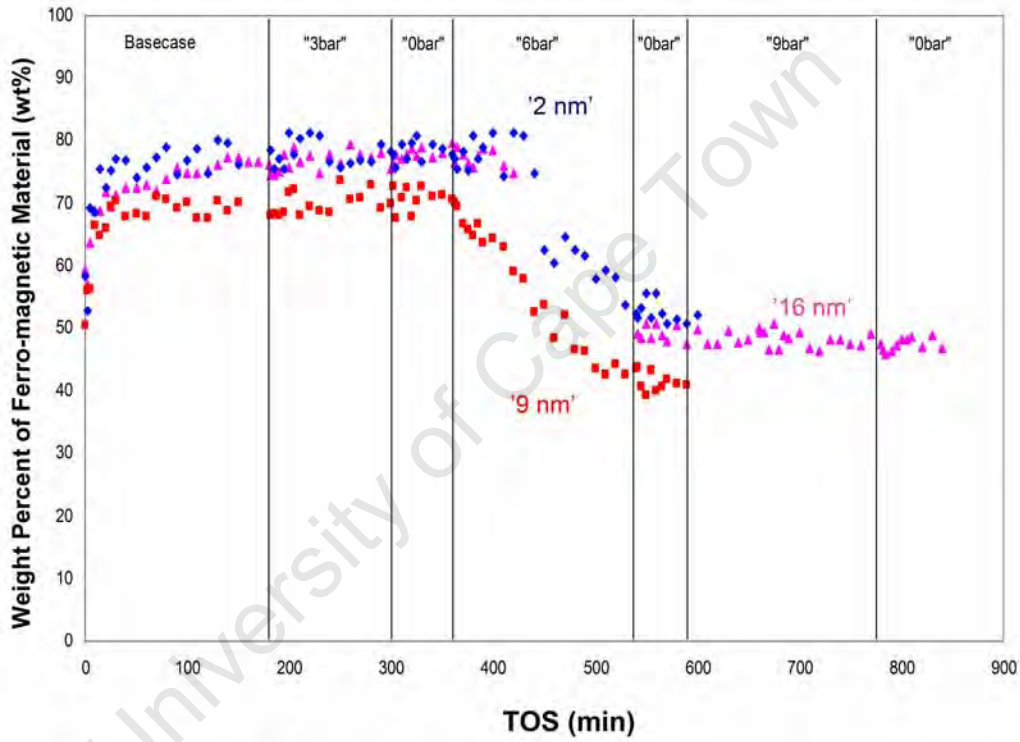

Figure 7.53: Percentage of ferro-magnetic material as function of time for 3 selected alumina supported model iron catalysts with stepwise variation of water partial pressure ('2 nm', '9 nm', '16 nm') (T = 240 °C, $P_{syn-gas}$ = 10 bar, H_2/CO ratio = 2)

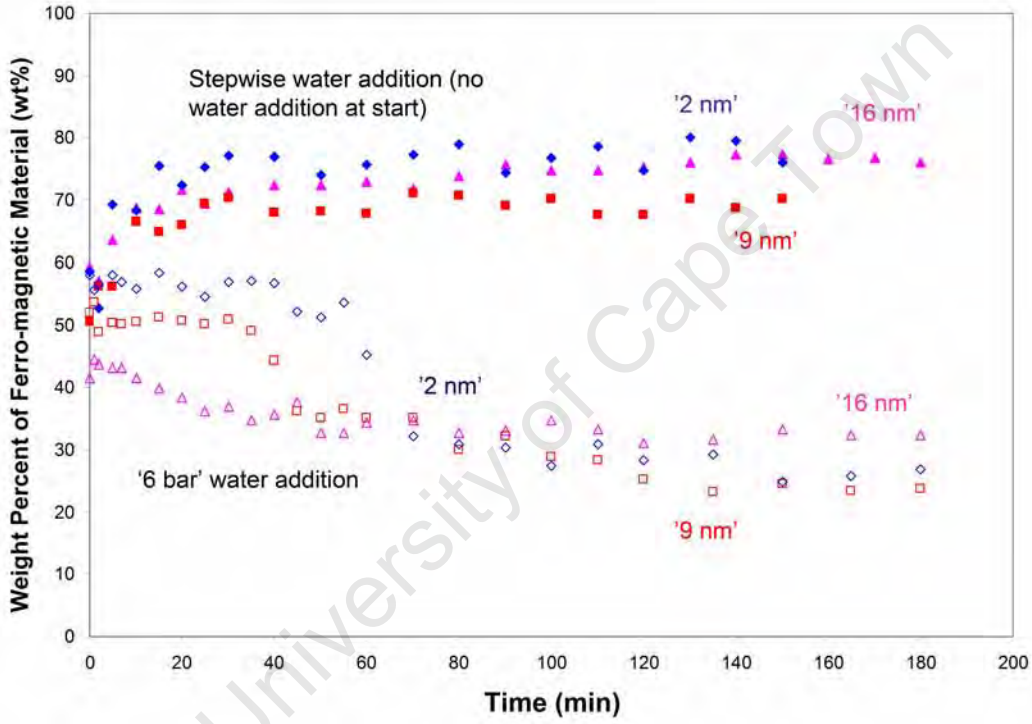

Figure 7.54: Percentage of ferro-magnetic material as function of time for 3 selected alumina supported iron catalysts ('2 nm', '9 nm', '16 nm') (T = 240 °C, $P_{syn-gas}$ = 10 bar, H_2/CO ratio = 2)

Chapter 8

Conclusions

This work can essentially be divided into 3 sections:

1. Preparation of a model alumina supported iron crystallites in the nanometer range between 2 and 16 nm.

2. Fischer-Tropsch testing of model catalyst systems of differing crystallite size and the characterisation of spent catalyst samples.

3. Fischer-Tropsch testing of model catalyst systems under different conditions of water addition and the characterisation of spent samples, including the $in-situ$ characterisation using a novel magnetic method.

Catalyst Preparation

The first major objective of this work was the preparation of a model catalyst sample, where a narrow size distribution could be achieved as well as a good distribution of the metal crystallites onto the support material. The requirement of a narrow size distribution has been successfully achieved by previous work by Mabaso (2005) and Welker (2007) through the utilisation of the reverse micelle technique. Size control can be achieved through variation of the water to surfactant ratio, with a high ratio leading to larger crystallites being formed.

An even distribution of metal crystallites onto the support material was more difficult to achieve. Therefore, four different support addition methods

were investigated as well as different support materials, drying conditions and calcination conditions. It was finally shown that the support addition method previously used by Mabaso (2005) was the one that lead to the best dispersion. Furthermore, alumina proved to be the best support material and the variation of drying and calcination conditions can have a large impact on the final catalyst. By varying the calcination temperature, it was shown that there exists a threshold temperature past which sintering of the metal crystallites occurs and dispersion of the crystallites is destroyed.

Model catalysts were successfully prepared with a narrow size distribution and a good dispersion of metal crystallites onto the support material. Six catalyst samples were prepared with average crystallite sizes ranging between 2 and 16 nm with a metal loading of 11 to 13 wt-%.

Fischer-Tropsch Testing

Fischer-Tropsch testing was carried out on all 6 catalyst samples of differing crystallite size. The testing was carried out in a u-tube fixed bed reactor at 240 °C, $P_{syn-gas}$ = 10 bar, H_2/CO ratio = 2, mild conditions were chosen and the conversion level kept below 10% so that the activity and selectivity results can be compared directly. Catalyst activity and product distributions were monitored over five hours of testing using both an on-line TCD and an off-line FID chromatograph.

The metal surface area specific Fischer-Tropsch rate shows a decrease with decreasing crystallite size. This change in rate has been theorized to be due to either the thermodynamically simpler oxidation of smaller crystallites or the lack of ensembles of atoms required for Fischer-Tropsch synthesis on smaller crystallites. Through the characterisation of spent samples, it has been shown that the 'Ensemble Effects' theory to be the more likely one as bulk oxidation was not observed.

In terms of product formation, smaller crystallites showed a higher inclination for the production of methane. This is further support for the 'Ensemble effects' theory, as this result leads to the conclusion that less chain growth sites and more methanation sites are available on smaller crystallites leading to an increased methane selectivity on small crystallites. Other

product selectivities such as olefin and oxygenate formation did not follow this trend, instead it was the catalyst samples in the middle metal crystallite size range that showed increased propensity towards secondary reactions. Previous work has theorized that these secondary reactions most effectively take place on edge atoms, results from this work do not support this theory, as secondary reactions should be most prevalent on the smallest crystallites. Therefore the theory may be extended to include the 'Ensemble Effects' theory that secondary reactions preferentially take place on the edge atoms, but ensembles of flat area atoms are required for the secondary reactions to occur. As such it is the catalyst samples in the middle crystallite range that best fits the criterion. Another possible explanation for the results observed in this work is the electronic effects that occur upon readsorption between the olefins required for secondary reactions and the metal surface.

Variation of Water Partial Pressure

A conversion level of below 10% was chosen for this work in order to fully and directly compare the activity and selectivity results of the various catalyst samples. However this condition means that the effect of higher conversion levels are not shown. In order to overcome this problem the water partial pressure was increased, where a higher water partial pressure simulates the conditions of higher conversion. The 'basecase' water partial pressure was set at '0 bar', while water addition conditions had water partial pressures of '3 bar' and '6 bar'.

In terms of specific Fischer-Tropsch rate it was shown that the addition of water leads to less active catalyst performance irrespective of crystallite size. This low activity has been theorized by previous work to be either due to oxidation or sintering. Some oxidation may have been obtained in magnetic measurement and the smallest crystallite catalyst ('2 nm') at 6 bar testing (Mössbauer spectroscopy). Again characterisation results show that oxidation is not the likely cause of this lower activity, instead the clustering and agglomeration of metal crystallites show that sintering is the more likely candidate.

Product formation results show that the addition of water leads to a decrease in methane selectivity and an increase in olefin production. It is theorized that these selectivity results are caused by water inhibiting desorption and readsorption mechanisms leading to increased chain growth and decreased secondary reactions respectively.

Chapter 9

Recommendations and Future Work

It is recommended that future work built upon this investigation should focus on:

- A more detailed study be undertaken on the physical properties of support materials used, such as pore volume and surface area.
- A more detailed investigation of the surface area of iron crystallites dispersed onto the support material, using CO chemisorption.
- The extension of catalyst samples of larger crystallite size to determine if the 'leveling out effect' shown in previous work does exist and if so at what crystallite size range.
- A more concentrated study on iron crystallites in the size range between 7 and 9 nm, in order to confirm and better understand the trend shown on middle sized crystallites by this PhD study.
- *In-situ* catalyst characterisation. The characterisation of the catalyst during the experimental run utilizing methods such as XRD could prove invaluable in distinguishing phase changes as they occur.
- More extensive used of the magnetometer to generate results on crystallite size and phase composition.

- Further calibration of the magnetometer to investigate size dependant behaviour of iron nano-crystallites as well as the calibration of the magnetometer using pure samples of various iron carbides and oxides. This may lead to a better interpretation of the results showing if phase change does occur and if so what phases are present.
- Theoretical studies on the effect of water addition on the mechanisms of desorption and readsorption.
- Compare the effect of water co-feeding versus water formed via Fischer-Tropsch synthesis.
- Extend these studies and include systematic variation of potassium promotion on selected, differently sized crystallites, while still keeping full control of the particle size and distribution.

Bibliography

Abrevaya, H. and Targos, W. (1987). Microemulsion impregnated catalyst composite and use thereof in a synthesis gas conversion process. *US Patent*, (4714692).

Adesina, A. A. (1996). Hydrocarbon synthesis via Fischer-Tropsch reaction: travails and triumphs. *Applied Catalysis A: General*, 138(2):345–367.

Anderson, R. B. (1984). *The Fischer-Tropsch Synthesis*. Academic Press, New York, USA.

Barbier, A., Hanif, A., Dalmon, J.-A., and Martin, G. A. (1998). Preparation and characterization of well-dispersed and stable Co/SiO_2 catalysts using the ammonia method. *Applied Catalysis A: General*, 168(2):333 – 343.

Barbier, A., Martin, G.-A., de la Piscina, P. R., and Homs, N. (2001). Co/SiO_2 catalysts prepared from $Co_2(CO)_8$ for CO hydrogenation into alcohols and hydrocarbons: characterization by magnetic methods and temperature-programmed hydrogenation. *Applied Catalysis A: General*, 210(1-2):75–81.

Barkhuizen, D., Mabaso, E., Viljoen, E., Welker, C., Claeys, M., van Steen, E., and Fletcher, J. (2006). Experimental approaches to the preparation of supported metal nanoparticles. *Pure and Applied Chemistry*, 78(9):1759–1769.

Bartholomew, C. H. (2001). Mechanisms of catalyst deactivation. *Applied Catalysis A: General*, 212(1-2):17–60.

Bertole, C. J., Mims, C. A., and Kiss, G. (2002). The effect of water on the cobalt-catalyzed Fischer-Tropsch synthesis. *Journal of Catalysis*, 210(1):84–96.

Bezemer, G. L., Bitter, J. H., Kuipers, H. P. C. E., Oosterbeek, H., Holewijn, J. E., Xu, X., Kapteijn, F., van Dillen, A. J., and de Jong., K. P. (2006). Cobalt particle size effects in the Fischer-Tropsch reaction studied with carbon nanofiber supported catalysts. *Journal of American Chemical Society*, 128:3956–3964.

Bian, G., Oonuki, A., Koizumi, N., Nomoto, H., and Yamada, M. (2002). Studies with a precipitated iron Fischer-Tropsch catalyst reduced by hydrogen or carbon monoxide. *Journal of Molecular Catalysis A: Chemical*, 186(1-2):203–213.

Bonneviot, L. and Olivier, D. (1994). Ferromagnetic resonance. In *Catalyst characterisation: Physical techniques for solid materials*. Plenum Press, New York, USA.

Boutonnet, M., Kizling, J., Mintsa-Eya, V., Choplin, A., Touroude, R., Maire, G., and Stenius, P. (1987). Monodisperse colloidal metal particles from nonaqueous solutions: Catalytic behavior in hydrogenation of but-1-ene of platinum, palladium, and rhodium particles supported on pumice. *Journal of Catalysis*, 103(1):95–104.

Boutonnet, M., Kizling, J., Stenius, P., and Maire, G. (1982). The preparation of monodisperse colloidal metal particles from microemulsions. *Colloids and Surfaces*, 5(3):209–225.

Bromfield, T. and Coville, N. (1999). The effect of sulfide ions on a precipitated iron Fischer-Tropsch catalyst. *Applied Catalysis A: General*, 186(1-2):297–307.

Cairns, P. (2009). *Oxygenates in Iron Fischer-Tropsch synthesis: is copper a selectivity promoter?* PhD thesis, University of Cape Town, South Africa.

Ciobica, I. M., Kleyn, A. W., and Van Santen, R. A. (2003). Adsorption and coadsorption of CO and H on ruthenium surfaces. *Journal of Physical Chemistry B*, 107(1):164–172.

Ciobica, I. M. and van Santen, R. A. (2003). Carbon monoxide dissociation on planar and stepped Ru(0001) surfaces. *Journal of Physical Chemistry B*, 107(16):3808–3812.

Claeys, M. (1997). *Selektivitat, Elementarschritte und kinetische Modellierung bei der Fischer-Tropsch-Synthese*. PhD thesis, Universitat Fridericiana Karlsruhe, Germany.

Claeys, M. (2008a). Development of a magnetometer for in-situ catalyst characterization. In *CATSA 2008*.

Claeys, M. (2008b). Development of in-situ magnetometer for catalyst characterization. In *International Catalysis Conference*.

Claeys, M. and van Steen, E. (2002). On the effect of water during Fischer-Tropsch synthesis with a ruthenium catalyst. *Catalysis Today*, 71(3-4):419–427.

Claeys, M. and van Steen, E. (2004). Basic studies. In Steynberg, A. and Dry, M., editors, *Fischer Tropsch Technology*, volume 152, page 601. Elsevier, Amsterdam, The Netherlands.

Claeys, M., van Steen, E., van de Loosdrecht, J., Visagie, K., Velly, S., and Krylon, I. (2009). Development of in-situ magnetometer for catalyst characterization. *Catalysis Today*, Submitted.

Dalmon, J. (1994). Magnetic measurements and catalysis. In Imelick, B. and Vedrine, J., editors, *Catalyst characterisation: Physical techniques for solid materials*, page 585. Plenum Press.

de Smit, E., Beale, A. M., Nikitenko, S., and Weckhuysen, B. M. (2009). Local and long range order in promoted iron-based Fischer-Tropsch catalysts: A combined in situ X-ray absorption spectroscopy/wide angle X-ray scattering study. *Journal of Catalysis*, In Press, Corrected Proof:–.

Delmon, B. (2008). Formation of the final catalyst. In Ertl, G., Knozinger, H., Schuth, F., and Weitkamp, J., editors, *Handbook of Heterogeneous Catalysis, Vol 1*. Weinheim, Germany.

Dry, M. E. (1981). *Catalysis Science and Technology*. Springer Verlag, New York, USA.

Dry, M. E. (2002). The Fischer-Tropsch process: 1950-2000. *Catalysis Today*, 71(3-4):227–241.

Dry, M. E. (2004). FT catalysts. In Steynberg, A. and Dry, M., editors, *Fischer-Tropsch Technology*, volume 152. Elsevier, Amsterdam, The Netherlands.

Duvenhage, D. J. and Coville, N. J. (2006). Deactivation of a precipitated iron Fischer-Tropsch catalyst–a pilot plant study. *Applied Catalysis A: General*, 298:211–216.

Eriksson, S., Nylen, U., Rojas, S., and Boutonnet, M. (2004). Preparation of catalysts from microemulsions and their applications in heterogeneous catalysis. *Applied Catalysis A: General*, 265(2):207–219.

Espinoza, R., Steynberg, A., Jager, B., and Vosloo, A. C. (1999). Low temperature Fischer-Tropsch synthesis from a Sasol perspective. *Applied Catalysis A: General*, 186:13.

Forzatti, P. and Lietti, L. (1999). Catalyst deactivation. *Catalysis Today*, 52(2-3):165–181.

Fu, L. and Bartholomew, C. H. (1985). Structure sensitivity and its effects on product distribution in co hydrogenation on cobalt/alumina. *Journal of Catalysis*, 92(2):376–387.

Ge, Q. and Neurock, M. (2004). Structure dependence of no adsorption and dissociation on platinum surfaces. *Journal of the American Chemical Society*, 126(5):1551–1559.

Ge, Q., Neurock, M., Wright, H. A., and Srinivasan, N. (2002). A first principles study of carbon-carbon coupling over the 0001 surfaces of Co and Ru. *The Journal of Physical Chemistry B*, 106(11):2826–2829.

Geus, J. and van Dillen, A. (2008). Supported catalysts. In Ertl, G., Knözinger, H., Schüth, F., and Weitkamp, J., editors, *Handbook of Heterogeneous Catalysis, Vol 1*. Weinheim, Germany.

Gideon Botes, F. (2008). The effects of water and CO_2 on the reaction kinetics in the iron-based low-temperature Fischer-Tropsch synthesis: A literature review. *Catalysis Reviews*, 50(4):471–491.

Hayashi, H., Chen, L. Z., Tago, T., Kishida, M., and Wakabayashi, K. (2002). Catalytic properties of Fe/SiO_2 catalysts prepared using microemulsion for CO hydrogenation. *Applied Catalysis A: General*, 231(1-2):81–89.

Hilmen, A. M., Schanke, D., Hanssen, K. F., and Holmen, A. (1999). Study of the effect of water on alumina supported cobalt Fischer-Tropsch catalysts. *Applied Catalysis A: General*, 186(1-2):169–188.

Hofer, L. and Cohn, E. (1950). Thermomagnetic determination of hägg carbide used in iron fischer-tropsch catalysts. *Analytical Chemistry*, 22:907–910.

Huff, G. A. and Satterfield, C. N. (1984). Evidence for two chain growth probabilities on iron catalysts in the Fischer-Tropsch synthesis. *Journal of Catalysis*, 85(2):370–379.

Iglesia, E. (1997). Design, synthesis, and use of cobalt-based Fischer-Tropsch synthesis catalysts. *Applied Catalysis A: General*, 161(1-2):59–78.

Iglesia, E., Reyes, S. C., Madon, R. J., and Solied, S. L. (1993). Selectivity control and catalyst design in the Fischer-Tropsch synthesis: Sites, pellets, and reactors. volume 39, pages 221–302. Academic Press.

Jacobs, G., Patterson, P. M., Das, T. K., Luo, M., and Davis, B. H. (2004). Fischer-tropsch synthesis: Effect of water on Co/Al_2O_3 catalysts and

XAFS characterization of reoxidation phenomena. *Applied Catalysis A: General*, 270(1-2):65–76.

Jager, B. and Espinoza, R. (1995). Advances in low temperature Fischer-Tropsch synthesis. *Catalysis Today*, 23(1):17–28.

Johnson, P. and Joyner, R. (1993). Structure-function relationships in heterogeneous catalysis: The embedded surface molecule approach and its applications. In Guczi, L., Solumoxi, F., and Tetenyi, P., editors, *Stud. Surf. Sci. Catal. Vol 75*, pages 165–174. Elsevier, Amsterdam.

Kaiser, R. (1969). *Chromatographie in der Gasphase*. Bibliographisches Institut, Mannheim, Germany.

Kishida, M., Ichiki, K.-i., Hanaoka, T., Nagata, H., and Wakabayashi, K. (1998). Preparation method for supported metal catalysts using w/o microemulsion: Study on immobilization conditions of metal particles by hydrolysis of alkoxide. *Catalysis Today*, 45(1-4):203–208.

Kuipers, E. W., Scheper, C., Wilson, J. H., Vinkenburg, I. H., and Oosterbeek, H. (1996). Non-asf product distributions due to secondary reactions during fischer-tropsch synthesis. *Journal of Catalysis*, 158(1):288 – 300.

Li, J., Jacobs, G., Das, T., Zhang, Y., and Davis, B. (2002a). Fischer-Tropsch synthesis: Effect of water on the catalytic properties of a Co/SiO_2 catalyst. *Applied Catalysis A: General*, 236(1-2):67–76.

Li, S., Krishnamoorthy, S., Li, A., Meitzner, G. D., and Iglesia, E. (2002b). Promoted iron-based catalysts for the Fischer-Tropsch synthesis: Design, synthesis, site densities, and catalytic properties. *Journal of Catalysis*, 206(2):202–217.

Lin, H.-Y., Chen, Y.-W., and Li, C. (2003). The mechanism of reduction of iron oxide by hydrogen. *Thermochimica Acta*, 400(1-2):61–67.

Lisiecki, I. and Pileni, M. P. (1993). Synthesis of copper metallic clusters using reverse micelles as microreactors. *Journal of the American Chemical Society*, 115(10):3887–3896.

Mabaso, E. (2005). *Nanosized iron crystallites for Fischer-Tropsch synthesis*. PhD thesis, University of Cape Town, South Africa.

Maitlis, P. M., Quyoum, R., Long, H. C., and Turner, M. L. (1999). Towards a chemical understanding of the Fischer-Tropsch reaction: Alkene formation. *Applied Catalysis A: General*, 186(1-2):363–374.

Mansker, L. D., Jin, Y., Bukur, D. B., and Datye, A. K. (1999). Characterization of slurry phase iron catalysts for Fischer-Tropsch synthesis. *Applied Catalysis A: General*, 186(1-2):277–296.

Marceau, E., Carrier, X., Che, M., Clause, O., and Marcilly, C. (2008). Ion exchange and impregnation. In Ertl, G., Knözinger, H., Schüth, F., and Weitkamp, J., editors, *Handbook of Heterogeneous Catalysis*. Weinheim, Germany.

Moodley, D., van de Loosdrecht, J., Saib, A., Overett, M., Datye, A., and Niemantsverdriet, J. (2009). Carbon deposition as a deactivation mechanism of cobalt-based Fischer-Tropsch synthesis catalysts under realistic conditions. *Applied Catalysis A: General*, 354(1-2):102–110.

Moulijn, J., van Diepen, A., and Kapteijn, F. (2001). Catalyst deactivation: Is it predictable? What to do? *Applied Catalysis A: General*, 212(1-2):3–16.

Niemantsverdriet, J. W., van der Kraan, A. M., van Dljk, W. L., and van der Baan, H. S. (1980). Behavior of metallic iron catalysts during Fischer-Tropsch synthesis studied with Mossbauer spectroscopy, X-ray diffraction, carbon content determination, and reaction kinetic measurements. *Journal of Physical Chemistry*, 84:3363–3370.

Ojeda, M., Rojas, S., Boutonnet, M., Perez-Alonso, F. J., Javier Garcia-Garcia, F., and Fierro, J. L. G. (2004). Synthesis of rh nano-particles by the microemulsion technology: Particle size effect on the $CO+H_2$ reaction. *Applied Catalysis A: General*, 274(1-2):33–41.

Phala, N. and van Steen, E. (2007). Intrinsic reactivity of gold nanoparticles: classical, semi-empirical and dft studies. *Gold Bulletin*, 40:2.

Phala, N. S., Klatt, G., and Steen, E. v. (2004). A DFT study of hydrogen and carbon monoxide chemisorption onto small gold clusters. *Chemical Physics Letters*, 395(1-3):33–37.

Pichler, H. and Schulz, H. (1970). Neue Erkenntinisse auf dem Gebiet der Synthese von Kohlenwasserstoffen aus CO und H_2. *Chem-Ing. Techn.*, 42(18):1162–1174.

Pileni, M. P. (1993a). Reverse micelles as microreactors. *Journal of Physical Chemistry*, 97(27):6961–6973.

Pileni, M.-P. (1993b). Water in oil colloidal droplets used as microreactors. *Advances in Colloid and Interface Science*, 46:139–163.

Pillai, V., Kumar, P., Hou, M. J., Ayyub, P., and Shah, D. O. (1995). Preparation of nanoparticles of silver halides, superconductors and magnetic materials using water-in-oil microemulsions as nano-reactors. *Advances in Colloid and Interface Science*, 55:241–269.

Rameswaran, M. and Bartholomew, C. H. (1989). Effects of preparation, dispersion, and extent of reduction on activity/selectivity properties of iron/alumina CO hydrogenation catalysts. *Journal of Catalysis*, 117(1):218–236.

Reuel, R. C. and Bartholomew, C. H. (1984). Effects of support and dispersion on the CO hydrogenation activity/selectivity properties of cobalt. *Journal of Catalysis*, 85(1):78–88.

Riedel, T., Schaub, G., Jun, K.-W., and Lee, K.-W. (2001). Kinetics of CO_2 hydrogenation on a K-promoted Fe catalyst. *Ind. Eng. Chem. Res*, 40:1355–1363.

Satterfield, C. N., Hanlon, R. T., Tung, S. E., Zou, Z. M., and Papaefthymiou, G. C. (1986). Effect of water on the iron-catalyzed Fischer-

Tropsch synthesis. *Industrial & Engineering Chemistry Product Research and Development*, 25(3):407–414.

Schulman, J. H. and Friend, J. A. (1949). Light scattering investigation of the structure of transparent oil-water disperse systems. II. *Journal of Colloid Science*, 4(5):497–509.

Schulz, H. (1999). Short history and present trends of Fischer-Tropsch synthesis. *Applied Catalysis A: General*, 186(1-2):3–12.

Schulz, H. (2003). Major and minor reactions in Fischer-Tropsch synthesis on cobalt catalysts. *Topics in Catalysis*, 26(1-4):73–85.

Schulz, H., Böhringer, W., Kohl, C., Rahman, N., and Will, A. (1984). Entwicklung und Anwendung der Kapillar-GC-Gesamtprobentechnick fur Gas/Dampf-Vielstoffgemische. *DGMK Forschungsbericht*, 1984-3:320–329.

Schulz, H. and Claeys, M. (1999a). Kinetic modelling of Fischer-Tropsch product distributions. *Applied Catalysis A: General*, 186(1-2):91–107.

Schulz, H. and Claeys, M. (1999b). Reactions of alpha-olefins of different chain length added duringFischer Tropsch synthesis on a cobalt catalyst in a slurry reactor. *Applied Catalysis A: General*, 186:71–90.

Schulz, H., Claeys, M., and Harms, S. (1997). Effect of water partial pressure on steady state Fischer-Tropsch activity and selectivity of a promoted cobalt catalyst. In M. de Pontes, R.L. Espinoza, C. N. J. S. and Scurrell, M., editors, *Natural Gas Conversion IV*, volume 107, pages 193–200. Elsevier, Amsterdam, The Netherlands.

Schulz, H., Nie, Z., and Ousmanov, F. (2002). Construction of the Fischer-Tropsch regime with cobalt catalysts. *Catalysis Today*, 71(3-4):351–360.

Schulz, H., Schaub, G., Claeys, M., and Riedel, T. (1999). Transient initial kinetic regimes of Fischer-Tropsch synthesis. *Applied Catalysis A: General*, 186(1-2):215–227.

Schulz, H., van Steen, E., and Claeys, M. (1994). Selectivity and mechanism of Fischer-Tropsch synthesis with iron and cobalt catalysts. In Curry-Hyde, H. and Howe, R., editors, *Studies in Surface Science and Catalysis*, volume 81, pages 455–460. Elsevier, Amsterdam, The Netherlands.

Schulz, H., van Steen, E., and Claeys, M. (1995). Specific inhibition as the kinetic principle of Fischer-Tropsch synthesis. *Topics in Catalysis*, 2(1-4):223–234.

Shetty, S., Jansen, A. P. J., and van Santen, R. A. (2008). Co dissociation on the ru(1121) surface. *The Journal of Physical Chemistry C*, 112(36):14027–14033.

Shultz, J., Hofer, L., Karn, F., and Anderson, R. (1962). Studies of the Fischer-Tropsch synthesis. *Journal of Physical Chemistry*, 66(3):501–506.

Stenius, P., Kizling, J., and Boutonnet, M. (1984). Liquid suspension of particles of a metal belonging to the platinum group and a method for the manufacture of such a suspension. *US Patent*, 4,425,261.

Sternberg, A. and Wender, J. (1959). In *Proc. Intern. Conf. Coord. Chem.* The Chemical Society, London, UK.

Steynberg, A. P. and Dry, M. (2004). *Fischer-Tropsch Technology, Vol 152 of Studies in Surface Science and Catalysis*. Elsevier Science, Amsterdam, The Netherlands.

Swart, J. C. W., van Helden, P., and van Steen, E. (2007). Surface energy estimation of catalytically relevant fcc transition metals using dft calculations on nanorods. *The Journal of Physical Chemistry C*, 111(13):4998–5005.

Tajima, S. and Hirano, S.-i. (1990). Synthesis and magnetic properties of fe_2c_3 particles with high saturation magnetization. *Japanese Journal of Applied Physics*, 29:662–668.

van de Loosdrecht, J. (1994). *Preparation and properties of supported Fischer-Tropsch catalysts Effects of alloying, promoters and supports*. PhD thesis, University of Utrecht, The Netherlands.

van Hardeveld, R. and Hartog, F. (1969). The statistics of surface atoms and aurface sites on metal crystals. *Surface Science*, 15:189–225.

van Steen, E. (2008). Electronic picture of size dependent behaviour in the Fischer-Tropsch synthesis.

van Steen, E. and Claeys, M. (2008). Fischer-Tropsch catalysts for the biomass-to-liquid process. *Chemical Engineering and Technology*, 31:655–666.

van Steen, E., Claeys, M., Dry, M. E., van de Loosdrecht, J., Viljoen, E. L., and Visagie, J. L. (2005). Stability of nanocrystals: Thermodynamic analysis of oxidation and re-reduction of cobalt in water/hydrogen mixtures. *J. Phys. Chem. B*, 109:3575–3577.

Welker, C. (2007). *Ruthenium based Fischer-Tropsch synthesis on crystallites and clusters of different sizes - Nano to angstrom*. PhD thesis, University of Cape Town, South Africa.

Appendix A

List of Chemicals

Table A.1: Chemicals used during model catalyst preparation and testing

Compound	Details
Acetone	Kimix (Ar, 99.5% purity)
Air, synthetic	Air products (21% O_2 in N_2)
Aluminium oxide	Puralox (Batch 9574), SCCa 5-150; Sasol Germany, S_{BET} = 162 m^2/g; V_{pore} = 0.47 cm^3/g; d_pore = 11.5 nm
Aluminium sulphate	Riedel-de Haën (51 - 59 % purity)
Ammonium carbonate	Kimix (CP, 30% purity)
Argon	Air Liquide (99.99%)
Carbon dioxide	Air Liquide (99.99%)
Carbon monoxide	Afrox (99.97%)
Iron (III) nitrate	Kimix (AR, 97% purity)
n-Hexane	Kimix (AR, 96% purity)
Hydrogen	Air Liquide (99.99%)
Nitrogen	Air Liquide (99.99%)
Penta-ethyleneglycol-dodecylether Berol 050	Akzo Nobel
Silica gel	Sigma Aldrich 60 - 100 mesh; SCCa 150
Silicon carbide	mesh size = 200 - 250 μm
Carbon monoxide	Air Liquide (99.99%)

Appendix B

Data Work-up : Anderson-Schulz-Flory Distributions

An Anderson-Schulz-Flory distribution has long been used to describe the product distribution of Fischer-Tropsch synthesis. An Anderson-Schulz-Flory graph showing a typical Fischer-Tropsch product distribution can be found in Figure B.1. This figure shows typical aspects of Fischer-Tropsch product distribution such as a high selectivity towards methane, followed by a low percentage of carbon number 2 products due to an increased ethene re-adsorption. Finally, starting at a carbon number of 3 there is a linear relationship between the log of mole percentages and carbon number. This linear relationship can be exploited and used for further calculations such as conversions and selectivities. This section will show a number of equations used in calculations associated with an Anderson-Schulz-Flory distribution.

The mole percentage of each component can be calculated according to Equation B.1. The mole percentages of components in a specific carbon number can be summed and logged, this number is then plotted against carbon number to achieve a graph similar to that shown in Figure B.1.

$$mol\% = [\frac{A_i f_i}{N_i}] / \sum \frac{A_i f_i}{N_i} \tag{B.1}$$

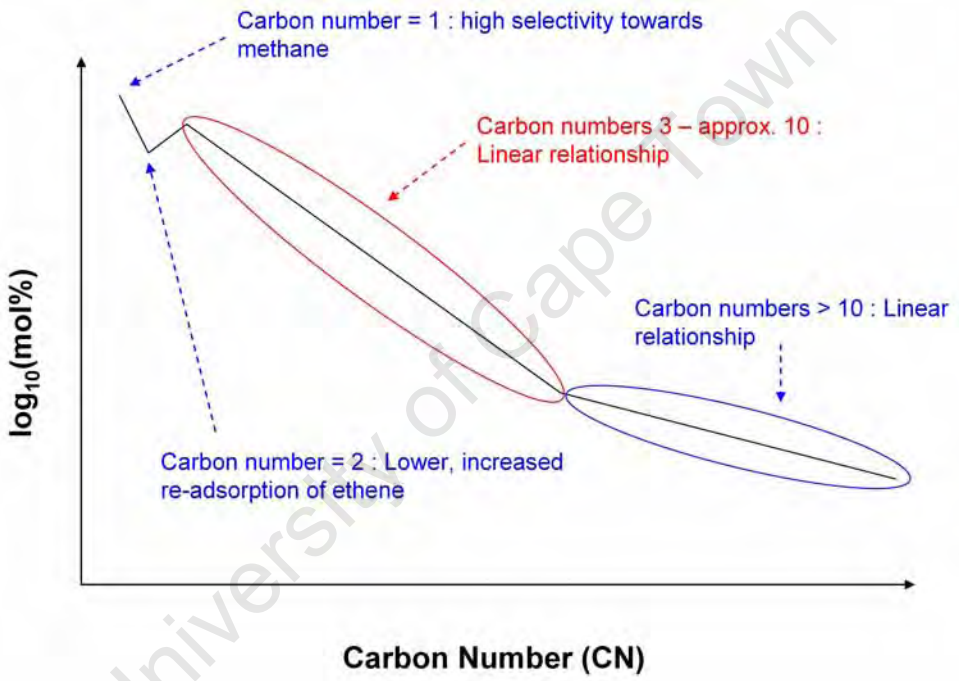

Figure B.1: Logarithm of mol-% as a function of carbon number, indicating a typical Anderson-Schulz-Flory distribution associated with Fischer-Tropsch synthesis

Linear regression tools can be used to calculate both the slope and intercept of the linear relationship section, this then allows for the extension of this linear relationship to larger carbon numbers, in this study to C_{100}. This knowledge combined with Equation 4.7 can be used to find the molar flow rates of specific carbon numbers. This then allows for the calculation of selectivities, as shown for methane selectivity in Equation B.2. Once methane selectivity has been calculated the use of Equations 4.9 and 4.10 results in carbon monoxide conversion.

$$S_{CH_4} = \frac{\dot{n}_{CH_4}}{\sum_{i=1}^{9} \dot{n}_{C_i}} \tag{B.2}$$

Appendix C

Fischer-Tropsch Testing

Table C.1: Results from Fischer-Tropsch testing in the initial stages of the experiment (10 - 20 min) on alumina supported iron catalysts of differing crystallite sizes ($T_{reaction}$ = 240 °C, $P_{syn-gas}$ = 10 bar, H_2/CO ratio = 2)

Sample Code		**2 nm**	**3 nm**	**7 nm**	**9 nm**	**14 nm**	**16 nm**
Reduced Size (nm)		3.77	4.17	6.89	8.83	12.60	15.72
Spent Size (nm)		5.55	5.60	7.87	10.83	13.30	16.75
Percentage Loading (%)		11.32	11.63	11.59	12.34	12.48	13.07
Degree of Reduction		0.98	0.98	0.83	0.84	0.72	0.79
Fischer-Tropsch Rate (mol-C/m^2Fe.min)		$1.65e-7$	$3.34e-7$	$7.63e-7$	$1.29e-6$	$1.76e-6$	$2.23e-6$
Carbon Monoxide Conversion		0.32	0.59	1.58	0.88	0.74	2.23
Carbon Dioxide Selectivity (%) [a]		35.77	24.06	11.52	13.76	43.21	54.11
Methane Selectivity (%) [b]		52.34	45.36	53.75	48.32	46.59	41.71
C_5+ Selectivity (%)		1.63	8.53	8.37	10.14	7.81	8.31
Paraffin Selectivity (%)	C_2 - C_4	6.46	9.27	14.96	13.43	11.61	11.75
	C_5+	0.35	1.20	3.57	1.17	2.17	2.20
	Total	6.82	10.47	18.53	14.60	13.78	13.95
Olefin Selectivity (%)	C_2 - C_4	26.19	17.72	15.29	18.17	29.59	31.68
	C_5+	1.12	2.67	3.67	1.59	4.64	4.95
	Total	27.31	20.39	18.96	19.75	34.22	36.62
Alcohol Selectivity (%)	C_2	2.70	1.05	2.85	0.23	1.94	2.73
	C_3+	0.00	0.25	0.79	0.21	0.46	0.74
Aldehyde Selectivity (%)	C_2	8.66	1.04	2.80	0.29	1.04	2.02
	C_3+	0.00	0.54	0.97	0.61	0.39	0.74
Ketone Selectivity (%)		0.00	0.13	0.12	0.06	0.33	0.16
Chain Growth Probability		0.3795	0.3633	0.4577	0.4754	0.4926	0.5078

[a] Selectivity with respect to total carbon monoxide conversion. As anaylyzed through TCD(CO_2) and FID(CO conversion).

[b] For all selectivities listed beyond this point, selectivity calculated with respect to total Volatile Organic Compounds (VOCs) as analyzed by FID.

Table C.2: Results from Fischer-Tropsch testing in the steady state stages of the experiment (50 - 300 min) on alumina supported iron catalysts of differing crystallite sizes ($T_{reaction}$ = 240 °C, $P_{syn-gas}$ = 10 bar, H_2/CO ratio = 2)

Sample Code		**2 nm**	**3 nm**	**7 nm**	**9 nm**	**14 nm**	**16 nm**
Reduced Size (nm)		3.77	4.17	6.89	8.83	12.60	15.72
Spent Size (nm)		5.55	5.60	7.87	10.83	13.30	16.75
Percentage Loading (%)		11.32	11.63	11.59	12.34	12.48	13.07
Degree of Reduction		0.98	0.98	0.83	0.84	0.72	0.79
Fischer-Tropsch Rate (mol-C/m^2Fe.min)		$3.91e-7$	$3.91e-7$	$3.78e-6$	$5.03e-6$	$4.72e-6$	$7.73e-6$
Carbon Monoxide Conversion (ratio)		0.75	0.83	4.40	4.52	3.01	3.98
Carbon Dioxide Selectivity (%) [a]		32.81	26.29	14.47	14.25	31.16	32.31
Methane Selectivity (%) [b]		51.77	43.26	47.60	46.11	45.26	35.98
C_5+ Selectivity (%)		1.80	8.66	7.06	7.55	9.52	10.70
Paraffin Selectivity (%)	C_2 - C_4	6.67	7.16	15.73	17.18	8.74	10.38
	C_5+	1.04	2.02	3.36	3.34	2.66	2.72
	Total	7.71	9.19	19.09	20.52	11.41	13.10
Olefin Selectivity (%)	C_2 - C_4	26.00	25.39	14.69	18.05	21.72	27.38
	C_5+	2.17	5.12	2.80	3.10	4.98	6.05
	Total	28.17	30.51	17.49	21.15	26.70	33.43
Alcohol Selectivity (%)	C_2	3.58	5.97	4.55	3.72	5.86	6.89
	C_3+	1.05	3.01	1.89	1.48	3.82	4.64
Aldehyde Selectivity (%)	C_2	5.60	5.64	6.29	5.09	4.78	3.19
	C_3+	0.16	0.71	0.95	0.70	0.63	1.02
Ketone Selectivity (%)		0.18	0.27	0.15	0.05	0.32	0.32
Chain Growth Probability		0.5672	0.5589	0.5726	0.5605	0.5649	0.5847

[a]Selectivity with respect to total carbon monoxide conversion. As anaylyzed through TCD(CO_2) and FID(CO conversion).

[b]For all selectivities listed beyond this point, selectivity calculated with respect to total Volatile Organic Compounds (VOCs) as analyzed by FID.

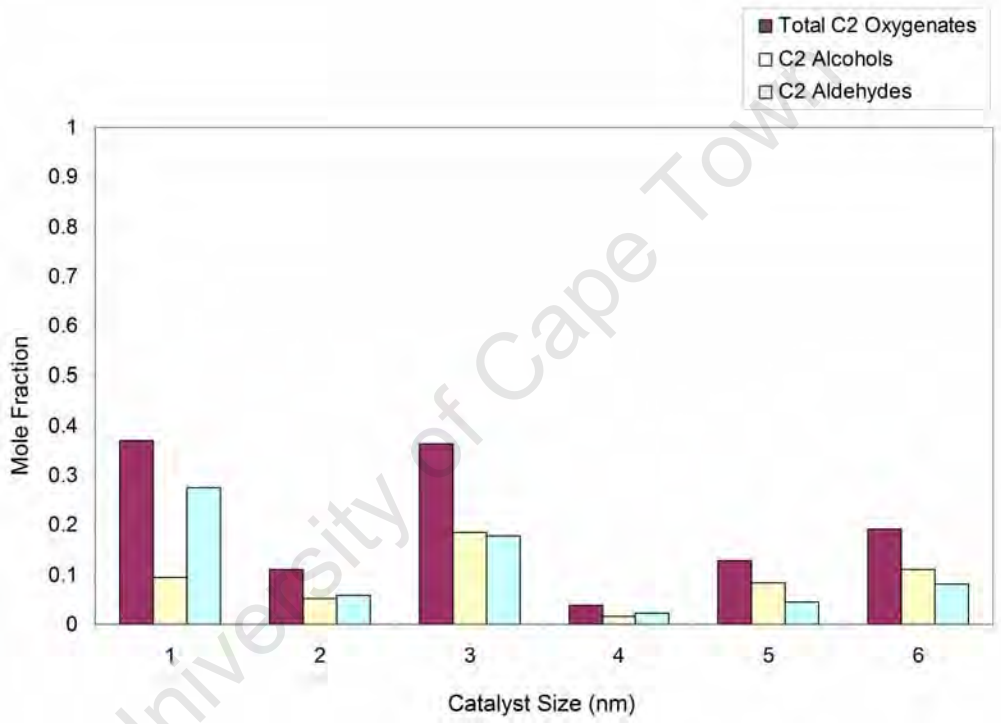

Figure C.1: Mole fraction of alcohols, aldehydes and total oxygenates in the C_2 fraction during initial state(10 - 20 min) on alumina supported model iron catalysts of differing crystallite sizes (T = 240 °C, P = 12 bar, $P_{syn-gas}$ = 10 bar, H_2/CO ratio = 2)

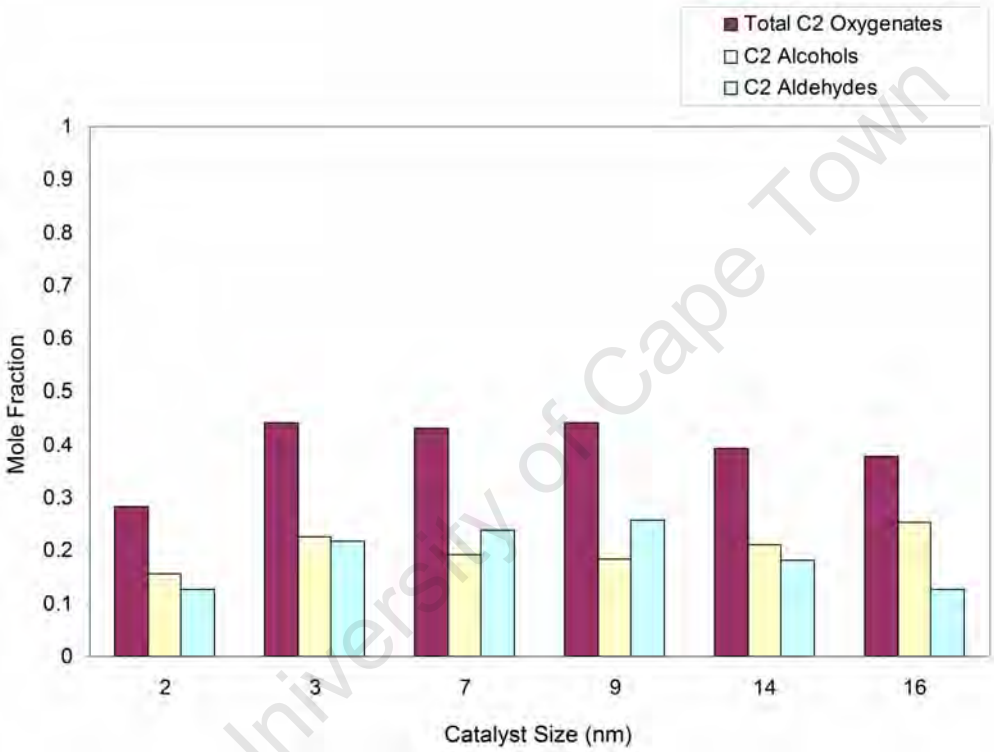

Figure C.2: Mole fraction of alcohols, aldehydes and total oxygenates in the C_2 fraction during steady state (50 - 300 min) on alumina supported model iron catalysts of differing crystallite sizes (T = 240 °C, P = 12 bar, $P_{syn-gas}$ = 10 bar, H_2/CO ratio = 2)

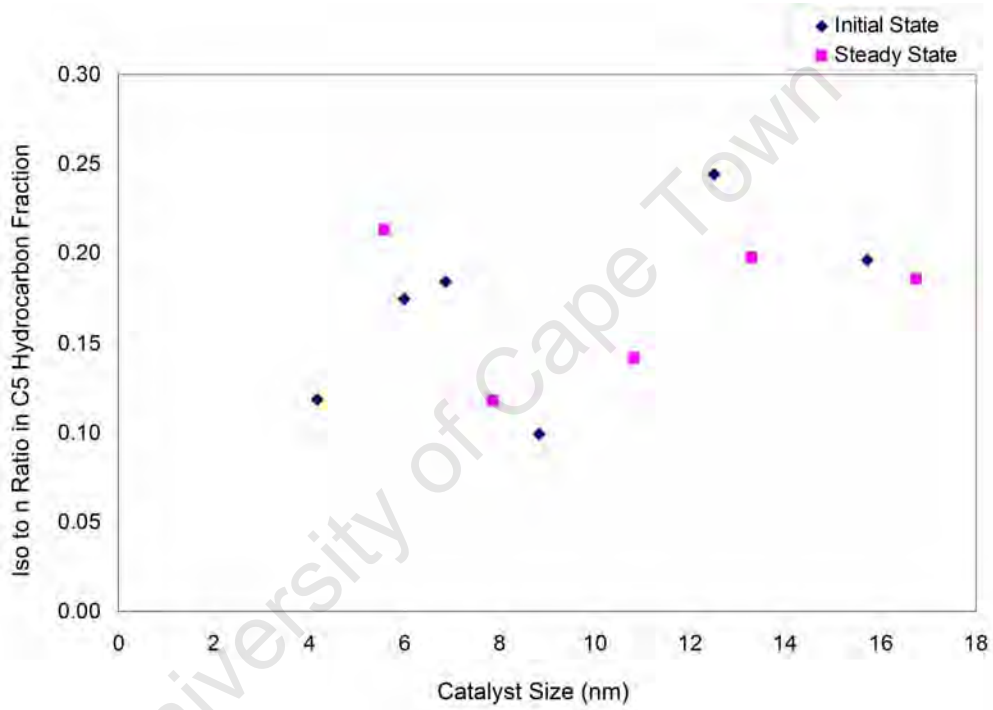

Figure C.3: Molar ratio of iso(branched) to n(straight) in the C_5 hydrocarbon fraction during both initial state (10 - 20 min at reduced crystallite sizes) and steady state (50 - 300 min at spent crystallite sizes) on alumina supported model iron catalysts (T = 240 °C, P = 12 bar, $P_{syn-gas}$ = 10 bar, H_2/CO ratio = 2)

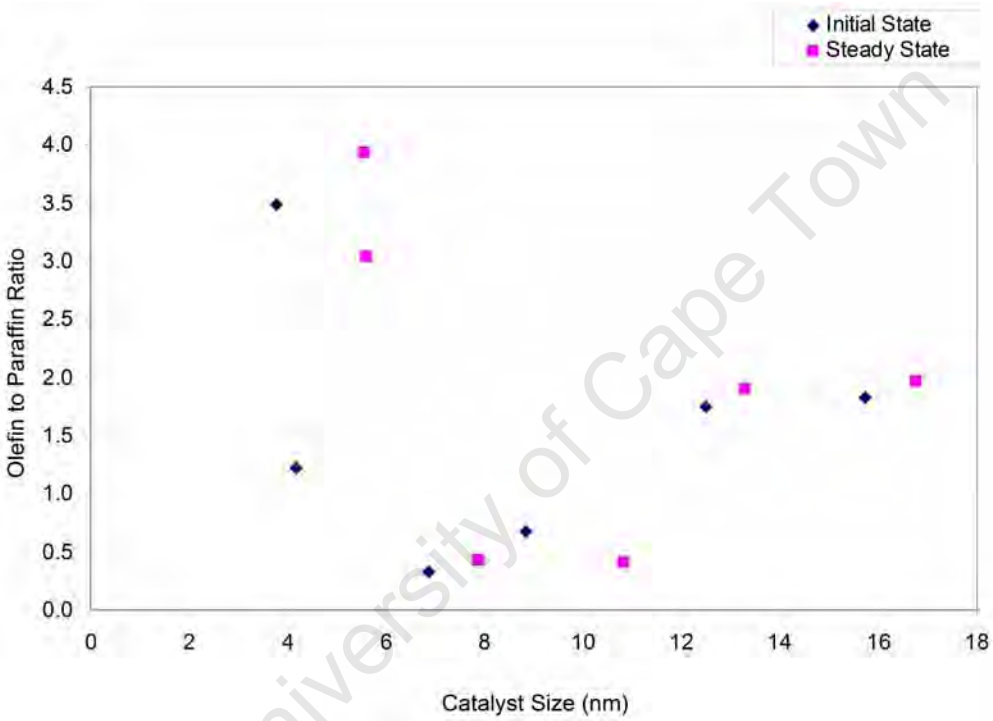

Figure C.4: Olefin to paraffin ratio in the C_2 hydrocarbon fraction during both initial state (10 - 20 min at reduced crystallite sizes) and steady state (50 - 300 min at spent crystallite sizes) on alumina supported model iron catalysts of differing crystallite sizes (T = 240 °C, P = 12 bar, $P_{syn-gas}$ = 10 bar, H_2/CO ratio = 2)

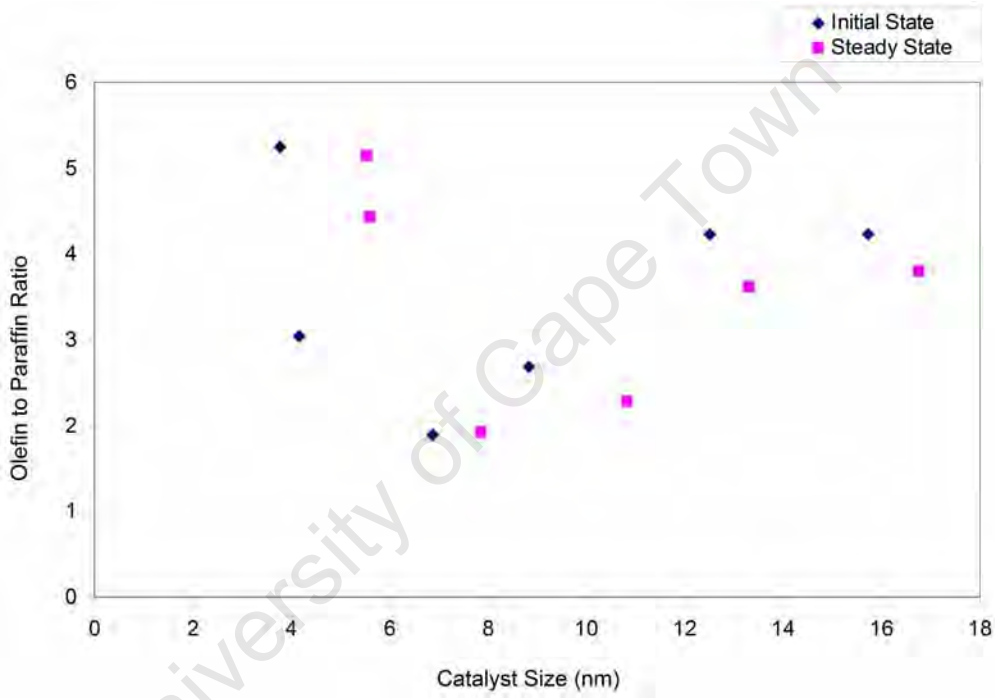

Figure C.5: Olefin to paraffin ratio in the C_3 hydrocarbon fraction during both initial state (10 - 20 min at reduced crystallite sizes) and steady state (50 - 300 min at spent crystallite sizes) on alumina supported model iron catalysts of differing crystallite sizes (T = 240 °C, P = 12 bar, $P_{syn-gas}$ = 10 bar, H_2/CO ratio = 2)

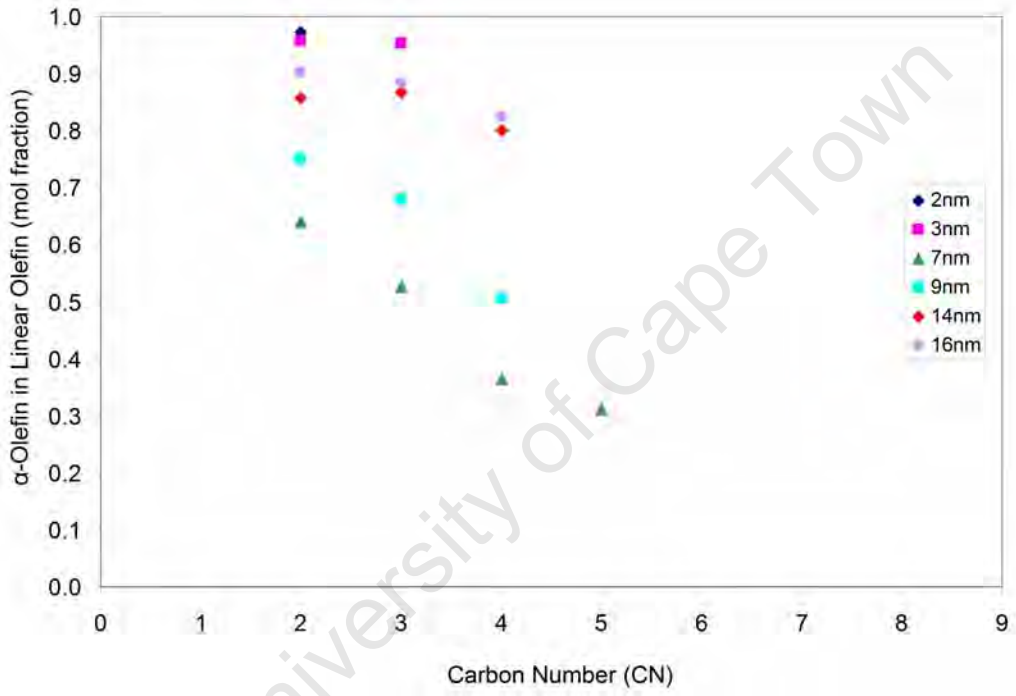

Figure C.6: Molar fraction of α-olefins in olefins during initial state (10 - 20 min at reduced crystallite sizes) and steady state (50 - 300 min at spent crystallite sizes) on alumina supported model iron catalysts of differing crystallite sizes (T = 240 °C, P = 12 bar, $P_{syn-gas}$ = 10 bar, H_2/CO ratio = 2)

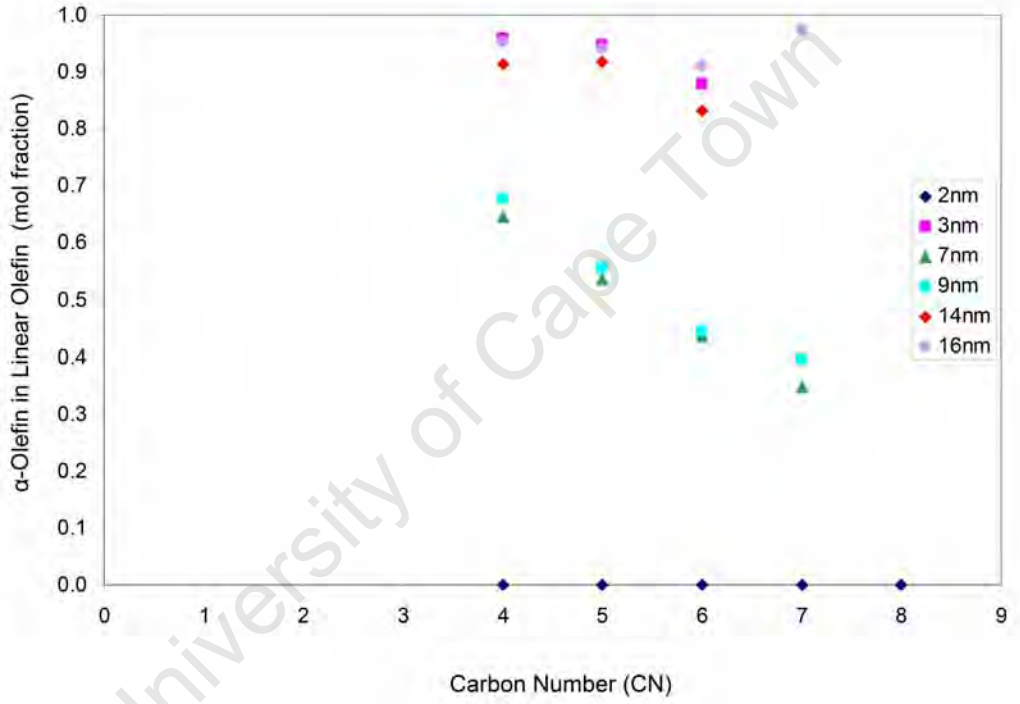

Figure C.7: Molar ratio of α-olefins in olefins as a function of carbon number during the steady state (50 - 300 min) on alumina supported model iron catalysts of differing crystallite sizes (T = 240 °C, P = 12 bar, $P_{syn-gas}$ = 10 bar, H_2/CO ratio = 2)

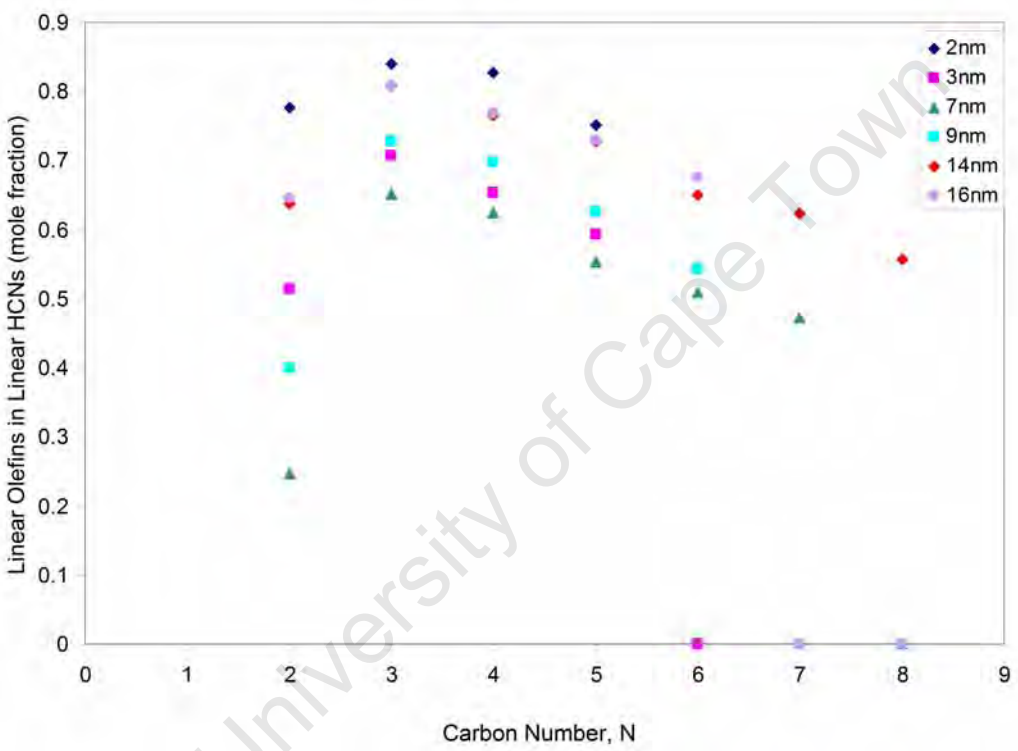

Figure C.8: Mole fraction of linear olefins in hydrocarbons during the initial state (10 - 20 min) on alumina supported model iron catalysts of differing crystallite sizes (T = 240 °C, P = 12 bar, $P_{syn-gas}$ = 10 bar, H_2/CO ratio = 2)

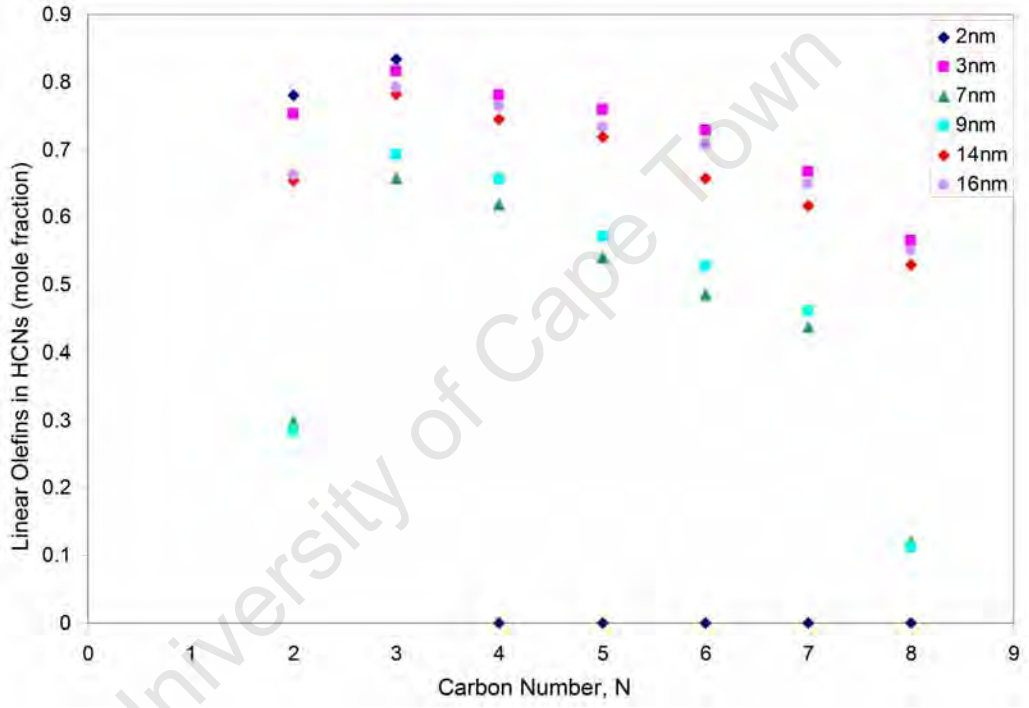

Figure C.9: Mole fraction of linear-olefins in hydrocarbon during the steady state (50 - 300 min) on alumina supported model iron catalysts of differing crystallite sizes (T = 240 °C, P = 12 bar, $P_{syn-gas}$ = 10 bar, H_2/CO ratio = 2)

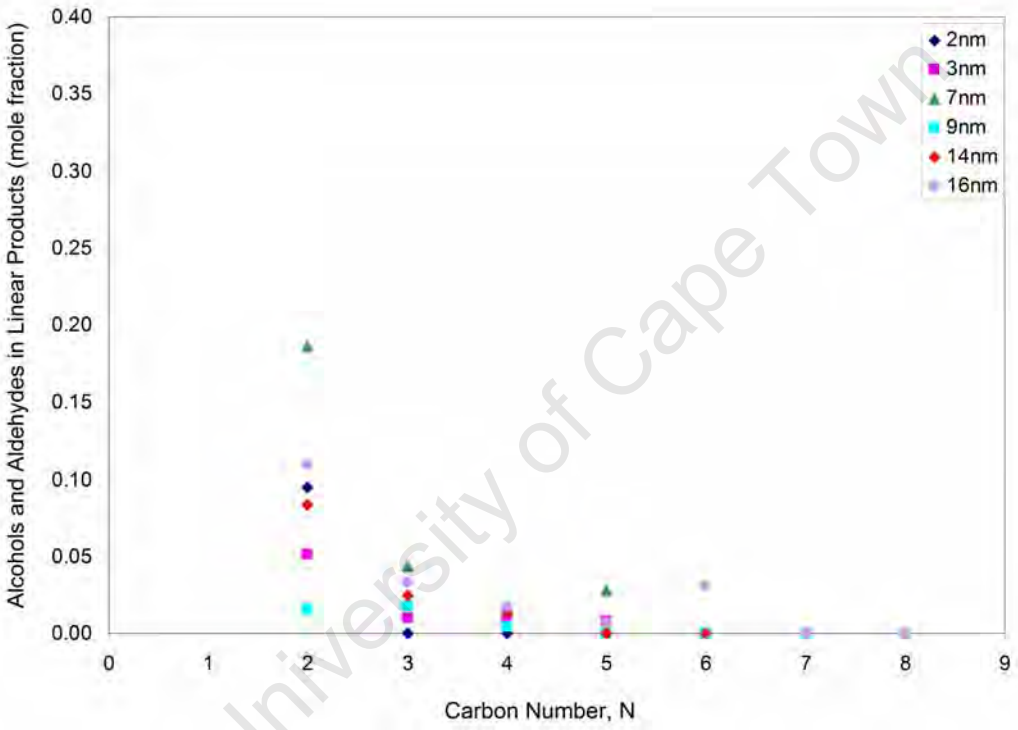

Figure C.10: Mole fraction of alchols and aldehydes in linear products as a function of carbon number during the initial (10 - 20 min) on alumina supported model iron catalysts of differing crystallite sizes (T = 240 °C, P = 12 bar, $P_{syn-gas}$ = 10 bar, H_2/CO ratio = 2)

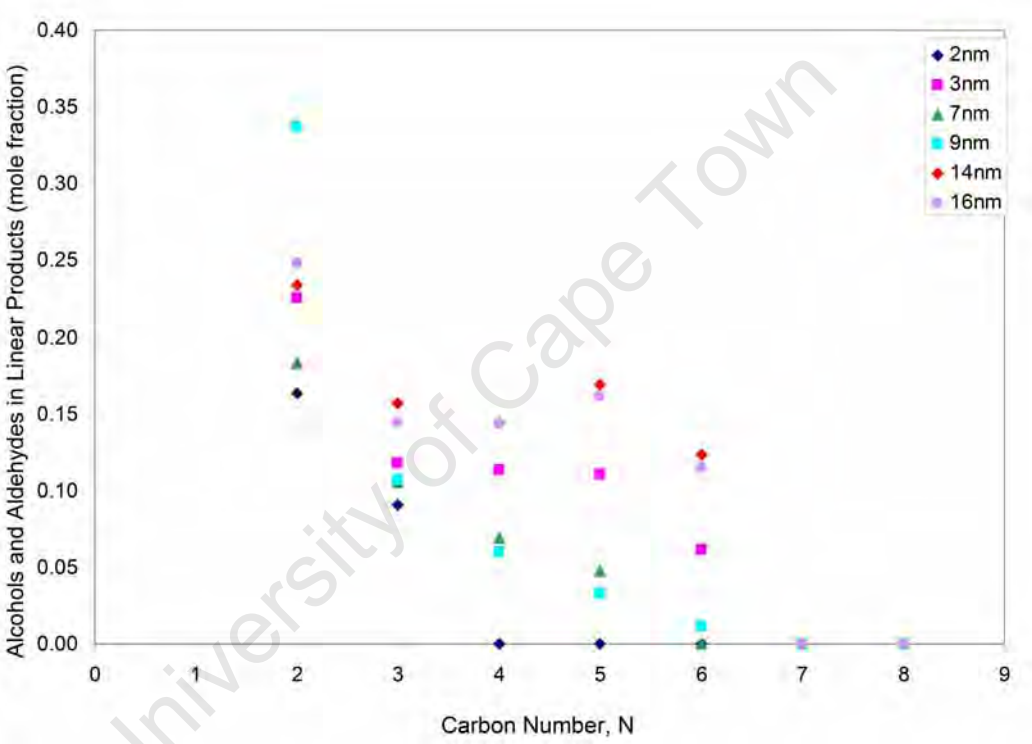

Figure C.11: Mole fraction of alchols and aldehydes in linear products as a function of carbon number during the steady state (50 - 300 min) on alumina supported model iron catalysts of differing crystallite sizes (T = 240 °C, P = 12 bar, $P_{syn-gas}$ = 10 bar, H_2/CO ratio = 2)

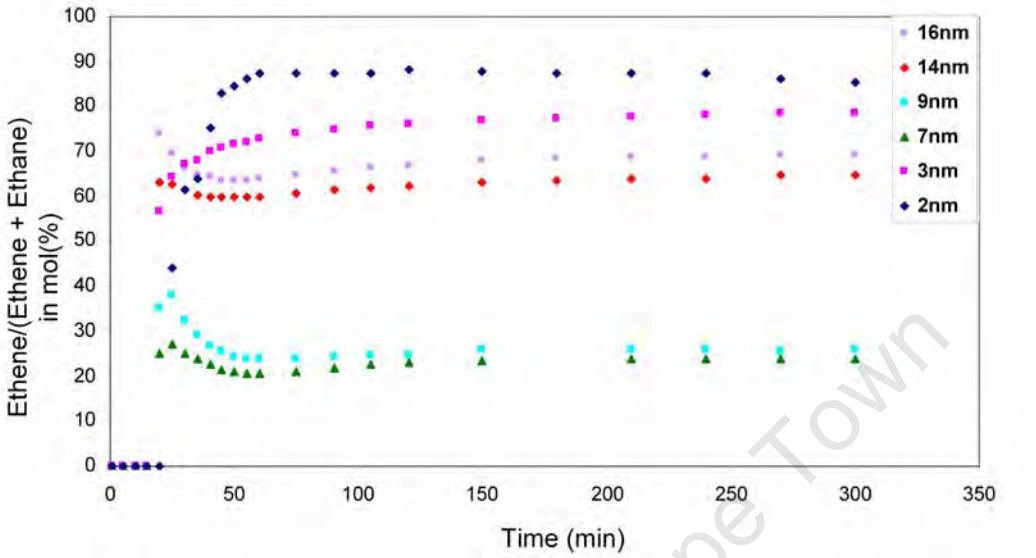

Figure C.12: Change in the olefin content of the C_2 fraction as a function of time (240 °C and 12 bar).

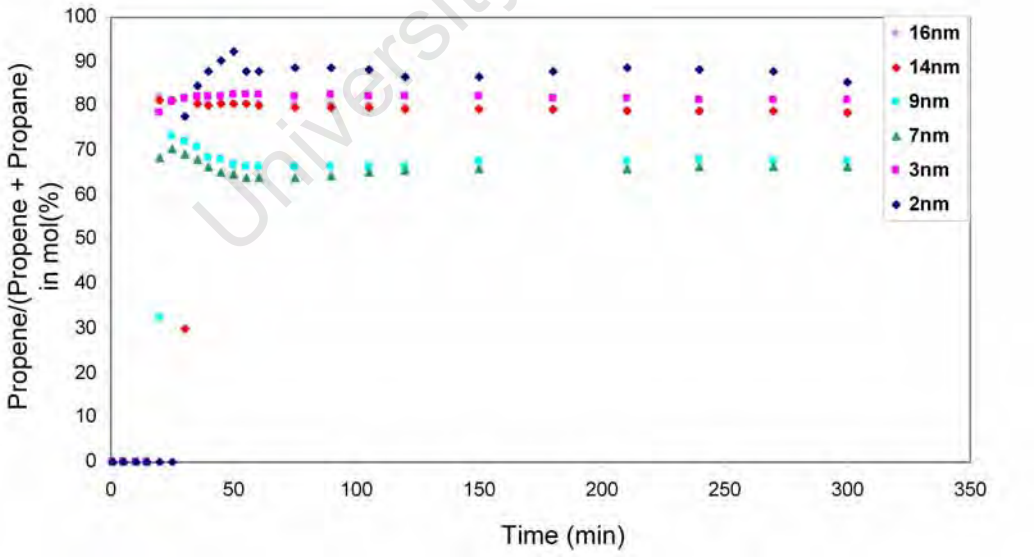

Figure C.13: Change in the olefin content of the C_3 fraction as a function of time (240 °C and 12 bar).

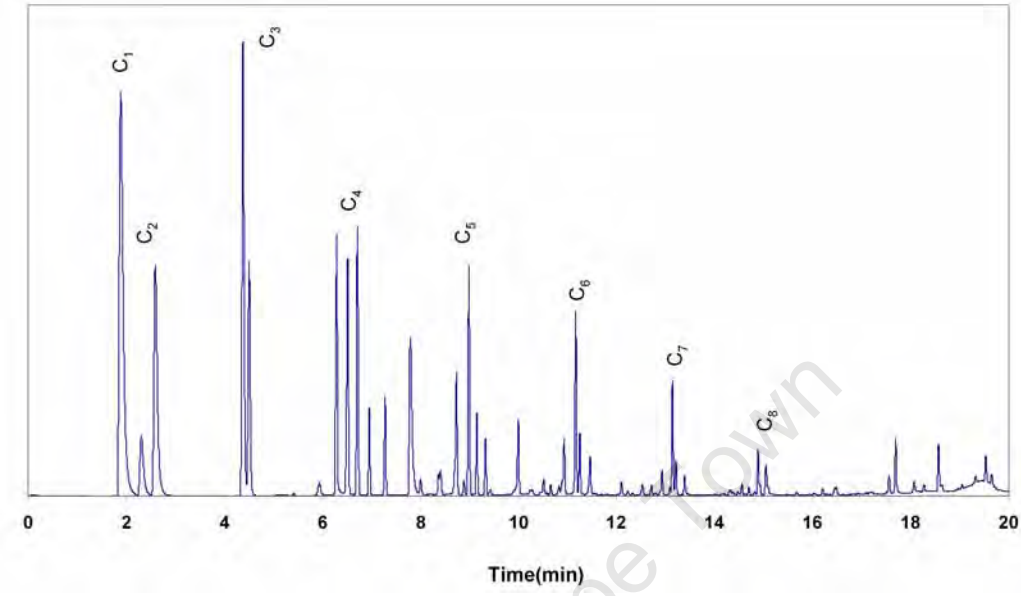

Figure C.14: A typical chromatogram obtained from GC-FID analysis of Fischer-Tropsch Synthesis at 240 °C and 12 bar. (Catalyst Sample : '7 nm', no water co-feed, 50 minutes run-time)

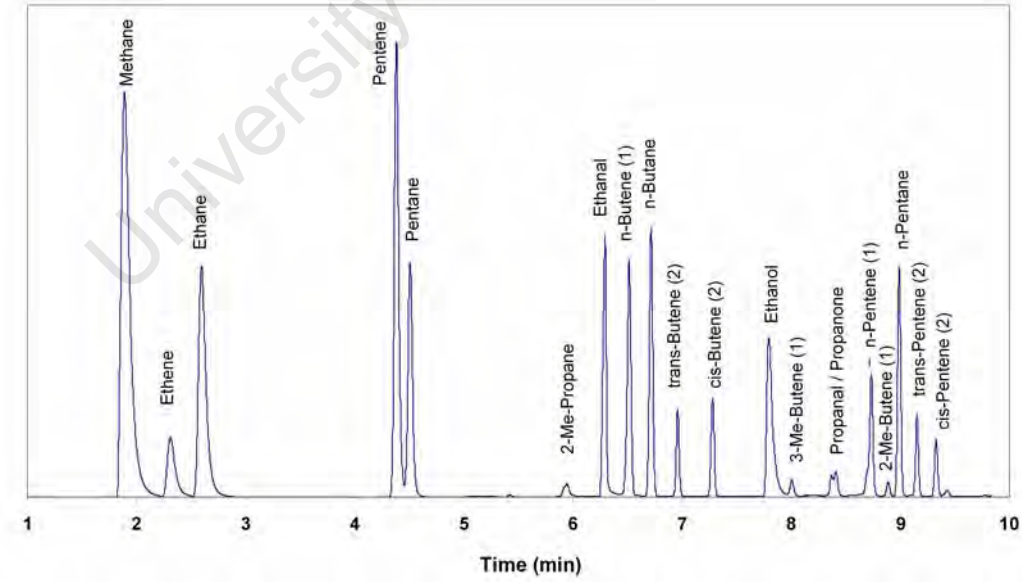

Figure C.15: A typical chromatogram of the first 10 min obtained from GC-FID analysis of Fischer-Tropsch Synthesis at 240 °C and 12 bar. (Catalyst Sample : '7 nm', no water co-feed, 50 min run-time)

Appendix D

Dependence on Water Partial Pressure

Table D.1: Results from Fischer-Tropsch testing in the initial stages of the experiment (10 - 20 min) on alumina supported iron catalysts of differing crystallite sizes ($T_{reaction}$ = 240 °C, $P_{syn-gas}$ = 10 bar, P_{water} = 3 bar, H_2/CO ratio = 2)

Sample Code		**2 nm**	**3 nm**	**7 nm**	**9 nm**	**14 nm**	**16 nm**
Reduced Size (nm)		3.77	4.17	6.89	8.83	12.60	15.72
Spent Size (nm)		8.61	8.19	24.63	25.10	19.97	18.89
Percentage Loading (%)		11.32	11.63	11.59	12.34	12.48	13.07
Degree of Reduction		0.98	0.98	0.83	0.84	0.72	0.79
Fischer-Tropsch Rate (mol-C/m^2Fe.min)		$4.74e-8$	$4.15e-8$	$1.33e-7$	$4.17e-7$	$6.79e-7$	$1.11e-6$
Carbon Monoxide Conversion		0.16	0.06	0.61	0.80	1.15	1.42
Carbon Dioxide Selectivity (%) [a]		64.14	67.78	69.55	35.21	48.01	86.99
Methane Selectivity (%) [b]		29.64	31.15	45.99	41.55	42.71	36.54
C_5+ Selectivity (%)		12.64	12.09	9.86	10.22	13.37	12.62
Paraffin Selectivity (%)	C_2 - C_4	10.55	13.13	16.81	13.94	7.24	11.45
	C_5+	2.50	3.24	3.66	3.03	3.63	3.36
	Total	13.06	16.38	19.70	16.97	10.88	14.81
Olefin Selectivity (%)	C_2 - C_4	38.38	34.66	25.17	24.78	27.98	33.52
	C_5+	8.02	7.04	2.39	5.57	7.69	7.80
	Total	46.40	41.70	29.95	30.35	35.67	41.32
Alcohol Selectivity (%)	C_2	2.39	4.30	0.23	1.91	2.33	0.89
	C_3+	0.71	0.74	0.14	0.54	2.61	0.54
Aldehyde Selectivity (%)	C_2	1.68	2.61	0.58	2.22	1.14	0.65
	C_3+	1.97	1.10	0.37	1.00	1.98	0.07
Ketone Selectivity (%)		0.28	0.35	0.03	0.12	0.48	0.19
Chain Growth Probability		0.4736	0.4871	0.5436	0.5353	0.6733	0.5373

[a] Selectivity with respect to total carbon monoxide conversion. As anaylyzed through TCD(CO_2) and FID(CO conversion).

[b] For all selectivities listed beyond this point, selectivity calculated with respect to total Volatile Organic Compounds (VOCs) as analyzed by FID.

Table D.2: Results from Fischer-Tropsch testing in the steady state stages of the experiment (50 - 300 min) on alumina supported iron catalysts of differing crystallite sizes ($T_{reaction}$ = 240 °C, $P_{syn-gas}$ = 10 bar, P_{water} = 3 bar, H_2/CO ratio = 2)

Sample Code		**2 nm**	**3 nm**	**7 nm**	**9 nm**	**14 nm**	**16 nm**
Reduced Size (nm)		4.17	3.77	6.89	8.83	12.60	15.72
Spent Size (nm)		8.61	8.19	24.63	25.10	19.97	18.89
Percentage Loading (%)		11.32	11.63	11.59	12.34	12.48	13.07
Degree of Reduction		0.98	0.98	0.83	0.84	0.72	0.79
Fischer-Tropsch Rate (mol-C/m^2Fe.min)		$5.81e-7$	$3.18e-7$	$5.46e-6$	$2.04e-6$	$3.21e-6$	$6.11e-6$
Carbon Monoxide Conversion (ratio)		0.15	0.07	0.60	1.86	1.96	3.16
Carbon Dioxide Selectivity (%) [a]		46.48	45.96	73.42	51.13	47.53	74.03
Methane Selectivity (%) [b]		28.27	30.60	41.57	36.15	40.10	33.94
C_5+ Selectivity (%)		13.11	12.68	10.47	13.87	14.69	11.82
Paraffin Selectivity (%)	C_2 - C_4	8.29	10.70	14.04	9.53	7.94	9.76
	C_5+	3.02	2.92	3.78	3.68	3.73	2.97
	Total	11.31	13.62	17.81	13.21	11.67	12.73
Olefin Selectivity (%)	C_2 - C_4	33.63	30.97	22.74	25.96	28.44	29.80
	C_5+	8.91	7.69	5.10	8.33	7.67	6.82
	Total	42.54	38.66	27.84	34.29	36.11	36.62
Alcohol Selectivity (%)	C_2	5.94	6.08	5.75	5.29	2.84	5.61
	C_3+	3.68	3.53	3.30	2.13	4.03	3.48
Aldehyde Selectivity (%)	C_2	2.97	4.04	5.30	6.40	2.15	3.08
	C_3+	1.86	0.92	1.10	0.51	2.10	0.94
Ketone Selectivity (%)		0.63	0.31	0.23	0.22	0.59	0.40
Chain Growth Probability		0.5773	0.5618	0.5754	0.6428	0.6719	0.5969

[a]Selectivity with respect to total carbon monoxide conversion. As anaylyzed through TCD(CO_2) and FID(CO conversion).

[b]For all selectivities listed beyond this point, selectivity calculated with respect to total Volatile Organic Compounds (VOCs) as analyzed by FID.

Table D.3: Results from Fischer-Tropsch testing in the initial stages of the experiment (10 - 20 min) on alumina supported iron catalysts of differing crystallite sizes ($T_{reaction}$ = 240 °C, $P_{syn-gas}$ = 10 bar, P_{water} = 6 bar, H_2/CO ratio = 2)

Sample Code		**2 nm**	**3 nm**	**7 nm**	**9 nm**	**14 nm**	**16 nm**
Reduced Size (nm)		3.77	4.17	6.89	8.83	12.60	15.72
Spent Size (nm)		10.94	11.41	29.93	23.32	22.84	21.55
Percentage Loading (%)		11.32	11.63	11.59	12.34	12.48	13.07
Degree of Reduction		0.98	0.98	0.83	0.84	0.72	0.79
Fischer-Tropsch Rate (mol-C/m^2Fe.min)		$4.42e-8$	$5.05e-8$	$1.56e-7$	$3.20e-7$	$6.95e-7$	$1.05e-6$
Carbon Monoxide Conversion		0.16	0.19	1.49	0.30	1.45	2.26
Carbon Dioxide Selectivity (%) [a]		66.94	78.12	28.39	65.96	32.85	80.91
Methane Selectivity (%) [b]		28.89	31.15	45.32	49.01	40.17	34.10
C_5+ Selectivity (%)		13.04	12.09	5.49	8.09	8.19	5.86
Paraffin Selectivity (%)	C_2 - C_4	10.97	13.13	15.98	7.50	17.62	14.62
	C_5+	3.17	3.24	3.86	0.88	3.33	1.50
	Total	14.14	16.38	19.85	8.38	20.95	16.12
Olefin Selectivity (%)	C_2 - C_4	33.91	34.66	18.89	17.76	17.62	33.88
	C_5+	7.19	7.04	2.91	2.42	3.29	3.32
	Total	41.11	41.70	21.80	20.18	20.91	37.20
Alcohol Selectivity (%)	C_2	2.32	4.30	1.41	3.22	3.20	1.01
	C_3+	1.72	0.74	0.61	1.05	1.96	0.19
Aldehyde Selectivity (%)	C_2	6.15	2.61	1.13	2.24	3.25	0.66
	C_3+	1.46	1.10	0.55	0.00	2.58	0.88
Ketone Selectivity (%)		0.24	0.35	0.09	2.95	0.30	0.16
Chain Growth Probability		0.4756	0.4871	0.5484	0.6986	0.6855	0.3999

[a] Selectivity with respect to total carbon monoxide conversion. As anaylyzed through TCD(CO_2) and FID(CO conversion).

[b] For all selectivities listed beyond this point, selectivity calculated with respect to total Volatile Organic Compounds (VOCs) as analyzed by FID.

Table D.4: Results from Fischer-Tropsch testing in the steady state stages of the experiment (50 - 300 min) on alumina supported iron catalysts of differing crystallite sizes ($T_{reaction}$ = 240 °C, $P_{syn-gas}$ = 10 bar, P_{water} = 6 bar, H_2/CO ratio = 2)

Sample Code		**2 nm**	**3 nm**	**7 nm**	**9 nm**	**14 nm**	**16 nm**
Reduced Size (nm)		4.17	3.77	6.89	8.83	12.60	15.72
Spent Size (nm)		8.61	8.19	24.63	25.10	19.97	18.89
Percentage Loading (%)		11.32	11.63	11.59	12.34	12.48	13.07
Degree of Reduction		0.98	0.98	0.83	0.84	0.72	0.79
Fischer-Tropsch Rate (mol-C/m^2Fe.min)		$2.23e-7$	$1.98e-7$	$1.26e-6$	$3.15e-6$	$5.69e-6$	$8.07e-6$
Carbon Monoxide Conversion (ratio)		0.43	0.04	1.47	3.45	3.70	4.30
Carbon Dioxide Selectivity (%) [a]		55.11	53.95	43.90	18.92	24.57	27.72
Methane Selectivity (%) [b]		27.35	30.60	44.69	40.09	36.20	30.95
C_5+ Selectivity (%)		14.63	12.68	10.07	10.54	9.83	12.60
Paraffin Selectivity (%)	C_2 - C_4	10.88	10.70	13.78	14.65	7.86	10.57
	C_5+	3.71	2.92	3.79	3.81	2.54	3.24
	Total	14.59	13.62	17.58	18.46	110.40	13.80
Olefin Selectivity (%)	C_2 - C_4	27.49	30.97	18.74	24.03	23.39	29.90
	C_5+	11.15	7.69	4.51	5.39	5.09	7.02
	Total	38.64	38.66	23.25	29.41	28.48	36.93
Alcohol Selectivity (%)	C_2	2.76	6.08	5.40	3.47	6.06	6.69
	C_3+	2.16	3.53	3.44	1.79	3.01	5.15
Aldehyde Selectivity (%)	C_2	5.49	4.04	4.70	4.39	8.29	3.50
	C_3+	2.66	0.92	0.55	0.77	1.52	1.05
Ketone Selectivity (%)		0.76	0.31	0.28	0.30	0.43	0.36
Chain Growth Probability		0.6158	0.5618	0.6043	0.5656	0.6045	0.5960

[a]Selectivity with respect to total carbon monoxide conversion. As anaylyzed through TCD(CO_2) and FID(CO conversion).

[b]For all selectivities listed beyond this point, selectivity calculated with respect to total Volatile Organic Compounds (VOCs) as analyzed by FID.

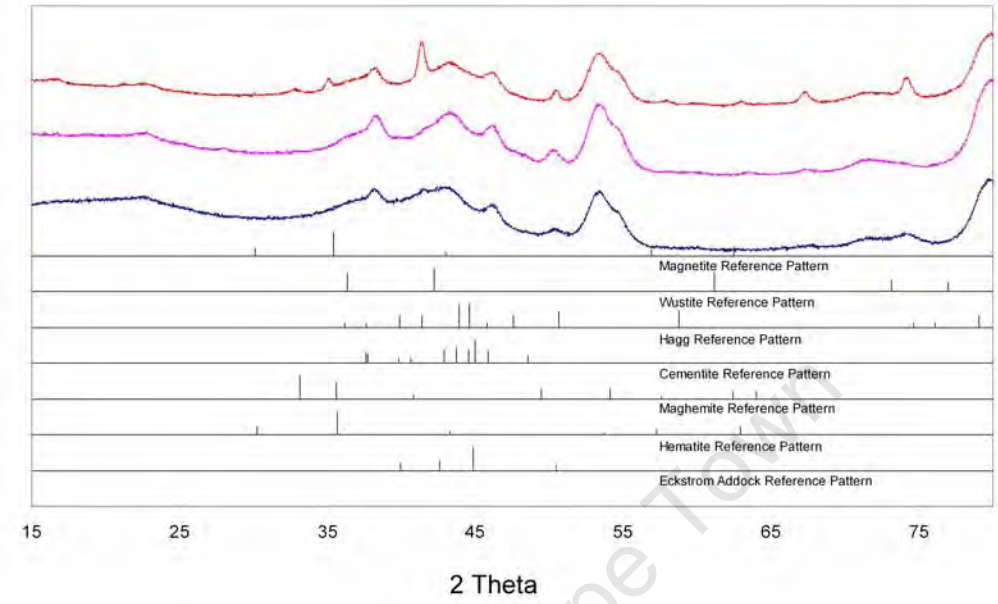

Figure D.1: Comparison of XRD patterns of '2 nm' catalyst at three different water partial pressure conditions (no water *(bottom)*, 3 bar water *(middle)* and 6 bar water *(top)*), 240 °C and $P_{syn-gas}$ = 10 bar, H_2/CO ratio = 2

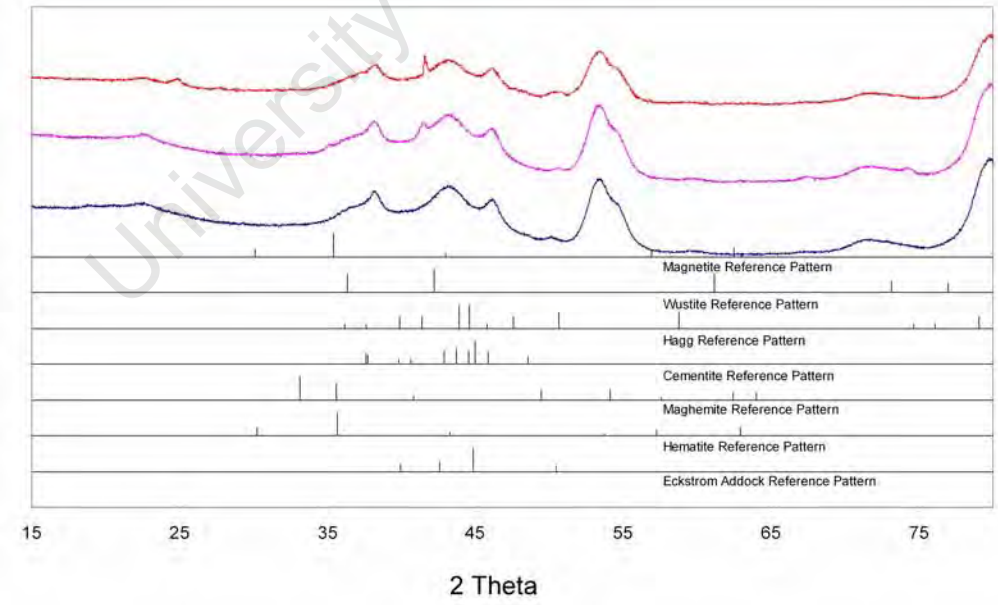

Figure D.2: Comparison of XRD patterns of '3 nm' catalyst at three different water partial pressure conditions (no water *(bottom)*, 3 bar water *(middle)* and 6 bar water *(top)*), 240 °C and $P_{syn-gas}$ = 10 bar, H_2/CO ratio = 2

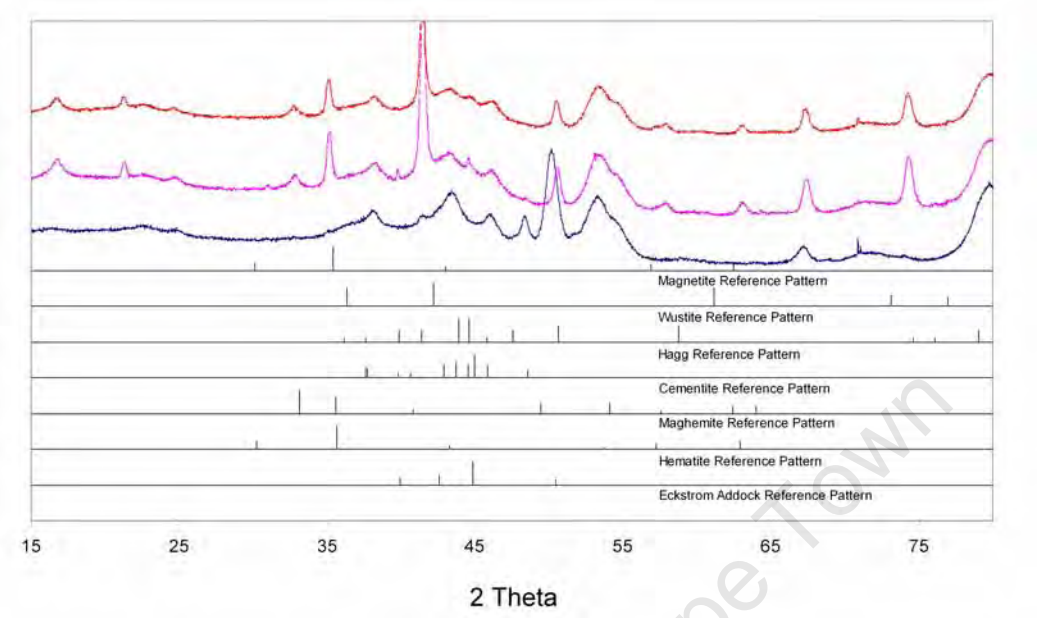

Figure D.3: Comparison of XRD patterns of '7 nm' catalyst at three different water partial pressure conditions ((no water *(bottom)*, 3 bar water *(middle)* and 6 bar water *(top)*), 240 °C and $P_{syn-gas}$ = 10 bar, H_2/CO ratio = 2

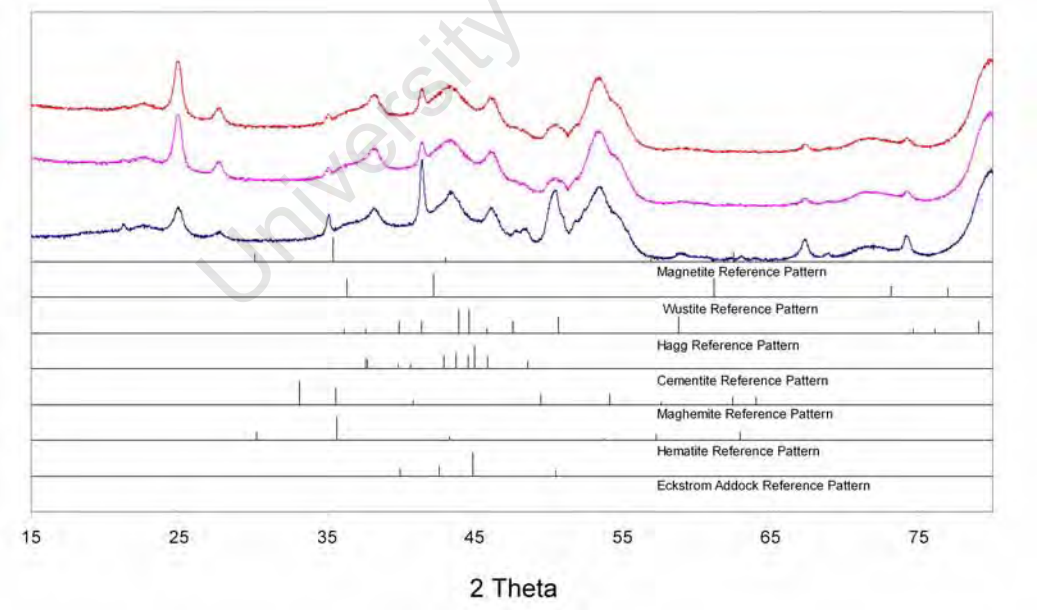

Figure D.4: Comparison of XRD patterns of '9 nm' catalyst at three different water partial pressure conditions (no water *(bottom)*, 3 bar water *(middle)* and 6 bar water *(top)*), 240 °C and $P_{syn-gas}$ = 10 bar, H_2/CO ratio = 2

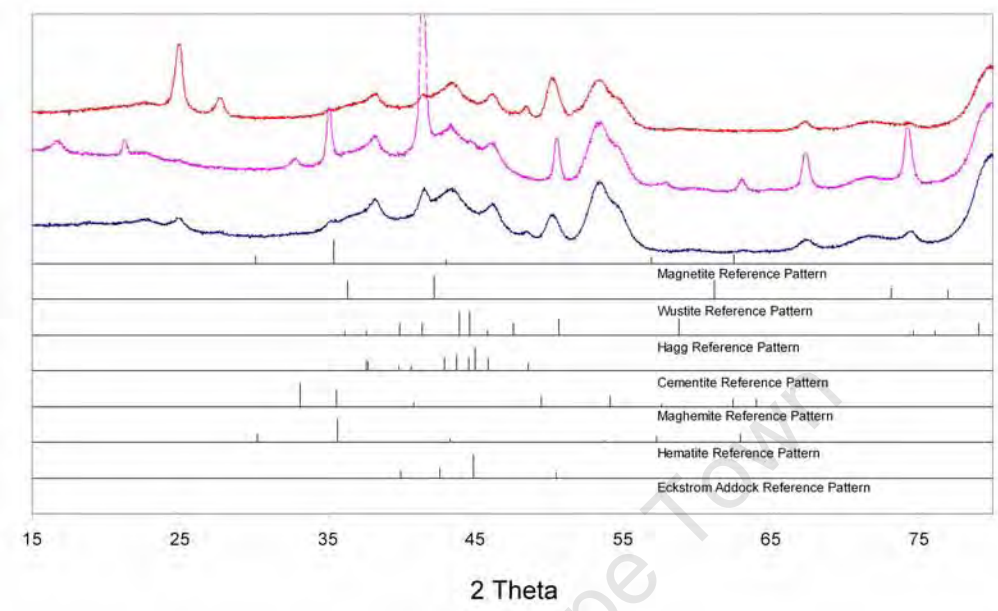

Figure D.5: Comparison of XRD patterns of '14 nm' catalyst at three different water partial pressure conditions (no water *(bottom)*, 3 bar water *(middle)* and 6 bar water *(top)*), 240 °C and $P_{syn-gas}$ = 10 bar, H_2/CO ratio = 2

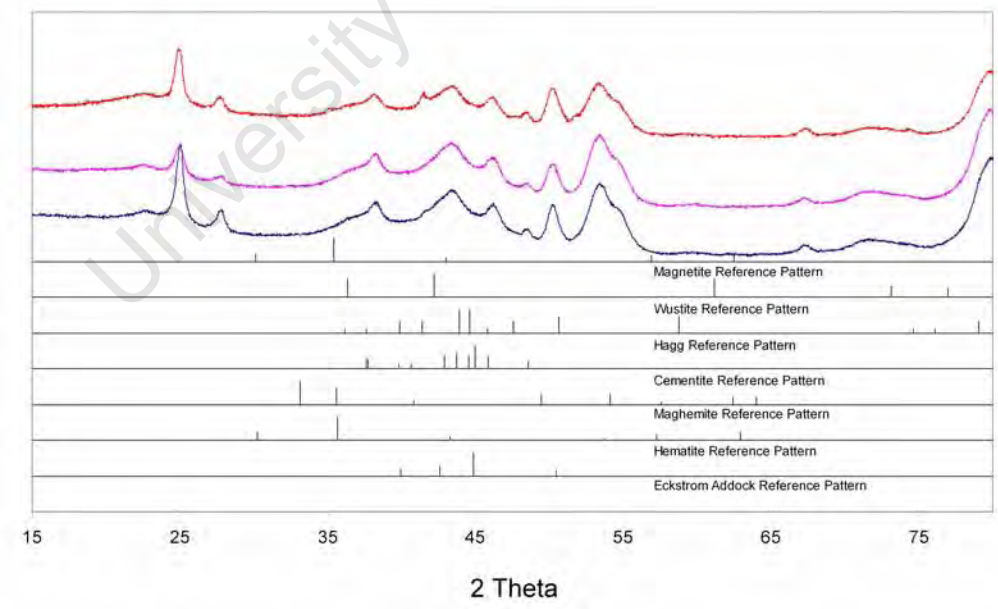

Figure D.6: Comparison of XRD patterns of 16nm catalyst at three different water partial pressure conditions (no water *(bottom)*, 3 bar water *(middle)* and 6 bar water *(top)*), 240 °C and $P_{syn-gas}$ = 10 bar, H_2/CO ratio = 2

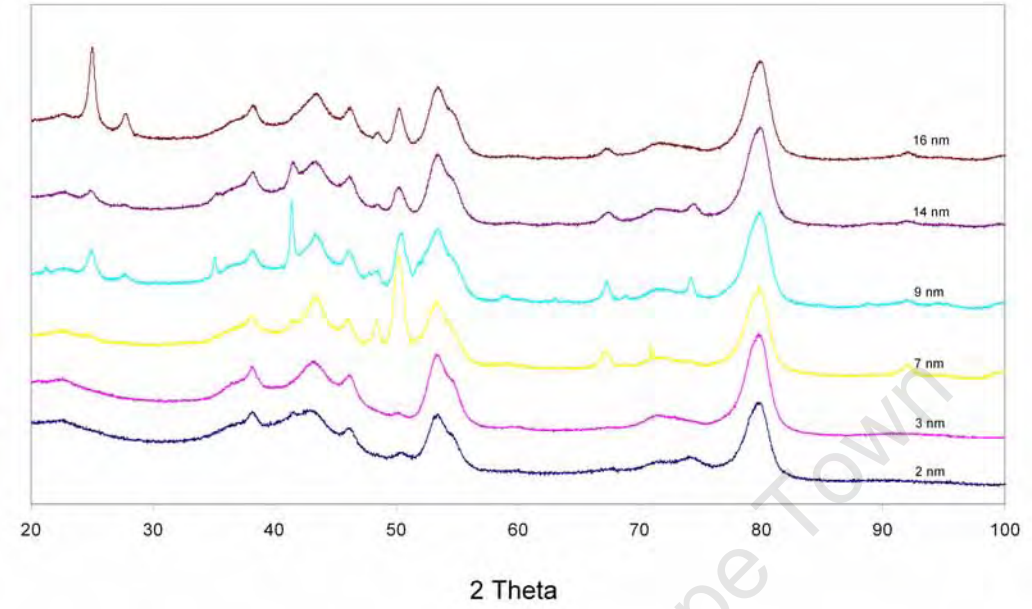

Figure D.7: Comparison of XRD patterns of all 6 catalyst samples at a condition of no water addition, 240 °C and $P_{syn-gas}$ = 10 bar, H_2/CO ratio = 2

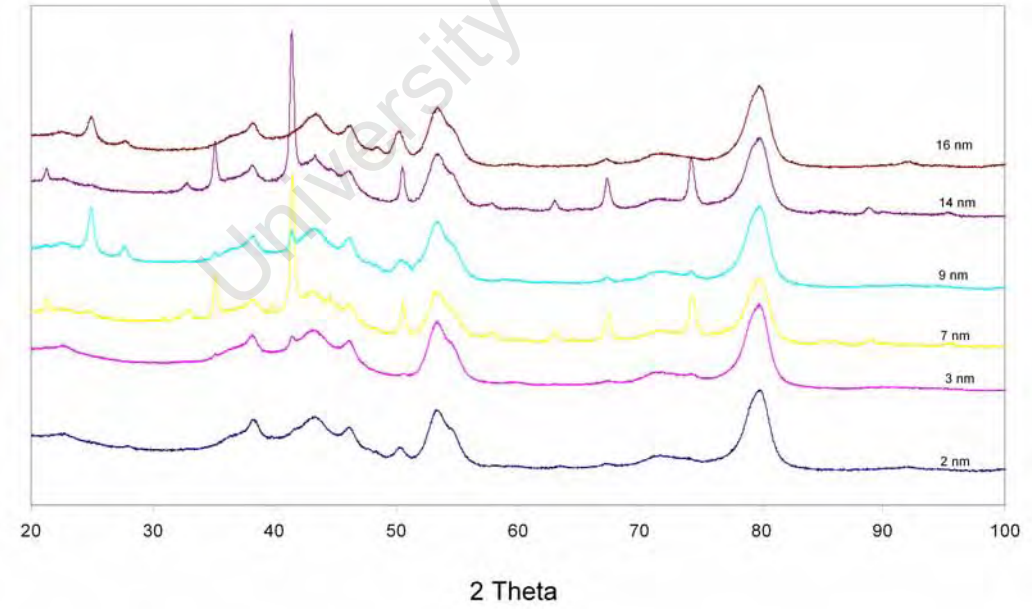

Figure D.8: Comparison of XRD patterns of all 6 catalyst samples at a condition of 3 bar water addition, 240 °C and $P_{syn-gas}$ = 10 bar, H_2/CO ratio = 2

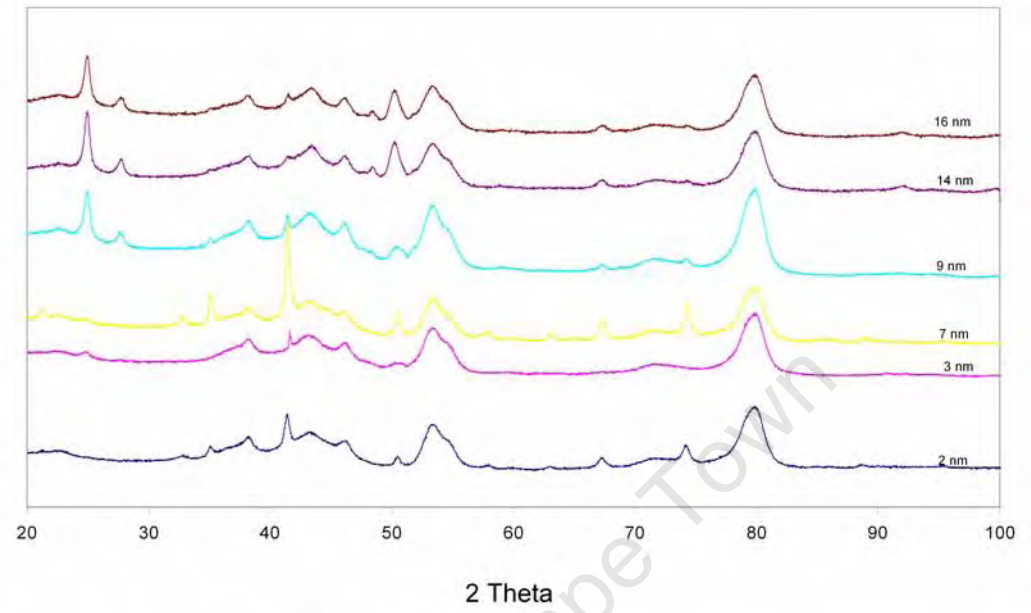

Figure D.9: Comparison of XRD patterns of all 6 catalyst samples at a condition of 6 bar water addition, 240 °C and $P_{syn-gas}$ = 10 bar, H_2/CO ratio = 2

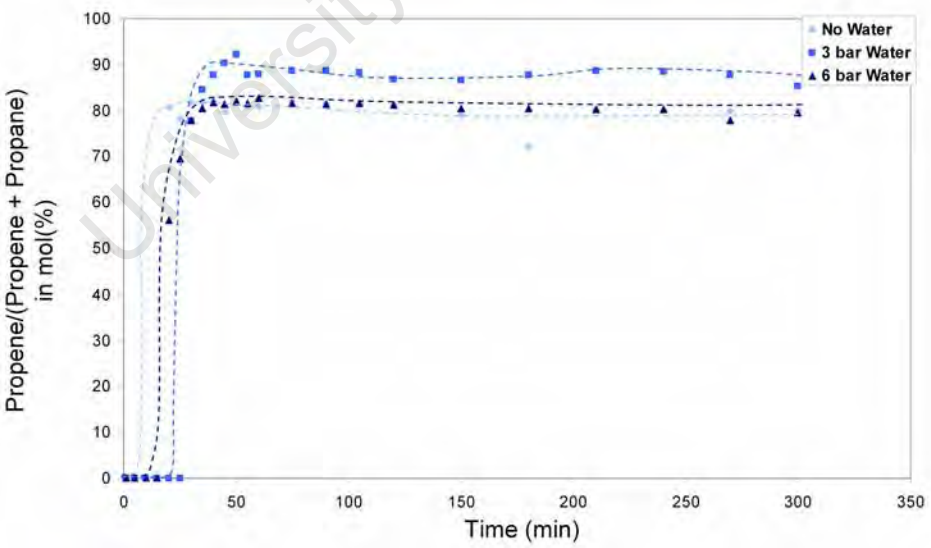

Figure D.10: Change in the olefin content of the C_3 fraction as a function of time of the '2 nm' catalyst at different water partial pressure conditions. $T_{reaction}$ = 240 °C, $P_{syn-gas}$ = 10 bar, H_2/CO ratio = 2).

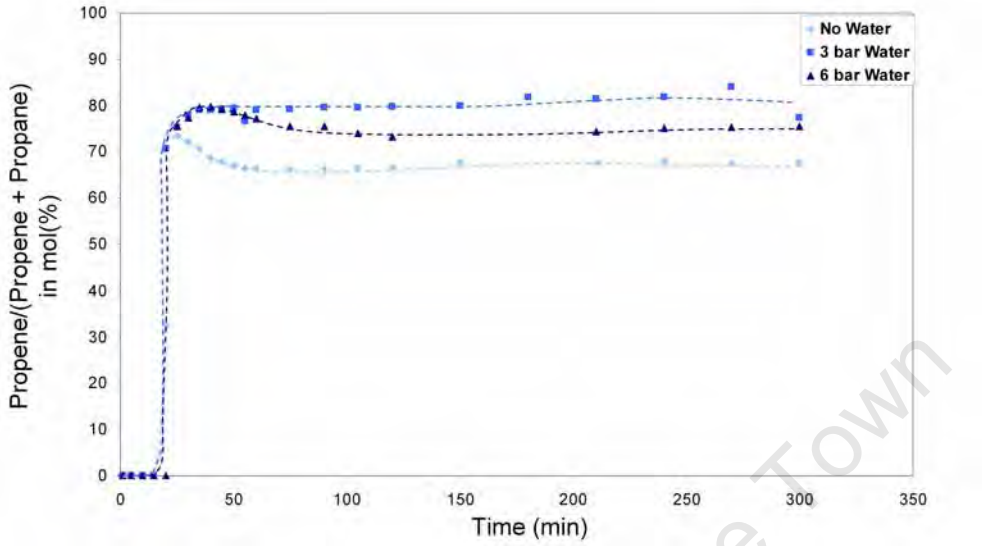

Figure D.11: Change in the olefin content of the C_3 fraction as a function of time of the '9 nm' catalyst at different water partial pressure conditions. $T_{reaction}$ = 240 °C, $P_{syn-gas}$ = 10 bar, H_2/CO ratio = 2).

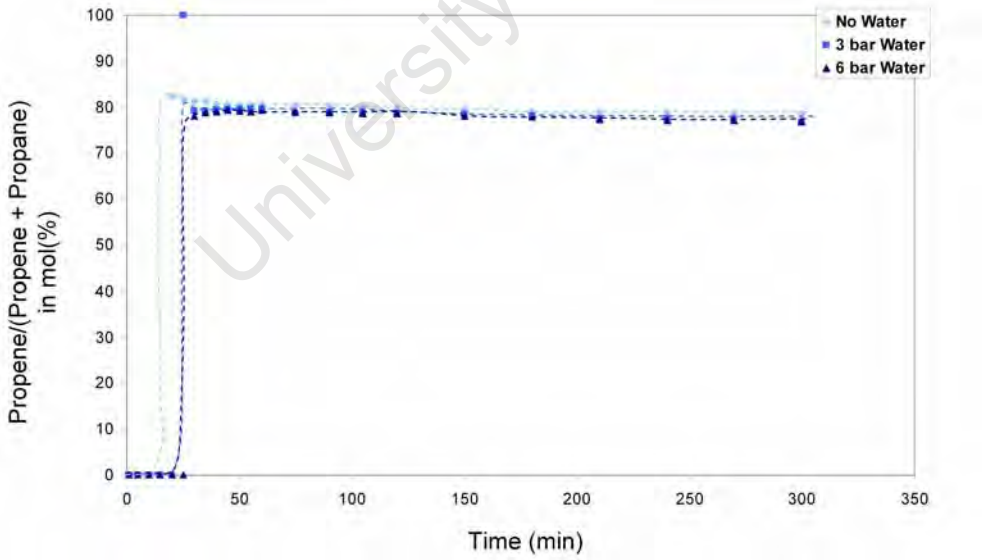

Figure D.12: Change in the olefin content of the C_3 fraction as a function of time of the '9 nm' catalyst at different water partial pressure conditions. $T_{reaction}$ = 240 °C, $P_{syn-gas}$ = 10 bar, H_2/CO ratio = 2).

Appendix E

Calculation of Surface Area

In the calculation of surface area, two possible methods can be used; firstly to use a single average crystallite size and secondly to use a size distribution. In this study the first method was used, as it was discovered that the two methods do not differ significantly in terms of the final results. A comparison between the two methods, calculated for a 9 nm catalyst, the percentage difference between the two methods was shown to be 5.5%.